**Czech Technical University in Prague**
**Faculty of Mechanical Engineering**

**Department of Technical Mathematics**
**Field of study: Mathematical and physical engineering**

# Numerical Simulation of Fluid-Structure-Acoustic Interaction in Human Phonation

DISSERTATION THESIS

Author: Ing. Jan Valášek
Supervisor: Doc. RNDr. Petr Sváček, Ph.D.
Year: 2021

**Statutory declaration**

I hereby declare that this thesis is my own work. Where other sources of information have been used, they have been acknowledged and referenced in the list of used literature and other sources.

I understand that my work relates to the rights and obligations under the Act No. 121/2000 Sb., the Copyright Act, as amended, in particular the fact that the Czech Technical University in Prague has the right to conclude a license agreement on the use of this work as a school work pursuant to Section 60 paragraph 1 of the Copyright Act.

In Prague .....

.....
Jan Valášek

**Acknowledgement**

I would like to express many thanks and sincere gratitude to my supervisor Petr Sváček for his judicious guidance, big patience and exceptional support during the whole time of my studies. I am also very grateful to Jaromír Horáček from the Institute of Thermomechanics of the Czech Academy of Sciences, who provided me with skilled advice, valuable suggestions and reading of (not only) this manuscript. Next, I would like to thankfully acknowledge the numerous discussions and consults with the Hynek Řezníček and other colleagues from the Department of Technical Mathematics and with Viktor Hruška from Faculty of Electrical Engineering, CTU in Prague. Further, I am indebted to prof. Manfred Kaltenbacher from the TU Wien who invited me to aeroacoustic problems and methods under his supervision. I am also obliged to Stefan Schoder, Klaus Roppert and other members of prof. Kaltenbacher research group for many inspired conversations on the topic and for accepting me into their collective.

Finally, the greatest appreciation goes to my family for their support during all of my studies and to my wife Markéta for her patience, caring and love.

This work was supported by the Student Grant Competition of CTU, namely by grants No. SGS13/174/OHK2/3T/12, SGS16/206/OHK2/3T/12 and SGS19/154/OHK2/3T/12, and by the Czech Science Foundation, namely grants No. GAP101/11/0207, GA16-01246S and GA19-04477S. Furthermore, my research was also partially supported by the Center of Advanced Aerospace Technology (CZ.02.1.01/0.0/0.0/16_019/0000826) in the framework of ESIF, EU Operational Programme Research, Development and Education.

Jan Valášek

*Název:*

**Numerická simulace interakce tekutiny, elastického tělesa a akustiky v problému lidské fonace**

*Autor:* Ing. Jan Valášek
*Obor:* Matematické a fyzikální inženýrství
*Druh práce:* Disertační práce
*Vedoucí práce:* Doc. RNDr. Petr Sváček, Ph.D.
Katedra technické matematiky, Fakulta strojní, ČVUT v Praze
*Konzultant:* Ing. Jaromír Horáček, DrSc.
Ústav termomechaniky, Akademie věd České republiky

*Abstrakt:* První část dizertační práce se zabývá numerickou simulací interakce proudící tekuitny a elastického tělesa (FSI) v 2D modelování vibrace lidských hlasivek vybuzených prouděním vzduchu. Deformace lidských hlasivek je popsána pomocí lineárního elastického modelu a proudění tekutiny je modelováno nestlačitelnými Navierovými-Stokesovými rovnicemi v ALE formulaci, která umožňuje zahrnout efekty časově proměnné oblasti proudění. Prostorová diskretizace obou podúloh je realizována metodou konečných prvků (FEM) a pro časovou diskretizaci elastického tělesa je použita Newmarkova metoda, zatímco problém proudění je aproximován v čase pomocí metody BDF2. Specialní pozornost je věnována stabilizaci FEM pro aproximaci proudění, výpočtu aerodynamických sil a okrajovým podmínkám předepsaným na vstupu do glotálního kanálu. Je porovnána penalizační okrajová podmínka s Dirichletovou a do-nothing okrajovou podmínkou a jsou ukázány její výhody pro řešení konfigurací vnitřní aerodynamiky, kdy dochází k uzavírání kanálu. Zejména je určena závislost kritické flutterové rychlosti proudění na penalizačním parametru a dále je analyzován přenos energie mezi proudící tekutinou a kmitajícím elastickým tělesem.

V druhé části dizertace je FSI problém rozšířen na problém na interakce proudící tekutiny, elastické struktury a akustiky. Tento problém zahrnuje popis aeroakustických a vibroakustických úloh motivovaných modelováním lidské fonace. Představený hybridní aeroakustický přístup dovoluje určit zvukovou hladinu na základě simulace nestlačitelného proudění, tj. akustický výpočet má formu postprocesingu výsledků FSI úlohy. Jsou popsány alternativní formulace zvukových zdrojů a jejich numerická implementace v několika vyšetřovaných případech. Numerické výsledky obsahují analýzu frekvenčních charakteristik několika modelů vokálního traktu (VT), které byly určeny pomocí řešení Helmholtzovy rovnice s využitím PML metody na konci VT pro modelování problému s volnou hranicí. Dále vypočtený zvuk vibroakustického původu, tj. vybuzený čistě kmitáním hlasivek, dosahuje výrazně nižší zvukové hladiny než zvuk aeroakustického původu. Aeroakustické simulace se skládají z výpočtu zvukových zdrojů na základě výsledků proudění, z interpolace zvukových zdrojů na akustickou síť a ze záverečného modelování postupného šíření těchto zdrojů v čase skrz vokální trakt. Jsou srovnány tři různé přístupy – Lighthillova akustické analogie (LH), (zjednodušená) perturbovaná konvektivní vlnová rovnice (sPCWE) a aeroakustická vlnová rovnice (AWE). Hladina zvuku vykazuje nadhodnocení v případě Lighthillovy analogie a téměř totožné výsledky při použití přístupů sPCWE a AWE. Ve všech případech jsou v získaných akustických spektrech dominantní akustické resonance (formanty) použitého modelu vokálního traktu.

*Klíčová slova:* Interakce proudění s elastickým tělesem, interakce proudění a elastického tělesa i akustiky, lineární elasticita, nestlačitelné proudění tekutiny, Navierovy-Stokesovy rovnice, Lighthillova akustická analogie, perturbovaná konvektivní vlnová rovnice, aeroakustická vlnová rovnice, metoda konečných prvků, ALE metoda, PML vrstva, modelování lidské fonace.

*Title:*

**Numerical Simulation of Fluid-Structure-Acoustic Interaction in Human Phonation**

*Author:* Ing. Jan Valášek

*Abstract:* The first part of dissertation thesis deals with the numerical simulation of the fluid-structure interaction (FSI) in 2D modelling the vocal folds vibration excited by airflow. The vocal fold (VF) deformation is described by the linear elasticity model and the flow is modelled by the incompressible Navier-Stokes equations in the arbitrary Lagrangian-Eulerian (ALE) formulation in order to take into account the time-dependence of the flow domain. The space discretization of both subproblems is realized by the finite element method (FEM) and the Newmark method for time discretization of the structure is applied while the fluid flow problem is approximated in time by the BDF2 method. A special attention is paid to the fluid flow stabilization, to the calculation of aerodynamic forces and to the airflow inlet boundary conditions at the entrance to the glottal channel. The penalization boundary condition is compared with the Dirichlet and the do-nothing boundary condition and its advantages are shown for solving of the internal aerodynamics configurations when the channel is closing. Particularly, the dependence of critical flutter airflow velocity on the penalization parameter is determined and the energy transfer between airflow and the vibrating elastic body is analyzed.

The second part of thesis extended FSI problem to the interaction of fluid flow, elastic body and acoustics. It addresses the aeroacoustic and the vibroacoustic problems motivated by human phonation. The presented hybrid aeroacoustic approaches allows to predict sound based on the incompressible flow simulation, i.e. acoustic computation has the form of the FSI results postprocessing. Alternative sound source formulations and their numerical implementations are described and applied in several investigated cases. The numerical results contain analysis of frequency characteristics of several vocal tract (VT) models which were determined by solving the Helmholtz equation with considered perfectly matched layer technique at the VT end representing open-boundary condition. Further the computed sound of vibroacoustic origin, i.e. excited purely by the VF vibration, reaches significantly lower sound pressure levels (SPL) than the sound of aeroacoustic origin. The aeroacoustic simulations comprise the sound sources evaluation in the computed airflow pattern, the sound sources interpolation on the acoustic grid and finally modelling of the sound sources transient propagation in the VT. Three different approaches – namely the Lighthill analogy (LH), the (simplified) perturbed convective wave equation (sPCWE) and the aeroacoustic wave equation (AWE), are compared. The SPL show overestimation in the case of LH and almost identical results of sPCWE and AWE. In all cases the excited spectra of acoustic pressures are dominated by the acoustic resonances (formants) of the vocal tract model.

*Key words:* Fluid-structure interaction, fluid-structure-acoustic interaction, linear elasticity, incompressible fluid flow, Navier-Stokes equations, Lighthill acoustic analogy, perturbed convective wave equation, aeroacoustic wave equation, finite element method, ALE method, perfectly-matched layer, human phonation modelling.

# Table of contents

# Chapter 1

# Introduction

Fluid-structure interaction (FSI) is a coupled problem, where the solutions of elastic body deformation subproblem and fluid flow subproblem depends on each other and thus they cannot be solved independently. It is also mathematically beautiful problem, which has many technical applications, e.g. the bridge or the airfoil design, [40], [47], and the liquid packing system, [60], or the paper transport in printing machines, see [138], etc. More recently FSI problems found usage also in biomechanical engineering, e.g. simulation of blood flow in vessels [34] and flow-induced vibrations of vocal folds, [98], [102], [95], etc.

Fluid-structure-acoustic interaction (FSAI) can be understood in this scope as multiphysical generalization of FSI, [90]. It consists of three different physical fields – the deformation of an elastic body, the complex fluid flow and the acoustics together with all mutual couplings. The solution of FSAI problem inherits difficulties of all the subproblems. Typical technical problems involving FSAI are e.g. design of ventilators, air-conditioning vents or engines, [82], [134], where the FSAI simulation can help already in first stages of design to reduce significantly the sound emission. The simulation of human phonation is a prominent example of other than purely technical application, [139], [166].

In this thesis the FSAI solution is sought with the help of mathematical modelling and numerical approximation by the finite element method (FEM), particularly, a specialized (and therefore more efficient) solver for solution of each subproblem is used. This approach is called partitioned scheme, see [89]. The coupled nature of the problem leads to iterative loop, where the fulfillment of coupling conditions is tested in every loop until a convergence criterion is reached. This results usually in high computational demands.

The thesis describes a general algorithm of FSAI numerical solution with the goal to apply all derived methodology to the simulation of human phonation. Prof. Kaltenbacher calls exaggeratedly this problem during his lectures as “Holy Grail of numerical simulation” due to complexity of all involved physics and presence of strong nonlinearities, see [157].

## 1.1 Motivation

The human phonation is highly interesting phenomenon under ongoing research, see for example [105]. Despite substantial advances in latest years the human phonation process has not been fully understood yet. A better understanding can help to improve the treatment of people with voice disorders, to design suitable vocal exercises for singers and other voice professionals or to help with the development of new voice prothesis, see [163]. Due to the practical inaccessibility of the human vocal folds for detail experimental investigations, the mathematical modelling and the numerical simulations have recently become to be an important tool used in the research, see e.g. [156].

The human voice is a part of our personality, patients with indisposed or impaired voice experience high psychological stress, hardly quantifiable. On the other hand the economic losses connected with the enforced absence in work, where voice is necessary, are only in USA estimated up to $160 billions per year, see [121].

The advancement in the mathematical formulation and the numerical simulation of the introduced problem can help also in many areas closely associated with the mechanisms present in FSI and especially in FSAI problems as described above, see e.g. [34], [103].

### 1.1.1 Human voice from medical point of view

Human voice is created by the flow-induced vibrations of vocal folds. The human vocal folds (VFs) are a part of the larynx situated in the anterior neck, see Figure 1.1. The larynx connecting the inferior part of the pharynx with the trachea is not only responsible for sound production, it also adjusts oral cavity volume and prevents swallowed material from entering the breathing airways. The walls of the larynx are composed of cartilages, ligaments, membranes, muscles and they are covered by the protecting respiratory mucosa. The vibrating part of the VF size is approximately: total length $10 - 16$mm, vertical thickness $9 - 10$mm and total depth in horizontal direction ca. 11mm, all depending on gender and age, see [156].

The larynx is composed of nine cartilages and the VFs are controlled by six muscles. The thyroid cartilage is the biggest and strongest laryngeal cartilage, which can be seen directly under the neck skin, also known as "Adam's apple". The set of cartilages bonded together with muscles provides firm, but flexible support to the larynx, [18].

Intrinsic muscles have two main functions – to control respiration and phonation. During the respiration the VFs are abducted, see Figure 1.2 middle. The another muscles draw VFs together to phonatory position, Figure 1.2 right. The two most important muscles are the cricothyroid and thyroarytenoid muscle. The cricothyroid is primarily responsible for modification of the vocal folds length. The activation of this muscle increases the VF tension and it plays a significant role in the setting of the voice fundamental phonation frequency. The thyroarytenoid (vocalis) muscles form the bulk of the vocal folds and their action mainly shorten the vocal folds and therefore it relaxes the vocal folds tension, see [156]

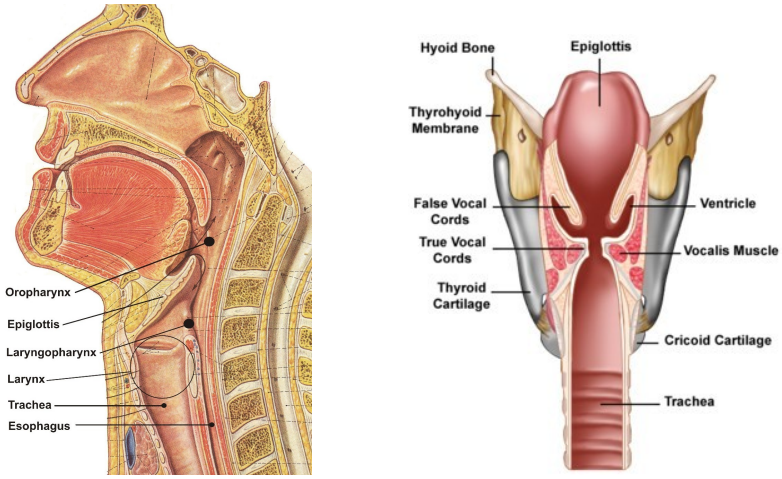


Figure 1.1: **Left:** Sagittal cut of upper airways – VFs are located in the circle denoting the larynx, see [99]. **Right:** Frontal cut of the larynx reveals the position and a complicated physiological structure of VFs, [18].

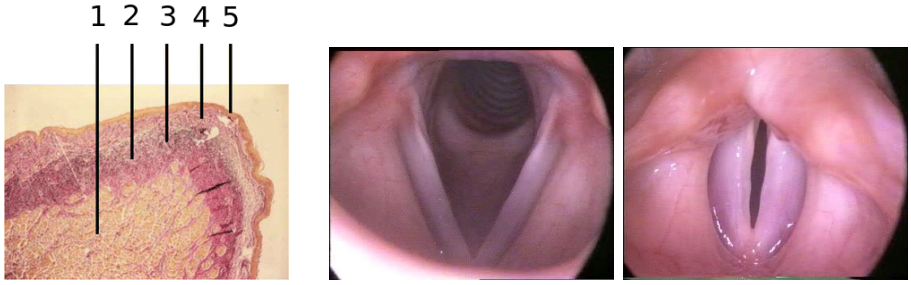


Figure 1.2: **Left:** Frontal cut of one VF with detailed tissue structure. 1 - thyroarytenoid muscle, 2 - lamina propria profunda, 3 - lamina propria media, 4 - lamina propria superficilias, 5 - epithelium, see [122]. **Right:** Laryngoscopic view of the vocal folds in respiratory (middle) and phonatory (right) position. During respiration, VFs attached on the arytenoid cartilages are abducted not to block trachea. Before phonation, VFs move closer into prephonatory position leaving only small gap between them. Overtaken from [136].

Above the VFs in the larynx the ventricle and the ventricular folds are located, sometimes called false vocal folds (FVFs). The ventricle is space between VFs and FVFs. The FVFs are largely immobile, composed of ligament. The current research indicates that they play not a negligible role in glottal flow dynamics and therefore they can influence also the produced sound, [105].

The morphological structure of VF is quite complicated. The VFs tissue structure is usually categorized into three main tissue layers: the epithelium, the lamina propria and the vocalis muscle. The epithelium is a thin tissue with main purpose of maintaining the VF shape. The lamina propria is underneath the epithelium. The three layers of lamina propria are distinguished according to the distribution of the elastic fibers: superficial, intermediate and deep layer. The vocalis muscle, the major bulk of the vocal fold, is the most inner and its thickness is circa 8 mm. Figure 1.2 left

shows VF tissues after resection, [122].

Here, we follow rather the classification based on the mechanical (elastic) properties, which accurate determination is highly difficult. It combines the intermediate and the deep lamina propria into a layer called ligament. Finally we distinguish four layers: the epithelium, the lamina propria (superficilias), the ligament and the vocalis muscle.

### 1.1.2 Human voice production from a physical point of view

The air stream coming from lungs excites vibrations of the vocal folds prepared in a prephonatory position. If the subglottal pressure is high enough, the amplitude of vibration steeply rises until the (full) contact of both VFs is achieved. The complete closure of the glottal channel is one of the major characteristics of the healthy human voice. The described mechanism of the flow-induced vocal fold vibrations represents the dynamic aeroelastic instability, usually referred in aeroelasticity as flutter, see [40]. According to [77] the flutter regime is the necessary condition for producing healthy voice because in this regime the energy is transferred from the flowing air into the vibrations of the vocal folds. The time of contact is for normal healthly voice approximately a half of one vibration period, [156], [105]. The VF opening and closing effectively controls the flow rate through the glottis, resulting in a confined jet. This jet in the supraglottal area breaks gradually into a full scale of vortices, therefore the flow field in this region is quite complex.

The basic sound is created by modulated glottal jet with the fundamental frequency given by the VFs vibration, i.e. for male it is in the range $85-155$ Hz and for female $165-255$ Hz, see e.g. [172]. This dominant sound is enriched by sound sources associated with supraglottal turbulence vortices and sound sources introduced by the VF vibration and collision. The superposition of all sound sources results in an acoustic signal, which contains in addition to the fundamental frequency many higher harmonics. However the frequency characteristic of sound sources is still substantially different from produced human voice, see [156], [157]. The sound originated by the sound sources propagates through a vocal tract, then it is articulated in mouth and finally this acoustic signal represents a human voice as we hear it. The basic physical conception of vocal tract function is, that it acts as an acoustic resonator with associated resonant frequencies, see source-filter theory in e.g. [54], [144]. It means that it amplifies frequencies in specific frequency ranges given by acoustic resonances of the vocal tract cavities. By doing so, it effectively transforms basic sound produced in the glottis into acoustic frequencies typical for each vowel. The resonant frequencies of vocal tract called formants depend on its length and shape, see [143]. For the higher acoustic intensities (typically singing or crying) the situation is substantially complicated because the phonation process including sound propagation through the vocal tract evidences strong nonlinearities and it could not be modelled any more by the source-filter approach, see [157].

## 1.2 State of the art

This section covers the most important aspects of vocal folds modelling evolution. Since the topic of this thesis is theoretical, the main attention is paid to the theoretical results even if these results first in the conjunction with experimental results can bring real progress in the human phonation research. The overview is focused on the FSI models with an extension to the FSAI models.

**Discrete models.** The mankind is fascinated with human voice production since prehistory. The systematic, scientific approach investigating human phonation dates back to sixties of 20. century, when first simple models of mass-spring coupled to fluid flow were established, see [59], [158]. These simple FSI models can illuminate basic principle of VF interaction with air stream, but it cannot explain the sustainable VF vibration, see [155]. Therefore more complicated physical models have emerged, consisting of two or more masses connected by damped springs, see [83], [97]. These models can estimate the instability boundary of the system by eigenvalue analysis, see [77].

These models were step by step improved and their outcomes were able to succesively predict the VF motion even in the case of contact, see [75], and to predict the impact stress within the VF, [72], which is an important quantity for underlying pathological processes and disorders occurring in the vocal fold tissue. Understanding these processes is crucial for designing of proper treatment strategies for the individual patients' problems.

**Fluid flow.** The 1D potential flow theory [77] or simplified nonlinear flow description [75] can be replaced by more realistic 2D continuum models [57] and recently also by 3D models as the computational power steeply increases [137]. However the simulation of the fluid flow is the most time consuming part of the FSI computation. This is caused by the complex phenomena present in the fluid flow described by Navier-Stokes equations, which are nonlinear. The accuracy of flow approximations mostly determines the accuracy of whole FSI algorithm. The importance of flow results accuracy for the purpose of follow-up aeroacoustic simulation is even higher.

One of the first studies solving 2D or 3D continuum model described by Navier-Stokes equations investigated the flow only through static larynx configuration, see e.g. [125] or [133]. They revealed that the flow field has highly transient character. The intensive jet starting in the glottis separates from the VF boundary and further downstream creates large, slowly decaying vortices. The jet alignment to one side of supraglottal channel althought initial symmetry configuration was regarded to be Coanda effect, see e.g. [150], which is according to [105] and [48] misleading[1].

Another results, [57], [62], providing the dynamical effects caused by the domain change were obtained by modification of flow solver, usually with the help of arbi-

[1] They argue that a variety of mechanisms for supraglottal flow asymmetries is present like e.g. high sensitivity of the pulsatile jet to perturbations and possible transmission of instabilities from different region.

trary Lagrangian-Eulerian (ALE) method, see [149]. Since the solution of full FSI problem, e.g. fluid flow coupled with structure, is multiple times computationally expensive than the sole fluid flow solution in time dependent domain, a simplified approach is often used. Therefore a variously complicated motion of fluid domain walls is prescribed in order to imitate the real VF motion, see e.g. [171], [113]. A similar approach is for the same reason used also for 3D computations, see [139] or [123]. An axi-symmetric flow model was used e.g. in [27].

In the supraglottal fluid field complex flow structures appears and possibly turbulence effects should be considered with e.g. a turbulence model. However, most turbulence models are usually well tuned to describe the fluid flow around an airfoil or plane wall and a choice of turbulence model, which gives also good results for the case with massive separations, is troublesome, see [95]. Thus most promising approach in this area seems to be the application of LES models. One of the first article using LES method for turbulence modelling in 2D static geometry was [145], for 3D static geometry see [133]. The LES model is also applied together with prescribed VF motion in recent studies [137], [95] or [124].

**FSI continuum models.** One of the first FSI continuum model of flow-induced VF vibration was published by [45], where the finite volume approximations were coupled with a two-mass dynamic model of the vocal fold. Similar approach was also used later in [150]. The full FSI problem approximated by the FEM was introduced in [112], [153] or see overview paper [21]. This approach is still used in many studies, e.g. [57] or [147]. It provides higher accuracy especially when the structure and the fluid mesh coincides on the interface. The drawback is the necessity to stabilize the FE flow simulation in order to obtain a robust scheme. In last decade the numerical approach based on the discountinous Galerkin (DG) methods can be found, see e.g. [93], where even the VF dynamics are modelled with geometric and material nonlinearities.

A very interesting alternative to FEM together with the ALE method provides immersed boundary method (IBM), where the overall simulation is solved on the Cartesian grid and in each time step a new interface is reconstructed, see e.g. [102] or [166] for 3D simulations. A big advantage is a possibility to treat substantial topology changes, a disadvantage is an inability to obtain refined mesh at boundary layer. This can be possibly overcome by h-adaptivity, see e.g. [19].

The FSI solvers are slowly becoming a standard component of the commercial numerical software, see e.g. COMSOL, ANSYS or ADINA etc. But anyway an user of numerical software must be careful with the the results interpretation and during the verification of the problem formulation as well as convergence of the numerical solution, see e.g. [67].

**FSAI continuum models.** The FSAI problem was addressed e.g. in [98] or [173]. First, they solved the FSI problem and then they computed the acoustics with the aid of acoustic analogies. As inputs for sound source calculation the computed flow field as well as the VF vibration were used.

More recently a different coupling of the fluid flow and the acoustics to the structure response was investigated, see [84]. The authors used for simulation of the VF motion the superposition of flow and acoustic pressure, where the acoustic pressure was obtained with the help of linearized perturbed compressible equations (LPCE) solved in the acoustic domain representing the whole vocal tract. The explicit partitioned approach in the numerical simulation of this FSAI problem was used. Unfortunately the applied sound soft boundary condition at mouth opening makes the results questionable.
Authors of paper [43] showed the effects of subglottal acoustics by using the barotropic model of Navier-Stokes equations. These effects have been previously seen in experimental studies and predicted theoretically, [157], [169]. As the computational VF model vibrated, standing pressure waves were seen in the subglottal duct for its certain lengths leading to variation of the phonation pressure threshold.

The FSI solution using the compressible model of Navier-Stokes equations, see e.g. [67], can replace the FSAI solution but as further explained in Section 6.1 the well resolved acoustic part of the solution is possible to be obtained only with solver of high accuracy and when suitable boundary conditions are applied.

**Mesh deformation.** The mesh motion (adaptation) is a part of commonly used FSI formulations based on the ALE method. The ALE mapping, bijective mapping from reference domain to deformed one, can be constructed by many strategies. The frequently used are the algebraic mesh motion, the elliptic smoothing, the pseudo-structure approach or the interpolation by radial basis functions (RBF), see [98]. The first method can be used only for very simple mesh motion, the second one already uses partial differential equations (PDE) to determine ALE mapping, but the resulting overall mesh quality is poor, see [118]. The pseudo-elastic approach has many advantages like robustness, easy implementation (basically the same as structure solver) and possibility to easily tune parameters controlling the deformation, [49]. Interpolation by RBF seems promising, [110], and it could be possibly computational less demanding. Very recently a new approach combining Eulerian and ALE framework involving so called cut elements was proposed, see [132].

**Boundary conditions for FSI problem.** The formulation of boundary conditions (BCs) depends on applied mathematical and numerical model. Here we focus on the boundary conditions for incompressible Navier-Stokes equation approximated by FEM.

For the interface between the fluid and the structure the physically correct combination of the Dirichlet and the Neumann BC is used. It can be derived from the requirement of continuity across the interface for displacements and normal stresses. It is also most suitable for the prescibred VF motion, see [174]. An interesting alternative is more general combination of the Robin-Robin coupling BCs, which can possibly accelerate the convergence of the coupled problem solution, see [26].

The influence of the inlet boundary conditions for the incompressible flow is even more important because the neccesity to model the periodic closure of the glottal

channel. The two frequently used BCs (in the FEM framework) are to prescribe either the classical Dirichlet BC in the form of prescribed velocity or the do-nothing type of BC with a given pressure drop between the inlet and the outlet. The Dirichlet condition has the drawback of high, unphysical oscillations of inlet pressure values during the channel closing phase, see [148]. The do-nothing type of BC usually leads to significant oscillation of the inlet velocity while keeping the pressure drop constant. Also such a behaviour is not relevant for the considered problem, e.g. it was not observed experimentally, see e.g. [73]. A remedy for this situation seems to be penalization approach with the idea proposed already in [25] for a scalar problem. Its potential for this configuration of inner fluid dynamics was newly discovered in [148].

The penalization approach imposes the inlet boundary conditions inside the weak formulation with a penalization parameter $\epsilon$. This is similar to the weakly enforced Dirichlet BC often used in the discontinuous-Galerkin method, see [93].

**Aeroacoustics.** The aeroacoustics is a part of acoustics with the aim to desribe the flow-induced sound, usually produced by flow around obstacles or by a high Reynolds number (turbulent) flow in free jets, see e.g. [91]. Intensive development of aeroacoustics was driven by the progressive expansion of aircrafts in the fifties of 20-th century. At this time the aeroacoustic knowledge has primarily the form of experimental results and expert experiences without theoretical fundamentals. The first mathematic model of aerodynamically produced sound known as Lighthill acoustic analogy was introduced by sir Lighthill, [96]. Acoustic analogy means some approximative transformation of Navier-Stokes equations, which compressible variant in general describes propagation of entropy, vorticity and acoustics, see [53], [107], [38], into PDE similar to wave equation for a representation of acoustic pressure. At Lighthill time there was no possibility to use computer for PDE solution, so his analogy can be solved analytically by application of Green's functions. The one of further improvements was a pretty mathematical treatment of flow-induced sound in the domain with static or moving bodies introduced by Ffowcs Williams and Hawkings [58]. Today, a lot of acoustical solvers in CFD programs are based on this approach.

However nowadays, with advance in a PDE numerical solution new methods became accessible. Modern computational aeroacoustics is based on the perturbation equations [90], where the splitting of flow variables into mean, acoustic and correction term is performed with the aim to describe purely acoustic wave propagation. Similar and quite popular sets of equations are called the acoustic perturbation equations (APE), [53], the perturbed compressible equations (PCE), [27], and linearized perturbed compressible equations (LPCE), [134]. The splitting approach was later generelized, see [82] or [91], leading to analogy called the perturbed convective wave equation (PCWE) with practical formulation for low Mach numbers flow regimes. For comprehensive overview of progress in the field of computational aeroacoustics see [128].

**Aeroacoustics of human phonation.** The theoretical background of sound production during voicing was described in works [171] and [168] using integral Ffowcs Williams–Hawkings analogy and sound classification as monopole, dipole and quadrupole (see Section 2.4). They found that the most dominant sound source during phonation is a dipole associated with net forces exerted by the surface of the VFs onto the airflow. The other strong source is a quadrupole connected with turbulence in the supraglottal area and the least prominent source is a monopole related to the air column movement induced by VF vibration. The similar sound sources structure was also reported by e.g. [145] or [139]. The article [71] tried to answer a question regarding the efficiency of placing the monopole, dipole and quadrupole sound sources into a resonator, i.e. in vocal tract. The Rossiter instability[2], a flow-acoustic resonance phenomenon typical for flow over open cavity, was discussed in the context of human phonation for static VF configuration in [168], [65]. The importance of (prescribed) glottis closure for healthy voice was studied e.g. in [27] utilizing PCE analogy in the axi-symmetric configuration.

In paper [98] the Lighthill analogy was applied using results of 2D FSI simulation in the computational domain consisting of short straight sub- and supra-glottal channel, i.e. without vocal tract model, which results in prediction of the sound sources frequencies only. In the study [134] high order IBM solver was used for solving fluid flow in a supraglottal region with prescribed time variable flow rate and then the LCPE analogy with inclusion of vocal tract model was applied. The aeroacoustic simulation of the specific human subject however considering static VF geometry was studied in [126]. In articles [139] and [95] the aeroacoustic 3D problem with vocal tract was successfully solved utilizing the Lighthill analogy and the PCWE approach, but it was based on the FSI solution with the prescribed movement of VF walls. Nevertheless it evinces a good match of vowel spectra [u:] and [i:] with experiments. The paper [175] extended used methodology also for the case of one side paralysed VF. The efficiency of aeroacoustic simulations based on PCWE was investigated in paper [131]. The thesis [100] presented a new and an interesting methodology called hybrid acoustic particle image velocimetry approach which combines experimental flow measurements and numerical acoustic simulations.

**Short summary of human phonation research**

The numerical simulations of human phonation using mathematical model of continuum can be basically split in two groups. The studies from the first group are interested in the solution of FSI problem of flow-induced VF vibration for realistic geometries and they usually do not considered the associated aeroacoustic problem, see e.g. [153], [170], [174], [57], [166]. The second group of results deals dominantly with the aeroacoustic treatment usually based on the roughly simplified fluid flow simulation in the glottis and in the larynx. The highly complex solution of FSI problem is often reduced by considering a rigid glottal model ([145], [65]) typically together with some apriori given fluctuating inlet flow profile like e.g. Liljencrants–Fant model, see e.g. [126], [134]. Another frequently used reduction of the complex FSI

[2]During the Rossiter instability the vortex shedding at leading edge of cavity convected to trailing edge causes there mass oscillations (emission of acoustic waves) which further in feedback loop induce vortex shedding at the leading edge.

problem can be realized by prescribing highly simplified apriori given VF motion, see e.g. [171], [27].

There are few research studies trying to join the both aforementioned approaches with all consequences. First, papers [139], [175], [131] calculated the resulting acoustic signal in front of mouth based on the 3D flow results obtained by finite volume method with sophisticated prescribed periodic VF motion simulating changing convergent-divergent VF position. Another studies [98], [43], considered the full FSAI problem however the acoustic simulation without inclusion of the vocal tract model did not provide relevant results.

## 1.3 Objectives of dissertation

The aim of this thesis is to simulate the process of human phonation numerically. The exact mathematical formulation of all relevant physical processes together with their mutual interaction must be unquestionable part of this work. Further the numerical schemes based on FEM are adopted, capable to simulate all main important phenomena involved, for the solution of underlying PDEs. The orientation only on the 2D coupled FSAI problem is caused by enormous rise of computational demand for 3D version, where the extension to 3D problem is more or less straightforward. The first two goals concern a numerical solution of the FSI problem.

**The first goal** is to investigate the possibilities of new penalization boundary condition and to compare it with the other commonly used possibilities within the FEM framework and to show how the application of them leads to the unphysical behaviour of airflow mainly during the phase of channel closing and opening. The preliminary results published in article [148] were obtained only for prescribed motion of structure and one selected value of penalization parameter $\epsilon$. The analysis how different values of $\epsilon$ influence the FSI solution as well as detail behaviour of the FSI solution close to maximal channel closure using this new approach is highly desired. Here, we would like to stress out that this goal is theoretical originating from mathematical analysis of FSI problem and it could have a practical application in the simulation of not only human phonation.

**The second goal** is to (numerically) study the stability boundary of the FSI problem. The knowledge of critical inlet airflow velocity is needed for determination of phonation onset, i.e. when flow-induced vocal fold vibrations start. Flutter velocity is one of the characteristics of the FSI system.

The second part of the thesis addresses the full problem of the human phonation process. Following the explanation in above mentioned paragraph *Short summary* the extension of (full) FSI problem to the FSAI problem would be a novel result. Although the similar approach was already used in [98] or [173] the authors did not obtain any reliable acoustic results because they did not include a vocal tract in the acoustic domain as an important component of the problem. The difference against the predominantly aeroacoustic studies or papers trying to cover both problems

[139], [175] is that our suggested model deals with full solution of the FSI problem instead of flow field solution only in the domain with prescribed structure motion.

**The third goal** is to connect the in-house solver FSIFEM of the FSI problem and the academic solver CFS++ of the multiphysics problems. The in-house program FSIFEM written in C language is developed by the author of the thesis and it implements numerical solution of FSI problem as described in chapter 4. The program Coupled Field Simulation known under CFS++ developed at TU Wien by team of prof. Kaltenbacher, see webpage `https://cfs-doc.mdmt.tuwien.ac.at/`, is capable to solve a lot of coupled problems like e.g. piezoelectrics-acoustics, electromagnetics-mechanics, electromagnetics-thermics, etc. Nevertheless this program is used in the thesis to solve the sound propagation problem because of implemented advanced damping layer called Perfectly matched layer (PML), see [90] or paragraph 6.1.4. Further it offers numerical routines for sound source computation and interpolation in the subprogram called CFSDat.

The easiest connection between solvers is realized through a support of the file format called Hierarchical Data Format version 5 (HDF5), which is an universal, very general format useful for large, complex and heterogeneous data, see [17]. Its advantage is that it is a standard file format with high performance of I/O operations, which is open source and widely used. The program CFS++ has already HDF5 format as a native input and output format[3] therefore the output support of HDF5 file format has to be added only to the in-house program FSIFEM .

**The fourth goal** is to perform the aeroacoustic simulation of human phonation based on the full FSI solution. The adopted hybrid approach usually consists of three steps. First, the sound sources need to be determined from the previously obtained fluid flow solution. Second, the sound sources are interpolated from a CFD mesh to a coarser acoustic mesh in order to reduce computational demands and third, the acoustic computation is finalized by numerical simulations of the sound sources propagation through an acoustic domain including vocal tract model.

The first two steps, namely the sound sources computation and interpolation, are decisive for accuracy of the whole acoustic computation. Therefore a special attention must be paid to numerical postprocessing of flow results in order to decrease numerical errors as much as possible. Further, there are a number of different aeroacoustic formulations and the comparison of chosen approaches could bring more light in their applicability in mathematical modelling of human phonation.

**The fifth goal** is to compare sound of aeroacoustic and vibroacoustic origin.

## 1.4 Structure of thesis

The structure of the thesis copies its objectives, i.e. the first half is devoted to the FSI problem and the second half then describes the FSAI problem.

[3]The program CFS++ utilizes a specific version of HDF5 format denoted by suffix *.cfs*, see documentation `https://cfs-doc.mdmt.tuwien.ac.at/mediawiki/index.php/HDF5_Data_Structure`.

The first chapter is comprehensive introduction of the fluid-structure-acoustic interaction problem related to physics of human phonation. The second chapter presents the basic mathematical notation and the most important theorems of functional analysis.

The third chapter contains mathematical description of the deformation of elastic bodies, fluid flow in time dependent domains and their coupling. Specifically, all boundary conditions and the interface conditions are presented in detail. In the fourth chapter the numerical schemes for FSI problem based on the FEM are explained and the whole sequence of single solution steps is given. The fifth chapter is devoted to FSI numerical results. The penalization inlet boundary condition is compared with other alternatives for hemi- and full larynx model. The influence of the penalization parameter on the critical flutter airflow velocity is discussed.

The aeroacoustic problem, the second major topic of the thesis, is introduced in the sixth chapter together with the chosen acoustic analogies as a favourable solution strategy. The numerical realization of the aeroacoustic problem and its coupling with FSI solution is given in the seventh chapter and a special attention is paid to the sound sources evaluation. The eighth chapter contains the results of numerical simulations of the human phonation. Besides the frequency spectra of numerically computed sound, the acoustic resonances of vocal tract model and the structure of sound sources are studied.

In the last ninth chapter the discussion of achieved results and wider conclusions are presented.

# Chapter 2

# Mathematical background

In this chapter several elementary definitions and theorems of functional analysis are summarized, see [20], [108].

## 2.1 Function spaces and norms

For the function space properties it is first important to characterize the set $\Omega$ over which they are constructed, for details see [20]:

We consider $\Omega$ to be a bounded domain, i.e. an open and connected subset of $R^d$, $d \in \mathbb{N}$.

Further we call the domain boundary $\partial\Omega$ Lipschitz continuous, if it satisfies: For any $z \in \partial\Omega$ there is a neighbourhood $U = U(z)$ such, that set $U \cap \partial\Omega$ can be in a Cartesian coordinate system $(x_1, \cdots, x_d)$ expressed as

$$x_d = F(x_1, \cdots, x_{d-1}), \tag{2.1}$$

and the set $U \cap \Omega$ can be described by inequality

$$x_d < F(x_1, \cdots, x_{d-1}), \tag{2.2}$$

where $F$ is a Lipschitz continuous function.

**Remark.** For domains with the Lipschitz continuous boundaries the unit outward normal vector is defined almost everywhere at $\partial\Omega$.

By symbol $C(\Omega)$ the space of real continuous functions on a domain $\Omega$ is denoted. For arbitrary natural number $k$ we denote $C^k(\Omega)$ the space of all functions $f$, which have continuous all partial derivatives $D^\alpha f$ of order $|\alpha| \leq k$ on $\Omega$. Further by $C^\infty(\Omega)$ the space of infinitely differentiable functions is denoted, see [20].

The support of function $f$ is the set $\overline{\{x \in \mathbb{R}^d | f(x) \neq 0\}}$ and it is denoted as supp $f$. Further the space $\mathscr{D}(\mathbb{R}^d) = \{f \in C^\infty(\mathbb{R}^d) |$ supp $f$ is bounded$\}$ is called the space of test functions, i.e. it consists of functions from the class $C^\infty(\mathbb{R}^d)$ with a compact

support. Similarly on the domain $\Omega$ the space $\{f \in C^\infty(\mathbb{R}^d) |\ \text{supp}\ f \subset \Omega\}$ is denoted by $\mathscr{D}(\Omega)$.

The space of generalized functions (or distributions) denoted as $\mathscr{D}'(\Omega)$ is a set of all linear and continuous functionals over $\mathscr{D}(\Omega)$, where the continuity is meant in the sense of convergence preserving on the space $\mathscr{D}(\Omega)$, see e.g. [108]. By this construction of the space $\mathscr{D}'(\Omega)$ it is allowed to define derivative also for generalized functions $f \in \mathscr{D}'(\Omega)$, see e.g. [20]. This property is highly desired in the theory of partial differential equations due to possibility to extend the concept of a solution to generalized functions.

A space of all bounded linear functionals defined on a Banach space $B$ is called the dual space and it is further denoted by $B^*$. On the space $B^*$ the norm is defined for $\phi \in B^*$ by

$$\|\phi\|_* = \sup_{u \in B,\, \|u\| \neq 0} \frac{|\phi(u)|}{\|u\|_V}. \tag{2.3}$$

**Lebesque spaces.** One of the most widely used function spaces is the Lebesque space $L^p(\Omega)$, where $1 \leq p < \infty$. These spaces are defined with the help of Lebesgue measure and integral, see e.g. [101]. The elements of the space $L^p(\Omega)$ are characterized by functions $f : \Omega \mapsto \mathbb{R}$, for which hold

$$\int_\Omega |f|^p \ dx < +\infty. \tag{2.4}$$

The spaces $L^p(\Omega)$ are the Banach spaces with the norm

$$\|u\|_{L^p(\Omega)} = \|u\|_p = \left( \int_\Omega |u|^p \ dx \right)^{\frac{1}{p}}, \tag{2.5}$$

for $1 \leq p < \infty$, see [20].

**Remark.** Similarly we work with the spaces $L^p(\partial\Omega)$, where $\partial\Omega$ is the boundary of the domain $\Omega$.

For $p = 2$ the space $L^2(\Omega)$ is the Hilbert space with the scalar product given by

$$(u, v)_{L^2(\Omega)} = \int_\Omega u\, v \ \mathrm{d}x. \tag{2.6}$$

In next the scalar product in $L^2(\Omega)$ is denoted shortly as $(\cdot, \cdot)_\Omega$.

For vector spaces $\mathbf{L}^2(\Omega) = [L^2(\Omega)]^d, d \in \mathbb{N}$ the scalar product is defined as

$$(\mathbf{f}, \mathbf{g})_\Omega = \sum_{i=1}^{d} (f_i, g_i)_\Omega, \tag{2.7}$$

where functions $\mathbf{f}, \mathbf{g} \in \mathbf{L}^2(\Omega)$ and $f_i, g_i$ denotes their $i$-th component.

**Sobolev spaces.** Similarly as in [20] we denote the derivative of multivariable functions over $\mathbb{R}^d$ with respect to multi-index $\alpha = (\alpha_1, \ldots, \alpha_d)$ with $\alpha_i \in \mathbb{Z}_0^+$ as the partial derivative $D^\alpha = \frac{\partial^{|\alpha|}}{\partial x_1^{\alpha_1} \ldots \partial x_d^{\alpha_d}}$, where $|\alpha| = \sum_{i=1}^d \alpha_i$ and $d \in \mathbb{N}$.

For $k \in \mathbb{N}$ and $1 \leq p < +\infty$ the Sobolev spaces are defined

$$W^{k,p}(\Omega) = \{u \in L^p(\Omega) |\ \forall \alpha \in (\mathbb{Z}_0^+)^d, |\alpha| \leq k, D^\alpha u \in L^p(\Omega)\}, \tag{2.8}$$

where the derivatives $D^\alpha u$ are considered in the sense of distributions, see [20], [108]. The norm on the space $W^{k,p}(\Omega)$ is defined by

$$\|u\|_{W^{k,p}(\Omega)} = \|u\|_{k,p,\Omega} = \sum_{|\alpha| \leq k} \left( \int_\Omega |D^\alpha u|^p \ dx \right)^{\frac{1}{p}}. \tag{2.9}$$

Similarly as for Lebesque space with $p = 2$ the space $W^{k,2}(\Omega)$ is the Hilbert space and it is further denoted as $H^k(\Omega),\ k \in \mathbb{N}$. Similarly, the by $\mathbf{H}^k(\Omega)$ the vector Sobolev spaces is meant, i.e. defined by the Cartesian product $\mathbf{H}^k(\Omega) = [H^k(\Omega)]^d, d \in \mathbb{N}$.

## 2.2 Important theorems

The existence of boundary values of functions from the Sobolev spaces postulates the trace theorem. Further essential results of functional analysis are also stated.

**Theorem: 1** (Trace theorem)**.** *Let $\Omega \subset \mathbb{R}^d$ be a bounded domain with Lipschitz continuous boundary. Then there exists unique continuous linear operator $T : H^1(\Omega) \mapsto L^2(\partial\Omega)$ such, that that $Tu = u|_{\partial\Omega}$ holds $\forall u \in C^\infty(\overline{\Omega})$.*

For the statement and proof see e.g. [108].

**Theorem: 2** (Substitution theorem)**.** *Let $U, V$ be closed sets in $\mathbb{R}^d$ with piecewise continuous boundary and let $\varphi$ be an bijective continuously differentiable mapping of the set $U$ onto $V$ with nonzero Jacobian $D\varphi$ for every $\hat{x} \in U$. Then for any function $f \in C(V)$ holds*

$$\int_V f(x)\ \mathrm{d}x = \int_U f(\varphi(\hat{x}))\, |D\varphi(\hat{x})|\ \mathrm{d}\hat{x}. \tag{2.10}$$

For proof see [116].

**Theorem: 3** (Green's theorem)**.** *Let $\Omega \subset \mathbb{R}^d$ be a bounded domain with a Lipschitz continous boundary $\partial\Omega$ and let functions $f, g \in C^1(\overline{\Omega})$. Then it holds*

$$\int_\Omega \frac{\partial f}{\partial x_i} g\ \mathrm{d}x = \int_{\partial\Omega} f g n_i\ \mathrm{d}S - \int_\Omega f \frac{\partial g}{\partial x_i}\ \mathrm{d}x, \qquad i = 1, \ldots, n, \tag{2.11}$$

*where $n_i$ is $i$-th component of the unit outer normal to $\partial\Omega$.*

For statement and proof see [55].

**Theorem: 4** (Gauss theorem)**.** *Let $\Omega \subset \mathbb{R}^d$ be a bounded domain with a piecewise smooth boundary $\partial\Omega$ and let be vector function $\mathbf{f} \in C^1(\overline{\Omega})$. Then it holds*

$$\int_{\partial\Omega} \mathbf{f} \cdot \mathbf{n} \, \mathrm{d}S = \int_{\Omega} \nabla \cdot \mathbf{f} \, \mathrm{d}x, \tag{2.12}$$

*where $\mathbf{n}$ denotes the unit outer normal to $\partial\Omega$.*

For statement and proof see [116].

**Theorem: 5** (Lax - Milgram theorem)**.** *Let $V$ be a Hilbert space, $a(\cdot,\cdot)$ be a bilinear form defined on $V \times V$ and $L(\cdot)$ be a linear bounded functional defined on $V$. Let further form $a(\cdot,\cdot)$ be*

1. *bounded on $V$, i.e. $\exists K > 0$, such that $|a(\mathbf{u},\mathbf{v})| \leq K\|\mathbf{u}\|_V\|\mathbf{v}\|_V \ \forall \mathbf{u},\mathbf{v} \in V$,*
2. *coercive on $V$, i.e. $\exists \alpha > 0$, such that $|a(\mathbf{v},\mathbf{v})| \geq \alpha\|\mathbf{v}\|_V^2 \ \forall \mathbf{v} \in V$.*

*Then there exists an unique function $\mathbf{u} \in V$ such, that $a(\mathbf{u},\mathbf{v}) = L(\mathbf{v}) \ \forall \mathbf{v} \in V$. Moreover it holds $\|\mathbf{u}\| \leq \frac{1}{\alpha}\|L\|_*$.*

For statement and proof see [116] or [52].

## 2.3 Fundamental solution of wave equation

The following two sections are devoted to basic properties of acoustics and aeroacoustics. Although the thesis deals with the 2D model of human phonation, the acoustics is a 3D phenomenon and therefore following two sections refer purely to 3D acoustic problem.

The basic model of pressure wave propagation generally in $\mathbb{R}^{3+1}$ (and also in $\mathbb{R}^{2+1}$) is governed by wave equation

$$\left(\frac{1}{c^2}\frac{\partial^2}{\partial t^2} - \Delta\right) p(x,t) = 0, \tag{2.13}$$

where $c$ is the speed of sound, see e.g. [164]. The solution $p(x,t)$ is sought in the sense of distributions, i.e. in the space $\mathscr{D}'(\mathbb{R}^{3+1})$, for definition see [164]. Let us consider wave equation (2.13) with a point source located in the point $y \in \mathbb{R}^3$ and occurring at time $\tau > 0$

$$\left(\frac{1}{c^2}\frac{\partial^2}{\partial t^2} - \Delta\right) G(x,t) = \delta(t-\tau)\ \delta(x-y), \tag{2.14}$$

where $\delta(\cdot)$ denotes the delta function and by $\delta(x-y)$ is meant $\delta(|x-y|)$, see [78]. Then $G(x,t)$ satysfing equation (2.14) is the fundamental solution of wave equation, which is called the Green's function. The Green's function, see e.g. [78], reads

$$G(x,t) = \frac{1}{4\pi|x-y|}\ \delta\left(t - \tau - \frac{|x-y|}{c}\right), \tag{2.15}$$

where the coordinates (arguments) $x, t$ represent the observer position at time $t$ whereas the coordinate $y$ means the position of the sound source at time $\tau$, see e.g. [46]. By $|x-y|$ the Euclidean distance of two points in $\mathbb{R}^3$ is denoted. More precisely, the Green's function $G = G(x,t)$ depends on four variables $G = G(x,t;y,\tau)$.

**Remark.** The Green's function for the wave equation in $\mathbb{R}^2$ has different form than (2.15). It is defined with the aid of the Heaviside function, thus its behaviour is fundamentally different compared to 3D problem, see [79].

**Remark.** The exact form of Green's function for the case of a bounded domain $\Omega$ depends on the chosen geometry configuration. The fundamental solution for the bounded domain (contrary to the considered unbounded 3D case) must also satisfy boundary conditions, see [79].

A solution of the wave equation for a more general sound source is now derived. A distributed sound source $\mathcal{F}(y,\tau)$ formally satisfies

$$\mathcal{F}(y,\tau) = \int_{-\infty}^{+\infty}\int_{\mathbb{R}^3} \mathcal{F}(x,t)\delta(x-y)\delta(t-\tau)\ \mathrm{d}x\ \mathrm{d}t. \tag{2.16}$$

Then the solution of wave equation with this distributed sound source $\mathcal{F}(y,\tau)$ can be written as

$$p(x,t) = \int_{-\infty}^{+\infty}\int_{\mathbb{R}^3} \mathcal{F}(y,\tau)G(x,t)\ \mathrm{d}y\ \mathrm{d}\tau = \frac{1}{4\pi}\int_{-\infty}^{+\infty}\int_{\mathbb{R}^3} \frac{\mathcal{F}(y,\tau)}{|x-y|}\ \delta\left(t-\tau-\frac{|x-y|}{c}\right)\ \mathrm{d}y\ \mathrm{d}\tau$$

$$= \frac{1}{4\pi}\int_{\mathbb{R}^3} \frac{\mathcal{F}\left(y, t-\frac{|x-y|}{c}\right)}{|x-y|}\ \mathrm{d}y, \qquad \text{for } t>0, x\in\mathbb{R}^3. \tag{2.17}$$

It means that the solution of the wave equation with distributed sound sources (2.17) at a time-point $x, t$ is composed of contributions from all points of the distributed source, which arrives at point $x$ at time $t$ (i.e. the contribution has to be emitted at time $t-\frac{|x-y|}{c}$ with $\frac{|x-y|}{c}$ being travel time) and which strength is attenuated by distance from observer (i.e. by $\frac{1}{|x-y|}$).

In acoustics the concept of compactness of sound sources is used quite often, see e.g. [79]. The acoustic source is called (acoustically) compact if its Helmholtz number $He \ll 1$. The Helmholtz number is (dimensionless) ratio of a geometrical length scale $l$ of acoustic sources (i.e. the smallest diameter of ball containing all acoustic sources) to their typical acoustic wavelength $\lambda$, i.e. $He := l/\lambda$. For compact sound sources the exact solution (2.17) can be substantially simplified. This simplification is recommended for practical purposes for $He < 1/4$, see [46].

The exact solution (2.17) of the wave equation with distributed compact sound sources can be approximated as

$$p(x,t) \approx \frac{1}{4\pi|x|}\int_{\mathbb{R}^3} \mathcal{F}\left(y, t-\frac{|x|}{c}+\frac{x\cdot y}{c|x|}\right)\ \mathrm{d}y, \tag{2.18}$$

for observer position $x$ far from the sources ($|x| \to +\infty$). The formula (2.18) is called Fraunhofer approximation, see e.g. [68]. From comparison of equations (2.17) and (2.18) follows that the distance attenuation $\frac{1}{|x-y|}$ is approximated by $\frac{1}{|x|}$ as $|x| \to +\infty$. However the arguments in the integrand needs to be approximated more carefully in order to preserve the information of the phase difference of sound sources, see [46]. By retaining the contribution $\frac{x \cdot y}{c|x|}$ in the argument of function $\mathcal{F}$ it is ensured that any interference between sound waves generated at different positions within the source region is correctly described by the far-field approximation, see [79].

## 2.4 Theoretical classification of sound sources

The arbitrary distributed, but acoustically compact source observed from large distance can be approximated by a point source, see e.g. [78]. The characteristics of this point source, i.e. radiation directivity and scaling laws, can be described by a multipole expansion, see e.g. [119]. The expansion members are called monopole, dipole, quadrupole, etc. The importance of expansion members usually decreases in the given order. Each of the expansion terms describes a different physical concept of sound production.

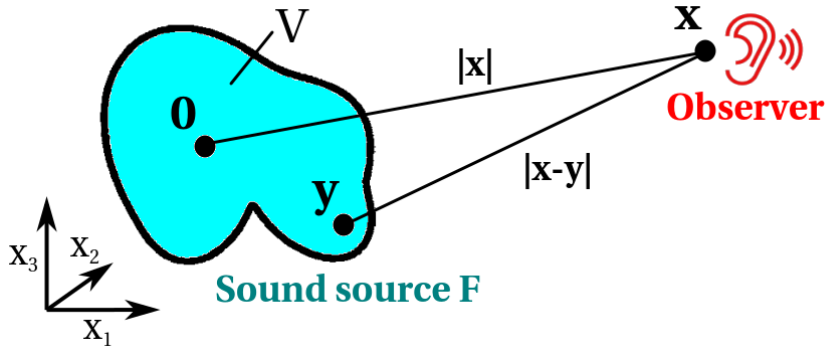


Figure 2.1: Scheme of sound source located around coordinates origin **0** and observer at position $x$. Distance $|x - y|$ between point $y$ in sound source region of volume $V$ and observer is marked.

Let be a given sound source $\mathcal{F}$ distributed in a small volume $V$ with its center located at the coordinates origin **0**, see Figure 2.1. Before proceeding to convolution with Green's function we perform Taylor expansion of $G(x, t; y, \tau)$ around **0** (in the sense of distributions) in the coordinate $y$

$$G(x,t;y,\tau) = G(x,t;\mathbf{0},\tau) + (\nabla_y G)\,|_{\mathbf{0}} \cdot y + \frac{1}{2!}\, y^T \cdot (\nabla_y \nabla_y G)\,|_{\mathbf{0}} \cdot y + \ldots, \qquad (2.19)$$

see [46]. Then according to equation (2.17) the solution of the wave equation with

distributed sound source $\mathcal{F}$ can be obtained as

$$p(x,t) = \int_{-\infty}^{+\infty} \int_{\mathbb{R}^3} \mathcal{F}(y,\tau) G(x,t;y,\tau) \, \mathrm{d}y \, \mathrm{d}\tau = \tag{2.20}$$
$$= \int_{-\infty}^{+\infty} G(x,t;\mathbf{0},\tau) \int_V \mathcal{F}(y,\tau) \, \mathrm{d}y \, \mathrm{d}\tau + \int_{-\infty}^{+\infty} (\nabla_y G)\,|_{\mathbf{0}} \cdot \int_V y\, \mathcal{F}(y,\tau) \, \mathrm{d}y \, \mathrm{d}\tau$$
$$+ \frac{1}{2} \int_{-\infty}^{+\infty} (\nabla_y \nabla_y G)\,|_{\mathbf{0}} : \int_V y \otimes y\, \mathcal{F}(y,\tau) \, \mathrm{d}y \, \mathrm{d}\tau + \ldots,$$

where symbol : denotes the double-dot product between two tensors and $\otimes$ denotes the tensor product, see e.g. [36].

Green's function $G(x,t;y,\tau)$ e.g. as given in (2.15) can be also written as function with arguments $G(|x-y|, t-\tau)$. Then it can be shown

$$\left. \frac{\partial^{i+j+k} G(|x-y|,t-\tau)}{\partial y_1^i \, \partial y_2^j \, \partial y_3^k} \right|_{\mathbf{0}} = (-1)^{i+j+k} \, \frac{\partial^{i+j+k} G(|x-\mathbf{0}|,t-\tau)}{\partial x_1^i \, \partial x_2^j \, \partial x_3^k}, \tag{2.21}$$

i.e. the derivatives of $G(|x-y|,t-\tau)$ evaluated at $y=\mathbf{0}$ do not depend on coordinates $y$, see e.g. [119]. According to [46] equation (2.20) can be rewritten in the componentwise notation with $|x-\mathbf{0}| = |x|$ by using equation (2.21) as

$$p(x,t) = \sum_{i,j,k=0}^{\infty} \int_{-\infty}^{+\infty} \frac{(-1)^{i+j+k}}{i!j!k!} \frac{\partial^{i+j+k} G(|x|,t-\tau)}{\partial x_1^i \, \partial x_2^j \, \partial x_3^k} \int_V y_1^i \, y_2^j \, y_3^k \, \mathcal{F}(y,\tau) \, \mathrm{d}y \, \mathrm{d}\tau. \tag{2.22}$$

**Remark.** No assumption on the exact form of Green's function in this section has been required up to now. It means that the same derivation can be repeated also with the fundamental solution of different problem configuration (e.g. with different boundary conditions), see [46].

Using the formula of free-space Green's function (2.15) with $|x-y|$ replaced by $|x-\mathbf{0}| =: |x|$, i.e. $G(|x-\mathbf{0}|,t-\tau) = \delta(t-\tau+|x|/c)/(4\pi|x|)$, and integration over time in (2.22) results to

$$p(x,t) = \sum_{i,j,k=0}^{\infty} (-1)^{i+j+k} \frac{\partial^{i+j+k}}{\partial x_1^i \, \partial x_2^j \, \partial x_3^k} \left( \frac{m_{ijk}(\tau_0)}{4\pi|x|} \right), \tag{2.23}$$

where functions $m_{ijk}$ given as

$$m_{ijk}(\tau_0) = \frac{1}{i!j!k!} \int_V y_1^i \, y_2^j \, y_3^k \, \mathcal{F}(y,\tau_0) \, \mathrm{d}y \tag{2.24}$$

are evaluated in retarded time, i.e. at time $\tau_0 = t - \frac{|x|}{c}$, so $m_{ijk}(\tau_0)$ still depend on $x$, see [46].

The summation terms $m_{ijk}$ are called multipole moments of order $2^{i+j+k}$ of the source $\mathcal{F}$. The zeroth term $m_{000}$ is called monopole moment, while all the first terms $m_{100}, m_{010}$ and $m_{001}$ are called dipole moments, see [119]. The next terms are then quadrupole ($i+j+k=2$), octupole ($i+j+k=3$), etc.

With the help of the Fraunhofer approximation the multipole expansion gets a more simple form. We obtain for very large distances $r_0 := |x|$ of the observer to the compact sound source using interchange of time and space derivatives, for details see e.g. [79],

$$p(x,t) \approx \frac{1}{4\pi r_0} \sum_{i,j,k=0}^{\infty} \frac{1}{c^{i+j+k}} \left(\frac{\partial r_0}{\partial x_1}\right)^i \left(\frac{\partial r_0}{\partial x_2}\right)^j \left(\frac{\partial r_0}{\partial x_3}\right)^k \frac{\partial^{i+j+k} m_{ijk}(\tau_0)}{\partial t^{i+j+k}}, \tag{2.25}$$

where $\tau_0$ depends on $t$ and all terms proportional to $\frac{1}{r^n}$, $n \geq 2$ were neglected, see also [46]. In spherical coordinates the terms $\frac{\partial r_0}{\partial x_l} = \cos\vartheta_l$, $l \in \{1,2,3\}$ represent the direction cosines relative to the coordinate axes $x_l$. They express the sound directivity and its plot is called the radiation pattern. The graphs of these radiation patterns in spherical coordinates create so called radiation lobes, see Figures 2.2, 2.3 and 2.4.

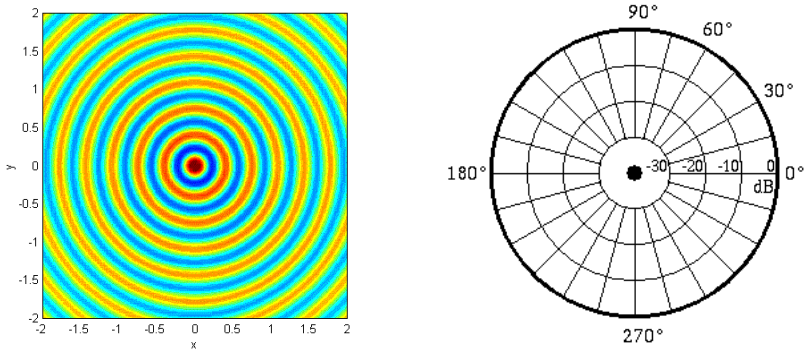


Figure 2.2: **Left:** Acoustic field induced by monopole point source located at axis origin. **Right:** Graph of radiation pattern. The sound emission is uniform in all directions.

**Monopole.** The basic model of the acoustic monopole is a volume source representing its expansion and contraction. Let point source be of the form $q(t)\delta(x)$ located at $y = \mathbf{0}$. Then the solution of wave equation (2.13) with this considered source is given by convolution of the source with the Green's function as

$$p(x,t) = \int_{-\infty}^{+\infty} \int_{\mathbb{R}^3} G(x,t;y,\tau)\; q(\tau)\delta(y)\; \mathrm{d}y\; \mathrm{d}\tau = \frac{1}{4\pi|x|}\; q\left(t - \frac{|x|}{c}\right), \tag{2.26}$$

i.e. the acoustic source will manifest at observer position after time delay $\frac{|x|}{c}$ needed for the signal to travel from the source position to the observer position. Formula (2.26) provides the scaling of pressure as $p \sim O(\frac{1}{|x|})$ for $|x| \to +\infty$ with the uniform sound directivity, see Figure 2.2. The monopole represents the most effective type of

aeroacoustic source concerning the radiation of acoustic energy to the surrounding, [78]. Examples of acoustic monopoles are e.g. model of pulsating sphere, explosion or exhaust pipe, [46].

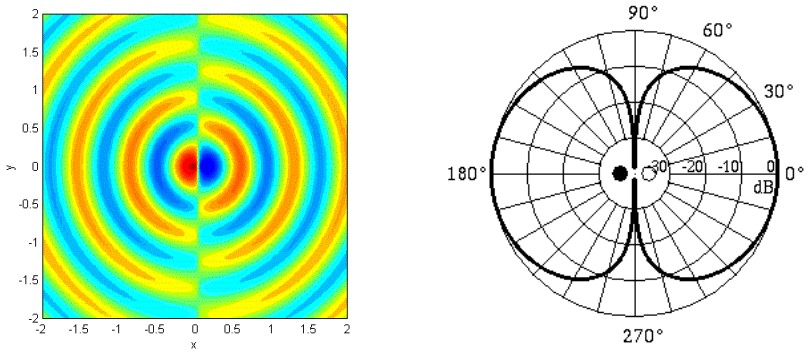


Figure 2.3: **Left:** Acoustic field induced by dipole point source located at axis origin. **Right:** Graph of radiation pattern. The sound emission is maximal at dipole axis, while in vicinity of 90° and 270° the emitted sound pressure level falls rapidly to zero (increasing diameter of concentric circles shows an increasing scale of sound pressure level).

**Dipole.** The dipole can be represented by two point sources (monopoles) of equal but opposite strengths placed a short distance apart (much smaller compared to the radiated sound wavelength). A generalized sound source $\mathcal{F}(x,t)$ in the case of the point dipole source has the form

$$\mathcal{F}(x,t) = \operatorname{div}\left(\mathbf{f}(t)\delta(x)\right) = \frac{\partial}{\partial x_j}(f_j(t)\delta(x)), \tag{2.27}$$

where $f_j$ are components of (volume) force density $\mathbf{f}$ applied to the fluid (for simplicity) at the origin, see e.g. [78], and the Einstein summation convention is used. It means that if any index appears in an expression repeatedly then the summation over it is performed, here in the range $1-3$. Then the solution of wave equation with dipole source on the right hand side (2.27) is given as

$$p(x,t) = \int_{-\infty}^{+\infty}\int_{\mathbb{R}^3} G(x,t;y,\tau)\ \frac{\partial}{\partial y_j}\left(f_j(\tau)\delta(y)\right)\ \mathrm{d}y\ \mathrm{d}\tau = \frac{\partial}{\partial x_j}\left(\frac{f_j(t-|x|/c)}{4\pi|x|}\right). \tag{2.28}$$

For far observer position ($x \to +\infty$) equation (2.28) can be approximated as

$$p(x,t) \approx \frac{x_j}{4\pi c|x|^2}\frac{\partial f_j}{\partial t}(t-|x|/c), \tag{2.29}$$

see e.g. [78]. The pressure for $|x| \to +\infty$ scales still as $p \sim O(\frac{1}{|x|})$ nevertheless the sound directivity is now dependent on one polar angle due to the term $\frac{x_j}{|x|}$. The directivity has peaks in direction parallel to the dipole axis, see Figure 2.3. In the case of dipole sound source produced aerodynamically, i.e. sound generated by a fluid flow with Mach number denoted by Ma, which is defined as the ratio

of characteristic flow velocity magnitude and speed of sound, the dipole radiation efficiency is lower approximately by factor of $\mathrm{Ma}^2$ compared to the monopole sound source, [78]. Examples of acoustic dipole is e.g. the (compact) force acting on the acoustic medium or cylinder in crossflow, [46].

**Quadrupole.** The basic physical conception of quadrupole is four identical point sources located close to each other with the sum of sources equal zero and with also all the dipole moments equal zero. A general (distributed) quadrupole source can be written as

$$\mathcal{F}(x,t) = \frac{\partial^2 f_{ij}}{\partial x_i \partial x_j}(x,t), \tag{2.30}$$

with $f_{ij}$ being components of the (fluid) stress tensor $\mathbf{F}$, see e.g. [78]. Then the solution of wave equation (2.13) with the quadrupole source in form (2.30) using Green's function (2.15) reads

$$p(x,t) = \int_{-\infty}^{+\infty} \int_{\mathbb{R}^3} G(x,t;y,\tau)\ \frac{\partial^2}{\partial y_i\, \partial y_j} f_{ij}(y,\tau)\ \mathrm{d}y\ \mathrm{d}\tau = \frac{\partial^2}{\partial x_i \partial x_j} \int_{\mathbb{R}^3} \frac{f_{ij}(y, t-|x-y|/c)}{4\pi|x-y|}\ \mathrm{d}y, \tag{2.31}$$

see e.g. [78]. Solution (2.31) can be approximated for the compact sound sources and for the far observer ($x \to +\infty$) by neglecting all the terms decaying faster than $O(\frac{1}{|x|})$, i.e.

$$p(x,t) \approx \frac{x_i x_j}{4\pi c^2 |x|^3} \frac{\partial^2}{\partial t^2} \int_{\mathbb{R}^3} f_{ij}\left(y, t - \frac{|x|}{c} + \frac{x\cdot y}{c|x|}\right)\ \mathrm{d}y, \tag{2.32}$$

see e.g. [119]. The sound directivity now depends on two angles, see Figure 2.4, [79]. It can be shown that the theoretical radiation efficiency of aeroacoustic quadrupole sound source is weaker than the dipole by additional $\mathrm{Ma}^2$, [78]. The typical examples of acoustic quadrupole is the turbulent stress distributions, see [78].

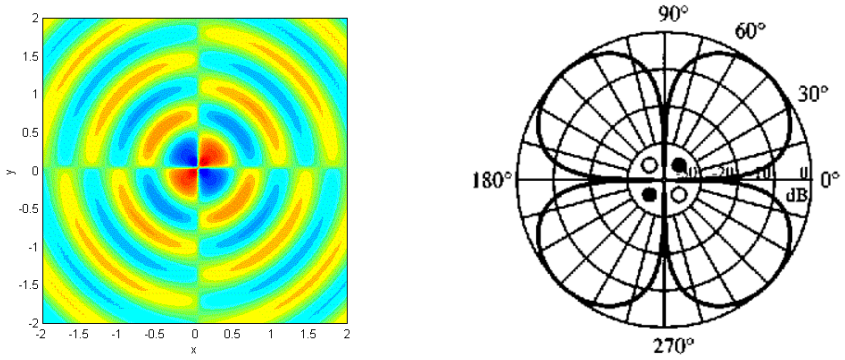


Figure 2.4: **Left:** Acoustic field induced by quadrupole point source located at axis origin. **Right:** Graph of radiation pattern. The sound emission is maximal at quadrupole axis, i.e. at angles of $\pm 45°$ and $\pm 135°$, while for the lines coincident with coordinate axis $x_1$ and $x_2$ the emitted sound pressure level is zero.

# Chapter 3

# Mathematical model of FSI problem

In this chapter the mathematical model of FSI problem is presented. It consists of the systems of equations describing the elastic body motion, the equations modelling the fluid flow and their couplings. In all cases the mathematical concept of continuum mechanics is used, i.e. we assume that it is possible to consider matter as a continuous medium described by continous (or even continuously differentiable) functions, e.g. mass is presented by density etc., see [36]. For the purpose of clarity the quantities connected with the fluid flow are denoted with the help of the upper index $f$, for the structure description the (upper) index $s$ is used.

This chapter is divided into five sections. First, the used coordinates systems are introduced together with the ALE method, then the elastic problem is described. The model of the compressible and the incompressible viscous fluid flow is given in the third and the fourth sections, respectively. The last section presents the mathematical formulation of the FSI coupled problem.

## Geometry of the FSI problem

Here, a simplified two-dimensional model of FSI problem is introduced, see Figure 3.1, where the reference and the deformed states are shown. For the description of the elastic structure deformation the reference coordinates are utilized, i.e. computational domain $\Omega^s = \Omega^s_t = \Omega^s_{\mathrm{ref}} \subset \mathbb{R}^2$ at arbitrary time $t$ is used.

Domain $\Omega^f_{\mathrm{ref}} \subset \mathbb{R}^2$ represents the reference fluid domain, e.g. the domain occupied by fluid at time instant $t = 0$ with the common interface $\Gamma_{\mathrm{W_{ref}}} = \Gamma_{\mathrm{W_0}}$ between the fluid and the structure domain. The deformation of reference domain $\Omega^f_{\mathrm{ref}}$ onto domain $\Omega^f_t \subset \mathbb{R}^2$ occupied by fluid at any time instant $t \in (0, \mathrm{T})$ is determined by the motion of the elastic structure and more specifically by the displacement of reference interface $\Gamma_{\mathrm{W_{ref}}}$ onto $\Gamma_{\mathrm{W_t}}$. It is treated with the aid of the ALE method.

We suppose that domains $\Omega^s$ and $\Omega^f_{\mathrm{ref}}$ are disjoint with the common non-empty interface $\Gamma_{\mathrm{W_{ref}}} = \overline{\Omega}^s \cap \overline{\Omega_{\mathrm{ref}}}^f$.

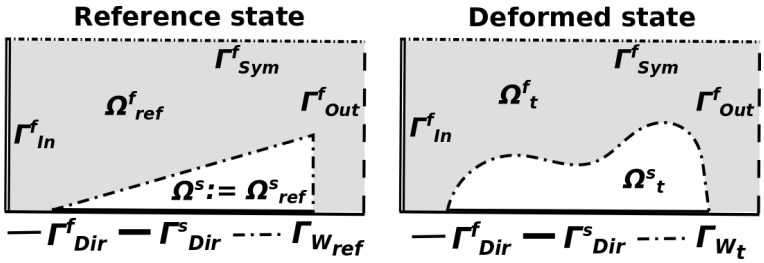


Figure 3.1: Scheme of FSI configuration in the reference state on the left and in a deformed state at arbitrary time $t$ on the right. The computational domain is composed of the elastic structure domain $\Omega^s$ and the fluid domain $\Omega^f_t$ together with boundaries: inlet $\Gamma^f_{\mathrm{In}}$, outlet $\Gamma^f_{\mathrm{Out}}$, symmetric boundary $\Gamma^f_{\mathrm{Sym}}$, walls $\Gamma^f_{\mathrm{Dir}}$, $\Gamma^s_{\mathrm{Dir}}$ and interface $\Gamma_{\mathrm{W}}$.

## 3.1 ALE method

First, the Eulerian and the Lagrangian descriptions are presented. Then, in order to treat the flow field description in time dependent domains, the ALE method is introduced, see e.g. [149].

### Lagrangian description

In the Lagrangian description, sometimes called the material description, a motion of every individual particle of continuum is followed using the Lagrangian mapping $\mathscr{L}$. The motion of the particle with a reference $X \in \mathcal{M}_0$ is described as

$$x = \mathscr{L}(X,t), \quad \forall t \in (0,\mathrm{T}). \tag{3.1}$$

Here, we assume that the reference is chosen as $\mathscr{L}(X,0) = X$. This means that the mapping $\mathscr{L}$ at any time $t$ determines the trajectory of the particle (point) $X$ from the reference domain $\mathcal{M}_0$ onto new configuration $\mathcal{M}_t$, which consists of the same fluid particles, i.e.

$$\mathcal{M}_t = \{x|\ x(t) = \mathscr{L}(X,t),\ X \in \mathcal{M}_0\},$$

see e.g. [55].

The mapping $\mathscr{L}$ is assumed to satisfy the following conditions

C1) $\mathscr{L}(X,0) = X$, for any $X \in \mathcal{M}_0$,

C2) for arbitrary $t \in (0,\mathrm{T})$ the mapping $X \longrightarrow \mathscr{L}(X,t)$ is bijective mapping of $\mathcal{M}_0$ onto $\mathcal{M}_t$,

C3) $\mathscr{L}$ is continuously differentiable,

C4) the Jacobian of mapping $\mathscr{L}$ satisfies $J(X,t) > 0$ for any $t > 0$ and $X \in \mathcal{M}_0$.

The conditions (C1-4) allow to define the velocity $\hat{\mathbf{v}}$ and the acceleration $\hat{\mathbf{a}}$ of a point $X \in \mathcal{M}_0$ as

$$\hat{\mathbf{v}}(X,t) = \frac{\partial \mathscr{L}}{\partial t}(X,t), \tag{3.2}$$

$$\hat{\mathbf{a}}(X,t) = \frac{\partial^2 \mathscr{L}}{\partial t^2}(X,t), \tag{3.3}$$

if the derivatives on the right hand side exist, see e.g. [55].

### Eulerian description

The Eulerian description, sometimes called also the spatial description, is based on the determination of fluid particle velocity $\mathbf{v}$ passing through a fixed point $x$ at time $t$. The velocity $\mathbf{v}$ is related to the Lagrangian velocity (3.2) by

$$\mathbf{v}(x,t) = \hat{\mathbf{v}}(X,t) = \frac{\partial \mathscr{L}}{\partial t}(X,t), \tag{3.4}$$

where $X$ is the reference of the point $x$ at time $t$, i.e. $x = \mathscr{L}(X,t)$ according to (3.1).

Based on (3.4) and (3.3) the acceleration can be computed under assumption $\mathbf{v} \in \mathbf{C}^1(\mathcal{M}_0 \times (0,\mathrm{T}))$ as

$$\mathbf{a}(x,t) = \frac{D\mathbf{v}(x,t)}{Dt} = \frac{\partial \mathbf{v}(x,t)}{\partial t} + \sum_{i=1}^{2} v_i(x,t) \frac{\partial \mathbf{v}(x,t)}{\partial x_i}, \tag{3.5}$$

where the symbol $\frac{D}{Dt}$ denotes the material (or the substantial) derivative $\frac{D}{Dt} = \frac{\partial}{\partial t} + \mathbf{v} \cdot \nabla$, see [55].

### ALE method

The ALE method (arbitrary Lagrangian-Eulerian method) can be understood as a generalization of the Eulerian and the Lagrangian descriptions, [81], see Figure 3.2. The ALE method is based on an one-to-one (arbitrary) mapping $A_t$ of the reference domain $\Omega^f_{\mathrm{ref}}$ onto the domain $\Omega^f_{\mathrm{t}}$ at any time instant $t \in (0,\mathrm{T})$, i.e. $x = A_t(X) \in \Omega^f_t$ for $X \in \Omega^f_{\mathrm{ref}}$.

The mapping $A_t$ is assumed to be diffeomorphism between $\Omega^f_{\mathrm{ref}}$ and $\Omega^f_{\mathrm{t}}$. Moreover it is assumed to satisfy

$$\frac{\partial A_t}{\partial t} \in C(\overline{\Omega^f_{\mathrm{ref}}}), \quad A_t(\partial\Omega^f_{\mathrm{ref}}) = \partial\Omega^f_{\mathrm{t}}, \quad \forall t \in (0,\mathrm{T}). \tag{3.6}$$

Particularly for the considered geometry, see Figure 3.1, it means that all boundaries with an exception of the moving interface remain static and that the reference interface $\Gamma_{\mathrm{W_{ref}}}$ is mapped onto the deformed one $\Gamma_{\mathrm{W_t}}$ at any time instant $t$, see Figure 3.2.

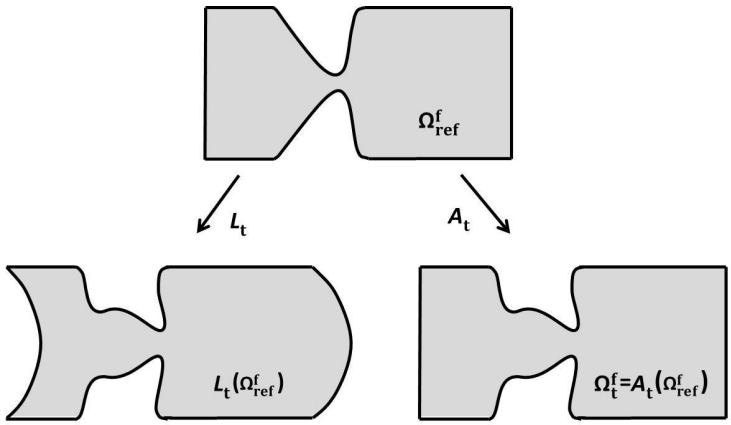


Figure 3.2: Schematic difference between the Lagrangian and the ALE descriptions of a fluid domain. The fixed domain $\Omega^f_{\text{ref}}$ described in the Eulerian coordinates is shown top, while the time evolution of domain $\Omega^f_{\text{ref}}$ given by Lagrangian mapping $L_t$ $(= \mathscr{L})$ is displayed bottom left. Bottom right is depicted the computational domain at time $t$ described with the help of the ALE method, i.e. the domain $\Omega^f_t = A_t(\Omega^f_{\text{ref}})$.

Let us denote for an arbitrary function $f(x,t)$ defined for $x \in \Omega^f_{\text{t}}$ and $t \in (0, \text{T})$ the transformed function on $\Omega^f_{\text{ref}}$ by $\hat{f}(X,t)$, i.e. $f(x,t) = f(A_t(X),t) = \hat{f}(X,t)$, where $x = A_t(X) \in \Omega^f_t$, $X \in \Omega^f_{\text{ref}}$.

One can see that a point $x = A_t(X)$ with a fixed reference $X \in \Omega^f_{\text{ref}}$ is moving in time with the so-called domain velocity which can be computed as

$$\mathbf{w}_D(x,t) = \hat{\mathbf{w}}_D(X,t) = \frac{\partial}{\partial t} A_t(X), \quad t \in (0, \text{T}),\ X \in \Omega^f_{\text{ref}}. \tag{3.7}$$

Further, the ALE derivative is introduced as the time derivative of an arbitrary continuous function $f(x,t) = f(A_t(X),t)$ with respect to a fixed point $X \in \Omega^f_{\text{ref}}$, i.e.

$$\frac{D^A}{Dt} f(x,t) = \frac{d}{dt}\left(f(A_t(X),t)\right) = \frac{\partial f}{\partial t}(x,t) + \mathbf{w}_D(x,t) \cdot \nabla f(x,t), \tag{3.8}$$

where the chain rule was applied. For more details and for the proof see [149] or [57].

**Remark.** In a general case if the ALE mapping would be chosen independently of described procedure as $A_t = \mathscr{L}_t$, then we would obtain the Lagrangian description and relation (3.8) would change to the material derivative as given by equation (3.5). On the other hand if the ALE mapping would be chosen as identity, i.e. $A_t = \mathcal{I}$, then we would get the Eulerian description and the relation (3.8) would become partial time derivative of function $f(x,t)$.

## 3.2 Elastic body

In this section the static and the dynamic linear elasticity problem is presented using the Lagrangian description.

### Elastic forces

Let us consider an elastic body represented by a bounded domain $\Omega^s \subset \mathbb{R}^2$ with the Lipschitz continuous boundary $\partial\Omega^s$. The two types of forces can act on arbitrary control volume of the elastic body – these are the volume and the surface forces. The volume force acts on every particle inside a volume element $\mathcal{V}$ with volume density $\mathbf{f}^s = (f_i^s)$. The surface forces are an external mechanical stresses, which act on the body surface. It can be described at any point of the body with the aid of (symmetric) Cauchy stress tensor $\boldsymbol{\tau}^s = (\tau_{ij}^s)$, see e.g. [36].

### Static and dynamic force balance

The (static) force balance between volume forces $\mathbf{f}^s$ and surface forces given by $\boldsymbol{\tau}^s$ at arbitrary point of the elastic body $X \in \Omega^s$ is described by

$$f_i^s + \frac{\partial \tau_{ij}^s}{\partial X_j} = 0, \tag{3.9}$$

see e.g. [109]. Let us emphasize that in equation (3.9) the Einstein summation convection (for $j = 1, 2$) is used. We shall use this convection also in what follows. Further let us mention that the balance of moments is automatically satisfied due to the symmetry of the tensor $\boldsymbol{\tau}^s$, see e.g. [36].

Assuming moreover that the functions $\boldsymbol{\tau}^s$, $\mathbf{f}^s$ and the displacement $\mathbf{u} = (u_1, u_2)$ depend also on time $t$, the equations of dynamic force balance reads, see e.g. [36],

$$-\rho^s \frac{\partial^2 u_i}{\partial t^2} + \frac{\partial \tau_{ij}^s}{\partial X_j} + f_i^s = 0 \qquad \text{in } \Omega^s, \tag{3.10}$$

where $\rho^s$ denotes the elastic body density and the term $-\rho^s \frac{\partial^2 u_i}{\partial t^2}$ represents inertia forces. In order to solve equation (3.9) or (3.10) the Hooke's law is used with the assumption of planar deformations.

### Hooke's law

The generalized Hooke's law describes linear dependence of the stress tensor components $(\tau_{ij}^s)$ on the strain tensor components $(e_{ij}^s)$ with the aid of a fourth order tensor $C_{ijkl}$, [109], i.e.

$$\tau_{ij}^s = C_{ijkl}\ e_{kl}^s, \tag{3.11}$$

where $k$ and $l$ are indices of summation. The fourth order tensor $C_{ijkl}$ is symmetric in index pairs $i$ and $j$, $k$ and $l$. It has in general 21 independent coefficients, called elastic coefficients, [36]. For the considered homogeneous isotropic body the number of independent coefficients reduces to two and the tensor $C_{ijkl}$ can be written with the aid of two Lamé coefficients $\lambda^s, \mu^s$. Thus equation (3.11) is simplified to

$$\tau_{ij}^s = \lambda^s \left(\operatorname{div} \mathbf{u}\right) \delta_{ij} + 2\mu^s e_{ij}^s, \tag{3.12}$$

where $\delta_{ij}$ denotes the Kronecker's delta. The Lamé coefficients can be determined from known material constants, e.g. from Young's modulus of elasticity $E^s$ and Poisson's ratio $\sigma^s$ according to the formulas

$$\lambda^s = \frac{E\sigma}{(1+\sigma)(1-2\sigma)}, \quad \mu^s = \frac{E}{2(1+\sigma)}, \tag{3.13}$$

see e.g. [140].

**Remark.** The linear relation between the Cauchy strain tensor and the stress tensor considered here and represented by Hooke's law is widely used in engineering practice. For more complicated, nonlinear relations, see e.g. [111].

### Elastic deformation

The elastic body deformation is described by the vector function of displacement $\mathbf{u}(X,t) = (u_1, u_2)$, where the components of $\mathbf{u}$ are the projections onto the coordinate axis. The components of the strain tensor $\boldsymbol{\epsilon}^s$, which expresses the change of the distance of two infinitesimally distant points, are given as

$$\epsilon^s_{jk} = \left( \frac{\partial u_j}{\partial X_k} + \frac{\partial u_k}{\partial X_j} + \frac{\partial u_i}{\partial X_j}\frac{\partial u_i}{\partial X_k} \right), \tag{3.14}$$

see e.g. [109]. For small displacements the second order terms can be neglected and the strain tensor can be replaced by the small strain tensor $\mathbf{e}^s$ with the components

$$e^s_{jk} = \frac{1}{2}\left( \frac{\partial u_j}{\partial X_k} + \frac{\partial u_k}{\partial X_j} \right). \tag{3.15}$$

The small strain tensor is the symmetric tensor of the second order, see e.g. [36].

**Remark.** The replacement of tensor $\boldsymbol{\epsilon}^s$ by small strain tensor $\mathbf{e}^s$ can be understand as a linearization (of the geometrical nonlinearity). For a large deformation, particularly for the case with substantial rotations of the structure, the use of $\mathbf{e}^s$ may lead to an incorrect modelling of the structure deformation, see [111], [93].

### Initial and boundary conditions

System of equations (3.10) needs to be equipped with initial and boundary conditions. The initial conditions for the displacement and for the velocity at time $t = 0$ and at any point $X \in \Omega^s$ read

$$\text{a)} \quad \mathbf{u}(X,0) = \mathbf{u}_0(X), \qquad \text{b)} \quad \frac{\partial \mathbf{u}}{\partial t}(X,0) = \mathbf{u}_1(X). \tag{3.16}$$

The boundary conditions for $t \in (0, \mathrm{T})$ are considered in the form

$$\begin{aligned} &\text{a)} && \mathbf{u}(X,t) = \mathbf{0}, && \text{for } X \in \Gamma^s_{\mathrm{Dir}}, \\ &\text{b)} && \tau^s_{ij}(X,t)\, n^s_j(X) = q^s_i(X,t), && \text{for } X \in \Gamma_{\mathrm{W_{ref}}}. \end{aligned} \tag{3.17}$$

The first equation of (3.17) is the zero Dirichlet boundary condition representing the firmly fixed boundary of the structure. The second equation is the Neumann boundary condition prescribing the action of the aerodynamic forces $\mathbf{q}^s = (q_1^s, q_2^s)$ on the interface $\Gamma_{\mathrm{W}}$ between the structure and the fluid. The both parts of boundary $\Gamma_{\mathrm{W}_{\mathrm{ref}}}, \Gamma^s_{\mathrm{Dir}}$ are mutually disjoint parts of the boundary $\partial\Omega^s = \Gamma_{\mathrm{W}_{\mathrm{ref}}} \cup \Gamma^s_{\mathrm{Dir}}$ (see Figure 3.1) and $n_j^s(X)$ are the components of the unit outer normal to $\Gamma_{\mathrm{W}_{\mathrm{ref}}}$.

## 3.3 Compressible fluid flow

For the considered case of air flow through the vocal tract during phonation the typical flow velocities are less than 0.3 Mach and in a such case the flow can be modelled as incompressible. However in order to address the acoustic phenomenon the compressibility needs to be taken into account. The flow of compressible fluid can be described by the Navier-Stokes equations, see e.g. [55]. Let us start with the compressible fluid flow description for a static fluid domain $\Omega^f_{\mathrm{ref}}$.

**Mass conservation.** The mass conservation is described by the continuity equation given by

$$\frac{\partial \rho^f}{\partial t} + \nabla \cdot (\rho^f \mathbf{v}) = 0, \qquad \text{in } \Omega^f_{\mathrm{ref}}, \tag{3.18}$$

where $\mathbf{v}$ denotes the fluid flow velocity and $\rho^f$ is the fluid density, [30].

**Momentum conservation.** The momentum conservation can be formulated in the so called conservative form

$$\frac{\partial(\rho^f \mathbf{v})}{\partial t} + \operatorname{div}(\rho^f \mathbf{v} \otimes \mathbf{v}) = \operatorname{div} \boldsymbol{\sigma}^f + \rho^f \mathbf{g}^f, \qquad \text{in } \Omega^f_{\mathrm{ref}}, \tag{3.19}$$

where $\boldsymbol{\sigma}^f$ denotes the Cauchy's stress tensor and vector $\rho^f \mathbf{g}^f$ is the volume force density, see e.g. [22]. The symbol $\otimes$ denotes the tensor product, see e.g. [36]. With the help of continuity equation (3.18) the momentum conservation can be rearranged into the equivalent, so-called non-conservative, form

$$\rho^f \left( \frac{\partial \mathbf{v}}{\partial t} + (\mathbf{v} \cdot \nabla)\mathbf{v} \right) = \operatorname{div} \boldsymbol{\sigma}^f + \rho^f \mathbf{g}^f. \tag{3.20}$$

Let us mention that the system of equations (3.18), (3.19) needs to be coupled with the equation for the energy conservation and enclosed by thermodynamic relations, see e.g. [55].

### Rheological relation

The Cauchy's (fluid) stress tensor is related to other fluid quantities by rheological relations, here the Newtonian fluid is assumed, see e.g. [30]. According to Stokes

postulates the constitutive law reads

$$\boldsymbol{\sigma}^f = (-p + \lambda^f \operatorname{div} \mathbf{v})\mathbb{I} + 2\mu^f \mathbb{D}(\mathbf{v}), \tag{3.21}$$

where $\lambda^f$ and $\mu^f$ are the first and the second viscosity coefficients, $\mathbb{I}$ denotes the identity $\mathbb{I} = (\delta_{ij})$ and $\mathbb{D}$ is the rate of deformation tensor $\mathbb{D} = \mathbb{D}(\mathbf{v}) = (d_{ij})$ with components $d_{ij} = \frac{1}{2}\left(\frac{\partial v_i}{\partial x_j} + \frac{\partial v_j}{\partial x_i}\right)$. The viscous part of the fluid stress tensor is given by

$$\boldsymbol{\tau}^f = \lambda^f (\operatorname{div} \mathbf{v})\mathbb{I} + 2\mu^f \mathbb{D}(\mathbf{v}), \tag{3.22}$$

see e.g. [55].

## 3.4 Incompressible fluid flow

In this section the compressible fluid flow model is simplified to the incompressible fluid flow model using the constant density assumption. Such a model is usable for almost incompressible fluid, e.g. for fluid with almost negligible density fluctuations. This is the case of a compressible fluid flow with low Mach numbers. Further the governing system of equations is rewritten in the ALE form, incorporating the effects of the time variable flow domain $\Omega_{\mathrm{t}}^f$. The final system of equations is then completed by initial and boundary conditions.

### Incompressibility

Let us consider here the density $\rho^f$ to be constant, i.e. $\rho^f(x,t) = \rho_0$. The mass conservation represented by (3.18) then reduces to the continuity equation in the form

$$\nabla \cdot \mathbf{v} = 0, \qquad \text{in } \Omega_{\mathrm{ref}}^f. \tag{3.23}$$

Similarly, the momentum conservation (3.20) gains the form

$$\rho_0 \left(\frac{\partial \mathbf{v}}{\partial t} + (\mathbf{v} \cdot \nabla)\mathbf{v}\right) = \rho_0 \mathbf{g}^f - \nabla p + \mu^f \Delta \mathbf{v}, \tag{3.24}$$

and after dividing equation (3.24) by $\rho_0$ we get

$$\frac{\partial \mathbf{v}}{\partial t} + (\mathbf{v} \cdot \nabla)\mathbf{v} = \mathbf{g}^f - \nabla \tilde{p} + \nu^f \Delta \mathbf{v}, \qquad \text{in } \Omega_{\mathrm{ref}}^f, \tag{3.25}$$

where $\nu^f = \frac{\mu^f}{\rho_0}$ is the kinematic fluid viscosity and $\tilde{p} = \frac{p}{\rho_0}$ is the kinematic pressure, see e.g. [30]. In what follows the tilde is for the sake of simplicity omitted, i.e. we will write $p = \tilde{p}$ and in the context of the fluid problem it means the kinematic pressure.

Now, the system of equations (3.23) and (3.25) is complete and no additional equation of energy conservation is needed because the assumption $\rho^f = const.$ decouples the energy equation from the mass and the momentum conservation equations.

For the case of human phonation simulation the incompressible viscous fluid flow model appears as a reasonable accurate approximation, see [105]. The highest flow velocity about $60\,\mathrm{m/s} \approx 0.2\,\mathrm{Ma}$ is achieved at the glottis, and the other phenomena connected with the need of compressible fluid flow model like shock waves, Rositta instability of boundary layer or heat transfer have not been observed or do not play any significant role, see [156].

**Remark.** More detailed arguments, when the use of incompressible fluid model is appropriate, are stated in e.g. [22] and [107]. The book [22] shows with simplified model that the value of $0.3\,\mathrm{Ma}$ presents a very approximate boundary below which the relative pressure difference of compressible and incompressible model is smaller than 5%. The article [107] explains that incompressible Navier-Stokes equations can be understood as limit of compressible Navier-Stokes equations for low Mach number approaching zero.

### ALE formulation

In order to describe a fluid flow in the time variable domain $\Omega_{\mathrm{t}}^f$ the ALE method is used. In this case the time derivative is replaced by the ALE derivative, which delivers us so-called ALE formulation of the incompressible Navier-Stokes equations, see e.g. [57], i.e. we get the system of equations

$$\frac{D^A\mathbf{v}}{Dt} + ((\mathbf{v} - \mathbf{w}_D)\cdot\nabla)\mathbf{v} + \nabla p = \nu^f \Delta\mathbf{v} + \mathbf{g}^f, \quad \operatorname{div}\mathbf{v} = 0, \quad \text{in } \Omega_t^f, \tag{3.26}$$

where $\frac{D^A}{Dt}$ denotes the ALE derivative and $\mathbf{w}_D$ denotes the ALE domain velocity, see Section 3.1.

### Initial and boundary conditions

Equations (3.26) must be supplied by relevant initial and boundary conditions. The deformation of $\Omega_{\mathrm{t}}^f$ (given by the ALE mapping $A_t$) is considered to be known for any time instant $t$, see next Section 3.5. The initial condition we assume in the form

$$\mathbf{v}(x,0) = \mathbf{v}_0(x), \quad x \in \Omega_0^f, \tag{3.27}$$

where velocity field $\mathbf{v}_0$ should satisfy $\operatorname{div}\mathbf{v}_0 = 0$, usually we set $\mathbf{v}_0 = \mathbf{0}$.

Further boundary $\partial\Omega_{\mathrm{t}}^f$ is assumed to be formed by the mutually disjoint parts $\partial\Omega_{\mathrm{t}}^f = \Gamma_{\mathrm{In}}^f \cup \Gamma_{\mathrm{Dir}}^f \cup \Gamma_{\mathrm{W_t}} \cup \Gamma_{\mathrm{Sym}}^f \cup \Gamma_{\mathrm{Out}}^f$ (here $\Gamma_{\mathrm{In}}^f$ denotes the inlet, $\Gamma_{\mathrm{Dir}}^f$ is the wall, $\Gamma_{\mathrm{W_t}}$ the moving interface, $\Gamma_{\mathrm{Sym}}^f$ is the boundary part with prescribed symmetry boundary condition and $\Gamma_{\mathrm{Out}}^f$ is the outlet, see Figure 3.1). The following boundary conditions

are prescribed:

$$\begin{aligned}
&\text{a)} && \mathbf{v}(x,t) = \mathbf{0} && \text{for } x \in \Gamma^f_{\mathrm{Dir}},\\
&\text{b)} && \mathbf{v}(x,t) = \mathbf{w}_D(x,t) && \text{for } x \in \Gamma_{\mathrm{W_t}},\\
&\text{c)} && \text{c1)}\ \ \mathbf{v}(x,t)\cdot\mathbf{n}^f = 0,\ \ \text{c2)}\ \ \frac{\partial(\mathbf{v}\cdot\mathbf{t}^f)}{\partial\mathbf{n}^f} = 0 && \text{for } x \in \Gamma^f_{\mathrm{Sym}},\\
&\text{d)} && (p(x,t)-p_{\mathrm{ref}})\mathbf{n}^f = \nu^f\frac{\partial\mathbf{v}}{\partial\mathbf{n}^f} - \frac{1}{2}\mathbf{v}(\mathbf{v}\cdot\mathbf{n}^f)^-, && \text{for } x \in \Gamma^f_{\mathrm{Out}},
\end{aligned} \tag{3.28}$$

for any $t \in (0, \mathrm{T})$. Vectors $\mathbf{n}^f$ and $\mathbf{t}^f$ are the unit outward normal and the unit tangent to boundary $\partial\Omega^f_{\mathrm{t}}$, respectively. Symbol $(\alpha)^-$ denotes the negative part of any real number $\alpha$, i.e. $(\alpha)^- = \min(\alpha, 0)$, and $p_{\mathrm{ref}}$ is a reference pressure. The symmetry boundary condition in our case $\Gamma^f_{\mathrm{Sym}} = \{x_1 \in \langle x_{\min}, x_{\max}\rangle,\ x_2 = 0\}$ simplifies to the form $v_2(x,t) = 0, \frac{\partial v_1}{\partial x_2} = 0$.

The outlet boundary condition (3.28 d) is a modified formulation of the do-nothing boundary condition (also called directional do-nothing BC, see [35]), and it increases the stability of the model by suppressing a possible backward flow through the outlet boundary according to the analysis given in [35], see its application example in [3].

At the inlet part of the boundary several possible forms of boundary conditions are considered. For this purpose the inlet boundary is formally divided into three disjoint parts: $\Gamma^f_{\mathrm{In}} = \Gamma^f_{\mathrm{In,dir}} \cup \Gamma^f_{\mathrm{In,p}} \cup \Gamma^f_{\mathrm{In},\epsilon}$. The following boundary conditions are prescribed for any $t \in (0, \mathrm{T})$:

$$\begin{aligned}
&\text{a)} && \mathbf{v}(x,t) = \mathbf{v}_{\mathrm{Dir}}(x,t), && \text{for } x \in \Gamma^f_{\mathrm{In,dir}},\\
&\text{b)} && (p(x,t)-p_{\mathrm{in}})\mathbf{n}^f - \nu^f\frac{\partial\mathbf{v}}{\partial\mathbf{n}^f}(x,t) = -\frac{1}{2}\mathbf{v}(\mathbf{v}\cdot\mathbf{n}^f)^-, && \text{for } x \in \Gamma^f_{\mathrm{In,p}},\\
&\text{c)} && (p(x,t)-p_{\mathrm{in}})\mathbf{n}^f - \nu^f\frac{\partial\mathbf{v}}{\partial\mathbf{n}^f}(x,t) = -\frac{1}{2}\mathbf{v}(\mathbf{v}\cdot\mathbf{n}^f)^- + \frac{1}{\epsilon}(\mathbf{v}-\mathbf{v}_{\mathrm{Dir}}), && \text{for } x \in \Gamma^f_{\mathrm{In},\epsilon}.
\end{aligned} \tag{3.29}$$

The choice of the inlet boundary condition is done e.g. by setting $\Gamma^f_{\mathrm{In}} = \Gamma^f_{\mathrm{In,dir}}$ and $\Gamma^f_{\mathrm{In,p}} = \Gamma^f_{\mathrm{In},\epsilon} = \emptyset$. This notation facilitates the explanation of the weak formulation in the next chapter.

Condition (3.29 a) represents the classical Dirichlet boundary condition for velocity. Condition (3.29 b) can be understood as prescribing pressure difference $\Delta p = p_{\mathrm{in}} - p_{\mathrm{ref}}$ between the inlet $\Gamma^f_{\mathrm{In}}$ and the outlet $\Gamma^f_{\mathrm{Out}}$. Boundary condition (3.29 c) prescribes inlet airflow velocity $\mathbf{v}_{\mathrm{Dir}}$ by the penalization approach with the help of a suitably chosen penalization parameter $\epsilon$, see [25], [148]. The inlet pressure $p_{\mathrm{in}}$ in condition (3.29 c) is set to zero. The value of parameter $\epsilon$ controls the switching between the Dirichlet boundary condition (limit $\epsilon \to 0^+$) and the pressure drop boundary condition (limit $\epsilon \to +\infty$). Further details describing the choice of parameter $\epsilon$ are presented in Sections 5.2 and 5.3.

## 3.5 Coupled FSI problem

In this section coupling conditions of the fluid and the structure subproblems are presented and the coupled problem formulation is summarized.

### 3.5.1 Fluid-structure coupling

First, as the FSI problem is a coupled problem the location of the common interface $\Gamma_{W_t}$ at time $t$ is unknown. Its location corresponds to an established force equilibrium between the aerodynamic and the elastic forces and it can be implicitly described with the aid of elastic body displacement $\mathbf{u}$ as

$$\Gamma_{\mathrm{W_t}} = \left\{ x \in \mathbb{R}^2 |\, x = X + \mathbf{u}(X,t),\, X \in \Gamma_{\mathrm{W_{ref}}} \right\}. \tag{3.30}$$

The structure and the fluid subproblems are coupled by the kinematic and the dynamic boundary condition prescribed at the common interface $\Gamma_{\mathrm{W_t}}$.

For the elastic body the so-called **dynamic boundary condition** is derived from the requirement of stress continuity across the interface $\Gamma_{\mathrm{W_t}}$ in the normal direction, see e.g. [90]. The prescribed Neumann type boundary condition has form (3.17 b), where the vector $\mathbf{q}^s = (q_i^s)$ reads

$$q_i^s(X,t) = -\sum_{j=1}^{2} \sigma_{ij}^f(x,t)\, n_j^f(x), \quad x = X + \mathbf{u}(X,t),\ X \in \Gamma_{\mathrm{W_{ref}}}, \tag{3.31}$$

where the components of $\sigma_{ij}^f$ are calculated for the considered formulation as $\sigma_{ij}^f = -\rho^f p\, \delta_{ij} + \rho^f \nu^f (\frac{\partial v_i}{\partial x_j} + \frac{\partial v_j}{\partial x_i})$, where $p$ denotes the kinematic pressure.

The so-called **kinematic boundary condition** follows from the continuity requirement of the fluid and the structural velocities at the interface $\Gamma_{\mathrm{W_t}}$, see e.g. [57]. Since the structure velocity $\frac{\partial \mathbf{u}}{\partial t}$ at the interface $\Gamma_{\mathrm{W_t}}$ is equal to the domain velocity $\mathbf{w}_D$, it has the form of Dirichlet boundary condition (3.28 b).

### 3.5.2 FSI formulation

The FSI problem formulation consists of the elastic subproblem and the fluid subproblem coupled via boundary conditions (3.31) and (3.28 b). Moreover for a complete formulation of the fluid flow subproblem an ALE mapping $A_t$ is sought based on the solution of the elastic subproblem, that satisfies

$$A_t : \Omega_{\mathrm{ref}}^f \to \Omega_{\mathrm{t}}^f, \quad A_t(\partial\Omega_{\mathrm{ref}}^f) \to \partial\Omega_{\mathrm{t}}^f \qquad \forall t \in (0, \mathrm{T}).$$

Once the mapping $A_t$ is known, the ALE domain velocity $\mathbf{w}_D$ is determined according to equation (3.7).

As a solution of the **elastic subproblem** we regard such function $\mathbf{u} \in \mathbf{C}^2(\Omega^s \times [0, \mathrm{T}])$, that equation (3.10) holds:

$$\rho^s \frac{\partial^2 \mathbf{u}}{\partial t^2} = \operatorname{div} \boldsymbol{\tau}^s + \mathbf{f}^s, \quad \text{in } \Omega^s \times (0, \mathrm{T}),$$

together with initial and boundary conditions (3.16) and (3.17). Stress tensor $\boldsymbol{\tau}^s$ is expressed by $\mathbf{u}$ using relation (3.12) with piecewise constant Lamé coefficients and the aerodynamic force $\mathbf{q}^s$ is given by equation (3.31).

We assume $\Omega^s \subset \mathbb{R}^2$ is a bounded domain with (piecewise) Lipschitz continuous boundary $\partial\Omega^s = \Gamma^s_{\mathrm{Dir}} \cup \Gamma^s_{\mathrm{W_{ref}}}$, where $\Gamma^s_{\mathrm{Dir}} \neq \emptyset$. Further we suppose, that $\mathbf{f}^s \in \mathbf{C}(\overline{\Omega}^s \times [0,\mathrm{T}])$, $\mathbf{u}_{\mathrm{Dir}} \in \mathbf{C}(\Gamma^s_{\mathrm{Dir}} \times [0,\mathrm{T}])$, $\mathbf{q}^s \in \mathbf{C}(\Gamma_{\mathrm{W_{ref}}} \times [0,\mathrm{T}])$ and $\mathbf{u}_0, \mathbf{u}_1 \in \mathbf{C}(\overline{\Omega}^s)$, $\rho^s$ is constant.

In the **fluid flow subproblem** we seek for velocity $\mathbf{v} \in \mathbf{C}^2(\Omega^f_t \times [0,\mathrm{T}])$ and pressure $p \in C^1(\Omega^f_t \times [0,\mathrm{T}])$ such, that they fulfill partial differential equations (3.26):

$$\frac{D^A\mathbf{v}}{Dt} + ((\mathbf{v} - \mathbf{w}_D)\cdot\nabla)\mathbf{v} + \nabla p = \nu^f \Delta\mathbf{v} + \mathbf{g}^f, \qquad \operatorname{div}\mathbf{v} = 0, \qquad \text{in } \Omega^t_t \times (0,\mathrm{T}),$$

together with initial and boundary conditions (3.27) and (3.28), (3.29). The ALE domain velocity $\mathbf{w}_D$ is given by (3.7), viscosity $\nu^f$ is constant.

Further we assume $\mathbf{g}^f \in \mathbf{C}(\overline{\Omega}^f_t \times [0,\mathrm{T}])$, $\mathbf{v}_{\mathrm{Dir}} \in \mathbf{C}(\Gamma^f_{\mathrm{Dir}} \times [0,\mathrm{T}])$, $\mathbf{v}_0 \in \mathbf{C}(\overline{\Omega}^f_t)$ and $p_{ref}$ and $\epsilon$ are appropriate constants. The fluid computational domain $\Omega^f_t \subset \mathbb{R}^2$ is assumed to be bounded with (piecewise) Lipschitz continuous boundary $\partial\Omega^f_t$ for $\forall t \in [0,\mathrm{T}]$. The boundary is composed of mutually disjoint parts: $\Gamma^f_{\mathrm{Dir}}, \Gamma^f_{\mathrm{Out}}, \Gamma^f_{\mathrm{W_t}}, \Gamma^f_{\mathrm{Sym}}, \Gamma^f_{\mathrm{In}}$. The inlet part $\Gamma^f_{\mathrm{In}}$ is further (formally) composed of $\Gamma^f_{\mathrm{In,dir}}, \Gamma^f_{\mathrm{In,p}}$ and $\Gamma^f_{\mathrm{In},\epsilon}$.

# Chapter 4

# Numerical model of FSI problem

This chapter contains a detailed description of numerical schemes based on the finite element method applied for approximation of the FSI problem. The first section describes the approximation of the elastic subproblem. In the second one the numerical scheme for the fluid flow subproblem is presented. The necessary stabilization of the method as well as the realization of different inlet boundary conditions is discussed. Third section is devoted to the construction of the ALE mapping, the computation of aerodynamic forces and the application of the strongly coupled algorithm for solution of the whole coupled FSI problem. The described procedures are implemented in the in-house program FSIFEM, see [1].

## 4.1 Elastic body

The spatial and the time discretization of linear elasticity problem (3.10) with boundary conditions (3.17) and initial conditions (3.16) is described in this section.

### 4.1.1 Spatial discretization

In order to apply FEM the classical formulation (3.10) is reformulated weakly.

#### Weak formulation

Starting with equation (3.10) we multiply it at a fixed time $t \in (0, \mathrm{T})$ by a test function $\boldsymbol{\psi} = (\psi^1, \psi^2)$ from space $\mathbf{V} = \{\mathbf{f} \in \mathbf{H}^1(\Omega^s) | \mathbf{f} = 0 \text{ on } \Gamma^s_{\mathrm{Dir}}\} \subset \mathbf{H}^1(\Omega^s)$, integrate it over $\Omega^s$ and apply Green's theorem (see Section 2.2). Thus we arrive to

$$\int_{\Omega^s} \rho^s \frac{\partial^2 u_i}{\partial t^2} \psi^i + \tau^s_{ij} \frac{\partial \psi^i}{\partial X_j} \, \mathrm{d}X = \int_{\Omega^s} f^s_i \ \psi^i \, \mathrm{d}X + \int_{\Gamma_{\mathrm{W_{ref}}}} q^s_i \ \psi^i \, \mathrm{d}S, \tag{4.1}$$

where the definition of space $\mathbf{V}$ and boundary condition (3.17 b) were used.

Further, using the symmetry of stress tensor $\boldsymbol{\tau}^s$, Hooke's law (3.11) and assuming an isotropic body we get

$$\int_{\Omega^s} \tau_{ij}^s \frac{\partial \psi^i}{\partial X_j} \, \mathrm{d}X = \int_{\Omega^s} \tau_{ij}^s(\mathbf{u}) e_{ij}^s(\boldsymbol{\psi}) \, \mathrm{d}X = \int_{\Omega^s} \left( \lambda^s \left( \operatorname{div} \mathbf{u} \right) \delta_{ij} + 2\mu^s e_{ij}^s(\mathbf{u}) \right) e_{ij}^s(\boldsymbol{\psi}) \, \mathrm{d}X, \tag{4.2}$$

see e.g. [39]. Then using (4.2) in (4.1) the weak form of equation (3.10) reads

$$\left( \rho^s \frac{\partial^2 u_i}{\partial t^2}, \psi^i \right)_{\Omega^s} + \left( \left( \lambda^s \delta_{ij} \left( \operatorname{div} \mathbf{u} \right) + 2\mu^s e_{ij}^s(\mathbf{u}) \right), e_{ij}^s(\boldsymbol{\psi}) \right)_{\Omega^s} = \left( f_i^s, \psi^i \right)_{\Omega^s} + \left( q_i^s, \psi^i \right)_{\Gamma_{\mathrm{W_{ref}}}}, \tag{4.3}$$

where by symbol $(\cdot, \cdot)_{\mathcal{D}}$ the scalar product in space $L^2(\mathcal{D})$ is denoted (see Chapter 2), see [80].

As *weak solution* of (3.10) at fixed time $t$ we call such function $\mathbf{u} : (0, \mathrm{T}) \mapsto \mathbf{H}^1(\Omega^s)$, that satisfies equation (4.3) for any $\boldsymbol{\psi} \in \mathbf{V}$, boundary condition (3.17 a) holds and the second partial derivative $\frac{\partial^2 \mathbf{u}}{\partial t^2}$ exists and $\frac{\partial^2 \mathbf{u}}{\partial t^2} \in L^2(\Omega^s)$.

Let us mention that the existence and uniqueness of weak solution for the stationary case, i.e. $\frac{\partial^2 \mathbf{u}}{\partial t^2} = \mathbf{0}$, follows from Lax-Milgram theorem, see Section 2.2. Its assumptions can be verified with the help of Friedrichs and Korn inequalities, see e.g. [109].

### Discrete formulation

The finite element method is used to approximate solution of problem (4.3). The finite element method is based on a decomposition of the computational domain $\Omega^s$ into finite number of polygons, e.g. triangles. For simplicity we assume that $\Omega^s \subset \mathbb{R}^2$ is polygonal domain covered by an admissible triangulation $\mathcal{T}_h^s$, see e.g. [39]. It means that triangles $K \in \mathcal{T}_h^s$ are closed, with mutually disjoint interiors and $\bigcup_{K \in \mathcal{T}_h^s} K = \overline{\Omega^s}$. The intersection of two elements (triangles) is either common vertex, edge or empty set, see Figure 4.1.

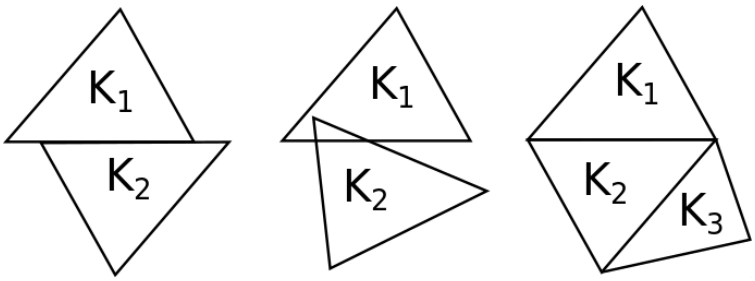


Figure 4.1: The first two pictures on the left show examples of inadmissible triangulation, while the picture on the right demonstrates an admissible triangulation.

The approximate solution $\mathbf{u}_h$ is sought in a finite dimensional finite element space $\mathbf{V}_h = V_h \times V_h$, where

$$V_h = \{ f \in C(\overline{\Omega^s}) | f = 0 \text{ on } \Gamma_{\mathrm{Dir}}^s, f|_K \in \mathbb{P}_1(K) \ \forall K \in \mathcal{T}_h^s \} \subset V, \tag{4.4}$$

where $\mathbb{P}_1(K)$ is the space of polynomials of degree less or equal one on the triangle $K$, i.e. the standard linear Lagrange triangular elements are used, see e.g. [39]. Let us denote by $N_h$ the dimension, i.e *dim* $V_h = N_h$. The basis functions $\psi_i \in V_h$ of the space $V_h$ are defined for $i = 1, \ldots, N_h$ by the formula $\psi_i(X_j) = \delta_{ij}, \quad j = 1, \ldots, N_h$, where by $X_j$ the vertices of the triangulation $\tau_h^s$ are denoted (with the exception of the triangulation vertices laying on the boundary $\Gamma^s_{\mathrm{Dir}}$). Further the basis functions of the space $\mathbf{V}_h$ are chosen as $\boldsymbol{\psi}_j(X) = \begin{pmatrix} \psi_j(X) \\ 0 \end{pmatrix}$ and $\boldsymbol{\psi}_{j+N_h}(X) = \begin{pmatrix} 0 \\ \psi_j(X) \end{pmatrix}$ for $j = 1, \ldots, N_h$.

The choice (4.4) of the approximation space $\mathbf{V}_h$ ensures a sparse structure of mass and stifness matrices and a possibility to use a simple affine equivalent elements leading to a simple practical implementation, see e.g. [86].

Any function of the space $\mathbf{V}_h$ can be expressed as a linear combination of the basis functions $\boldsymbol{\psi}_1, \ldots, \boldsymbol{\psi}_{2N_h}$. The approximate solution $\mathbf{u}_h$ at time $t \in (0, \mathrm{T})$ can be written as

$$\mathbf{u}_h(X, t) = \sum_{j=1}^{2N_h} \alpha_j(t)\, \boldsymbol{\psi}_j(X), \tag{4.5}$$

where we assume that unknown coefficients of the linear combination are $\alpha_j(t) \in C^2([0, \mathrm{T}])$. Particularly for the presented choice of the basis functions, the coefficients $\alpha_j$ and $\alpha_{j+N_h}$ denote the values of $u_{h,1}$ and $u_{h,2}$ at the vertex $X_j$, respectively.

Using $\mathbf{u}_h$ in the form (4.5) and taking the test functions $\boldsymbol{\psi}$ in equation (4.3) from the space $\mathbf{V}_h$ leads to the system of $2N_h$ ordinary differential equations of the second order for the unknown vector of coefficients $\boldsymbol{\alpha}(t) = (\alpha_j(t))_{j=1}^{2N_h}$

$$\mathbb{M}\ddot{\boldsymbol{\alpha}} + \mathbb{D}\dot{\boldsymbol{\alpha}} + \mathbb{K}\boldsymbol{\alpha} = \mathbf{b}(t), \tag{4.6}$$

where the term $\mathbb{D}\dot{\boldsymbol{\alpha}}$ was added with the matrix $\mathbb{D} = \epsilon_1^s \mathbb{M} + \epsilon_2^s \mathbb{K}$ representing the proportional damping model with suitably chosen parameters $\epsilon_1^s, \epsilon_2^s$, see paragraph 5.1.1. The vector $\mathbf{b} = \mathbf{b}(t)$ has the components

$$b_i = (\mathbf{f}^s, \boldsymbol{\psi}_i)_{\Omega^s} + (\mathbf{q}^s, \boldsymbol{\psi}_i)_{\Gamma_{\mathrm{W_{ref}}}} \tag{4.7}$$

and the elements of matrices $\mathbb{M} = (m_{ij}), \mathbb{K} = (k_{ij})$ are given by

$$m_{ij} = (\rho^s \boldsymbol{\psi}_j, \boldsymbol{\psi}_i)_{\Omega^s}, \qquad k_{ij} = (\lambda^s (\mathrm{div}\ \boldsymbol{\psi}_j)\, \delta_{ij} + 2\mu^s \mathbf{e}^s(\boldsymbol{\psi}_j), \mathbf{e}^s(\boldsymbol{\psi}_i))_{\Omega^s}. \tag{4.8}$$

The matrices $\mathbb{K}$ and $\mathbb{M}$ are usually called the stiffness matrix and the mass matrix, respectively. The matrices $\mathbb{K}, \mathbb{M}$ are symmetric and positive-definite matrices, see e.g. [146], [39].

The convergence analysis for the stationary case can be found e.g. in book [39]. In practical implementation the numerical quadrature with accuracy up to the second order replaces the integration formulas given by (4.7) and (4.8), see e.g. [31].

**Initial conditions**

The system (4.6) needs to be equipped by an initial condition for $\boldsymbol{\alpha}(0)$ and $\dot{\boldsymbol{\alpha}}(0)$. This can be accomplished by the projection of the given functions $\mathbf{u}_0, \mathbf{u}_1 \in \mathbf{C}(\overline{\Omega^s})$ on the space $\mathbf{V}_h$ at time $t = 0$, i.e.

$$(\mathbf{u}_h(X,0) - \mathbf{u}_0(X), \boldsymbol{\psi}_h(X))_{\Omega^s} = 0 \quad \text{and} \quad (\frac{\partial \mathbf{u}_h}{\partial t}(X,0) - \mathbf{u}_1(X), \boldsymbol{\psi}_h(X))_{\Omega^s} = 0, \tag{4.9}$$

for all $\boldsymbol{\psi}_h \in \mathbf{V}_h$.

### 4.1.2 Time discretization

The time discretization of problem (4.6) is realized by the Newmark method. Its advantages are the tailored design for second order systems, the unconditionally stability and the second order accuracy, see e.g. [42], [80]. In order to describe the time discretization, the time interval $[0, \mathrm{T}]$ is divided into $N$ equidistant intervals, where $t_n = n\Delta t$ for $n = 0, 1, \ldots, N$ and $\Delta t = \frac{T}{N}$. The same time interval partition is also considered for the time discretization of the fluid flow problem.

**Newmark method**

Application of the Newmark method is explained here first for a general second order ordinary differential equation (ODE) written as

$$\ddot{y}(t) = f(t, y(t), \dot{y}(t)), \qquad \text{for } t \in (0, \mathrm{T}), \tag{4.10}$$

with the initial conditions

$$y(0) = y_0, \quad \dot{y}(0) = y_1,$$

where $f : [0, \mathrm{T}] \times \mathbb{R} \times \mathbb{R} \mapsto \mathbb{R}$ is supposed to be a continuous function and $y_0, y_1 \in \mathbb{R}$.

Using the time discretization we introduce approximations $y^n \approx y(t_n)$, $\dot{y}^n \approx \dot{y}(t_n)$ and $f^n = f(t_n, y^n, \dot{y}^n)$. Then the numerical scheme can be written in a following way

$$y^{n+1} = y^n + \Delta t \dot{y}^n + \Delta t^2 \left( \beta f^{n+1} + (\frac{1}{2} - \beta) f^n \right), \tag{4.11}$$

$$\dot{y}^{n+1} = \dot{y}^n + \Delta t \left( \gamma f^{n+1} + (1 - \gamma) f^n \right), \tag{4.12}$$

where $\beta$ and $\gamma$ are parameters, $\beta \in [0, \frac{1}{2}]$ and $\gamma \in [0, 1]$. For the choice $\gamma = \frac{1}{2}, \beta = \frac{1}{4}$ the Newmark method is of second order accuracy and unconditionally stable, see [42].

The Newmark method given by (4.11) and (4.12) represents an implicit scheme due to the presence of the term $f^{n+1}$ on the right hand side of (4.11) and (4.12). The arising nonlinear equation needs to be solved e.g. by Newton method. However, if the Newmark method is applied on a linear equation or on a linear system of equations (as in the case of the system (4.6)), then the resulting scheme is also linear and its solution is straightforward.

**Application of the Newmark method**

The choice $t = t_{n+1}$ for system (4.6) yields

$$\mathbb{M}\ddot{\boldsymbol{\alpha}}(t_{n+1}) + \mathbb{D}\dot{\boldsymbol{\alpha}}(t_{n+1}) + \mathbb{K}\boldsymbol{\alpha}(t_{n+1}) = \mathbf{b}(t_{n+1}). \tag{4.13}$$

Replacing $\boldsymbol{\alpha}(t_{n+1})$ by $\boldsymbol{\alpha}^{n+1}$ and $\dot{\boldsymbol{\alpha}}(t_{n+1}), \ddot{\boldsymbol{\alpha}}(t_{n+1})$ by the approximations $\dot{\boldsymbol{\alpha}}^{n+1}, \ddot{\boldsymbol{\alpha}}^{n+1}$ given by relations (4.11), (4.12) we obtain

$$\begin{aligned}\mathbb{M}\ddot{\boldsymbol{\alpha}}^{n+1} + \mathbb{D}\left(\dot{\boldsymbol{\alpha}}^{n} + \Delta t(1-\gamma)\ddot{\boldsymbol{\alpha}}^{n} + \Delta t\gamma\ddot{\boldsymbol{\alpha}}^{n+1}\right) + \\ + \mathbb{K}\left(\boldsymbol{\alpha}^{n} + \Delta t\dot{\boldsymbol{\alpha}}^{n} + \frac{1-2\beta}{2}\Delta t^2\ddot{\boldsymbol{\alpha}}^{n} + \beta\Delta t^2\ddot{\boldsymbol{\alpha}}^{n+1}\right) = \mathbf{b}^{n+1}.\end{aligned} \tag{4.14}$$

Using some algebra equation (4.14) can be rearranged as

$$\mathbb{A}\ddot{\boldsymbol{\alpha}}^{n+1} = \mathbf{g}^{n+1}, \tag{4.15}$$

where $\mathbb{A}$ is the matrix $\mathbb{A} = (\mathbb{M} + \gamma\Delta t\mathbb{D} + \beta(\Delta t)^2\mathbb{K})$ and the vector $\mathbf{g}^{n+1}$ is given by

$$\mathbf{g}^{n+1} = \mathbf{b}^{n+1} - \mathbb{D}\dot{\boldsymbol{\alpha}}^{n} - (1-\gamma)\Delta t\mathbb{D}\ddot{\boldsymbol{\alpha}}^{n} - \mathbb{K}\boldsymbol{\alpha}^{n} - \Delta t\mathbb{K}\dot{\boldsymbol{\alpha}}^{n} - \frac{1-2\beta}{2}(\Delta t)^2\mathbb{K}\ddot{\boldsymbol{\alpha}}^{n}, \tag{4.16}$$

see e.g. [90].
The procedure of numerical solution is following:

From the initial conditions at time $t_0 = 0$ the displacement $\boldsymbol{\alpha}^0$ and the velocity $\dot{\boldsymbol{\alpha}}^0$ are determined using equations (4.9). The acceleration $\ddot{\boldsymbol{\alpha}}^0$ is computed from the system of linear equations (4.6) for $t = t_0$.

Now for arbitrary $n = 0, 1, 2, \ldots$ we repeat:
The acceleration $\ddot{\boldsymbol{\alpha}}^{n+1}$ at $t_{n+1}$ is computed by solving the system (4.15), where the known values $\boldsymbol{\alpha}^n, \dot{\boldsymbol{\alpha}}^n, \ddot{\boldsymbol{\alpha}}^n$ are used to compute $\mathbf{g}^{n+1}$ from (4.16). Then employing the relations analogous to (4.11) and (4.12) the velocity and the displacement approximations $\dot{\boldsymbol{\alpha}}^{n+1}$ and $\boldsymbol{\alpha}^{n+1}$ at $t_{n+1}$ are computed, respectively.

## 4.2 Fluid flow

In order to approximate the fluid flow problem one needs to take into an account the nonlinearity due to present convection and another difficulty is caused by the incompressibility constraint. Moreover the dominating convection has to be treated. The time discretization is applied before the derivation of the weak formulation, where a special attention is paid to the application of the considered boundary conditions. At the end of this section the stabilization and the linearization of the obtained nonlinear system of algebraic equations are described.

### 4.2.1 Time discretization

Similarly as for the elasticity problem the equidistant division of the time interval is used with the same time step $\Delta t$, i.e. the time interval $[0, \mathrm{T}]$ is divided into intervals

given by the partition $t_n = n\Delta t$ for $n = 0, 1, \ldots, N$. Further the approximations at the $n$-th time level are denoted by $\mathbf{v}^n \approx \mathbf{v}(t_n), \mathbf{w}_D^n \approx \mathbf{w}_D(t_n), p^n \approx p(t_n), \mathbf{g}^n \approx \mathbf{g}(t_n)$.

According to [62] the overall accuracy of FSI algorithm is determined by the used approximation of the lowest order of accuracy. In order to maintain the second order of accuracy in time the ALE derivative is approximated with the backward difference formula of second order (BDF2) as

$$\frac{D^A\mathbf{v}}{Dt}(t_{n+1}) \approx \frac{3\mathbf{v}^{n+1} - 4\overline{\mathbf{v}}^n + \overline{\mathbf{v}}^{n-1}}{2\Delta t}, \tag{4.17}$$

where for a fixed time instant $t_{n+1}$ we denote $\overline{\mathbf{v}}^i(x) = \mathbf{v}^i(\tilde{x})$ for $\tilde{x} = A_{t_i}(A_{t_{n+1}}^{-1}(x))$, $i \in \{n-1, n\}$ and $x \in \Omega_{t_{n+1}}^f$.

Further, for the sake of simplicity we focus on the discretization at a fixed time instant $t_{n+1}$ and thus in next sections we omit the index $n+1$, i.e. we denote $\mathbf{v} := \mathbf{v}^{n+1}, \Omega^f := \Omega_{t_{n+1}}^f$, etc.

### 4.2.2 Weak formulation

In order to obtain the weak formulation of fluid flow problem (3.26) in space, the first and the second equation of (3.26) are multiplied by test functions $\boldsymbol{\varphi} \in \mathbf{X}$ and $q \in M$, respectively. Here the space $\mathbf{X} = X_1 \times X_2$ is defined as $X_1 = \{f \in H^1(\Omega^f) |\, f = 0 \text{ on } \Gamma_{\text{Dir}}^f \cup \Gamma_{\text{In,dir}}^f \cup \Gamma_{\text{W}_\text{t}}^f\} \subset H^1(\Omega^f)$, $X_2 = \{f \in X_1 |\, f = 0 \text{ on } \Gamma_{\text{Sym}}^f\}$ and $M = L^2(\Omega^f)$. Then both equations (3.26) are integrated over the fluid domain $\Omega^f$ and summed up into a single equation. Finally the use of Green's theorem on the pressure and the viscous terms with considered $\mathbf{g} = \mathbf{0}$ yields, see e.g. [152],

$$\begin{aligned} &\left(\frac{3\mathbf{v}}{2\Delta t}, \boldsymbol{\varphi}\right)_{\Omega^f} + (((\mathbf{v} - \mathbf{w}_D)\cdot\nabla)\mathbf{v}, \boldsymbol{\varphi})_{\Omega^f} + \nu^f(\nabla\mathbf{v}, \nabla\boldsymbol{\varphi})_{\Omega^f} - (p, \operatorname{div}\boldsymbol{\varphi})_{\Omega^f} + \\ &+ \quad (q, \operatorname{div}\mathbf{v})_{\Omega^f} \;= \left(\frac{4\overline{\mathbf{v}}^n - \overline{\mathbf{v}}^{n-1}}{2\Delta t}, \boldsymbol{\varphi}\right)_{\Omega^f} + \left(\nu^f \frac{\partial\mathbf{v}}{\partial\mathbf{n}^f} - p\mathbf{n}^f, \boldsymbol{\varphi}\right)_{\partial\Omega^f}. \end{aligned} \tag{4.18}$$

The contribution to the last term on the right hand side of (4.18) is equal zero at boundaries $\Gamma_{\text{Dir}}^f, \Gamma_{\text{W}_\text{t}}^f$ and $\Gamma_{\text{In,dir}}^f$ according to the definition of the space $\mathbf{X}$, as well as at the $\Gamma_{\text{Sym}}^f$ because the second (normal) component of the test function $\boldsymbol{\varphi}$ equals zero ($\boldsymbol{\varphi} \in \mathbf{X}$) due to the outer normal $\mathbf{n}^f = (0, 1)^T$ at the boundary $\Gamma_{\text{Sym}}^f$, see Figure 5.1.

Therefore the term $\left(\nu^f \frac{\partial\mathbf{v}}{\partial\mathbf{n}^f} - p\mathbf{n}^f, \boldsymbol{\varphi}\right)_{\partial\Omega^f}$ can be nonzero only at boundaries $\Gamma_{\text{In,p}}^f, \Gamma_{\text{In,}\epsilon}^f$ and $\Gamma_{\text{Out}}^f$. This is why for the FE method usually the classical do-nothing boundary is realized by setting this term equal to zero due to the prescription of the condition $\nu^f \frac{\partial\mathbf{v}}{\partial\mathbf{n}^f} - p\mathbf{n}^f = 0$ at the outlet part of the domain ($\Gamma_{\text{Out}}^f$), see e.g. [64]. However, such a boundary condition leads possibly to instability in particular for the case, when strong vortices leave the outflow part of boundary causing backward inflow into $\Omega_t^f$.

In order to overcome this issue the convective term is further reformulated as

$$(((\mathbf{v}-\mathbf{w}_D)\cdot\nabla)\mathbf{v},\boldsymbol{\varphi})_{\Omega^f} = \frac{1}{2}\left(((\mathbf{v}-2\mathbf{w}_D)\cdot\nabla)\mathbf{v},\boldsymbol{\varphi}\right)_{\Omega^f} - \frac{1}{2}\left((\mathbf{v}\cdot\nabla)\boldsymbol{\varphi},\mathbf{v}\right)_{\Omega^f} + \\ + \frac{1}{2}\left((\mathbf{v}\cdot\mathbf{n}^f)^+\mathbf{v},\boldsymbol{\varphi}\right)_{\partial\Omega^f} + \frac{1}{2}\left((\mathbf{v}\cdot\mathbf{n}^f)^-\mathbf{v},\boldsymbol{\varphi}\right)_{\partial\Omega^f}, \quad (4.19)$$

where $(\alpha)^+$ is $\max\{0,\alpha\}$ and $(\alpha)^-$ is $\min\{0,\alpha\}$, $\alpha\in\mathbb{R}$. The first three terms of (4.19) are included into the weak formulation, whereas the last term is nonzero only at boundaries $\Gamma^f_{\mathrm{Out}}$, $\Gamma^f_{\mathrm{In,p}}$ and $\Gamma^f_{\mathrm{In},\epsilon}$ due to the definition of the space $\mathbf{X}$ and condition (3.28 c).

The summation of the last terms of equations (4.18) and (4.19) motivates the specification of the outlet boundary condition prescribed at $\Gamma^f_{\mathrm{Out}}$

$$(p(x,t)-p_{\mathrm{ref}})\mathbf{n}^f - \nu^f\frac{\partial\mathbf{v}}{\partial\mathbf{n}^f} = -\frac{1}{2}\mathbf{v}(\mathbf{v}\cdot\mathbf{n}^f)^-, \quad (4.20)$$

where $p_{\mathrm{ref}}$ is a reference pressure value at $\Gamma^f_{\mathrm{Out}}$, see [57], [148]. Condition (4.20) is called the directional do-nothing boundary condition.

Let us further concentrate on the inlet boundary conditions prescribed at the formally divided inlet part of boundary $\Gamma^f_{\mathrm{In}} = \Gamma^f_{\mathrm{In,dir}}\cup\Gamma^f_{\mathrm{In,p}}\cup\Gamma^f_{\mathrm{In},\epsilon}$. The boundary condition at the part of boundary $\Gamma^f_{\mathrm{In,p}}$ is given by (4.20), where the reference pressure is replaced by the inlet pressure $p_{\mathrm{in}}$. The formulation of boundary condition (3.29 c) at $\Gamma^f_{\mathrm{In},\epsilon}$ follows the same procedure, where the reference pressure is set $p_{\mathrm{ref}}=0$ and penalization term $\frac{1}{\epsilon}(\mathbf{v}-\mathbf{v}_{\mathrm{Dir}},\boldsymbol{\varphi})_{\Gamma^f_{\mathrm{In},\epsilon}}$ is added to the weak formulation with $\epsilon>0$. At boundary $\Gamma^f_{\mathrm{In,dir}}$ the boundary condition gets the form $\mathbf{v}=\mathbf{v}_{\mathrm{Dir}}$.

Finally, a solution of the *weak formulation* of problem (3.26) at time $t_{n+1}$ is a such function pair $V=(\mathbf{v},p)\in\mathbf{H}^1(\Omega^f)\times M$, that

$$a(V,V,\Phi) = f(\Phi) \quad (4.21)$$

is satisfied for any test function pair $\Phi=(\boldsymbol{\varphi},q)$ from space $\mathbf{X}\times M$ and moreover velocity $\mathbf{v}$ satisfies boundary conditions (3.28 a, b, c1) and (3.29 a) and $\frac{D^A\mathbf{v}}{Dt}\in L^2(\Omega^f)$.

Here, the trilinear form $a(\cdot,\cdot,\cdot)$ with arguments $V^*=(\mathbf{v}^*,p^*), V=(\mathbf{v},p)$ and $\Phi=(\boldsymbol{\varphi},q)$ is given as

$$a(V^*,V,\Phi) = \left(\frac{3\mathbf{v}}{2\Delta t},\boldsymbol{\varphi}\right)_{\Omega^f} + \frac{1}{2}(((\mathbf{v}^*-2\mathbf{w}_D)\cdot\nabla)\mathbf{v},\boldsymbol{\varphi})_{\Omega^f} - \frac{1}{2}((\mathbf{v}^*\cdot\nabla)\boldsymbol{\varphi},\mathbf{v})_{\Omega^f} + \\ + \frac{1}{2}((\mathbf{v}^*\cdot\mathbf{n})^+\mathbf{v},\boldsymbol{\varphi})_{\Gamma^f_{\mathrm{Out}}} + \nu^f(\nabla\mathbf{v},\nabla\boldsymbol{\varphi})_{\Omega^f} - (p,\operatorname{div}\boldsymbol{\varphi})_{\Omega^f} + (q,\operatorname{div}\mathbf{v})_{\Omega^f} + \\ + \frac{1}{2}((\mathbf{v}^*\cdot\mathbf{n})^+\mathbf{v},\boldsymbol{\varphi})_{\Gamma^f_{\mathrm{In,p}\cup\epsilon}} + \frac{1}{\epsilon}(\mathbf{v},\boldsymbol{\varphi})_{\Gamma^f_{\mathrm{In},\epsilon}}, \quad (4.22)$$

where the union $\Gamma^f_{\mathrm{In,p}}\cup\Gamma^f_{\mathrm{In},\epsilon}$ is abbreviated as $\Gamma^f_{\mathrm{In,p}\cup\epsilon}$. The linear functional $f(\cdot)$ reads

$$f(\Phi) = \left(\frac{4\overline{\mathbf{v}}^n-\overline{\mathbf{v}}^{n-1}}{2\Delta t},\boldsymbol{\varphi}\right)_{\Omega^f} + (p_{\mathrm{ref}}\mathbf{n}^f,\boldsymbol{\varphi})_{\Gamma^f_{\mathrm{Out}}} + \left(p_{\mathrm{in}}\,\mathbf{n}^f,\boldsymbol{\varphi}\right)_{\Gamma^f_{\mathrm{In,p}}} + \frac{1}{\epsilon}(\mathbf{v}_{Dir},\boldsymbol{\varphi})_{\Gamma^f_{\mathrm{In},\epsilon}}. \quad (4.23)$$

Let us recall that in practice only one of the sets $\Gamma^f_{\mathrm{In,dir}}, \Gamma^f_{\mathrm{In,p}}, \Gamma^f_{\mathrm{In},\epsilon}$ is chosen to be nonempty leading to significant reduction of boundary terms in (4.22) and (4.23).

**Remark.** Similarly as for the stationary elastic problem the proof of existence and uniqueness for the stationary formulation of fluid problem 4.18 on fixed domain $\Omega^f$ and moreover with zero Dirichlet boundary condition can be found for example in book [114] under the assumption of "small data". In the same book it is explained, that for instationary case, when the aforementioned equation is extended by term $(\frac{\partial \mathbf{v}}{\partial t}, \boldsymbol{\varphi})_{\Omega^f}$, a general question of existence and uniquiness is still opened. Some results exist only for specific cases besides others depending on the value of viscosity and the problem dimension has to be also taken into account. More detailed explanation can be found in [152].

### 4.2.3 Finite element approximation

During discretization of problem (4.21) the velocity and the pressure spaces are replaced by finite element subspaces $\mathbf{H}_h \subset \mathbf{H}^1(\Omega^f)$ and $\mathbf{X}_h = \mathbf{X} \cap \mathbf{H}_h$, $M_h \subset M$. In order to obtain stable method the finite element spaces $\mathbf{X}_h, M_h$ have to fulfill the Babuška–Brezzi condition, also called *inf-sup condition*, see e.g. [64]. The discrete Babuška–Brezzi inf-sup condition is satisfied if there exists a constant $C > 0$ independent of mesh parameter $h$ such that

$$\inf_{p_h \in M_h, p_h \neq 0} \sup_{\mathbf{v}_h \in \mathbf{X}_h, \mathbf{v}_h \neq \mathbf{0}} \frac{|(p_h, \nabla \cdot \mathbf{v}_h)_{\Omega^f}|}{\|p_h\|_{L^2(\Omega^f)} \|\mathbf{v}_h\|_{H^1(\Omega^f)}} \geq C. \tag{4.24}$$

If the inf-sup condition is not fulfilled, then the numerical scheme is unstable, see e.g. [114]. For erudite theoretical analysis of inf-sup problems see e.g. [52].

#### Finite element spaces

Similarly as for the elasticity problem we assume that domain $\Omega^f_t \subset \mathbb{R}^2$ is polygonal and it is covered by an admissible triangulation $\mathcal{T}^f_h$. Based on this triangulation the finite elements known as minielements (P1-bubble/P1 elements) are used, see [114]. It means that spaces $\mathbf{H}_h, \mathbf{X}_h, M_h$ for velocity and pressure approximations are chosen as

$$\begin{aligned}
\mathbf{H}_h &= \{f_i \in C(\overline{\Omega^f}) |\ f_i|_K \in \mathbb{P}_1^{bub}(K)\ \forall K \in \mathcal{T}^f_h\}, \\
\mathbf{X}_h &= \{\mathbf{f} \in \mathbf{H}_h |\ \mathbf{f} = 0 \text{ on } \Gamma^f_{\mathrm{Dir}} \cup \Gamma^f_{\mathrm{In,dir}} \cup \Gamma^f_{\mathrm{w_t}}\} \subset \mathbf{X}, \\
M_h &= \{f \in C(\overline{\Omega^f}) |\ f|_K \in \mathbb{P}_1(K)\ \forall K \in \mathcal{T}^f_h\},
\end{aligned} \tag{4.25}$$

where $\mathbb{P}_1(K)$ is the space of at most first degree polynomials on the triangle $K$ and the space $\mathbb{P}_1^{bub}(K) = \mathbb{P}_1(K) \cup \{\boldsymbol{\varphi}_{bub}\}$ is the $\mathbb{P}_1$ space enriched by the cubic bubble function $\boldsymbol{\varphi}_{bub}$, which can be written using the barycentric coordinates $\lambda_i$ as $\boldsymbol{\varphi}_{bub} = \lambda_1 \cdot \lambda_2 \cdot \lambda_3$, see e.g. [52]. The degrees of freedom for the minielement are shown in Figure 4.2. The choice of minielement satisfies the Babuška-Brezzi (inf-sup) condition, see e.g. [114], what ensures the stability of the numerical scheme.

**Remark.** The extension of space $\mathbb{P}_1$ by the (cubic) bubble function can be also understood as a method how to stabilize the finite element with equal orders of polynomials used for the approximation of velocity space $\mathbf{X}_h$ and pressure space $M_h$, see [114].

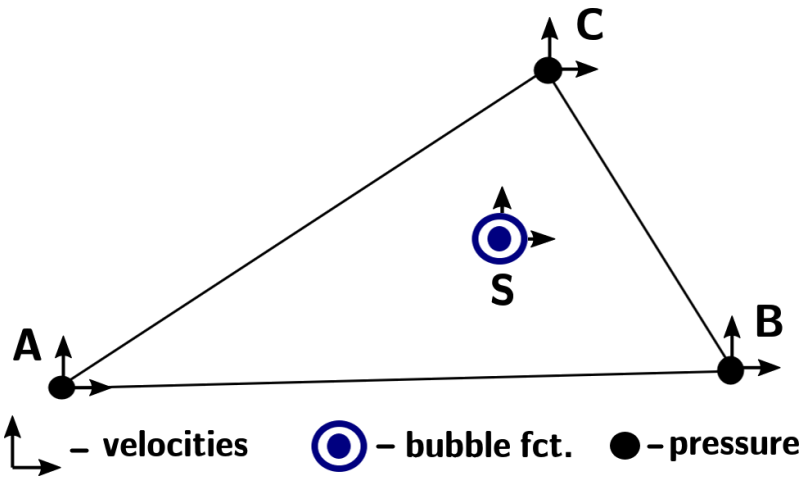


Figure 4.2: P1-bubble/P1 finite element. The dots in vertices denote unknown values of pressure basis functions, the arrows mark points associated with unknown values of velocities. The triangle center of mass $S$ is related to basis (bubble) function $\boldsymbol{\varphi}_{bub}$.

#### Discrete problem

The discrete problem reads: find $V_h = (\mathbf{v}_h, p_h) \in \mathbf{H}_h \times M_h$ such, that

$$a(V_h, V_h, \Phi_h) = f(\Phi_h) \tag{4.26}$$

holds for any test function pair $\Phi_h = (\boldsymbol{\varphi}_h, q_h) \in \mathbf{X}_h \times M_h$ and moreover $\mathbf{v}_h$ satisfies boundary conditions (3.28 a, b, c1) and (3.29 a).

The system (4.26) as well as (4.21) is nonlinear due to the convective terms in the definition of the form $a(\cdot,\cdot,\cdot)$. The method of linearization is described later, nevertheless (nonlinear as well as linearized) system (4.26) has saddle-point structure which algebraic solution is more demanding compared to symmetric and positive system in the case of the elasticity problem.

### 4.2.4 Stabilization

The choice of the minielement guarantees only the stability due to possible incompatibility of velocity-pressure spaces. Still another possible source of instability appears in the considered problem: For high Reynolds numbers the use of Galerkin approximations leads (at least on coarse meshes) to the non-physical oscillations of the numerical solution, also called Gibbs phenomenon, see e.g. [56]. The necessary mesh refinement to avoid it usually results in large systems of nonlinear equations, which

are computationally very expensive to solve. Thus, an alternative is to introduce an additional stabilization as upwind, see e.g. [56]. In order to introduce such stabilization, let us emphasize that the instability is principally caused by unresolved velocity gradients due to too coarse grid. The regions with unresolved high velocity gradients can be characterized by high values of local Reynold number $Re_K$, see e.g. [56, 146].

The numerical solution can be stabilized with the aid of an added streamline diffusion however this simple approch makes the scheme only first order accurate, see [86]. On the other hand the streamline diffusion can be included formally as a modification of test functions, see [86]. This approach keeps the stabilized problem fully consistent with the original one. Therefore it is possible to reach higher order convergence or in some cases even the optimal convergence rates, see e.g. [63], [86] or [62].

In order to overcome the possible numerical instability a combination of the streamline-upwind/Petrov-Galerkin method (SUPG) and pressure-stabilization method (PSPG) together with *div-div* stabilization are applied. The stabilized problem reads: Find a function pair $V_h = (\mathbf{v}_h, p_h) \in \mathbf{H}^1_h(\Omega^f) \times M_h$ such, that $\mathbf{v}_h$ satisfies the boundary conditions (3.28 a, b, c1) and (3.29 a) and

$$a(V_h; V_h, \Phi_h) + L_h(V_h; V_h, \Phi_h) + P_h(V_h; V_h, \Phi_h) + D_h(V_h; V_h, \Phi_h) = \\ = f(\Phi_h) + F_h(V_h; \Phi_h) + G_h(V_h; \Phi_h), \tag{4.27}$$

is satisfied for any test functions $\Phi_h = (\boldsymbol{\varphi}_h, q_h) \in \mathbf{X}_h \times M_h$, where the (nonlinear) forms $L_h(\cdot,\cdot,\cdot), P_h(\cdot,\cdot,\cdot)$ and $D_h(\cdot,\cdot)$ are defined as

$$\begin{aligned} L_h(V^*; V, \Phi) &= \sum_{K \in \mathcal{T}_h} \delta_K \left( \frac{3\mathbf{v}}{2\Delta t} + ((\mathbf{v}^* - \mathbf{w}_D) \cdot \nabla)\mathbf{v} + \nabla p - \nu \Delta \mathbf{v},\, ((\mathbf{v}^* - \mathbf{w}_D) \cdot \nabla)\boldsymbol{\varphi} \right)_K, \\ P_h(V^*; V, \Phi) &= \sum_{K \in \mathcal{T}_h} \delta_K \left( \frac{3\mathbf{v}}{2\Delta t} + ((\mathbf{v}^* - \mathbf{w}_D) \cdot \nabla)\mathbf{v} + \nabla p - \nu \Delta \mathbf{v},\, \nabla q \right)_K, \\ D_h(V^*; V, \Phi) &= \sum_{K \in \mathcal{T}_h} \tau_K \left( \operatorname{div} \mathbf{v}, \operatorname{div} \boldsymbol{\varphi} \right)_K, \end{aligned} \tag{4.28}$$

and the functionals $F_h(\cdot), G_h(\cdot)$ are given as

$$\begin{aligned} F_h(V^*; \Phi) &= \sum_{K \in \mathcal{T}_h} \delta_K \left( \frac{4\overline{\mathbf{v}}^n - \overline{\mathbf{v}}^{n-1}}{2\Delta t},\, ((\mathbf{v}^* - \mathbf{w}_D) \cdot \nabla)\boldsymbol{\varphi} \right)_K, \\ G_h(V^*; \Phi) &= \sum_{K \in \mathcal{T}_h} \delta_K \left( \frac{4\overline{\mathbf{v}}^n - \overline{\mathbf{v}}^{n-1}}{2\Delta t},\, \nabla q \right)_K. \end{aligned} \tag{4.29}$$

The parameters $\tau_K, \delta_K$ are dependent on the local transport velocity $\mathbf{v}^*$, i.e. $\tau_K = \tau_K(V^*), \delta_K = \delta_K(V^*)$. They are (locally) determined as

$$\tau_K = \nu \left( 1 + Re_K + 2\frac{h_K^2}{\nu \Delta t} \right), \qquad \delta_K = \frac{h_K^2}{\tau_K}, \tag{4.30}$$

based on the local Reynold number $Re_K$ defined as

$$Re_K = \frac{h_K ||\mathbf{v}^* - \mathbf{w}_D||_{L^2(K)}}{2\nu} \tag{4.31}$$

and the local element length $h_K$. Here, $h_K$ is taken as square root of the triangle $K$ volume, see [57], [62].

### Linearization

The nonlinear system of equations (4.27) is solved with the aid of fixed point iterations, see [51], [159]. Starting from an initial estimate $V_h^0$ we seek the sequence of approximations $V_h^{j+1} = (\mathbf{v}_h^{\bullet,j+1}, p_h^{\bullet,j+1}) \in \mathbf{H}_h^1(\Omega^f) \times M_h$, $j = 0, 1, 2, \ldots$ such, that $\mathbf{v}_h^{\bullet,j+1}$ satisfies the boundary conditions (3.28 a, b, c1), (3.29 a) and

$$a(V_h^j; V_h^{j+1}, \Phi_h) + L_h(V_h^j; V_h^{j+1}, \Phi_h) + P_h(V_h^j; V_h^{j+1}, \Phi_h) + D_h(V_h^j; V_h^{j+1}, \Phi_h) = \\ = f(\Phi_h) + F_h(V_h^j; \Phi_h) + G_h(V_h^j; \Phi_h) \quad (4.32)$$

holds for any $\Phi_h \in \mathbf{X}_h \times M_h$. The process is repeated until the convergence criterion

$$\|V_h^{j+1} - V_h^j\|^2_{\mathbf{L}^2(\Omega^f)} < \epsilon^f \quad (4.33)$$

is reached with a prescribed $\epsilon^f > 0$.

The linear system of equations (4.32) is solved with the help of the mathematical library UMFPACK implementing the unsymmetric multifrontal method, see [44]. The library implements the direct solver based on the LU matrix decomposition for sparse matrices with native Compressed Column Format (CCF). An alternative could be e.g. the Math Kernel Library (MKL) developed by Intel Corporation, see [16].

## 4.3 FSI coupling

This section presents two ingredients of FSI numerical solution – the construction of ALE mapping using pseudo-elastic approach for the fluid computational domain and the way how are the kinematic and the dynamic coupling conditions realized. Then the coupling procedure of the FSI solution is given.

### 4.3.1 Construction of ALE mapping

The mathematical description of fluid flow problem (3.26) is based on the ALE mapping $A_t$, a smooth mapping of $\Omega^f_{\mathrm{ref}}$ onto $\Omega^f_{\mathrm{t}}$ for any $t \in (0, \mathrm{T})$. In practical implementation such mapping needs to be constructed only at discrete time instants. One possibility how to construct ALE mapping at a fixed time instant $t_{n+1}$ is to use the pseudo-elastic approach, see e.g. [98].

In the pseudo-elastic approach the mapping $A_t$ is sought in the form of displacement of the original configuration subject to pseudo-elastic equations. This stationary problem solved in the Lagrangian coordinates is supplied with the Dirichlet boundary conditions for the known displacement of boundary $\partial\Omega^f$, where specially the

displacement of boundary $\Gamma_{\mathrm{W_{ref}}}$ is given by the known displacement of structure $\mathbf{u}$. The pseudo-elastic problem reads: Find an unknown displacement $\mathbf{d}(X) = (d_1, d_2)$ of points $X \in \Omega^f_{\mathrm{ref}}$ satisfying the boundary conditions

$$\begin{aligned} &\mathbf{d}(X) = \mathbf{0}, && \text{on } \Gamma^f_{\mathrm{Dir}} \cup \Gamma^f_{\mathrm{In}} \cup \Gamma^f_{\mathrm{Out}}, \\ &\mathbf{d}(X) = \mathbf{u}(X, t_{n+1}), && \text{on } \Gamma_{\mathrm{W_{ref}}}, \\ &\mathbf{d}(X) \cdot \mathbf{n}^f = 0, \quad \mathbf{t}^f \cdot \tau^{ale}_{ij}(X) \cdot \mathbf{n}^f = 0, && \text{on } \Gamma^f_{\mathrm{Sym}}, \end{aligned} \tag{4.34}$$

and the pseudo-elastic equations

$$\frac{\partial \tau^{ale}_{ij}}{\partial X_j} = 0, \qquad \text{in } \Omega^f_{\mathrm{ref}}, \tag{4.35}$$

where $\tau^{ale}_{ij} = \lambda^{ale}(\mathrm{div}\ \mathbf{d})\,\delta_{ij} + 2\mu^{ale} e^s_{ij}(\mathbf{d})$ and $\lambda^{ale}, \mu^{ale}$ are artificial Lamé coefficients. Let us emphasize that it was found out to be a significant advantage to prescribe only the normal component of the displacement and to keep the tangential displacement free on the boundary $\Gamma^f_{\mathrm{Sym}}$. This condition allows to handle a substantially larger deformation of the computational fluid mesh.

Similarly as described in paragraph 4.1.1 the system of equations (4.35) is weakly formulated and the displacement $\mathbf{d}$ is approximated by $\mathbf{d}_h$ taken as a linear combination of basis functions from space $\mathbf{W}_h \subset \mathbf{H}^1(\Omega^f_{\mathrm{ref}})$. Here, the piecewise linear finite element functions are used, i.e. $\mathbf{W}_h = W_h \times \widetilde{W}_h$ is defined as

$$W_h = \{f \in C(\overline{\Omega^s}) | f = 0 \text{ on } \Gamma^f_{\mathrm{Dir}} \cup \Gamma^f_{\mathrm{In}} \cup \Gamma^f_{\mathrm{Out}} \cup \Gamma_{\mathrm{W_{ref}}}, f|_K \in \mathbb{P}_1(K)\ \forall K \in \mathcal{T}^f_h\} \tag{4.36}$$

and $\widetilde{W}_h = \{f \in W_h | f = 0 \text{ on } \Gamma^f_{\mathrm{Sym}}\}$ due to considered geometry of $\Omega^f_{\mathrm{ref}}$ with $\mathbf{n}^f(x) = (0,1)^T$ for $x \in \Gamma^f_{\mathrm{Sym}}$ and the last two boundary conditions (4.34). The basis functions $\boldsymbol{\psi}_i \in \mathbf{W}_h$ are chosen as Lagrange finite elements of first order, see previous paragraph 4.1.1. The same discretization procedure leads to the algebraic system for unknown vector $\boldsymbol{\alpha}^{ale}$ as described in paragraph 4.1.1, i.e.

$$\mathbb{K}^{ale} \boldsymbol{\alpha}^{ale} = \mathbf{0}, \tag{4.37}$$

where the components of matrix $\mathbb{K}^{ale} = (k^{ale}_{ij})$ are given as

$$k^{ale}_{ij} = (\lambda^{ale}(\mathrm{div}\ \boldsymbol{\psi}_j)\,\delta_{ij} + 2\mu^{ale}\mathbf{e}^s(\boldsymbol{\psi}_j), \mathbf{e}^s(\boldsymbol{\psi}_i))_{\Omega^f_{\mathrm{ref}}}. \tag{4.38}$$

The robustness of ALE mapping construction is very important for the whole FSI algorithm. This robustness can be increased by a suitable choice of the parameters $\lambda^{ale}, \mu^{ale}$ such, that the ALE mapping constructed by pseudo-elastic approach delivers regular mesh on $\Omega^f_t$ also for highly deformed boundaries, e.g. given by large deformation of the interface $\Gamma^f_{\mathrm{W_t}}$. For instance, the unphysical choice of $\lambda^{ale} = -\mu^{ale}$ was recommended in [49] as it should allow a rigid structure rotation without introducing large deformation in the surrounding computational mesh (where the associated stress $\boldsymbol{\sigma}^{ale}$ should be theoretically zero). Another possibility is to scale $\lambda^{ale}$ with the triangle area or the distance from boundary $\Gamma^f_{\mathrm{Sym}}$ in order to make small

triangles, e.g. near boundaries with VF, more stiff, see [98]. Last, the best robustness was obtained with $\lambda^{ale}, \mu^{ale}$ chosen to be constants based on our experience for the considered geometry.

In the next paragraph the numerical approximation of the domain velocity computed from the constructed ALE mapping is described. By this it is also determined the numerical implementation of the kinematic coupling condition.

#### Numerical realization of domain velocity

The (discrete) domain velocity is a part of the fluid flow formulation (4.22) as well as a part of kinematic boundary condition (3.28 b). The discrete domain velocity $\mathbf{w}_{D,h}$ at any vertex $x_j$ of $\mathcal{T}_h^f$ at time $t_{n+1}$ is approximated with the help of BDF2 formula using the displacements $\mathbf{d}_h$ computed from pseudo-elastic equations (4.37) in time instants $t_{n+1}, t_n, t_{n-1}$ as

$$\mathbf{w}_{D,h}^{n+1}(x_j) = \frac{3\mathbf{d}_h^{n+1}(X_j) - 4\mathbf{d}_h^n(X_j) + \mathbf{d}_h^{n-1}(X_j)}{2\Delta t}, \tag{4.39}$$

where $x_j = A_t(X_j)$. This discretization satisfies the geometry conservation law, see e.g. [61].

### 4.3.2 Dynamic coupling condition

In order to take into account also the dynamic coupling condition of form (3.17 b) the aerodynamic forces acting on the structure needs to be evaluated. Here, three applicable methods of the aerodynamic forces evaluation are described, see also author's analysis [9].

#### Extrapolation from interior of fluid domain

The first approach of the dynamic coupling condition evaluation is to extrapolate the aerodynamic quantities from the interior of the fluid domain onto boundary $\Gamma_{\mathrm{W_t}}$ and then use these extrapolated values to approximate aerodynamic forces $\mathbf{q}^s$ given by (3.31). The structural and the fluid computational meshes (for the reference domain) are chosen to be conforming over the common interface $\Gamma_{\mathrm{W_{ref}}}$, i.e. the vertices lying on $\Gamma_{\mathrm{W_{ref}}}$ are common for both meshes, see Figure 4.3. This fact together with the implemented finite elements of the first order (bubble function is vanishing at each triangle boundary) simplifies the situation. For any edge $S$ from the common interface the components of the fluid stress tensor are extrapolated from the fluid mesh element $K_S$ adjacent to the edge $S$. The boundary integrals are then approximated with the help of a numerical quadrature formula.

#### Local reconstruction technique

The second possibility is the application of the local reconstruction technique introduced by Babuška, see e.g. [24], which can possibly increase the accuracy of

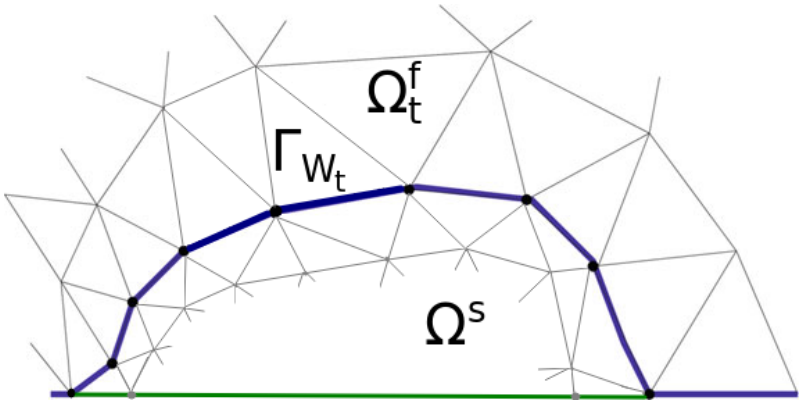


Figure 4.3: Illustration of conforming meshes of structure domain $\Omega^s$ and fluid domain $\Omega_t^f$ with interface $\Gamma_{\mathrm{W_t}}$.

aerodynamic forces computation in comparison with the previous approach. The idea is based on the reconstruction of the velocity gradient at arbitrary vertex $A$ of fluid mesh $\mathcal{T}_h^f$ (denoted as $\nabla \mathbf{v}_{\mathrm{reconstr}}(A)$). In our case only the vertices located at the boundary $\Gamma_{\mathrm{W_t}}^f$ are considered. The procedure is following:

To reconstruct the gradient of velocity $\mathbf{v}_h$ at a vertex $A$ located on $\Gamma_{\mathrm{W_t}}$, the local patch of elements $\mathcal{P}_A$, see Figure 4.4, is used. The local patch $\mathcal{P}_A$ is composed of all triangles $K \in \mathcal{T}_h^f$ being neighbour of vertex $A$. Its number is denoted by $N$. In every triangle of the patch the gradient $\nabla \mathbf{v}_h(S_j)$ located at the center of the $j$-th triangle $S_j$ is computed.

In the case of $N = 1$ we use directly value $\nabla \mathbf{v}_h(S_1)$ as $\nabla \mathbf{v}_{\mathrm{reconstr}}(A)$. For $N = 2$ the average of $\nabla \mathbf{v}_h(S_1)$ and $\nabla \mathbf{v}_h(S_2)$ weighted by triangle areas is used. For $N \geq 3$ the least square method for fitting data $\nabla \mathbf{v}_h(S_j)$ for all $K_j \in \mathcal{P}_A$ to determine $\nabla \mathbf{v}_{\mathrm{reconstr}}(A)$ is applied, see [24].

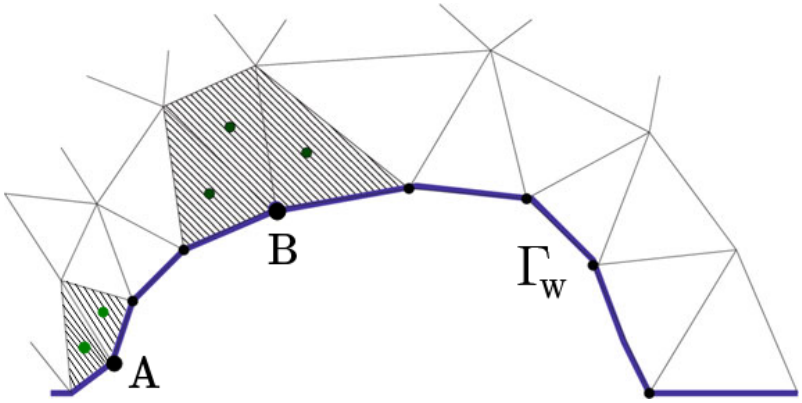


Figure 4.4: Example of two local patches. The local patch of point $A$ consists of two triangles, while the local patch of point $B$ is constituted by three adjacent triangles.

The local reconstruction procedure is used only for the computation of velocity gradients as the pressure approximation is in our case chosen as a continuous function. The evaluation of the aerodynamic forces is then done with a numerical quadrature

(used for boundary integral), similarly as above. The local reconstruction is the default option of the aerodynamic force calculation in program FSIFEM . It is further used in the numerical simulations of Chapter 5 since it provides theoretically higher accuracy compared to the extrapolation procedure.

**Weak reformulation of aerodynamic forces**

The third possibility how to calculate the aerodynamic forces is to use their weak reformulation. In this case boundary condition (3.17 b) is rather evaluated in the weak form given by the second term of (4.7), i.e. by $(\mathbf{q}^s, \boldsymbol{\psi}_i)_{\Gamma_{\mathrm{W_{ref}}}}$, see e.g. [62], [9]. Here for the sake of simplicity the same FE linear Lagrange basis functions $\boldsymbol{\psi}_i$ as chosen in the practical implementation for the elasticity problem and moreover being non-zero on $\Gamma_{\mathrm{W_{ref}}}$ are considered, i.e. $\boldsymbol{\psi}_i \in \mathbf{V}_h$ with indices $i$ from a set $J$ which is $J \subsetneq \{1, \ldots, 2N_h\}$.

Let us consider fluid domain $\Omega_{\mathrm{t}}^f$ and structure domain $\Omega^s$ at a fixed time instant $t_{n+1}$, see Figure 4.5. We denote one-layer strip of fluid elements around the interface as $\Omega_{strip} = A_{t_{n+1}}(\mathcal{P}_{\Gamma_W})$, where the patch $\mathcal{P}_{\Gamma_W}$ is given as $\mathcal{P}_{\Gamma_W} = \bigcup\{K \in \mathcal{T}_h^f | K \cap \Gamma_{\mathrm{W_{ref}}} \neq \emptyset\}$. Next we consider vector function $\boldsymbol{\varphi}_W \in \mathbf{H}^1(\Omega^f_{\mathrm{t_{n+1}}})$ which components $\boldsymbol{\varphi}_W = (\varphi_W^1, \varphi_W^2)$ equal one on boundary $\Gamma_{\mathrm{W_{t_{n+1}}}}$ and outside domain $\Omega_{strip}$ are zero, i.e. for $j = 1, 2$

$$\varphi_W^j(x) = 1 \quad \text{for } x \in \Gamma_{\mathrm{W_{t_{n+1}}}}, \qquad \varphi_W^j(x) = 0 \quad \text{for } x \in \Omega^f_{\mathrm{t_{n+1}}} \setminus \Omega_{strip}. \tag{4.40}$$

Further, the vector equation (3.26) is multiplied by the constant fluid density $\rho_0^f$ and by the function $\boldsymbol{\varphi}_W$, integrated over the domain $\Omega_{strip}$ leading to

$$\rho_0^f \left( \frac{D^A \mathbf{v}}{Dt} + ((\mathbf{v} - \mathbf{w}_D) \cdot \nabla)\mathbf{v}, \boldsymbol{\varphi}_W \right)_{\Omega_{strip}} - (\operatorname{div} \boldsymbol{\sigma}^f, \boldsymbol{\varphi}_W)_{\Omega_{strip}} = 0. \tag{4.41}$$

The application of the Green's theorem on the term containing the fluid stress tensor, using the BDF2 formula for the approximation of the ALE derivative and the subsequent spatial discretization as described previously leads to

$$(\boldsymbol{\sigma}_h^f \mathbf{n}^f, \boldsymbol{\varphi}_W)_{\Gamma_{\mathrm{W_{t_{n+1}}}}} \doteq \rho_0^f \left( \frac{3\mathbf{v}_h^{n+1} - 4\overline{\mathbf{v}}_h^n + \overline{\mathbf{v}}_h^{n-1}}{2\Delta t}, \boldsymbol{\varphi}_W \right)_{\Omega_{strip}} + \tag{4.42}$$

$$+ \left( \rho_0^f ((\mathbf{v}_h^{n+1} - \mathbf{w}_{D,h}^{n+1}) \cdot \nabla)\mathbf{v}_h^{n+1}, \boldsymbol{\varphi}_W \right)_{\Omega_{strip}} + \mu^f (\nabla \mathbf{v}_h^{n+1}, \nabla \boldsymbol{\varphi}_W)_{\Omega_{strip}} - \rho_0^f (p_h^{n+1}, \operatorname{div} \boldsymbol{\varphi}_W)_{\Omega_{strip}},$$

where the last two terms are volume integrals obtained by the definition of fluid stress tensor (3.21) (in the case of incompressible fluid flow) and particularly $p_h^{n+1}$ is the approximation of the kinematic pressure at $t_{n+1}$.

Then the function $\boldsymbol{\varphi}_W$ is written with the aid of the linear Lagrange FE basis consisting of functions $\boldsymbol{\varphi}_{W,k}$, i.e. the same basis functions as used for the velocity discretization of the fluid flow problem on boundary $\Gamma_{\mathrm{W_t}}$. Let us recall that the components of these functions $\boldsymbol{\varphi}_{W,k} = \begin{pmatrix} \varphi_{W,k} \\ 0 \end{pmatrix}$, $\boldsymbol{\varphi}_{W,\,k+N_\Gamma} = \begin{pmatrix} 0 \\ \varphi_{W,k} \end{pmatrix}$ satisfy

$$\varphi_{W,k}(x_l) = \delta_{kl}, \tag{4.43}$$

where $x_l$ is $l$-th one of $N_\Gamma$ vertices of the (fluid) triangulation of boundary $\Gamma_{\mathrm{W}_{t_{n+1}}}$.[1]

Finally due to the assumed mesh conformity over the interface $\Gamma_{\mathrm{W}}$ there exists for each index $i \in J$ an unique index $k_i \in \{1, \ldots, 2N_\Gamma\}$ for which holds $\boldsymbol{\psi}_i(X) = \boldsymbol{\varphi}_{W,k_i}(x)$, where $x = A_{t_{n+1}}(X),\ X \in \Gamma_{\mathrm{W}_{\mathrm{ref}}}$. From the mesh conformity and equation (3.31) already follows

$$(\mathbf{q}^s, \boldsymbol{\psi}_i)_{\Gamma_{\mathrm{W}_{\mathrm{ref}}}} = -(\boldsymbol{\sigma}_h^f \mathbf{n}^f, \boldsymbol{\varphi}_{W,k_i})_{\Gamma_{\mathrm{W}_{t_{n+1}}}}. \tag{4.44}$$

Equations (4.42) and (4.44) offer another variant how to compute the contributions of the aerodynamic forces to right hand side vector (4.7).

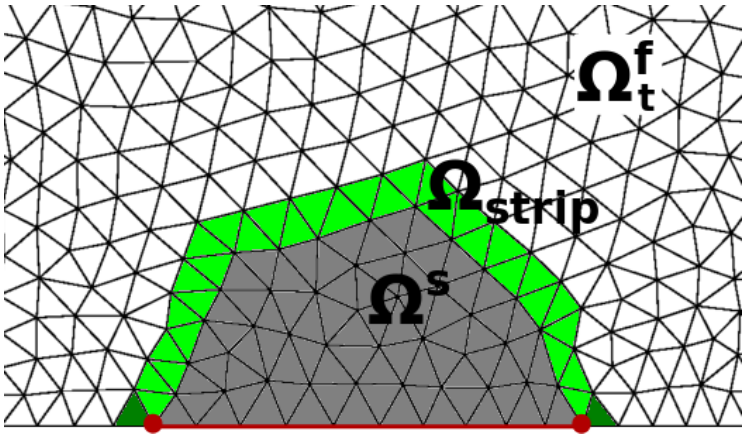


Figure 4.5: Scheme of (gray) elastic body domain $\Omega^s$ surrounded by (white) fluid domain $\Omega_t^f$ with subdomain $\Omega_{strip} \subset \Omega_t^f$ marked by green. The vertices of intersection $\overline{\Gamma_{\mathrm{W_t}}} \cap \overline{\Gamma^s_{\mathrm{Dir}}}$, where the Dirichlet boundary condition for the elastic body has priority over the dynamic boundary condition, are highlighted by red dots.

### 4.3.3 Solution of FSI coupled problem

For the solution of the FSI problem the strongly coupled partitioned algorithm is implemented, see Figure 4.6. It means that the fluid flow and the structure subproblem is iteratively solved until the convergence test at the end of each cycle is passed, see e.g. [57] or [89].
Let us consider a fixed time instant $t_n$ at which the values $\mathbf{v}^n, p^n, \mathbf{u}^n, (\mathbf{q}^s)_n, A_{t_n}$ and $\Omega_{t_n}^f$ were determined. Further

0. Extrapolate the effect of the aerodynamic forces from the previous time level $\mathbf{q}^s_{n+1,0} = \mathbf{q}^s_n$.

Then for $l = 0, 1, \ldots$ we proceed the computation in the following steps:

[1] The two functions $\boldsymbol{\varphi}_{W,k}$ associated with the vertices at intersection $\Gamma_{\mathrm{W}_{t_{n+1}}} \cap \Gamma^s_{\mathrm{Dir}}$ are in implementation excluded because the Dirichlet boundary condition has higher priority (no aerodynamic forces act here) for the elastic body at these vertices, see Figure 4.5.

1. Solve elastodynamic problem (4.6) with $\mathbf{q}^s_{n+1,l}$ in order to approximate displacement $\mathbf{u}^{n+1,l}$ at time $t_{n+1}$.

2. Determine $\Omega^f_{t_{n+1,l}}$ and construct ALE mapping $A_{t_{n+1,l}}$ based on found deformation $\mathbf{u}^{n+1,l}$ of interface $\Gamma^f_{\mathrm{W}_{\mathrm{t_{n+1,l}}}}$. Approximate domain velocity $\mathbf{w}^{n+1,l}_{D,h}$ based on $A_{t_{n+1,l}}$ according to (4.39).

3. Solve the fluid flow problem represented by system (4.32) to acquire $\mathbf{v}^{n+1,l}, p^{n+1,l}$ defined on $\Omega^f_{t_{n+1,l}}$.

4. Determine aerodynamic forces $\mathbf{q}^s_{n+1,l+1}$ on interface $\Gamma^f_{\mathrm{W}_{\mathrm{t_{n+1,l}}}}$ given by (3.31) from known values $\mathbf{v}^{n+1,l}, p^{n+1,l}$ according to one of described procedures in paragraph 4.3.2.

5. Check if condition $||\mathbf{q}^s_{n+1,l+1} - \mathbf{q}^s_{n+1,l}||_{L^\infty(\Gamma^s_{\mathrm{W_t}})} < \epsilon^{fsi}$ is satisfied.

   - If **yes**, denote all quantities $f^{n+1} := f^{n+1,l}$, increase the time index $n := n+1$, set $l := 0$ and continue with step 0.
   - If **no**, increase the iteration index $l := l+1$ and continue with step 1.

In practical implementation the algorithm performs usually $3-8$ inner loops for chosen $\epsilon^{fsi} = 10^{-3}$ until the convergence criterion is met.

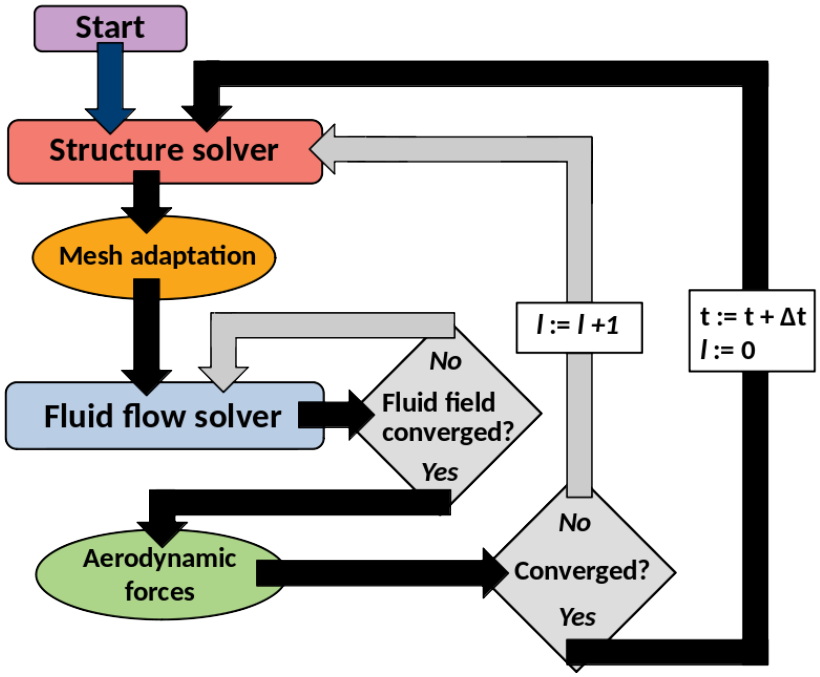


Figure 4.6: Diagram shows consequent steps of strongly coupled FSI algorithm with inner cycles marked by gray arrows.

# Chapter 5

# Numerical results of FSI problem

In the beginning of this chapter the settings of numerical simulations including the description of FSI computational domains are given. Next three sections contain the following numerical results: First, the results for a prescribed vocal folds motion and for different inlet boundary conditions are presented. The sensitivity analysis of flow characteristics in the dependence on the penalization parameter $\epsilon$ is shown. Second, the full FSI interaction system is approximated for hemi-larynx configuration and the critical flutter velocity is determined. Third, the flow-induced vocal folds vibrations for the full configuration of the glottal channel are computed. The presented results are detailed version of published results in [4, 7, 6, 11].

## 5.1 Description of FSI problem

The following choice of physical quantities is made: The constant time step $\Delta t$ is chosen as $2.5 \cdot 10^{-5}\,\mathrm{s}$. The structure density $\rho^s$ is set to $\rho^s = 1000\,\mathrm{kg/m^3}$, the fluid density $\rho_0^f = 1.185\,\mathrm{kg/m^3}$ and the kinematic fluid viscosity $\nu^f = 1.47 \cdot 10^{-5}\,\mathrm{m^2/s}$. The Young modulus and the Poisson ratio are chosen as $E^s = 8\,\mathrm{kPa}$ and $\sigma^s = 0.4$, respectively. The damping parameters for vocal folds are chosen as $\epsilon_1^s = 5\,\mathrm{s}^{-1}, \epsilon_2^s = 2.0 \cdot 10^{-5}\,\mathrm{s}$ as described in following paragraph 5.1.1. The pseudo-elastic parameters used for mesh deformation are set to $\lambda^{ale} = 10, \mu^{ale} = 2.5$.

First, the presented numerical results have been obtained with the symmetric glottal channel model labeled as MALE-SYM, shown in Figure 5.1. The shape of vocal fold is taken from the article [148], where a simplified model of the human vocal fold is used in a generic glottal channel, see [75, 76, 77]. The vocal fold shape is additionally very slightly rounded at the top sharp corner, see Figure 5.1 – in order to increase the stability of the FSI approximation for the case of almost closed channel. The FSI configuration is for the sake of simplicity considered as axially symmetric with symmetry axis $y = 0$. Here, the half-gap $g_0(t)$, which denotes the distance between the top of the vocal fold and the symmetry axis of the channel, is initially set as $g_{0,init} = 0.4\,\mathrm{mm}$. The MALE-SYM vocal fold model is considered to be composed of one uniform tissue with Young modulus $E^s = 8\,\mathrm{kPa}$ and Poisson ratio $\sigma^s = 0.4$. At the top of the elastic body the sensor S having coordinates $[4.99; -0.505]$ mm in

the reference domain is located and used for postprocessing of the results.

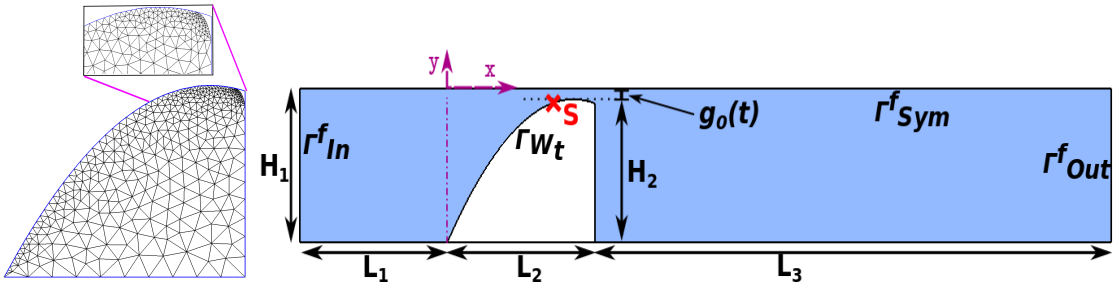


Figure 5.1: **Left**: The meshed VF with a detail of rounded top of originally sharp VF corner. **Right**: The FSI domains with marked boundaries, half-gap distance $g_0(t)$ and point S, where the VF vibrations are analyzed. The considered dimensions are: $H_1 = 5.8\,\text{mm}$, $H_2 = 5.4\,\text{mm}$, $g_0(0) = 0.4\text{mm}$, $L_1 = 6.8\,\text{mm}$, $L_2 = 6.8\,\text{mm}$ and $L_3 = 23.8\,\text{mm}$.

The other considered configuration of the vocal fold model labeled as MALE arises by removing the symmetry assumption, i.e. when the full channel with two identical VFs is considered (i.e. the boundary $\Gamma^f_{\text{Sym}} = \emptyset$), see Figure 5.23.

The modal analysis of the VF model MALE-SYM is performed, for details see Appendix A. The first four eigenmodes and eigenfrequencies of the VF model are shown in Figures 5.2 and 5.3. The two lowest eigenfrequencies are $f_1 = 76.8$ Hz and $f_2 = 156.7$ Hz, which are similar to frequencies considered in article [147] (100 Hz and 160 Hz) and they are practically[1] in interval of male VF vibration fundamental frequency $85 - 155$ Hz as published by [156].

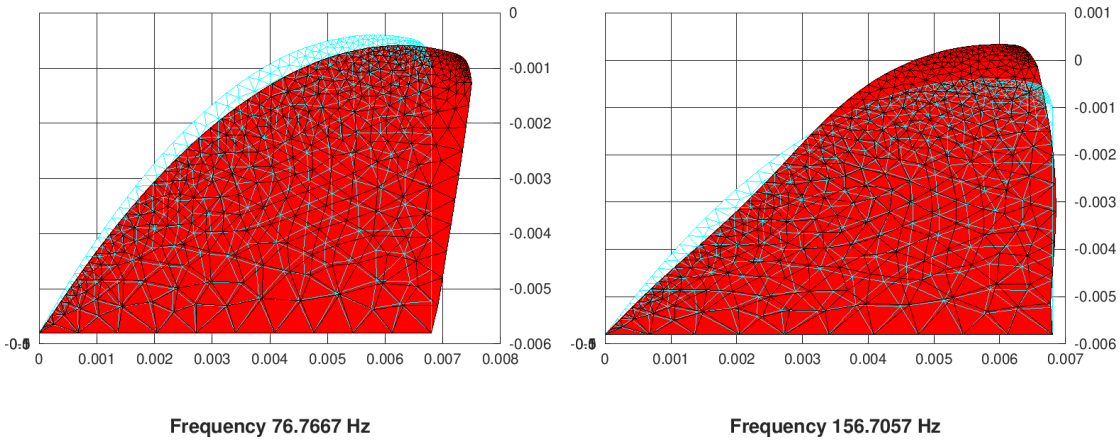


Figure 5.2: First two eigenmodes of vocal fold model MALE-SYM with related eigenfrequencies $f_1 = 76.8$ Hz and $f_2 = 156.7$ Hz.

[1]The VF vibration fundamental frequency is usually somewhere between the first two eigenfrequencies, see e.g. [153].

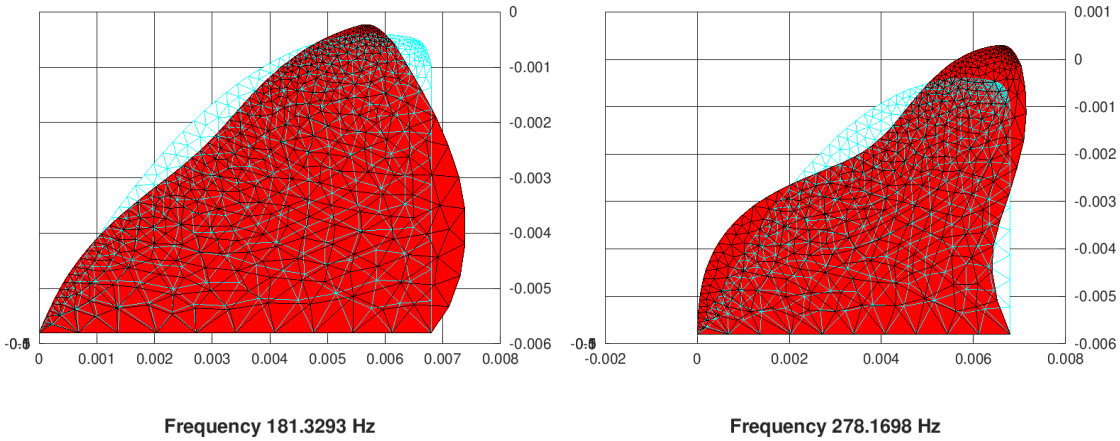


Figure 5.3: Third and fourth eigenmode of vocal fold model MALE-SYM with related eigenfrequencies $f_3 = 181.3$ Hz and $f_4 = 278.2$ Hz obtained by modal analysis.

### 5.1.1 Model of proportional damping

Proportional damping or Rayleigh damping, see e.g. [31], is commonly used linear model of damping. The damping model is described by matrix $\mathbb{D}$, see equation (4.6), which is proportional to the FE mass and stiffness matrices $\mathbb{M}$ and $\mathbb{K}$ with the proportionality (damping) parameters $\epsilon_1^s$ and $\epsilon_2^s$, respectively. Further it can be shown that for a solution of ODE system (4.6), which is composed of modes superposition, the $i$-th modal damping factor $\xi_i$ is

$$\xi_i = \frac{\epsilon_1^s}{2\omega_i} + \frac{\omega_i \epsilon_2^s}{2}, \tag{5.1}$$

where $\omega_i = 2\pi f_i$ is the angular eigenfrequency of the $i$-th eigenmode of the undamped system (4.6), see e.g. [90]. It is obvious that parameter $\epsilon_1^s$ controls low-frequency damping, see Figure 5.4, while $\epsilon_2^s$ steers the high-frequency damping.

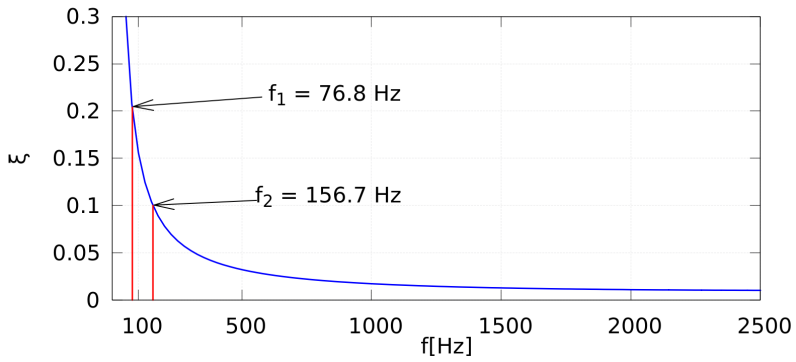


Figure 5.4: The typical behaviour of modal damping factor $\xi$ as a function of frequency $f$. The graph is plotted with values $\epsilon_1^s = 5\,\mathrm{s}^{-1}$ and $\epsilon_2^s = 2 \cdot 10^{-5}$s. The damping modal factors of the first two eigenfrequencies $f_1$ and $f_2$ of MALE-SYM model can be read to be $\xi(f_1) \doteq 0.2$ and $\xi(f_2) \doteq 0.1$.

The application of proportional damping model usually leads to weakly damped a

relatively narrow frequency range and the damping outside this frequency range described by the modal damping factor substantially grows. In order to adjust damping parameters for the given frequency range of interest, the parameters are selected by the following process:
The damping parameters $\epsilon_1^s, \epsilon_2^s$ are usually sought as the solution of algebraic system of two equations arising from equation (5.1)

$$\begin{aligned} \epsilon_1^s + \epsilon_2^s \omega_1^2 &= 2\omega_1 \xi(\omega_1), \\ \epsilon_1^s + \epsilon_2^s \omega_2^2 &= 2\omega_2 \xi(\omega_2), \end{aligned} \tag{5.2}$$

where $\xi(\omega_1)$ and $\xi(\omega_2)$ are given (e.g. measured damping factors at boundaries of the frequency range given by $\omega_1$ and by $\omega_2$, respectively), see e.g. [172].
Alternatively, the system of two equations (5.2) can be extended by additional measurements of modal damping factors at different frequencies and the resulting overdetermined system can be solved by the least square method in order to obtain better damping characteristic over the chosen frequency interval, see e.g. [76].

For the considered choice of $\epsilon_1^s = 5\,\mathrm{s}^{-1}$ and $\epsilon_2^s = 2 \cdot 10^{-5}$s the damping of first two eigenmodes lies in the interval $\xi \approx 0.1 - 0.3$ as reported by the measurements of the excised human larynges [37]. The determination of damping characteristics is highly difficult due to the small dimensions of VF tissue, which is composed of more layers, and the frequency dependent character of damping with high frequency of interest $f > 100\,\mathrm{Hz}$, see [37].

### Static force supporting vocal folds

In order to ensure that the gap (or the half-gap) between the channel walls at the glottis agrees with the prescribed values in references [148] or [77] the static part of the aerodynamic force loading the elastic structure is eliminated from the dynamic response of the structure. The static force $\mathbf{q}^s_{\mathrm{stat}}$ is computed from the numerical solution of the flow field at the chosen time instant $t_{\mathrm{release}} > 0$ using the fixed channel configuration, i.e. $\mathbf{q}^s_{\mathrm{stat}}(X) := \mathbf{q}^s(X, t_{\mathrm{release}}),\ X \in \Gamma_{\mathrm{W_{ref}}}$. Here, $t_{\mathrm{release}}$ is chosen to be such high time instant at which the fluid flow transitional effects almost completely disappeared. Then for $t > t_{\mathrm{release}}$ the interaction is modified by subtracting this static part, i.e. the modified aerodynamic force $\mathbf{q}^s_{\mathrm{mod}}$ is prescribed by

$$\mathbf{q}^s_{\mathrm{mod}}(X, t) = \mathbf{q}^s(X, t) - \mathbf{q}^s_{\mathrm{stat}}(X). \tag{5.3}$$

The modified aerodynamic force has actually a meaning of force fluctuations around the new equilibrium position equal to the original initial (half-) gap position.

## 5.2 Prescribed motion of structure

This section presents the results of numerical simulations for a prescribed motion of vocal folds, see [4]. These results are organized in three paragraphs. In the first paragraph the results for three previously considered inlet boundary conditions are

shown. In the second paragraph the sensitivity of the FSI process in dependence on the choice of penalization parameter $\epsilon$ is investigated, and in the last paragraph the numerical results are related to the available experimental data.

In all cases the periodical motion of vocal fold represented by the model MALE-SYM, see Figure 5.1, is prescribed. The displacement of the structure at point $[x, y] \in \Omega^s$ and at time $t \in [0, \mathrm{T}]$ is prescribed by

$$u_1(x, y, t) = 0, \qquad u_2(x, y, t) = \frac{C_{\mathrm{driven}}}{100} \cdot (y + g_{0,init} + H_2) \cdot \sin(2\pi f_{\mathrm{driven}} t), \quad (5.4)$$

where $H_2$ is the VF height, $C_{\mathrm{driven}}$ is a free parameter and the parameters $f_{\mathrm{driven}} = 100$ Hz and $g_{0,init} = g_0(0) = 0.4\,\mathrm{mm}$ are fixed.

### 5.2.1 Effect of the inlet boundary conditions on flow characteristics

The performance of considered boundary conditions (3.29) is tested for the case of prescribed VF motion of form (5.4) with choice $C_{\mathrm{driven}} = 7.2$, further referred as the reference prescribed motion. This prescribed motion of the VF enables nearly full closing of the channel up to the minimal half-gap $g^{ref}_{0,min} = 0.0114\,\mathrm{mm}$.

Three inlet boundary conditions are considered:

1) case "vel": Dirichlet boundary condition (3.29 a) with the given inlet airflow velocity $\mathbf{v}_{\mathrm{Dir}} = (1.7, 0)\,\mathrm{m/s}$,

2) case "pres": the prescribed pressure drop $\Delta p = 400\,\mathrm{Pa}$ by condition (3.29 b). The pressure drop choice is such that airflow rate of cases "pres" and "vel" is comparable;

3) case "pen": penalization boundary condition (3.29 c) with the given velocity $\mathbf{v}_{\mathrm{Dir}}$ and with the penalization parameter $\epsilon = 5 \cdot 10^{-4}\,\mathrm{s/m}$.

The results in terms of the inlet quantities are shown in Figure 5.5. The time behaviour of the inlet flow velocity (averaged over boundary $\Gamma^f_{\mathrm{In}}$) reveals the different behaviour in all three studied cases. The inlet velocity is constant for the case "vel" and oscillating for the case "pres" around its mean value (approximately the same as for "vel"). In the case "pen" the inlet velocity for maximally open channel is almost the same as for the case "vel", but during the channel closing it rapidly drops near to zero (similarly as in case "pres").

In the case "pres" the pressure drop, i.e. the difference between pressure values monitored at boundaries $\Gamma^f_{\mathrm{In}}$ and $\Gamma^f_{\mathrm{Out}}$[2], is almost constant, while for the case "vel" the pressure grows fast to unphysically high albeit expected values during the channel closing. For the limit case of the completely closed channel the theoretical value of pressure drop would reach infinity. In the case "pen" the pressure drop remains bounded with a reasonable amplitude comparable with experiments, see [73]. The maximal value of the pressure drop is therein after also referenced as the pressure peak.

[2]More precisely the pressure drop is often labeled as the transglottal pressure, see e.g. [74].

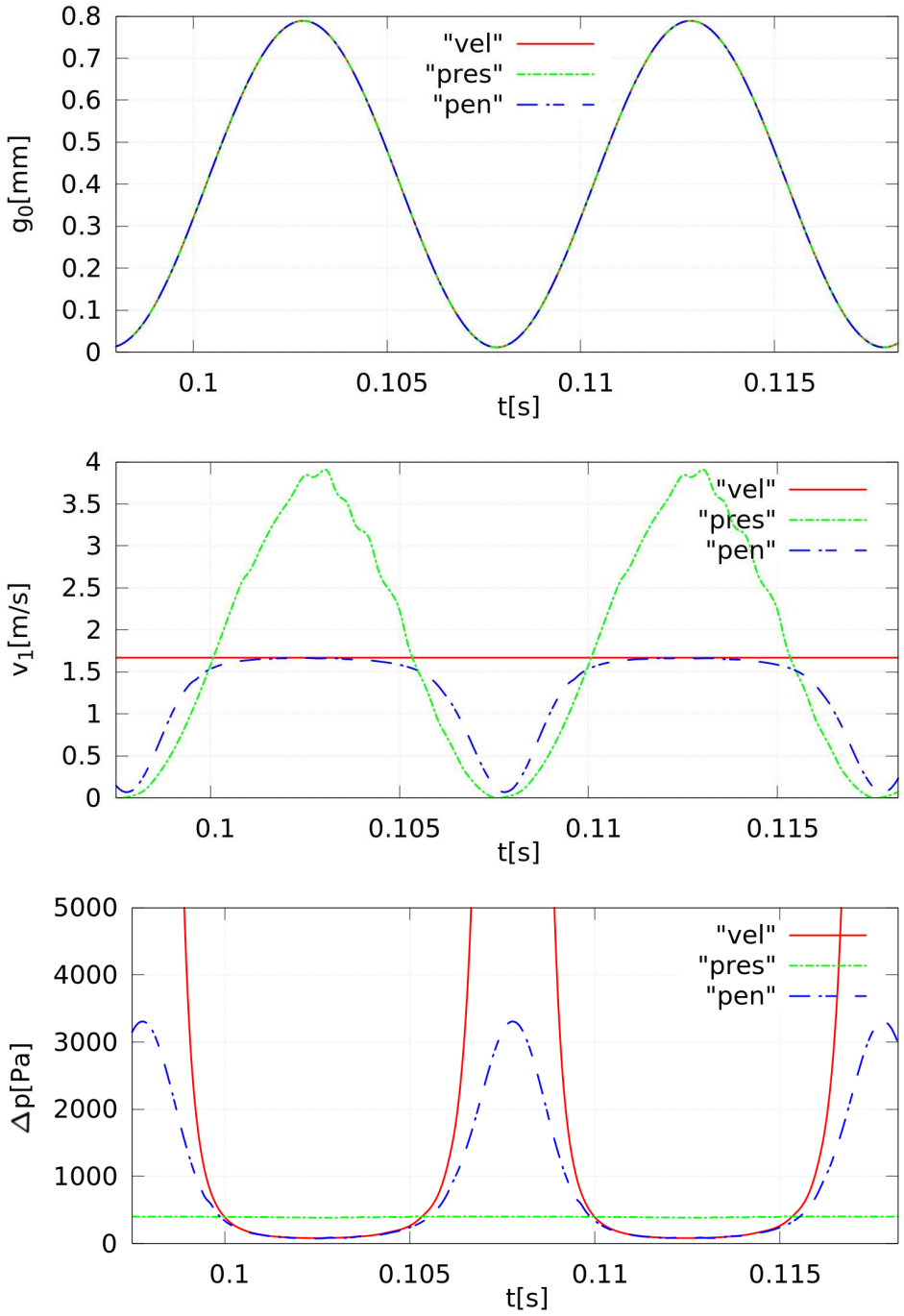


Figure 5.5: Comparison of flow characteristics for three different inlet boundary conditions. The top panel shows the half-gap in dependence on time for the reference prescribed VF motion in form (5.4). The middle panel shows the inlet velocity (averaged over $\Gamma_{\text{In}}^f$) in the dependence on time. The bottom figure presents detail of the pressure drop during two periods of the reference prescribed motion. The pressure drop in the case "vel" has unrealistic high maximum of circa 472 kPa.

For the case "pen" the flow velocity magnitude distribution in the channel is shown in Figure 5.6. It can be noticed that during the channel closing the velocity magnitude is decreasing what is on the contrary to the behaviour for case "vel", where based on the continuity equation the local velocity theoretically tends to infinity. In the case "pen" the maximal velocity at the narrowest part of the channel for the time instant of minimal half-gap $g_{0,min}^{ref} = 0.0114\,\text{mm}$ (numerically practically closed) equals 25.0 m/s that is comparable with the maximal velocity 28.9 m/s for the time instant, when the half-gap $g_0(t)$ equals the initial half-gap $g_{0,init} = 0.4\,\text{mm}$. On the other hand for the case "vel" the maximal velocity in the narrowest part of the channel at time of $g_{0,min}^{ref}$ exceeds an unrealistic high value of cca 300 m/s.

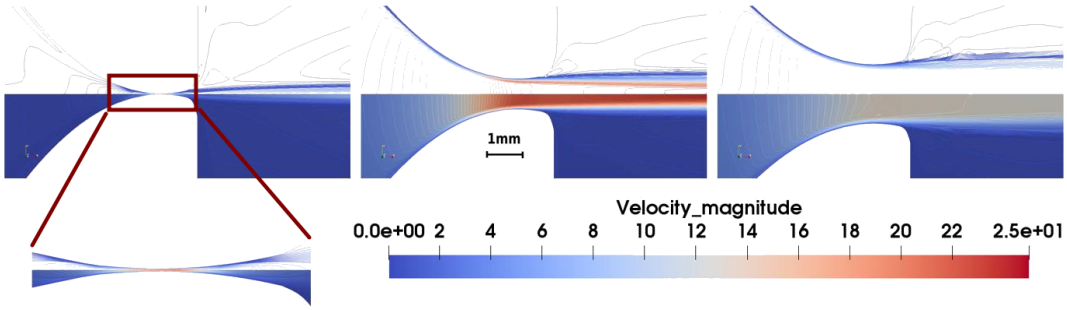


Figure 5.6: The magnitude of flow velocity distribution around vibrating structure at three time instants for the case "pen". The picture on the left shows the time instant for which minimal half-gap occurs, the middle one has half-gap equal to the initial one and the picture on the right depicts the time instant with the maximally open channel. The scale of velocity contours is common for all three pictures. The detail of the glottis in the moment of minimal half-gap is shown bottom left.

### 5.2.2 Parametric study of an optimal value of the penalty parameter

The sensitivity of the flow field characteristics to the changes of the penalization parameter were tested for the reference prescribed motion of the structure similarly as in paragraph 5.2.1. The dependence of the (maximal) pressure drop between inlet $\Gamma_{\text{In}}^f$ and outlet $\Gamma_{\text{Out}}^f$ on the penalization parameter $\epsilon$ is shown in Figure 5.7, which presents also the dependence of the maximal, the average and the minimal flow rate $Q^3$ on the parameter $\epsilon$. The maximal and the minimal flow rate or pressure drop means that the maximal and the minimal instant value of quantity over the whole simulation time interval is considered, respectively. The most rapid changes occur for the penalization parameter in the range $10^{-7} - 10^{-4}\,\text{s/m}$, where the pressure peaks demonstrate a steep decrease from its maximum (circa 500 kPa) close to minimal values ($< 20\,\text{kPa}$) and the average flow rate is still close to its maximum.

[3]The flow rate is multiplied by 2 and by *width* such as if the full channel configuration with width 0.91 cm (third dimension) would be used.

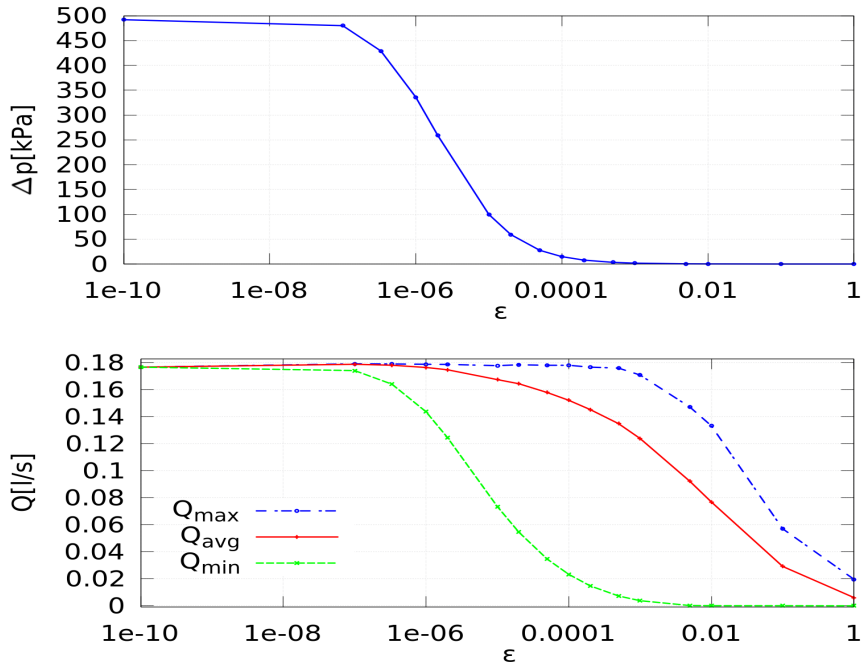


Figure 5.7: The dependence of the maximal pressure drop and the inlet flow rate on the penalization parameter $\epsilon$ is plotted at the top and at the bottom, respectively.

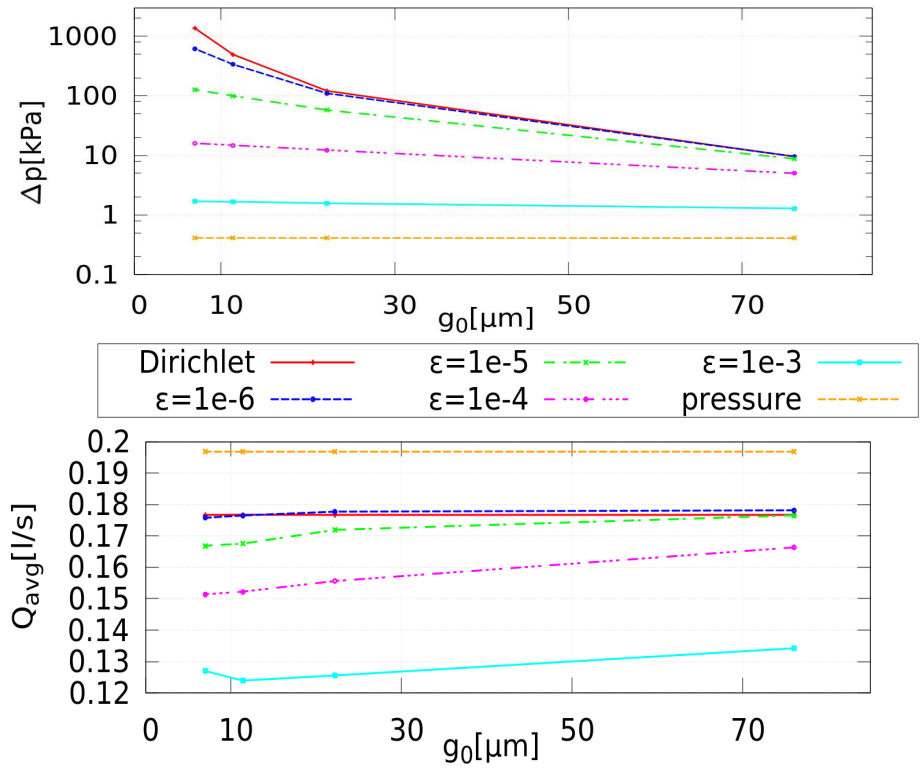


Figure 5.8: Computed isolines of $\epsilon$ for cases, where the inlet velocity is prescribed by the penalty approach or by the Dirichlet inlet boundary condition (case "vel") or where the prescribed pressure drop (case "pres") is given. The top and the bottom graph shows the dependence of the maximal pressure drop $\Delta p$ and the average flow rate $Q_{\text{avg}}$ on the minimal half-gap $g_0$ of the prescribed VF motion, respectively.

The flow characteristics are quite sensitive to the prescribed minimal half-gap, as expected. The sensitivity of the flow field in the channel was tested on series of simulations with the prescribed motion of the structure given by formula (5.4) with the values of $C_{\text{driven}} \in \{6.0, 7.0, 7.2, 7.28\}$. The top graph in Figure 5.8 shows the dependence of the maximal pressure drop (compare with Figure 5.5) on the gradually decreasing minimal value of half-gap up to $g_{0,min} = 0.0071\,\text{mm}$ corresponding to $C_{\text{driven}} = 7.28$. The bottom graph reports the dependence of the average flow rate evaluated in the channel inlet on the minimal half-gap. In both graphs, the results obtained for the same value of the penalization parameter $\epsilon$ are connected with a line representing actually $\epsilon$-isocurve. An interesting part is near $g_0$ approaching zero, where the line of the maximal pressure differences (between the inlet and the outlet) changes gradually slope, i.e. the pressure drops grow faster (as $g_0 \to 0$) for values of $\epsilon < 10^{-6}$, imitating the Dirichlet boundary condition, while the average flow rate does not depend on the minimal half-gap in this range of the parameter $\epsilon$.

The graphs shown in Figures 5.7 and 5.8 allow to estimate a suitable value of the penalization parameter according to measured or expected pressure drop and flow rate values relevant to similar FSI problems. For the simulation of flow-induced vocal fold vibrations the typical range of transglottal pressures and flow rates are approximately $0.1 - 2.0\,\text{kPa}$ and $0.05 - 0.5\,\text{l/s}$, resp., see [156]. Then for the current setting (with the given periodically changing gap and the given inlet velocity) is reasonable to choose the penalization parameter in range $2 \cdot 10^{-4} < \epsilon < 5 \cdot 10^{-3}$ (i.e. $\frac{1}{5000} < \epsilon < \frac{1}{200}$) according to the results summarized in Table 5.1, compare it with Figures 5.7 and 5.8. The described technique how to choose penalization parameter $\epsilon$ is applicable also for a more general case not only restricted to the simulation of vocal folds vibrations.

| $\epsilon$ [s/m] | max $\Delta p(t)$ [Pa] | $Q_{avg}$ [l/s] |
|---|---|---|
| $2 \cdot 10^{-4}$ | 7827.5 | 0.145 |
| $5 \cdot 10^{-4}$ | 3305.1 | 0.135 |
| $1 \cdot 10^{-3}$ | 1670.7 | 0.124 |
| $5 \cdot 10^{-3}$ | 345.16 | 0.092 |

Table 5.1: Table summarizing the maximal pressure drops and the average flow rates in the dependence on the recommended range of penalization parameter $2 \cdot 10^{-4} < \epsilon < 5 \cdot 10^{-3}$. The listed values are obtained for the reference prescribed VF motion and given inlet velocity $\mathbf{v}_{\text{Dir}} = (1.7, 0)$ m/s.

### 5.2.3 Choice of the parameters according to experimental data

Here we show the dependence of the pressure drop on the gap area[4] during one regular VF oscillation cycle as it was measured in laboratory experiment, see [74]. This

[4]The dependence of the pressure drop on the gap can be obtained e.g. from the first and the third graph of Figure 5.5 by elimination of time, see e.g. [74].

dependence, see Figure 5.9, allows to estimate the (averaged mechanical) transferred energy from airflow to VF vibration $E_{transf}$ during one oscillation cycle by means of the (oriented) area $A$ closed inside the pressure-gap curve as

$$E_{transf} \approx A = \oint_{\partial\Delta A} F_{eq}\, \mathrm{d}\, GO_{eq} = \int_0^{T_0} F_{eq}(t) \frac{d\ GO_{eq}(t)}{dt}\ \mathrm{d}t = T \int_0^{T_0} p_{\mathrm{trans}}(t) \frac{d\ GA(t)}{dt}\ \mathrm{d}t, \tag{5.5}$$

where $F_{eq}(t) = T\, l\, p_{\mathrm{trans}}(t)$ is a roughly estimated force loading the VF surface approximated by the area $T\, l$ given by the VFs' thickness $T$ and length $l$; further $GO_{eq}(t) = GA(t)/l$ is an equivalent glottal width, $GA(t)$ and $p_{\mathrm{trans}}(t)$ are the measured glottal area and transglottal pressure (in our simulations denoted as the pressure drop), respectively; finally $T_0$ denotes oscillation period, see [74].

Figure 5.9 shows the accumulated energy $E_{transf}$ in the case of self-induced vibration of VFs as measured by [74] on the VF model[5], here with included the vocal tract model of vowel [u:] and driven by constant flow rate $Q = 0.2\,\mathrm{l/s}$. The accumulated energy $E_{transf}$ in this case is positive due to clockwise orientation of the pressure-gap area curve what means that the energy is transferred from airflow to the vibration of VFs.

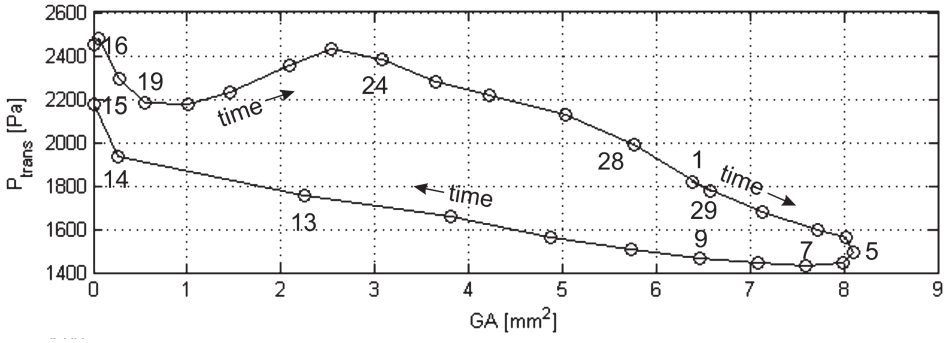


Figure 5.9: Typical behaviour of the transglottal pressure in the dependence on the glottal gap area (GA) during one oscillation cycle, see original paper [74].

The pressure-gap dependence is constructed based on the previously presented FSI simulations with the prescribed vibration given by formula (5.4) with $C_{\mathrm{driven}} = 7.28$ and $f_{\mathrm{driven}} = 100$ Hz and shown in Figure 5.10. As expected, in the case when the inlet velocity is prescribed by the Dirichlet boundary condition ($\mathbf{v}_{\mathrm{Dir}} = (1.7, 0)$ m/s) the pressure (drop) maximum is unrealistically big ($\sim 1.6$ MPa). Similarly if the same inlet velocity is prescribed by the penalization approach with parameter $\epsilon = 10^{-6}$ s/m the behaviour resembles previous one with lower, nevertheless still unphysical pressure maximum ($\sim 0.6$ MPa). For the prescribed pressure drop of value $\Delta p = 400$ Pa the pressure remains almost constant. Finally choice of the penalization approach with parameter $\epsilon = 10^{-3}$ s/m demonstrates the qualitative

[5]The model is 1:1 scaled three-layered VF model partly filled by water with fundamental frequency $F_0$ of approx. 80 Hz. The VF model dimensions were: length 10.3 mm, height 8 mm and width 20 mm.

agreement with results published in [74] concerning similar difference between the maximal and the minimal transglottal pressure. The sum of transferred energy is negative in all cases due to an anticlockwise curve orientation as explained later.

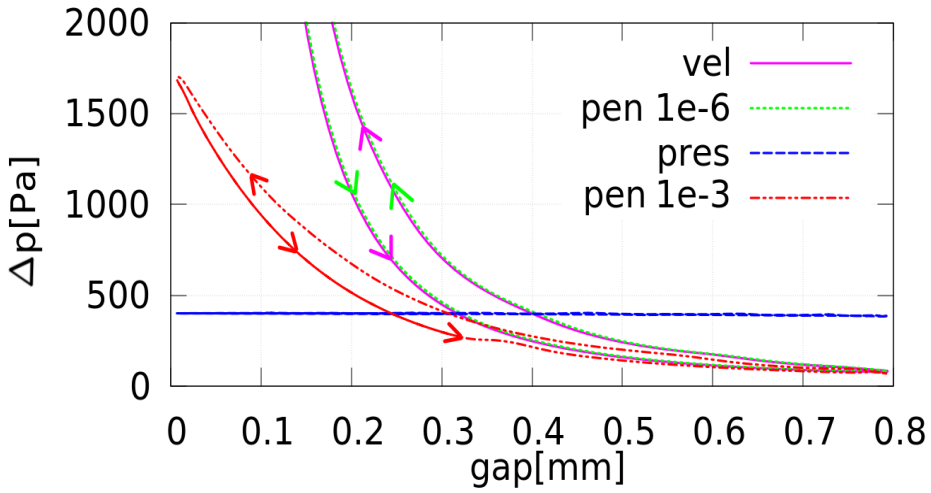


Figure 5.10: Dependence of the transglottal pressure on the gap for simulation cases with prescribed Dirichlet boundary condition (**vel**), pressure drop (**pres**) and two penalization boundary conditions (**pen_1e-6** and **pen_1e-3**). The pressure maxima for cases **vel** and **pen_1e-6** are approximately 1.6 MPa and 0.6 MPa, resp. The arrows show the (time) direction of curve circulation.

In order to obtain the pressure-gap area dependence as in Figure 5.9 the gap, i.e. $x$-axis of graph 5.10, is rescaled. The gap is multiplied by such constant width (third dimension), that the average of flow rate over one simulation period is equal $Q = 0.2\,\mathrm{l/s}$, see Figure 5.11 for three simulations with different penalization parameters. This width for case **pen_2e-3** is chosen 1.65 cm, for case **pen_1e-3** is 1.48 cm and case **pen_5e-4** is scaled by the width of 1.37 cm.[6]. The theoretical glottis reference dimension would be then two-times *width* times half-gap, which is in all cases equal $g_0 = 0.4\,\mathrm{mm}$. The most similar working pressure range as the laboratory experiment has the simulation with penalization parameter $\epsilon = 10^{-3}\,\mathrm{s/m}$ (case **pen_1e-3**) although also cases with $\epsilon = 5 \cdot 10^{-4}\,\mathrm{s/m}$ (**pen_5e-4**) and $\epsilon = 2 \cdot 10^{-3}\,\mathrm{s/m}$ (**pen_2e-3**) show reasonable behaviour.

Nevertheless we have to note that the curves orientation in Figures 5.10, 5.11 is reverse related to the results in [74]. It signalizes that the energy is transferred from VF vibration to the airflow, what is typical for the prescribed harmonic motion of VF (numerical simulation) contrary to the natural flow-induced VF vibration (laboratory measurement), see e.g. [155] and also paragraph 5.3.3 for further investigation. The pressure-gap dependence for the full FSI simulations with apriori unknown VF motion, where the curve is oriented in agreement with results [74], i.e. the energy transfer to VFs is positive, is shown in Figure C.3 in Appendix C.

[6]The calculated flow rate is doubled because of the considered hemi-larynx simulation configuration.

The conclusions of this qualitative comparison have to be done very carefully because the both graphs (Figs. 5.10 and 5.11) are obtained in highly different configurations. Namely we compare the numerical simulations with the prescribed motion versus the FSI phenomenon neglecting differences in the VF shapes, materials and possible nonlinear behaviour of real silicone model and neglecting further physical phenomena naturally present in measurement like air compressibility and acoustical couplings. However the numerical simulation with the penalization approach seems to be able to describe important physical characteristics during the FSI simulation if the penalization parameter is chosen appropriately.

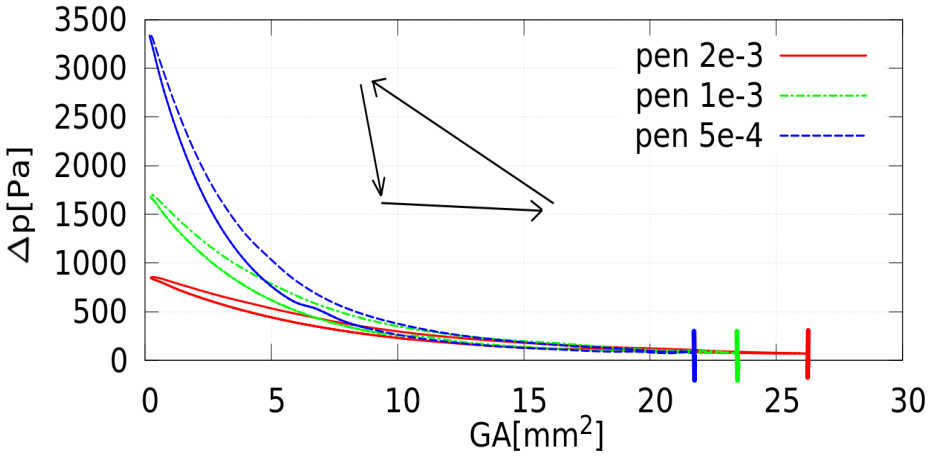


Figure 5.11: Dependence of the transglottal pressure on the gap area (GA) simulated for inlet velocity prescribed by three different penalization parameters, particularly case **pen_2e-3** with $\epsilon = 2 \cdot 10^{-3}$ s/m, case **pen_1e-3** ($\epsilon = 10^{-3}$ s/m) and case **pen_5e-4** ($\epsilon = 5 \cdot 10^{-4}$ s/m). The cases were rescaled by a the third dimension (width) to have the average flow rate $Q = 0.2$l/s. Arrows show the curve orientation, the colored lines on the $x$-axis denotes the maximal GA for each case.

## 5.3 Fluid-structure interaction of the hemi-larynx configuration

This section contains numerical simulations of full FSI problem in the hemi-larynx configuration with the VF model MALE-SYM, i.e. particularly $\Gamma^f_{\text{Sym}} \neq \emptyset$. The prephonatory half-gap is chosen 0.4 mm as described in Section 5.1. In the first paragraph the differences caused by the choice of the inlet boundary conditions are discussed, the second paragraph concentrates on the determination of the critical flutter velocity. In this case also the sensitivity of the flutter airflow velocity with respect to the choice of the penalization parameter $\epsilon$ is investigated, see author's publication [7]. The last paragraph of this section describes the energy exchange between the airflow and the vibrating vocal fold.

The FSI problem is numerically solved with $t_{\text{release}} > 0$ and the unstable behaviour of the FSI system can appear. The stability boundary is given by the critical inlet flow velocity [7] $v_{\text{flutter}}$ of the flutter type aeroelastic instability, see e.g. [40]. After exceeding the critical flow velocity the amplitudes of the structure vibrations start to exponentially grow. In phonation the maximal amplitude is restricted by contact of VFs, see e.g. [156]. In dynamics of nonlinear systems is this regime called limit cycle oscillation. The critical flow velocity depends on an interplay of many factors – besides physical parameters and the geometric configuration[8], in the case of numerical simulation also on the choice of boundary conditions at the glottal channel inlet and outlet can influence the value of $v_{\text{flutter}}$, see e.g. [148].

### 5.3.1 Influence of the inlet boundary conditions on the flow-induced vibrations

Similarly as in the previous section the influence of inlet boundary conditions (3.29) is here studied on the examples of four numerical simulations. The inlet velocity $v_{\text{Dir},1} = 1.9\,\text{m/s}$ is prescribed by condition (3.29 a) (case "Vel") and by (3.29 c) with two different choices of penalization parameter $\epsilon = 10^{-5}\,\text{s/m}$ and $\epsilon = 5 \cdot 10^{-4}\,\text{s/m}$. These two cases are denoted as "Pen-S" (strong) and "Pen-W" (weak) case, respectively. The case of the applied condition (3.29 b) is labeled as "Pres" with chosen pressure drop $\Delta p = p_{\text{in}} - 0 = 450\,\text{Pa}$, which slightly overestimates the computed pressure drop in case "Vel".

The simulation of full interaction starts at time $t_{\text{release}} = 0.035\,\text{s}$ when the flow field is already fully developed and the static force $\mathbf{q}^s_{\text{stat}}$ is determined, see Figure 5.12. Then the VF is released for interaction. The series of illustrative snapshots for case "Pen-W" are shown in Figure C.1 in Appendix C.

The averaged airflow velocity over inlet boundary $\Gamma^f_{\text{In}}$ for the different boundary conditions is shown in Figure 5.13. Classic Dirichlet boundary condition (3.29 a) keeps

[7] The occurrence of self-sustained VF oscillations, i.e. appearance of flutter regime, is usually reported in voice studies instead of the critical velocity in terms of the phonation onset threshold pressure (PTP) or the phonation onset threshold flow (PTF), see e.g. [73].

[8] Especially, the value of $v_{\text{flutter}}$ grows with increasing initial glottal gap, see e.g. [77], [147].

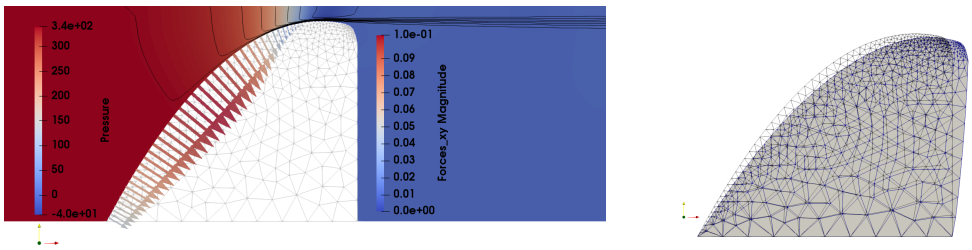


Figure 5.12: **Left:** The detail of static aerodynamic force $\mathbf{q}^s_{\text{stat}}$ determined at $t_{\text{release}} = 0.035\,\text{s}$ in simulation "Pen-W". **Right:** The hypothetic deformation under the load of static force $\mathbf{q}^s_{\text{stat}}$.

the inlet velocity constant, while the prescribed pressure drop – condition (3.29c), leads to oscillating inlet velocity with a fast growing amplitude, i.e. to the flutter instability of the system. The inlet velocity in the both cases of penalization approach given by (3.29 b) has an oscillating character with a slightly increasing amplitude around a little lower average value than in the case with the Dirichlet condition. These oscillations are larger in case "Pen-W" than in case "Pen-S", fully in agreement with the previous results of paragraph 5.2.2 with prescribed VF vibrations.

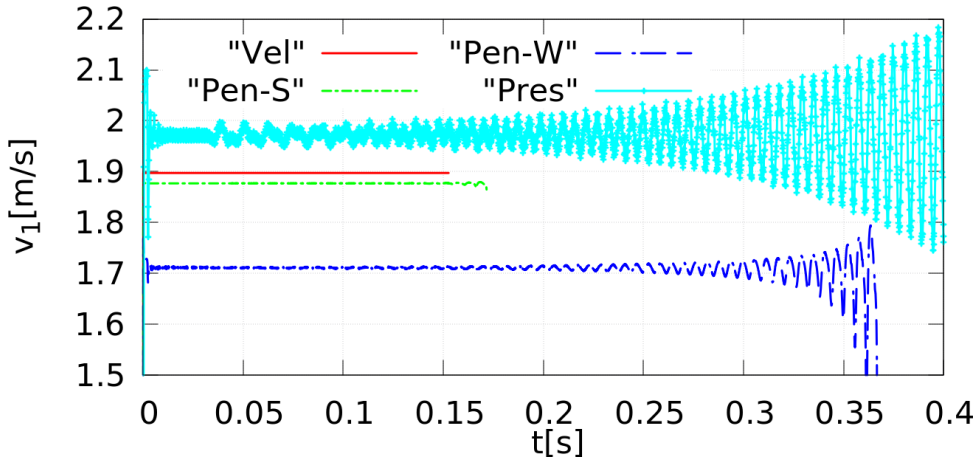


Figure 5.13: The inlet airflow velocity for cases "Vel", "Pen-S", "Pen-W" and "Pres", plotted values are averaged over boundary $\Gamma^f_{\text{In}}$.

The corresponding results computed for waveform of the pressure drop between the inlet $\Gamma^f_{\text{In}}$ and the outlet $\Gamma^f_{\text{Out}}$ and for the half-gap $g_0(t)$ are displayed in Figures 5.14 and 5.15, respectively. The pressure drop in case "Pres" is almost constant. For the prescribed inlet velocity in cases "Vel", "Pen-S" and "Pen-W" the pressure drop shows significant oscillating behaviour connected with the increasing VFs vibration amplitude monitored in Figure 5.15. In the case of penalization approach the pressure drop oscillation is delayed analogously as the VF vibration is delayed, see Figure 5.15, case "Pen-W" is delayed more than case "Pen-S".

Neither boundary condition (3.29 a) nor boundary condition (3.29 c) corresponds to reality because both the inlet flow velocity and the inlet pressure should fluctuate

as it was observed e.g. in measurements [73]. This behaviour is recovered using the penalization approach, see Figures 5.13 and 5.14.

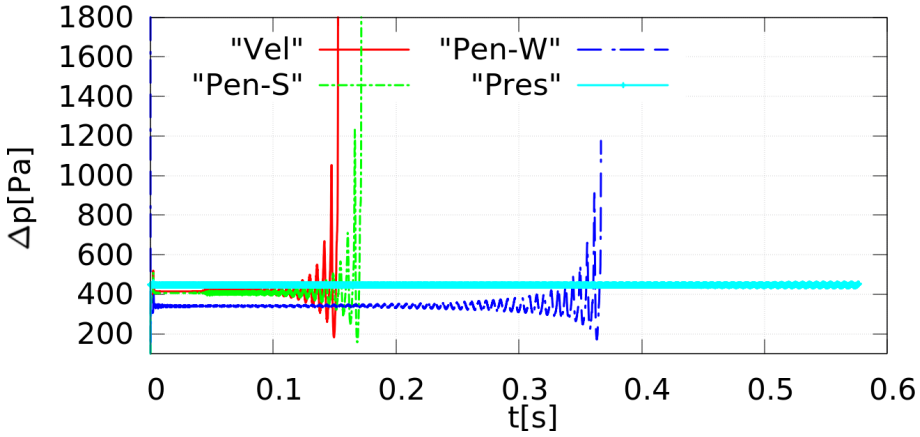


Figure 5.14: Pressure drop between the inlet and the outlet part of boundary in cases "Vel", "Pen-S", "Pen-W" and "Pres".

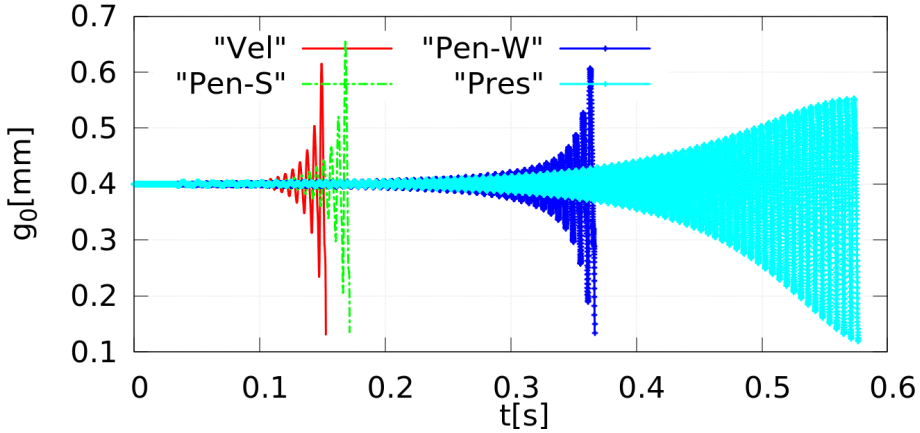


Figure 5.15: Time development of the half-gap plotted for cases "Vel", "Pen-S", "Pen-W" and "Pres".

Figures 5.13 –5.15 document that the penalization approach is a generalization of the Dirichlet boundary condition and the prescribed pressure drop (directional do-nothing boundary condition). As penalization parameter $\epsilon$ goes from $0^+$ to $+\infty$ the characteristic fluid flow behaviour tends to switch between these two types of boundary conditions.

In all four cases the inlet flow velocity exceeds the stability limit given by the critical flutter velocity $v_{\text{flutter}} \approx 1.86\,\text{m/s}$ (or by the phonation onset threshold pressure) as will be determined in the next paragraph. Consequently, the magnitude of structural vibration amplitudes is exponentially increasing and the simulations in all four cases end by the fluid flow solver failure. This is caused by too distorted fluid computational mesh near the top of the elastic body although the considered half-gap is still quite large ($g_0(t) > 0.1\,\text{mm}$). This is partly due to the fact that during the VF oscillations a more general 2D motion in both directions $x$ and $y$ is observed compared to the prescribed vibrations, see the phase portrait of point S in Figure 5.19.

### 5.3.2 Determining the boundary of the flutter instability

Here, the self-induced vibrations of the vocal folds model MALE-SYM are studied for the different inlet velocity prescribed by penalization inflow boundary condition (3.29 c) with the choice of one penalization parameter $\epsilon = 5 \cdot 10^{-4}\,\mathrm{s/m}$ (compare it with previous case "Pen-W"). The displacement of point S from the top of the vocal fold surface (see Figure 5.1) is plotted in Figure 5.16 for three different inlet flow velocities leading to three different behaviour of the FSI system.

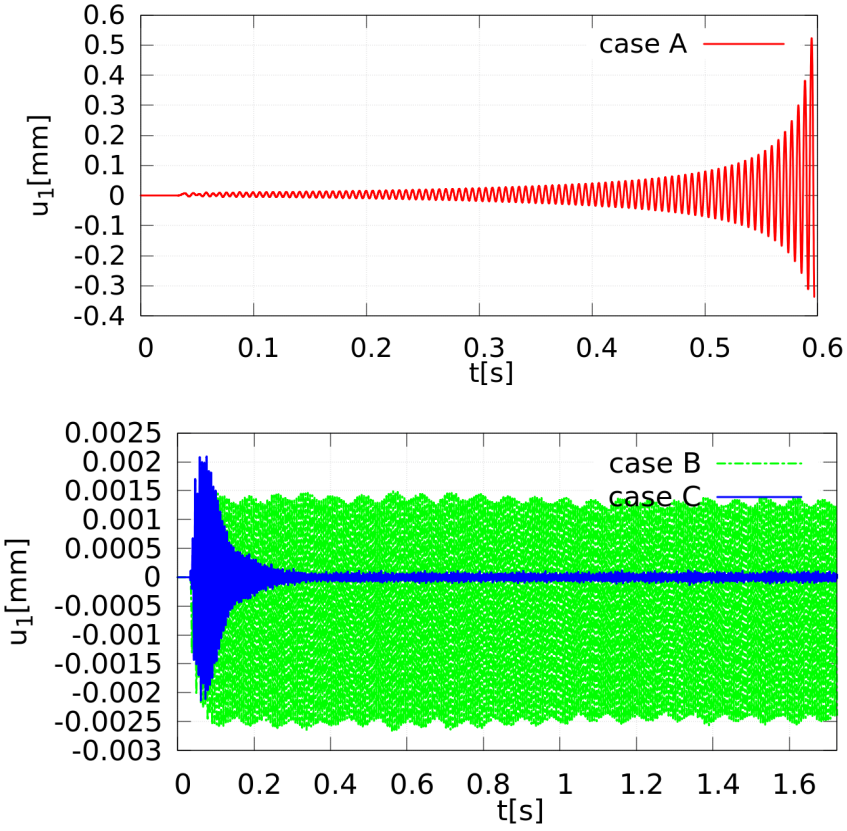


Figure 5.16: The time development of $u_1$ ($x$-component of displacement) at point S is shown in the case of three different inlet velocities: A) 1.87 m/s, B) 1.85 m/s, and C) 1.8 m/s, all prescribed by penalization approach with $\epsilon = 5 \cdot 10^{-4}\,\mathrm{s/m}$. Note the different scaling of axes for the top and the bottom figure.

For inlet velocity $v_{\mathrm{Dir},1} = 1.8\,\mathrm{m/s}$ (case C) the vibrations are damped and after a short transition regime the vibration amplitude decreases to a very low level of stationary vibrations. For the inlet velocity equal $v_{\mathrm{Dir},1} = 1.85\,\mathrm{m/s}$ (case B) the displacements of point S remain bounded. For inlet velocity $v_{\mathrm{Dir},1} = 1.87\,\mathrm{m/s}$ (case A) the magnitude of the vibrations is exponentially growing. We note that the vibration amplitudes in $y$-direction are of about five times smaller than in $x$-direction but with the same behaviour in the time domain as in Figure 5.16. Therefore the critical flutter velocity is determined as $v_{\mathrm{flutter}} \approx 1.86\,\mathrm{m/s}$ for this model setting.

**Remark.** The determination of the critical velocity for original VF model of type

MALE-SYM without top rounded corner (see e.g. [77]) is reported in [147], where the flutter velocity was determined $v_{\text{flutter}} \approx 1.85\,\text{m/s}$ by using a simplified 2-DOF VF model with the Dirichlet inlet boundary condition.

**Sensitivity of stability boundary to the penalization parameter**

By the procedure described in the previous paragraph the dependence of critical velocity $v_{\text{flutter}}$ on the penalization parameter $\epsilon$ is investigated and summarized in Figure 5.17. The simulation with the Dirichlet boundary condition is here plotted as point $\epsilon = 10^{-10}$ and it gives $v_{\text{flutter}} \approx 1.68\,\text{m/s}$, i.e. the lowest value. The influence of penalization parameter is proven to be negligible for values $\epsilon < 10^{-4}$, while for $\epsilon > 10^{-4}$ the influence is quickly increasing. For values $\epsilon > 2 \cdot 10^{-3}$ the critical velocity differs by more than 50%. This can be explained by substantial decreasing of the average flow rate connected with the increased penalization parameter, what is in accordance with findings of paragraph 5.2.2 – compare Figures 5.17 and 5.7. Therefore we recommend to restrict the suitable range of penalization parameter $\epsilon$ for the simulation of flow-induced VF vibrations to range $2 \cdot 10^{-4} < \epsilon < 1 \cdot 10^{-3}$, i.e. $\frac{1}{5000} < \epsilon < \frac{1}{1000}$. For the (similar) flutter dependence on the penalization parameter for the full channel configuration of VF model MALE see publication [14].

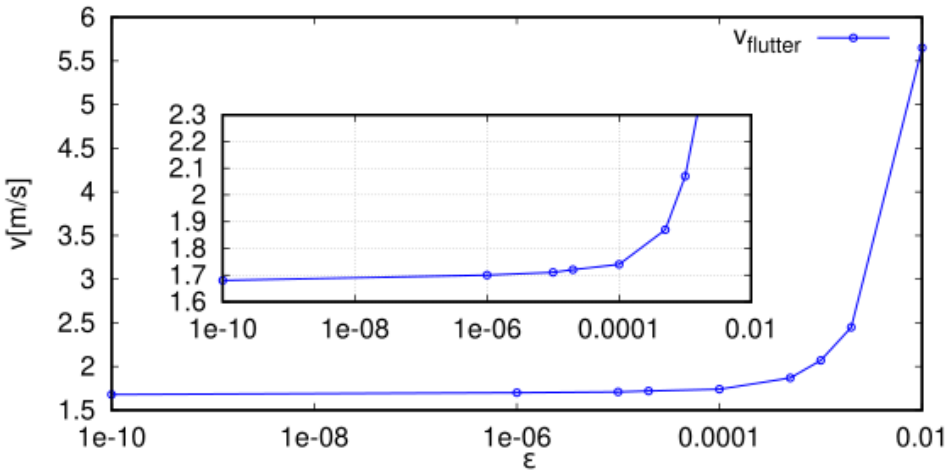


Figure 5.17: Dependence of the critical flutter velocity for the hemi-larynx configuration on the penalization parameter. The inner graph presents the detail of critical velocity behaviour for lower values of $\epsilon$.

### 5.3.3 Energetic considerations related to the VF flutter

Flutter phenomenon of the FSI system can in general emerge and can be maintained if the total energy gained from airflow by structure exceeds the energy loss caused by the structure damping and the damping due to the fluid viscosity. A positive flow of energy from the airstream to the structure tissue occurs if the aerodynamic (VF driving) force is in phase with the tissue velocity. According to analysis of [155], the positive flow of energy to VF can be hypothetically achieved by two scenarios – either

in the case of oppositely phased supraglottal and subglottal acoustic pressures during one vibration period[9] or by varying the glottal geometry during one vibration period in such a way, that bigger aerodynamic force acts together with in-phase structure motion and smaller aerodynamic force acts against structure motion. In normal phonation both mechanisms may occur simultaneously however the experimental and the numerical results support the second hypothesis to be more prominent, see e.g. [153], [170]. The well-known changing of VF shape denoted as the switching between the convergent and divergent shape connected with the VF opening and closing phase is a typical example of the second described scenario. In this case the airflow pressure (dominant component of aerodynamic force) is typically in phase with VF motion during opening phase (convergent shape) and it reaches higher values than during the VF closing phase (divergent shape), when airflow pressure is smaller and acts oppositely to the VF motion, see [155], [153], [124].

In this paragraph, first the VF vibration energy is studied and then the energy exchange between vibrating VF and airflow is quantified based on the previously presented numerical simulations. These results are extended version of publication [11].

### Vocal folds energy

The total energy $E^s$ of the VF represented by domain $\Omega^s$ at time $t$ can be approximated as

$$E^s = E^s_{kin} + E^s_{pot} = \frac{1}{2}\int_{\Omega^s} \rho^s \dot{\mathbf{u}}^2 \,\mathrm{d}x + \frac{1}{2}\int_{\Omega^s} \left(\lambda^s \operatorname{div}\mathbf{u}\,\delta_{ij} + 2\mu^s e^s_{ij}(\mathbf{u})\right) e^s_{ij}(\mathbf{u}) \,\mathrm{d}x$$
$$\approx \frac{1}{2}\dot{\mathbf{u}}^T \mathbb{M}\dot{\mathbf{u}} + \frac{1}{2}\mathbf{u}^T \mathbb{K}\mathbf{u}. \tag{5.6}$$

For the simulation from the previous paragraph labeled as case A (inlet velocity $v_{\mathrm{Dir},1} = 1.87\,\mathrm{m/s} > v_{\mathrm{flutter}}$) VF energy $E^s$ rapidly increases in the time domain, see Figure 5.18. The energy rise has an exponential character, typical for the flutter phenomena, [40], and vice versa the total energy $E^s$ is not increasing in cases B and C (not plotted).

The flutter vibration has dominant frequency at about 171 Hz as seen from the Fourier transform of $x$- and $y$-displacement of point S, see Figure 5.19. The dominant frequency corresponds to a frequency between the second and the third eigenfrequency of the elastic body (see Figures 5.2 and 5.3), what is in agreement with theoretical analysis [170].

### Energy transfer from airflow to vocal folds

In general, the rate of energy transfer (power) is the product of force and velocity. For the case of fluid flow and a moving surface, the rate of energy transfer $\dot{E}_{transf}$ at time instant $t$ done by fluid stress on the (structure) surface is given by, see [153],

[9] Titze deduced that the oppositely phased acoustic pressures are caused by the time delay needed for acceleration of air column at glottis, see [155].

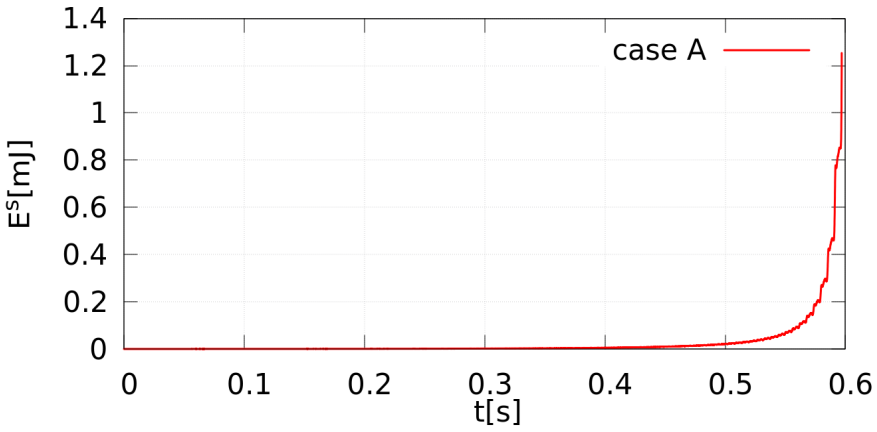


Figure 5.18: Time evolution of the total energy of elastic body $\Omega^s$ for the flutter instability given by inlet flow velocity 1.87 m/s (case A).

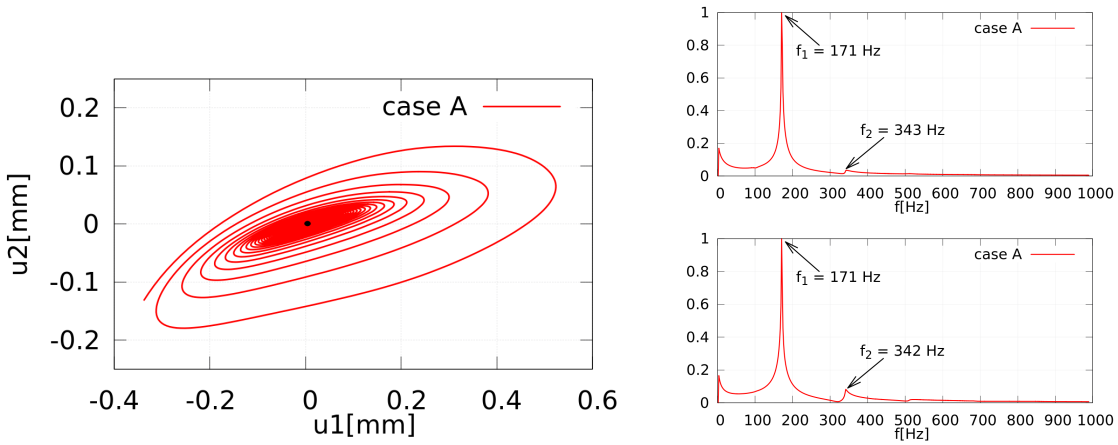


Figure 5.19: **Left**: Trajectory of point S in the X–Y plane. The black dot represents the starting point of the trajectory. **Right**: The (normalized) Fourier transform of point S displacement in $x$ and $y$ direction shown top and bottom, resp. The all graphs are related to prescribed inlet flow velocity $v_{\mathrm{Dir},1} = 1.87\,\mathrm{m/s}$ (case A).

$$\dot{E}_{transf} = \int_{\Gamma_{\mathrm{W_t}}} v_i\, \sigma_{ij}^f\, (-n_j^f)\, dS = \int_{\Gamma_{\mathrm{W_t}}} \frac{\partial u_i}{\partial t}\, \sigma_{ij}^f\, n_j^s\, dS, \tag{5.7}$$

where the equality $\mathbf{v} = \frac{\partial \mathbf{u}}{\partial t}$ at $\Gamma_{\mathrm{W_t}}$ follows from condition (3.28 b) and the sign is changed due to $\mathbf{n}^f = -\mathbf{n}^s$ for points on $\Gamma_{\mathrm{W_t}}$. The dominant component of tensor $\boldsymbol{\sigma}^f$ is the pressure (normal component), i.e. the major of power is done by the pressure. The total transferred energy (work) during a certain time interval can be calculated by integrating power $\dot{E}_{transf}$ over time. The cumulative energy transfer function can be introduced as, see [153],

$$E_{cumul}(t) = \int_0^t \dot{E}_{transf}(\tau)\, \mathrm{d}\tau. \tag{5.8}$$

The computed energy transfer function $\dot{E}_{transf}$ and the cumulative energy transfer

function $E_{cumul}$ are shown in Figure 5.20 for the previously presented numerical results of paragraph 5.3.1, namely for the simulation of (full) FSI problem labeled "Vel", "Pen-S" and "Pres". Moreover one simulation with the prescribed harmonic VF motion labeled as case "pen" in paragraph 5.2.1 and here denoted as "Driven" is included for an illustration. The dominant frequencies of VF vibrations are listed in Table 5.2.

In all full FSI cases the energy transfer function oscillates around zero with growing amplitude, see Figure 5.20. The function $\dot{E}_{transf}$ develops in time the most intensively for case "Vel" followed by case "Pen-S", in case "Pres" the oscillation magnitude of function $\dot{E}_{transf}$ grows slowly. The cumulative transfer function practically copies the behaviour of the energy transfer function with an exponentially increasing average value, around which it oscillates. It is expected behaviour, because the prescribed inlet velocity or pressure drop is higher than the critical flutter velocity or the phonation onset threshold pressure ($\Delta p_{crit} \approx 450\,\mathrm{Pa}$ was determined for $g_0 = 0.4\,\mathrm{mm}$ in paper [147]) and the energy growth confirms previously observed flutter instability.

In case "Driven" the function $E_{cumul}$ is linearly decreasing, see Figure 5.20, as it was already noticed in paragraph 5.2.3. More detailed graph of functions $E_{cumul}$ – Figure 5.21, shows the total transferred energy to VF per one oscillation period is negative because external force (given by prescribed VF motion pattern) removes a fluid flow volume and also the pressure and displacement $u_2$ are in phase. That the total transferred energy per one vibration period is negative can be noticed also from behaviour of the function $\dot{E}_{transf}$, having more negative peak value during VF closing ($t \leq 0.097\,\mathrm{s}$) than the positive peak during VF opening phase ($t \geq 0.098\,\mathrm{s}$), see Figure 5.21. We note that in the prescribed motion of the VF given by formula (5.7) the VF is not allowed to change the convergent-divergent shape of the glottis having a consequence of the impossibility to achieve the phase shift between the airflow pressure and the VF motion. For detail of the aerodynamic forces action during one oscillation period, see Figure C.2 in Appendix C.

The detailed behaviour of functions $\dot{E}_{transf}$ and $E_{cumul}$ for cases "Vel", "Pen-S", "Pres" during one period of VF motion[10] is shown in Figure 5.21 together with the details of the pressure drop and displacement $u_2$ of point S[11]. The displacement $u_2$ is slightly phase delayed in relation to the pressure for all FSI cases, see top graphs of Figure 5.21. Together with the details of VF deformation evolution, see Figure 5.22, it suggests us to be a manifestation of so called mucosal wave, an inherent property of healthy VF vibration, see e.g. [156]. The appearance of mucosal wave can be also viewed as one of characteristics of previously described convergent-divergent VF changing shape.

In all simulated cases the energy transfer function changes the sign from positive to negative during transition from the channel opening to the channel closing phase, compare it with the details of vocal fold deformations in Figure 5.22. In the cases of the flutter behaviour, i.e. in cases "Vel", "Pen-S" and "Pres", the asymmetry

[10] One period of VF motion is here determined by the crossing of function $\dot{E}_{transf}$ through zero.

[11] It is better to plot displacement $u_2$ at point S than the time development of half-gap $g_0$, because the half-gap is almost perfectly correlated with the pressure (drop).

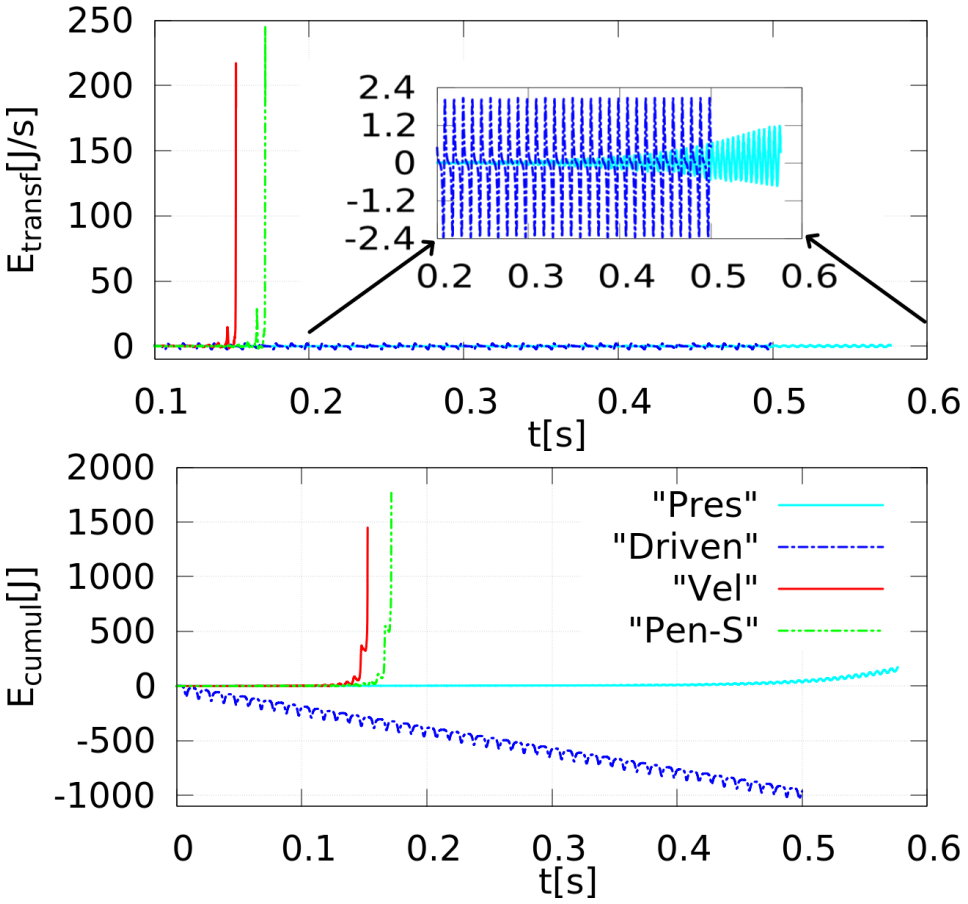


Figure 5.20: Energy transfer function (top) and energy cumulative function (bottom) for cases "Vel", "Pen-S", "Pres" and "Driven". The top graph contains the detail of cases "Pres" and "Driven" inside. Labels are common for both graphs.

of function $\dot{E}_{transf}$ appears and the total energy transferred from airflow to vocal fold during one period is positive, see values of the cumulative function at the end of period in Figure 5.21. The energy gain differs, it is quite high for cases "Vel" and "Pen-S" (the next-to-last periods before the fall of simulation were chosen in Figure 5.21) compared to case "Pres"(the sixth period before the fall of simulation is plotted), where the asymmetry of $\dot{E}_{transf}$ is not so obvious. The behaviour of functions $\dot{E}_{transf}, E_{cumul}$ (at least for cases "Vel" and "Pen-S") is very similar to the results [153][12] or [124][13], where also the clear asymmetry of $\dot{E}_{transf}$ and therefore a noticeable increase of $E_{cumul}$ per one oscillation period was reported.

Figure 5.22 shows the aerodynamic forces superposed on the deformed vocal fold during one oscillation period (the same period as in Figure 5.21 is chosen). In case "Pres" the energy exchange takes dominantly place at the top of leading edge of the vocal folds (the aerodynamic forces are there the highest), see Figure 5.22, while for cases "Vel" and "Pen-S" the whole surface of VF leading edge participates in the energy exchange. The most different behaviour connected with the significantly

[12]The results of [153] were achieved with the prescribed periodically changing pressure drop.

[13]The simulations of [124] were performed with a complicated prescribed changes of convergent-divergent VF position and the given constant pressure drop.

increased transglottal pressure of cases “Vel” and “Pen-S” contrary to case “Pres” (see also Figure 5.14) occurs shortly before and during vocal folds opening phase, i.e. compare graphs a3) and b3) with c3) of Figure 5.22. The increased pressure as dominant aerodynamic force component results also afterwards in a higher intensity of VF power loading given by $\dot{E}_{transf}$ (during VF opening).

| Case | “Vel” | “Pen-S” | “Pres” | “Driven” |
|---|---|---|---|---|
| F0 | 176 Hz | 172 Hz | 177 Hz | 100 Hz |
| $T_{end}$ | 0.12 s | 0.14 s | 0.54 s | F0 apriori known |

Table 5.2: Dominant frequencies of VF vibrations for the presented flutter simulations with the exception of case “Driven”, when the VF motion was prescribed. The time interval length used for the Fourier transform is denoted by $T_{end}$.

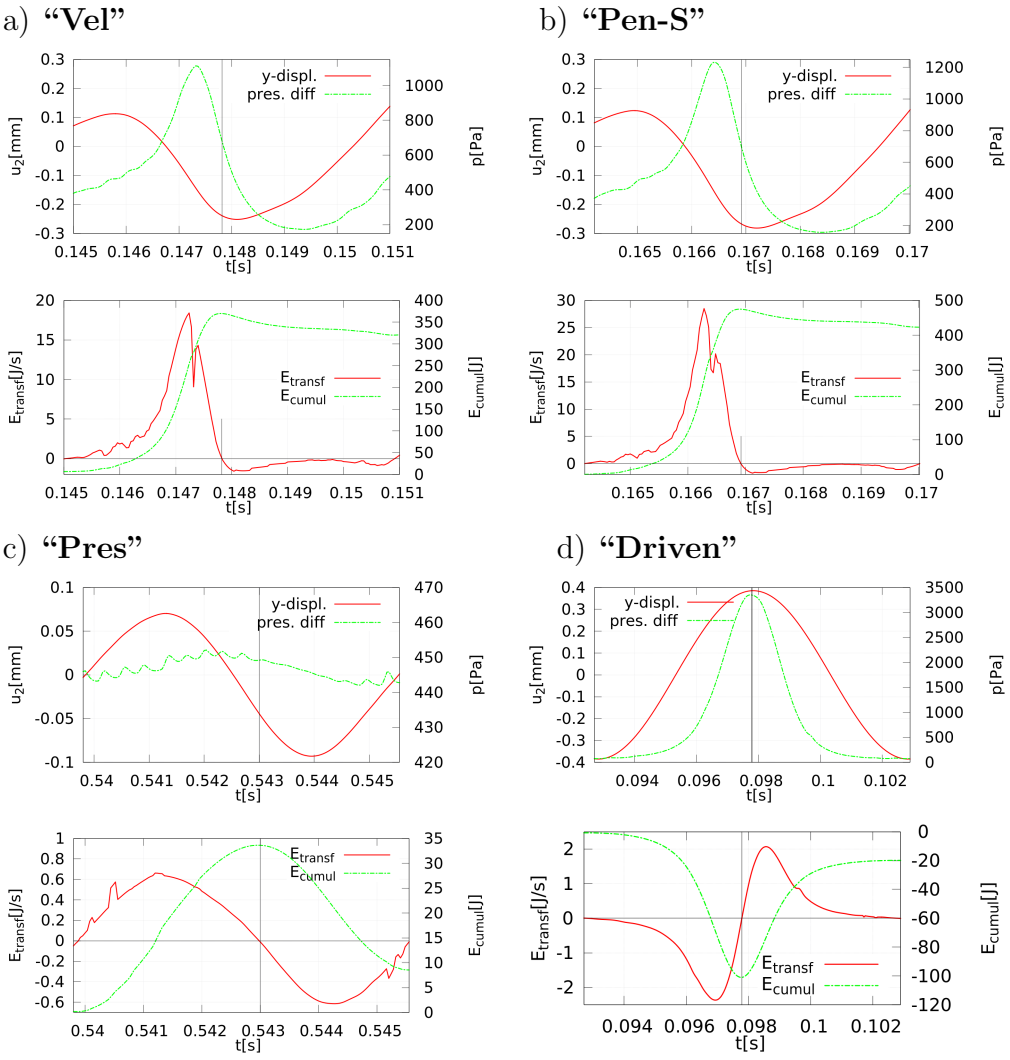


Figure 5.21: Details of the FSI system behaviour during one oscillation period for considered cases: a) “Vel”, b) “Pen-S”, c) “Pres” and d) “Driven”. The top graph of each figure pair shows the $y$-displacement of point $S$ and the pressure drop (labeled as *pres. diff*) (on the right axis), while all bottom graphs display the detail behaviour of functions $\dot{E}_{transf}$ and $E_{cumul}$ (on the right axis).

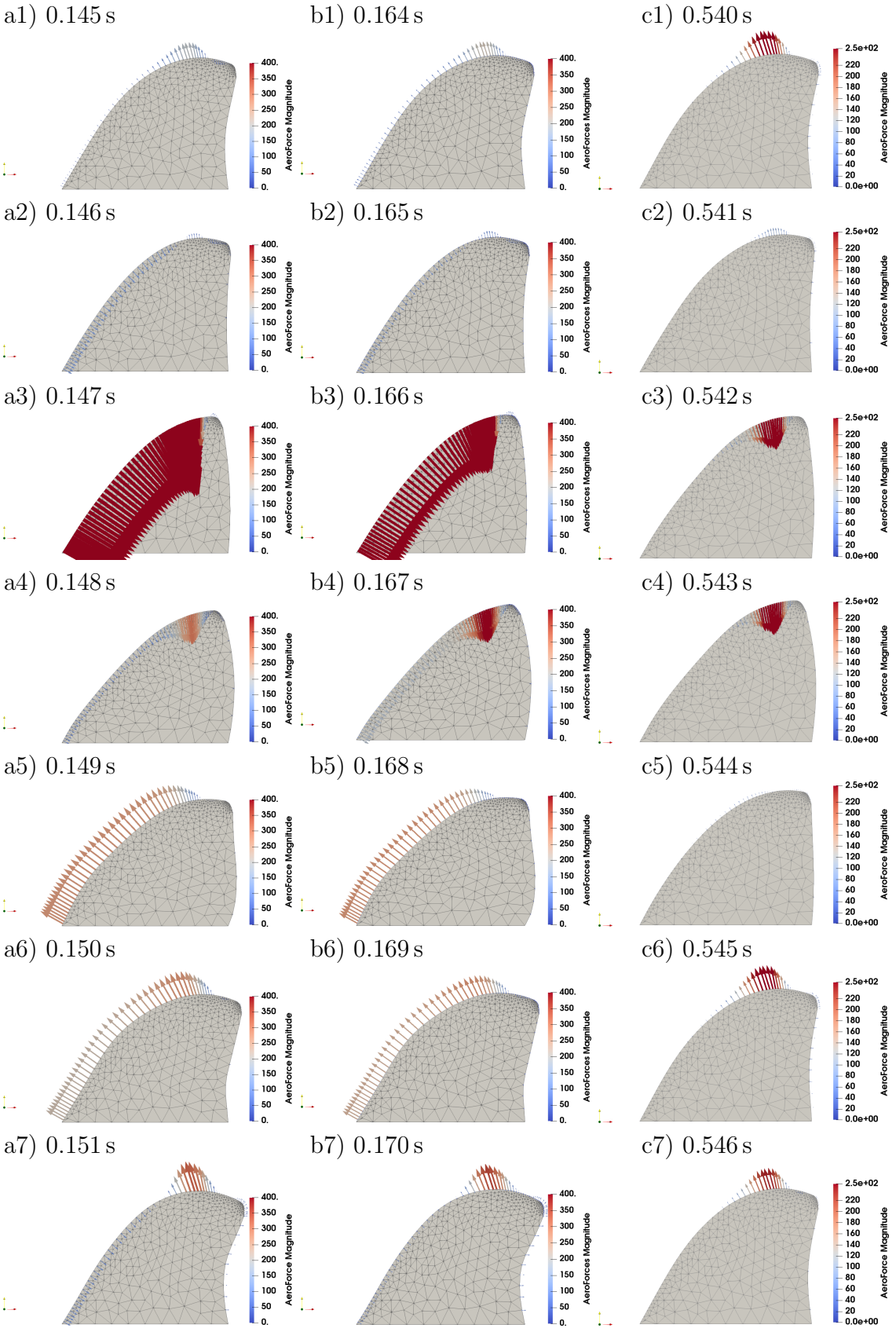


Figure 5.22: Details of the VF deformation and the acting aerodynamic forces during one oscillation period for cases: A) "Vel", B) "Pen-S" and C) "Pres". Colours and vectors have a little different scale among cases.

## 5.4 Fluid-structure interaction of the full-larynx configuration

In this section the FSI problem is solved in the full channel with vocal fold model MALE, i.e. the assumption of the flow symmetry along $x$-axis is removed and moreover the computational fluid domain at the outlet is prolonged to $L3 = 44.2\,\text{mm}$, see Figure 5.1. The all material parameters remain the same as described in Section 5.1. The starting time of the interaction is now set to $t_{\text{release}} = 0.03\,\text{s}$, i.e. at the time instant before attachment of the glottal jet to one channel wall, see static aerodynamic force $\mathbf{q}^s_{\text{stat}}$ in Figure C.4. The computational time (approx. 15 days on notebook with processor Intel i7-5600U and RAM 8GB) for the non-symmetrical arrangement is approximately three times longer than for the symmetrical configuration due to a more complex fluid field and much higher number of DOFs.

First, the illustrative snapshots of simulation conducted with airflow inlet velocity $\mathbf{v}_{\text{dir}} = (2.1, 0.0)\,\text{m/s}$ prescribed with the aid of penalization parameter $\epsilon = 5 \cdot 10^{-4}\,\text{s/m}$ are depicted in Figures 5.23 and 5.24. This simulation is further referred as the case *PEN-W*. The more complicated flow pattern during a typical vibration cycle occurred when compared to the case with the prescribed symmetry of airflow, compare Figures 5.23 and C.1, respectively. In Figure 5.23 the change of VFs position between convergent to divergent and back can be seen. Further, the intensity of glottal jet during opening phase is increasing up to the maximum, then it starts to fade for fully open glottis and it reaches minimum at the time instant prior to maximally closed VFs. The large vortices formed downstream from the glottis (visible only first one in the snapshots) are slowly decaying into smaller ones. The very similar character of the flow field was obtained e.g. in [93] and [29].

### Comparison of numerical simulations for different inlet boundary conditions

Similarly as in Section 5.3 and for numerical settings as described above the simulations of flow-induced vibrations of VFs with four different inlet boundary conditions are compared, for more details see publication [6]. Namely, the cases labeled as *VEL* (Dirichlet BC (3.29 a) with $\mathbf{v}_{\text{dir}}$), *PEN-S* (velocity $\mathbf{v}_{\text{dir}}$ prescribed with the aid of penalization parameter $\epsilon = 10^{-5}\,\text{s/m}$, see condition (3.29 b) ), *PEN-W* and *PRES* (prescribed pressure $\Delta p_{\text{nonsym}} = 400\,\text{Pa}$ by condition (3.29 c) ) were studied. The inlet flow velocity, the pressure drop and the (whole) gap width are displayed in time domain in Figures 5.25 – 5.27.

The numerical results are similar as for the symmetrical configuration (see Figures 5.13 – 5.15). All cases terminated by a solver failure due too large structure vibration amplitudes. The case *PRES* needed more time to reach this limit of the gap width. The explanation can be found in smaller prescribed pressure drop $\Delta p_{\text{nonsym}} = 400\,\text{Pa}$ laying obviously very close to the stability boundary contrary to previously prescribed $\Delta p = 450\,\text{Pa}$ (in symmetric case "Pres"), which evidently exceeded the stability boundary. Additionally, the phase portraits of point S for all four considered simulations are shown in Figure C.5 in Appendix C.

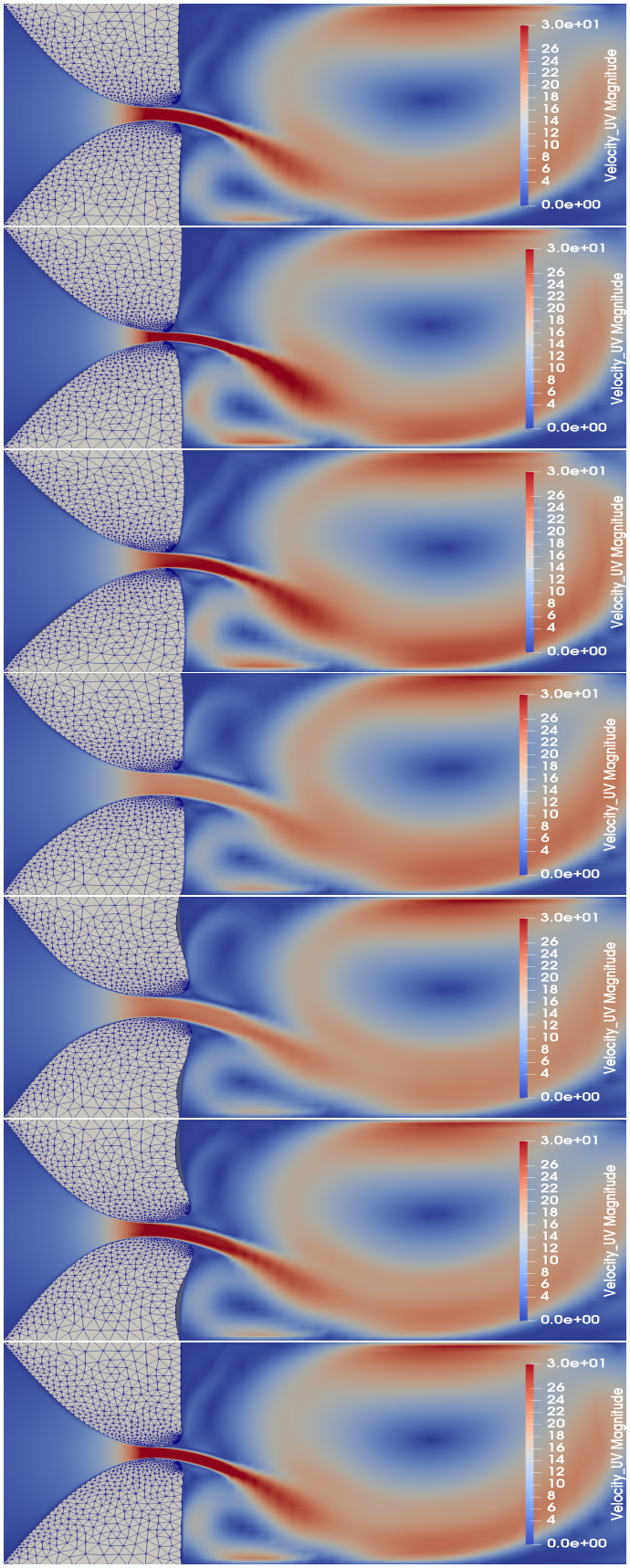


Figure 5.23: Airflow pattern showing the velocity magnitude in case *PEN-W* for seven time instants during one vibration cycle of VFs with duration of approx. 7 ms. The domain $\Omega_t^f$ is in figures truncated.

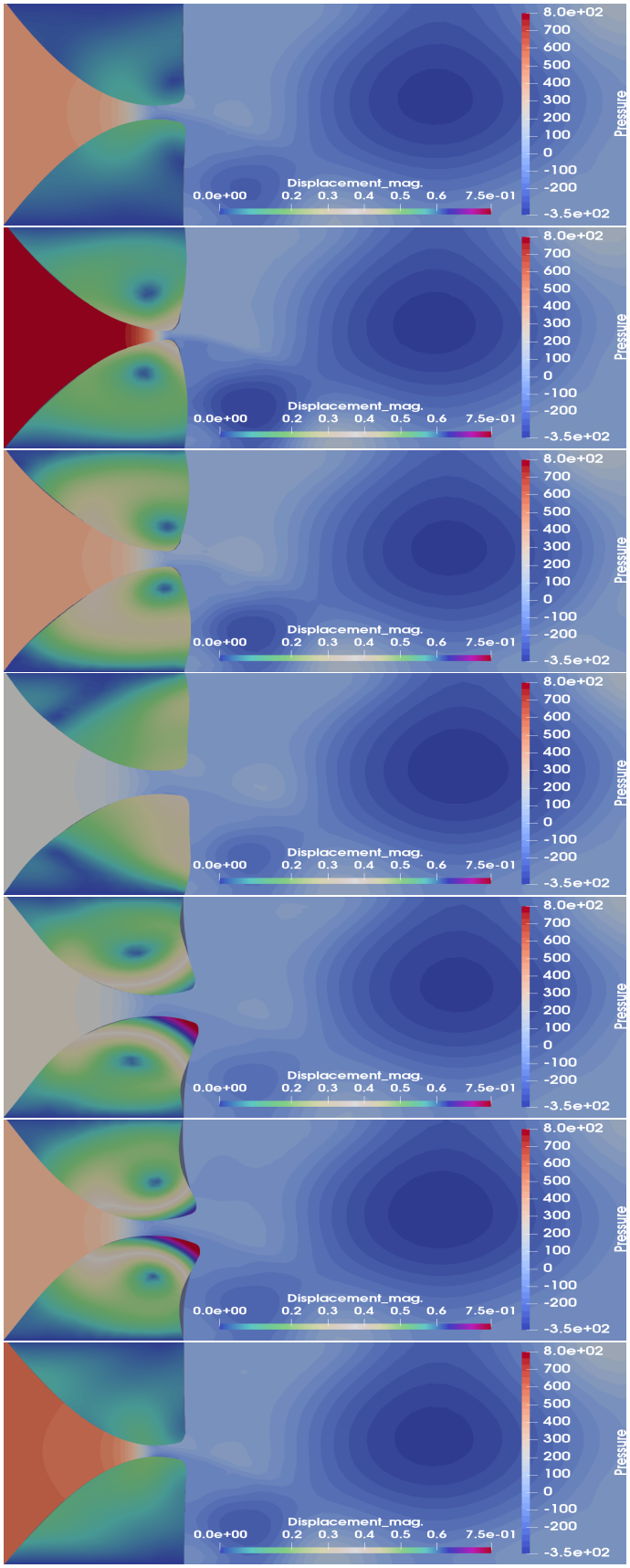


Figure 5.24: Airflow pressure and magnitude of the VF displacement in mm shown for seven time instants during one vibration cycle of VFs with duration of approx. 7 ms. Simulation of case *PEN-W*. Only the selection of the CFD domain is plotted.

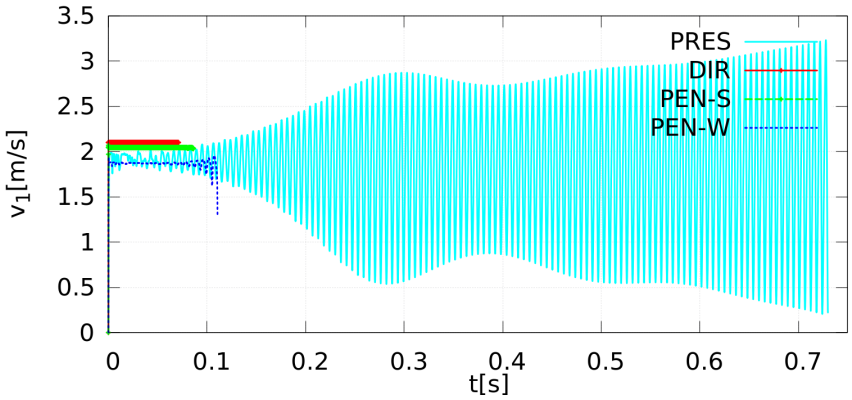


Figure 5.25: The numerically simulated inlet airflow velocity plotted for cases *VEL*, *PEN-S*, *PEN-W* and *PRES*, the values are averaged over boundary $\Gamma^f_{\text{In}}$.

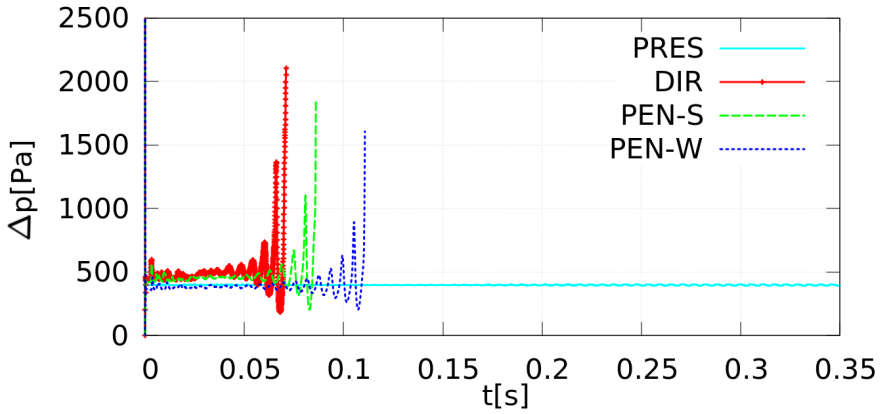


Figure 5.26: The numerically simulated pressure difference between the inlet and the outlet of the channel for cases *VEL*, *PEN-S*, *PEN-W* and *PRES*.

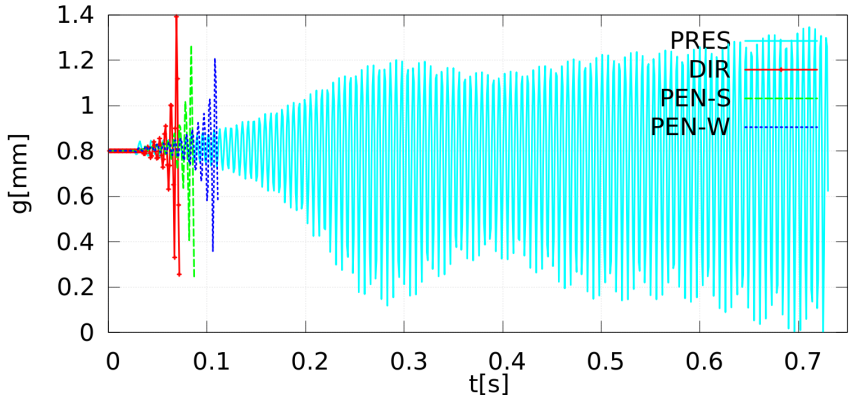


Figure 5.27: Time development of the (whole) gap numerically simulated for cases *VEL*, *PEN-S*, *PEN-W* and *PRES*. (The graph envelope of case *PRES* is undulated due to too low sampling rate of the data saving for drawings.)

# Chapter 6

# Mathematical models of acoustic and aeroacoustic problems

This chapter is devoted to the mathematical modelling of acoustic problems with focus on aeroacoustics. The first section introduces the aeroacoustics and the hybrid approach established by acoustic analogies or perturbation equations. In the second section the coupling of acoustics with structural or flow problems are given. We start now with the description of computational domain $\Omega^a$ for solution of the acoustic problem in a vocal tract model.

## Acoustic domain

Let us consider simplified 2D acoustical domain $\Omega^a$ composed of two subdomains $\Omega^a_{\text{prop}}, \Omega^a_{\text{pml}}$, i.e. $\overline{\Omega^a} = \overline{\Omega^a_{\text{prop}}} \cup \overline{\Omega^a_{\text{pml}}}$. The domain of acoustic propagation $\Omega^a_{\text{prop}}$ consists of three parts $\Omega^a_{\text{src}}, \Omega^a_{\text{tract}}$ and $\Omega^a_{\text{free}}$, i.e. $\overline{\Omega^a_{\text{prop}}} = \overline{\Omega^a_{\text{src}}} \cup \overline{\Omega^a_{\text{tract}}} \cup \overline{\Omega^a_{\text{free}}}$, see Figure 6.1. Here, $\Omega^a_{\text{src}}$ is the domain, where the acoustic sources are evaluated from the simulated flow field. The deformation of acoustic domain $\Omega^a_{\text{src}}$ is neglected and it equals to the reference fluid domain, i.e. $\Omega^a_{\text{src}} = \Omega^f_{\text{ref}}$. Domain $\Omega^a_{\text{tract}}$ represents the vocal tract geometry and domain $\Omega^a_{\text{free}}$ models outer space, i.e. a free field region (of acoustic propagation). Finally, the perfectly matched layer (PML) domain $\Omega^a_{\text{pml}}$ encloses domain $\Omega^a_{\text{free}}$ in order to absorb the outgoing sound waves at the free boundaries of the acoustic domain, i.e. at boundaries of the free field region. The acoustic problem is described in the Lagrangian coordinates although coordinates notation $x$ instead of previously introduced $X$ is used.

The problem of sound propagation is solved in the whole domain $\Omega^a$ with boundary $\partial\Omega^a$, which is assumed to be Lipschitz continuous. Boundary $\partial\Omega^a$ is divided in two parts $\partial\Omega^a = \Gamma^a_{\text{hard}} \cup \Gamma^a_{\text{soft}}$, where sound hard and sound soft boundary conditions are considered (in what follows $\Gamma^a_{\text{soft}} = \emptyset$). Further, the sound propagation is always solved without the previously used symmetry assumption, thus the boundary part $\Gamma^f_{\text{Sym}} \subset \Gamma^a_{\text{hard}}$ is considered to be empty.

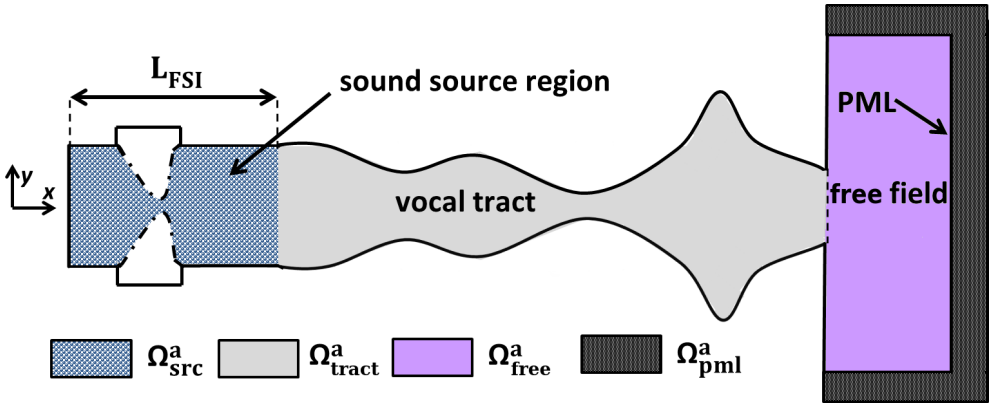


Figure 6.1: Scheme of acoustic domain. The propagation domain consists of the sound source region, the vocal tract and the free field. The propagation region is enclosed by the PML region. By $L_{\mathrm{FSI}}$ is denoted the length of fluid part of the FSI domain.

## 6.1 Aeroacoustics

Acoustics studies mechanical (acoustic) waves in various media (liquids, gases, solids or structures) while aeroacoustics is interested in aerodynamically produced sound in air. Typical situation is the sound generated by flow around obstacles, turbulent flows or mixing shear layers, see e.g. [90], [78].

The flow-induced sound propagation can be described by the compressible Navier–Stokes equations (NSE) which in general describes all aspects of fluid flow including acoustics. However the acoustic part is only a very tiny component of the overall NSE solution, see e.g. [79], and thus it is very difficult to approximate it numerically. The solution of compressible NSE, where the acoustic and the flow fields are solved together, restricts usually the simulations only to simple scenarios, see e.g. [65]. Consequently in the technical applications hybrid methodologies have been established as the most practical methods for aeroacoustic computations, see [90]. They separate the description of the fluid flow and the acoustic problem. This allows to use different numerical schemes for the flow and for the acoustic computations with benefits. Nevertheless by utilizing the hybrid approach the influence of the acoustic field on the flow field is neglected.

There are two families of hybrid methods based on either acoustic analogies or perturbation equations, [128]. The difference between the acoustic analogies and the perturbation equations is such that in the case of acoustic analogies the NSE are first reformulated to wave equation shifting the nonlinear parts to the right hand side and then these parts are linearized. For the perturbation equations approach the NSE are first decomposed in acoustic and hydrodynamic[1] components and then linearized into an equation similar to the wave equation. The linearization in both

[1]By the hydrodynamic components we mean generally the (flow) components, which perturbations are not connected with the change of density as a primary physical quantity describing the propagation of acoustic waves, see e.g. [70]. An example of the hydrodynamic quantity could be a change of the pressure caused by creation of a vortex in the incompressible fluid flow regime.

cases has to be performed carefully in order to identify main sound mechanisms, see [78].

Even though the hybrid approaches simplify the solution of the acoustic problems, still there are a lot of difficulties connected with any numerical realization of aeroacoustic problem, which has to be overcome in order to get an effective and accurate computation of the radiated sound, see [90, 41, 69]:

- **Energy disparity and acoustic inefficiency**. Only a very small part of the overall energy of the fluid flow transforms into the radiated acoustic energy. As formulated by Crighton: *" The total energy radiated as sound during take-off roll of the "terrifyingly loud"Boeing 707 is only about enough to cook one egg!"*, see [41]. For free turbulence (described by the quadrupole sound source) the total radiated acoustic power scales with $O(\frac{v^8}{c^5})$ for $c$ being the speed of sound and $v$ magnitude of the characteristic flow velocity, see [96]. The presence of a reflecting boundary in the acoustic domain can significantly change the amount of radiated sound, e.g. typical case of flow impinging on the solid wall (described by dipole source structure) produces sound with the radiated acoustic power scaling $O(\frac{v^6}{c^3})$, see [79].

- **Length scale disparity**: Large disparity also occurs between the size of an eddy in turbulent flow and the wavelength of the generated acoustic noise, see [41]. Let a turbulent eddy have a characteristic length scale $l$ and a frequency $f$ in a flow with low Mach number defined as $\mathrm{Ma} = \frac{v}{c}$. This eddy radiates acoustic waves of the same characteristic frequency, but with much larger wavelength $\lambda$ given as

$$\lambda = \frac{c}{f} \approx l \ \frac{v}{f\,l} \ \frac{c}{v} = \frac{l}{\mathrm{Ma}\,\mathrm{St}}. \tag{6.1}$$

  where $\mathrm{St} = \frac{f\,l}{v}$ is the Strouhal number with $f$ denoting characteristic frequency of flow disturbances, i.e. flow-induced sound, [90]. Estimation (6.1) underlines the fact that a turbulent eddy can radiate sound of one or more magnitude larger wavelength than its length scale $l$, see [53]. For example a turbulent eddy with $l = 1\,\mathrm{mm}$ in the larynx with the flow characteristics $\mathrm{Ma} = 0.05$ and $\mathrm{St} = 0.2$ produces approximately sound waves of hundred times larger wavelength $\lambda = 10\,\mathrm{cm}$.

- **Preservation of multipole character**: The numerical computation must preserve the multipole structure of acoustic sources (see definition in Section 2.4) in order to correctly simulate acoustic radiation characteristics, see [41]. The acoustic power radiated by each multipole component scales differently, see e.g. the first point of this list.

- **Dispersion and dissipation**: The discrete form of the wave equation introduces the dispersion of acoustic waves while the original continuous solution of the wave equation is non-dispersive. The numerical approximation of the wave equation must minimize the (numerical) dissipative errors, as the wave equation itself has a non-dissipative behaviour and both the amplitude as well as the phase of acoustic wave are of crucial importance, see [69].

- **Simulation in unbounded domains**: Since numerical methods are usually based on domain discretization, the simulations in unbounded domains must rely on truncating of the computational domain by an artificial boundary. The application of boundary conditions at the artificial boundary avoiding a reflection of outgoing waves remains an open problem, see [103].

- **Other issues:** Problems like numerical simulation of high Reynolds number flows, influence of acoustic nonlinearity, etc. needs to be adressed, see [90, 69].

The recent aeroacoustic methods can overcome only some of these numerical and physical issues, see [90]. Nevertheless the hybrid methods has a great advantage of possible application of solver tailored for acoustic problems. Thus the energy and the length scale disparities (and other points of the list) do not pose so difficult problem as in the case of full NSE solution.

In next paragraph the Lighthill acoustic analogy, as a representant of acoustic analogies class, is described. Further, two approaches based on the perturbations equations are presented, see [91]. In the end the acoustic boundary conditions are discussed and the PML approach is described.

### 6.1.1 Lighthill analogy

The Lighthill analogy was introduced by sir Lighthill in [96]. In this section the Lighthill analogy is presented as described in [79].

The sound propagation, i.e. density fluctuations, in uniform medium is governed by the classical wave equation, see [103]. Similarly the acoustic propagation in the fluid flow domain should be described by the same equation while keeping valid the description by the compressible NSE. How are these two descriptions compatible and how is the (aero)acoustics driven? According to sir Lighthill, [96]: *"The difference between the two sets of equations will be considered as if it were the effect of a fluctuating external force field, known if the flow is known, acting on the said uniform acoustic medium at rest, and hence radiating sound in it according to the ordinary laws of acoustics."* In what follows it is described how to determine this hypothetical external force field.

Let us assume a small domain $\Omega_t^f$ with flow described by velocity $\mathbf{v}$ and fluctuating pressure $p' = p - p_0$ and fluctuating density $\rho' = \rho - \rho_0$ inside a large fluid volume $\Omega^a_{\text{prop}}$ at rest with the mean density $\rho_0$, the mean pressure $p_0$ and the speed of sound $c_0$, see Figure 6.2.

We start with equation of momentum conservation (3.19) written as

$$\frac{\partial \rho v_i}{\partial t} + \frac{\partial \pi_{ij}}{\partial x_j} = 0, \tag{6.2}$$

where $\boldsymbol{\pi} = (\pi_{ij})$ denotes the tensor of momentum flux given by

$$\pi_{ij} = \rho v_i v_j + (p - p_0)\delta_{ij} - \tau^f_{ij}, \tag{6.3}$$

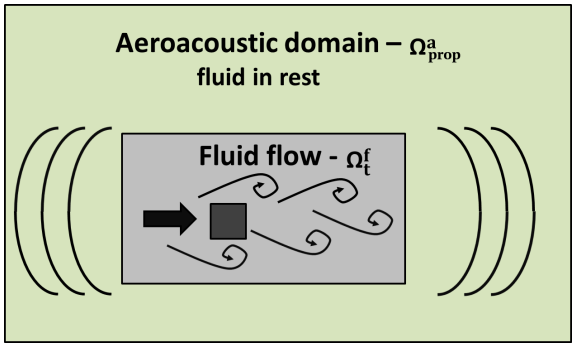


Figure 6.2: Scheme of a large acoustic domain $\Omega^a_{\text{prop}}$ with small region $\Omega^f_t$ inside it, where a fluid flow appears and generates sound waves.

and tensor $\boldsymbol{\tau}^f = \tau^f_{ij}$ denotes components of the viscous fluid stress tensor, see its definition (3.22).

First, we derive the equations describing the fluid motion (waves) **outside the fluid flow domain**. For the fluid in rest the momentum flux $(\pi_{ij})$ simplifies to $(\pi^0_{ij})$ as

$$\pi^0_{ij} = (p - p_0)\delta_{ij} \doteq c_0^2(\rho - \rho_0)\delta_{ij}, \tag{6.4}$$

where relation $(p-p_0) \doteq c_0^2(\rho-\rho_0)$ valid for isentropic flow was used, see [79]. Using equation (6.4) in (6.2) we get the conservation of momentum written as

$$\frac{\partial(\rho v_i)}{\partial t} + \frac{\partial}{\partial x_i}\left(c_0^2(\rho - \rho_0)\right) = 0, \tag{6.5}$$

and similarly we write the mass conservation law (3.18) in the form

$$\frac{\partial}{\partial t}(\rho - \rho_0) + \frac{\partial \rho v_i}{\partial x_i} = 0. \tag{6.6}$$

By differentiating equation (6.5) with respect to $x_i$, equation (6.6) with respect to $t$ and by subtracting of the differentiated equations we get

$$\left(\frac{1}{c_0^2}\frac{\partial^2}{\partial t^2} - \Delta\right)(p - p_0) = 0, \tag{6.7}$$

where the replacement of $c_0^2(\rho - \rho_0)$ by $p - p_0$ was used again. Equation (6.7) is the wave equation for the unknown pressure fluctuation $p' = p - p_0$ describing sound propagation in the domain $\Omega^a_{\text{prop}} \setminus \Omega^f_t$.

Let us consider now **the sound propagation inside** $\Omega^f_t$, where the fluid flow needs to be taken into an account. Particularly we shall consider the full version of the momentum flux tensor $\boldsymbol{\pi}$. Consider again $\pi^0_{ij} = (\rho - \rho_0)\delta_{ij}$ and add the term $\frac{\partial \pi^0_{ij}}{\partial x_j}$ to both sides of equation (6.2), which yields

$$\frac{\partial \rho v_i}{\partial t} + \frac{\partial \pi^0_{ij}}{\partial x_j} = -\frac{\partial(\pi_{ij} - \pi^0_{ij})}{\partial x_j}, \tag{6.8}$$

where on the right hand side the so-called Lighthill tensor $\mathbf{T} = (T_{ij})$ arises[2] given by

$$T_{ij} = \pi_{ij} - \pi_{ij}^0 = \rho v_i v_j + \big((p - p_0) - c_0^2(\rho - \rho_0)\big)\,\delta_{ij} - \tau_{ij}^f. \tag{6.9}$$

Using the same trick as above with the mass conservation equation yields the inhomogeneous wave equation for the unknown pressure fluctuation $p' = p - p_0$

$$\left(\frac{1}{c_0^2}\frac{\partial^2}{\partial t^2} - \Delta\right)(p - p_0) = \frac{\partial^2 T_{ij}}{\partial x_i \partial x_j}, \tag{6.10}$$

where on the right hand side the sound sources are given by the divergence of the divergence of the Lighthill tensor. Let us emphasize that equation (6.10) is nonlinear equation as its right hand also depends on the pressure fluctuation $p'$, see equation (6.9). As solution of the Lighthill analogy in formulation (6.10) is difficult, the sound sources on the right hand side are in practice simplified.

### Sound source structure

In order to approximate the Lighthill tensor we start with a description of the sound sources structure. The full Lighthill tensor can be written as sum of three terms

$$T_{ij} = \underbrace{\rho v_i v_j}_{\text{I}} + \underbrace{\big((p - p_0) - c_0^2(\rho - \rho_0)\big)\,\delta_{ij}}_{\text{II}} - \underbrace{\tau_{ij}^f}_{\text{III}}, \tag{6.11}$$

where the term denoted by I corresponds to the fluid motion, the second term II is generally associated with non-isentropic processes and the third term III is linked with the viscous stresses, see e.g. [96], [91]. For low Mach number flows usually the approximation

$$T_{ij} \approx \rho_0 v_i v_j \tag{6.12}$$

is used, which was already suggested in the original paper [96]. Then the formulation of Lighthill analogy (6.10) with (6.12) already presents linear problem:

$$\left(\frac{1}{c_0^2}\frac{\partial^2}{\partial t^2} - \Delta\right)p' = \rho_0 \frac{\partial^2 v_i v_j}{\partial x_i \partial x_j}. \tag{6.13}$$

An alternative way how to approximate Lighthill tensor (6.9) in the case of the incompressible flow is to rewrite momentum conservation (3.20) and neglect the viscous terms (assuming zero volume forces) what yields

$$\rho_0 \nabla \cdot \big(\mathbf{v}^{\mathrm{ic}} \otimes \mathbf{v}^{\mathrm{ic}}\big) \doteq -\rho_0 \frac{\partial \mathbf{v}^{\mathrm{ic}}}{\partial t} - \nabla p^{\mathrm{ic}}, \tag{6.14}$$

[2]The divergence of the Lighthill tensor – see the right hand side of equation (6.8), is actually the sought hypothetical external force field, see [96].

where by the top index $ic$ are denoted the quantities obtained from the incompressible flow simulation, where the (fluid) density $\rho$ is assumed to be constant $\rho = \rho_0$. Then applying the divergence operator on equation (6.14) gives the sound sources of the form

$$\operatorname{div}\operatorname{div}\mathbf{T} \doteq \rho_0 \nabla \cdot \left(\nabla \cdot \left(\mathbf{v}^{\mathrm{ic}} \otimes \mathbf{v}^{\mathrm{ic}}\right)\right) = -\Delta p^{\mathrm{ic}}, \tag{6.15}$$

because for the incompressible case is $\nabla \cdot \mathbf{v}^{\mathrm{ic}} = 0$ as well as $\nabla \cdot \left(\frac{\partial \mathbf{v}^{\mathrm{ic}}}{\partial t}\right) = 0$. Expression (6.15) presents another possibility how to express sound sources, here purely from the pressure field, see [117], [90].

#### Properties of Lighthill analogy

The advantage of the Lighthill analogy given by (6.10) is that it was derived without any additional assumptions or approximations. Thus it is also called exact equation (in physical sense), because its (possible) exact solution would contain acoustic nonlinear effects as the convection of sound waves by the mean flow velocity, the refraction or the sound attenuation, see [78]. In order to model the concrete sound generation mechanism the general formulation can be further adapted by the choice of proper approximation of Lighthill tensor (6.11).

The drawback of the Lighthill analogy is, that the pressure fluctuation $p'$ is in general not equal to the acoustic pressure $p^a$ and they coincide only outside the flow domain. It is because the pressure fluctuation $p'$ must be regarded as a superposition of the acoustic and the hydrodynamic pressure inside the source region, see e.g. [79]. In this context by the hydrodynamic pressure is meant the pressure of the incompressible flow solution, i.e. one fluctuating component of the overall pressure solution of the compressible fluid flow problem, see [90]. The demonstrative examples of difference between $p'$ and $p^a$ can be found in [90].

### 6.1.2 Hybrid methods based on perturbation equations

Here, the perturbed convective wave equation (PCWE) and the aeroacoustic wave equation (AWE) approaches are presented, which are based on the acoustic/hydrodynamic splitting of the flow variables as introduced in works of [82] and [172]. The splitting according to these works is motivated by three properties of the acoustic field: a) it is fluctuating, b) it is irrotational[3] and c) the acoustic pressure $p^a$ does not coincide in general with pressure fluctuations $p'$, see [82], [91].
The proposed splitting decomposes physical quantities into time mean $\overline{\mathbf{v}}, \overline{p}, \overline{\rho}$ and fluctuating parts $\mathbf{v}', p', \rho'$. The fluctuating parts $\mathbf{v}', p', \rho'$ are further split into vortical (non-acoustic) components $\mathbf{v}^{\mathrm{v}}, p^{\mathrm{v}}$ and compressible (acoustic) parts $\mathbf{v}^a, p^a, \rho^a$.

[3] More precisely the (linear) acoustic field in an uniform acoustic medium is irrotational, see [119].

This splitting reads

$$\begin{aligned} \mathbf{v} &= \overline{\mathbf{v}} + \mathbf{v}'(t) = \overline{\mathbf{v}} + \mathbf{v}^{\mathrm{v}}(t) + \mathbf{v}^{a}(t), \\ p &= \overline{p} + p'(t) = \overline{p} + p^{\mathrm{v}}(t) + p^{a}(t), \\ \rho &= \overline{\rho} + \rho'(t) = \overline{\rho} + \rho^{1}(t) + \rho^{a}(t), \end{aligned} \tag{6.16}$$

where $\rho^1$ represents the density change due to the hydrodynamic pressure perturbation estimated as $\rho^1 \approx \frac{p^{\mathrm{ic}} - \overline{p^{\mathrm{ic}}}}{c_0^2} = \frac{p^{\mathrm{v}}}{c_0^2}$, see page 82 in [82]. The splitting of velocities is based on the Helmholtz decomposition of velocity field, see e.g. [106], (or more generally the Helmholtz-Hodge decomposition, see [129, 92, 128]), i.e. the velocity field can be expressed as the sum of an irrotational, a solenoidal and a harmonic field. The solenoidal field $\mathbf{v}^{\mathrm{v}}$ is divergence-free ($\nabla \cdot \mathbf{v}^{\mathrm{v}} = 0$), the irrotational field $\mathbf{v}^a$ is curl-free ($\nabla \times \mathbf{v}^a = \mathbf{0}$) and the harmonic field being divergence-free and curl-free. The splitting approach is problematic in regard of the interpretation of the pressure and the density components because it is unclear how to separate (explicitly) the hydrodynamic pressure fluctuations from the acoustic ones, see [82] and [127].

### Derivation of perturbation equations

First, we start with the momentum conservation equation. Subtracting incompressible momentum equation (3.25) from equation (3.20), where the incompressible quantities are taken as $\mathbf{v}^{\mathrm{ic}} = \overline{\mathbf{v}} + \mathbf{v}^{\mathrm{v}}$, $p^{\mathrm{ic}} = \overline{p} + p^{\mathrm{v}}$, using splitting (6.16) in momentum conservation (3.20), and neglecting the nonlinear term $(\mathbf{v}^a \cdot \nabla)\mathbf{v}^a$ and the (first) volume viscosity $\lambda^f$ term in the fluid stress tensor $\boldsymbol{\sigma}^f$ results in

$$\frac{\partial \mathbf{v}^a}{\partial t} + (\mathbf{v}^a \cdot \nabla)(\overline{\mathbf{v}} + \mathbf{v}^{\mathrm{v}}) + ((\overline{\mathbf{v}} + \mathbf{v}^{\mathrm{v}}) \cdot \nabla)\mathbf{v}^a + \frac{\nabla p}{\rho} - \frac{1}{\overline{\rho}} \nabla p^{\mathrm{ic}} = 0. \tag{6.17}$$

In equation (6.17) we use the approximation

$$\frac{\nabla p}{\rho} - \frac{\nabla p^{\mathrm{ic}}}{\overline{\rho}} \approx \frac{\nabla p^a}{\overline{\rho}} \tag{6.18}$$

valid for adiabatic processes, see e.g. [53]. We neglect the coupling of vortical and acoustic quantities, see analysis [135][4], and we apply the approximation

$$(\overline{\mathbf{v}} \cdot \nabla)\mathbf{v}^a + (\mathbf{v}^a \cdot \nabla)\overline{\mathbf{v}} = \nabla(\overline{\mathbf{v}} \cdot \mathbf{v}^a) + \nabla \times \overline{\mathbf{v}} \times \mathbf{v}^a + \underbrace{\nabla \times \mathbf{v}^a \times \overline{\mathbf{v}}}_{=0} \approx \nabla(\overline{\mathbf{v}} \cdot \mathbf{v}^a), \tag{6.19}$$

where the last term is zero due to the assumption of irrotational acoustic field and the second term is neglected as the unwanted coupling between the mean flow vorticity and the acoustic velocity. This finally leads to the first perturbation equation for the acoustic velocity and the acoustic pressure

$$\frac{\partial \mathbf{v}^a}{\partial t} + \nabla(\overline{\mathbf{v}} \cdot \mathbf{v}^a) + \frac{1}{\overline{\rho}} \nabla p^a = 0. \tag{6.20}$$

[4] For low Mach number flows the coupling of the vortical and other quantities does not contribute to acoustics and it presents only a possible source of simulation instability.

The **second perturbation equation** is based on mass conservation equation (3.18). First, using decomposition (6.16) in mass conservation (3.18) provides us

$$\begin{aligned}\frac{\partial \rho^a}{\partial t} + \nabla \cdot \left(\overline{\rho}\mathbf{v}^a + \rho^a\overline{\mathbf{v}} + \rho^a\mathbf{v}^a\right) = \\ = -\frac{\partial \rho^1}{\partial t} - \nabla \cdot \left(\rho^1\overline{\mathbf{v}}\right) - \mathbf{v}^{\mathrm{v}} \cdot \nabla\left(\overline{\rho} + \rho'\right) - \nabla \cdot \left(\rho^1\mathbf{v}^a\right) - \nabla \cdot \left(\overline{\rho}\,\overline{\mathbf{v}}\right).\end{aligned} \tag{6.21}$$

Further, the time average of equation (3.18) yields

$$0 = \overline{\frac{\partial \rho}{\partial t}} + \overline{\nabla \cdot (\rho\mathbf{v})} = \overline{\mathbf{v}^{\mathrm{v}} \cdot \nabla\rho'} + \overline{\nabla \cdot (\rho^1\mathbf{v}^a)} + \nabla \cdot (\overline{\mathbf{v}}\,\overline{\rho}), \tag{6.22}$$

see also [82], page 84. Suming up equations (6.21) and (6.22) together leads to

$$\frac{\partial \rho^a}{\partial t} + \nabla \cdot (\overline{\rho}\mathbf{v}^a) + \nabla \cdot (\rho^a\overline{\mathbf{v}}) = -\frac{\partial \rho^1}{\partial t} - \nabla \cdot \left(\rho^1\overline{\mathbf{v}}\right) - (\mathbf{v}^{\mathrm{v}} \cdot \nabla\rho')' - \nabla \cdot \left(\rho^1\mathbf{v}^a\right)' - \mathbf{v}^{\mathrm{v}} \cdot \nabla\overline{\rho}, \tag{6.23}$$

where the nonlinear term $\nabla \cdot (\rho^a\mathbf{v}^a)$ was neglected and by $(\cdot)'$ the fluctuating part of the term in bracket is denoted. In this work we are mostly interested in the sound generated for low Mach number regime, where the fluid flow can be considered incompressible. Thus the mean density is constant $\overline{\rho} = \rho_0 = const$, further $\nabla \cdot \overline{\mathbf{v}} = 0$ holds and equation (6.23) turns into

$$\frac{\partial \rho^a}{\partial t} + \rho_0\,\nabla \cdot \mathbf{v}^a + \overline{\mathbf{v}} \cdot \nabla\rho^a = -\frac{\partial \rho^1}{\partial t} - \overline{\mathbf{v}} \cdot \nabla\rho^1, \tag{6.24}$$

where the terms $\nabla \cdot (\rho^1\mathbf{v}^a)'$ and $(\mathbf{v}^{\mathrm{v}} \cdot \nabla\rho')'$ were neglected as insignificant, for details see [82] page 92.

Equation (6.24) can be rewritten for the unknown acoustic pressure instead of the acoustic density by assuming isentropic process $p' - c_0^2\rho' = const$ and by introducing the notation for incompressible quantities as earlier $\mathbf{v}^{\mathrm{ic}} = \overline{\mathbf{v}} + \mathbf{v}^{\mathrm{v}}$, $p^{\mathrm{ic}} = \overline{p} + p^{\mathrm{v}}$ to the final form

$$\frac{\partial p^a}{\partial t} + c_0^2\rho_0(\nabla \cdot \mathbf{v}^a) + \overline{\mathbf{v}} \cdot \nabla p^a = -\frac{\partial p^{ic}}{\partial t} - \overline{\mathbf{v}} \cdot \nabla p^{ic}. \tag{6.25}$$

The perturbation equations (6.20) and (6.25) represents system of one scalar and one vector PDE for unknown $p^a$ and $\mathbf{v}^a$.

### Perturbed convective wave equation

The formulation given by equations (6.20) and (6.25) can be rewritten in one scalar equation with the help of the substantial derivative $\frac{D}{Dt} = \frac{\partial}{\partial t} + \overline{\mathbf{v}} \cdot \nabla$ and the introduction of acoustic potential[5] $\psi^a$ related to acoustic velocity $\mathbf{v}^a$ by relation $\mathbf{v}^a = -\nabla\psi^a$. Then replacing $\mathbf{v}^a$ by acoustic potential in equation (6.20) leads to the expression

[5]The possibility to introduce the acoustic potential is based on initial assumption of the irrotational acoustic velocity. Then there exists a scalar potential associated to it.

for $p^a = \rho_0 \frac{\partial \psi^a}{\partial t} + \rho_0 \overline{\mathbf{v}} \cdot \nabla \psi^a = \rho_0 \frac{D\psi^a}{Dt}$. Equation (6.25) after the substitution for $p^a$ can be transformed to

$$\frac{1}{c_0^2} \frac{D^2 \psi^a}{Dt^2} - \Delta \psi^a = -\frac{1}{\rho_0 c_0^2} \frac{Dp^{\mathrm{ic}}}{Dt}. \tag{6.26}$$

This equation is according to [91] called perturbed convective wave equation (PCWE).

**Remark.** In numerical simulations we further simplify PCWE equation by disregarding the convection effects on the left-hand side of equation (6.26). On the other hand in order to incorporate sound sources arising in the glottis connected with steady pressure gradient the full version of the right hand side is used, see [2][6]. Therefore the sound sources given by right hand side of (6.26) will be referred as *PCWE* sources but the acoustic pressure obtained as the solution of (6.26) will be referred as the simplified PCWE (*sPCWE*).

### Aeroacoustic wave equation

Aeroacoustic wave equation (AWE) is further simplification of the PCWE formulation given by equations (6.20) and (6.25). In this simplification the influence of the mean flow velocity is completely omitted, i.e. small Mach number flows are supposed and the supposedly small convection effects are completely disregarded $\overline{\mathbf{v}} = \mathbf{0}$. By differentiation (6.20) with respect to $x_i$ and by differentiation (6.25) with respect to $t$ and subtracting both the modified equations we obtain the final formulation of AWE

$$\frac{1}{c_0^2} \frac{\partial^2 p^a}{\partial t^2} - \Delta p^a = -\frac{1}{c_0^2} \frac{\partial^2 p^{\mathrm{ic}}}{\partial t^2}, \tag{6.27}$$

where $p^a$ is the acoustic pressure and $p^{\mathrm{ic}}$ is the pressure obtained by incompressible simulation, see [91] or [117].

**Remark.** Equation (6.27) can be also obtained from Lighthill analogy (6.10) by substituting the second spatial derivative of the Lighthill tensor by the Laplacian of the flow pressure – see equation (6.15) (assuming incompressible fluid flow simulation). Using the decomposition of the fluctuating pressure $p' = p^v + p^a$ in (6.10) then yields (6.27), see [91]. It shows the connection of both theories under additional assumptions, see e.g. [128].

### Properties of perturbation equations

The advantage of the PCWE and the AWE approach is that these are direct formulations for the acoustic pressure (or the acoustic potential) what allows to obtain also the acoustic field inside sound source domain $\Omega^a_{\mathrm{src}}$, see examples in [90]. However both PCWE and AWE are designed to model only sound production for low Mach

[6] In the published version of [2] is unfortunately a mistake in the wrong replacement of $\frac{D^2}{Dt^2}$ by $\frac{\partial^2}{\partial t^2}$ in the full version of PCWE equation, see equation (16) in [2].

number flows. In other cases the so called Acoustic Perturbation Equations (APEs) needs to be used, see [53], [128].

Another advantage of PCWE approach is its stability contrary to linearized Euler equations (LEE), see e.g. [28]. The LEE approach, where the decomposition only into the mean and the fluctuating components is used, has no guaranty that the perturbation quantities are purely acoustic quantities, e.g. $\nabla \times \mathbf{v}' \neq \mathbf{0}$. Therefore LEE approach describes also the transport of vortical components, which can cause numerical instability, see [135]. The stability of PCWE follows from proposed splitting (6.16) and the derivation procedure, where the convection of the vorticity perturbations is prevented, see [53][7].

### 6.1.3 Initial and boundary conditions of acoustics

The acoustic problem needs to be equipped by the initial and the boundary conditions. For simplicity zero initial conditions are used.

At boundary of the acoustic domain $\Gamma^a_{\text{hard}}$ the sound hard boundary condition is applied

$$\frac{\partial \psi}{\partial \mathbf{n}^a}(x,t) = 0 \qquad \text{for } x \in \ \Gamma^a_{\text{hard}},\ t \in (0,\mathrm{T}), \tag{6.28}$$

where $\mathbf{n}^a$ denotes the outward unit normal and by $\psi(x,t)$ the relevant acoustic quantity is understood, i.e. either $\psi = p'$ in the case of Eq. (6.10) or $\psi = \psi^a$ in the case of Eq. (6.26) or $\psi = p^a$ in the case of Eq. (6.27) or $\psi = p^{\text{va}}$ in the case of vibroacoustic problem described later. The sound hard BC means that the sound waves are fully reflected at $\Gamma^a_{\text{hard}}$ back to acoustic domain $\Omega^a$. A real-life example of boundary with such ideal behaviour is a smooth concrete wall, while other materials evince much complex behaviour, usually with nonperfect reflection and frequency dependent characteristics. In order to treat such phenomena see dissertations [23, 144] or book [90].

Another frequently used BC is the sound soft boundary condition which reads

$$\psi(x,t) = 0, \qquad \text{for } x \in \ \Gamma^a_{\text{soft}},\ t \in (0,\mathrm{T}). \tag{6.29}$$

This BC prescribes zero value of the incident acoustic wave at boundary $\Gamma^a_{\text{soft}}$, which is fully reflected back to the acoustic domain with the opposite phase, see e.g. [33]. However this BC is sometimes used to model open boundary, typically in the case of open end of a resonator, see e.g. [115], where it can be understood as a rough, low frequency approximation, see [33]. In this thesis the boundaries of acoustic domain $\Omega^a$ are chosen as $\Gamma^a_{\text{soft}} = \emptyset, \Gamma^a_{\text{hard}} = \partial\Omega^a$ [8].

[7] The PCWE formulation is numerically equivalent to APEs, for which the stability is proven.

[8] A part of boundary $\partial\Omega^a$ is the boundary of the PML layer, where the choice of the boundary condition does not play any role, see e.g. [90]

### 6.1.4 Perfectly matched layer

Let us mention that the simulation of acoustic problems in unbounded domains, practically realized by truncating of the computational domain with an artificial boundary (see example in Figure 6.3 left) is still an open question. For the overview of various techniques dealing with these problems see e.g. book [103], and approaches like infinite elements, characteristics-based techniques, absorbing boundary conditions (ABC), exact non-local ABC, ETA method ([50]), etc. Here, the technique called perfectly matched layer is chosen, see [87].

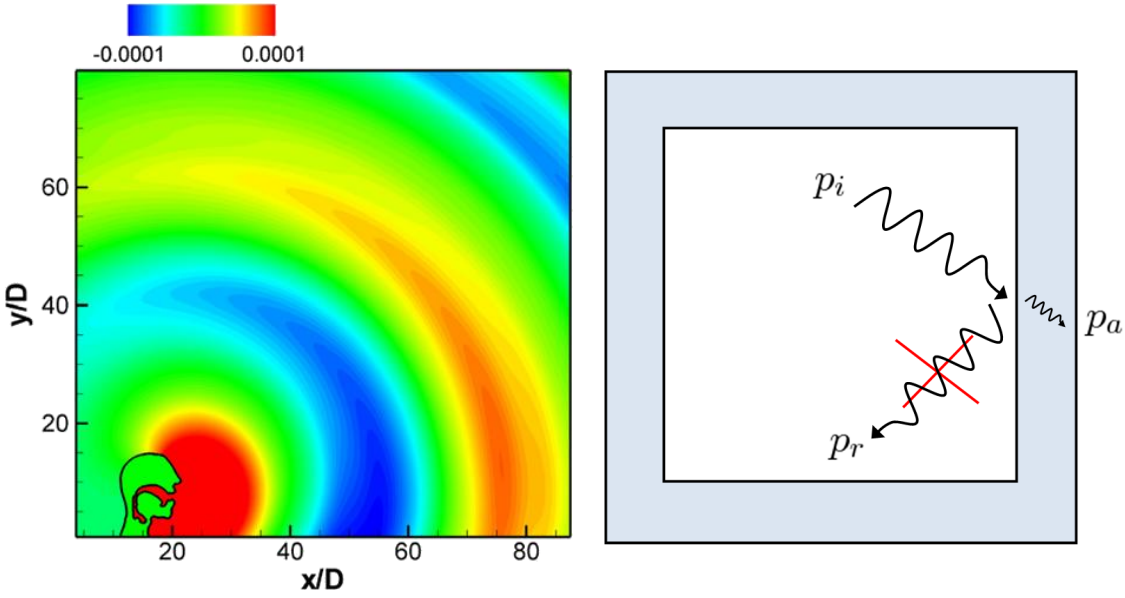


Figure 6.3: **Left:** Example of artificial domain truncation, where no unwanted reflections of acoustic waves occur at artificial boundaries. The picture is overtaken from [134] and it depicts the non-dimensionalized pressure fluctuations. **Right:** Schematic figure of acoustic domain enclosed by PML domain (gray area). As an incident wave $p_i$ impinges on the PML interface, it is (fully) absorbed ($p_a$) inside the PML and no reflected wave $p_r$ occurs, [23].

The perfectly matched layer (PML) is a technique for simulation of open-boundary problems introduced by Berenger in 1994, see [32]. PML consists of a few additional layers of elements with artificial damping of the sound waves. The most important property is that there is no reflection at the interface between the propagation domain and the PML domain as sketched in Figure 6.3 right.

The modified wave equation for unknown (acoustic) pressure $p$ inside PML domain $\Omega^a_{\text{pml}}$ according to [90] reads

$$\begin{aligned} \frac{1}{c^2}\frac{\partial^2 p}{\partial t^2} - \Delta p - \nabla \cdot \mathbf{u} + \alpha \frac{\partial p}{\partial t} + \beta p + \gamma v = 0, \\ \frac{\partial \mathbf{u}}{\partial t} + \mathbb{A}\mathbf{u} - \mathbb{B}\nabla p - \mathbb{C}\nabla v = \mathbf{0}, \\ \frac{\partial v}{\partial t} = p, \end{aligned} \tag{6.30}$$

where $\alpha, \beta, \gamma$ are positive coefficients, $\mathbb{A}, \mathbb{B}, \mathbb{C}$ are diagonal matrices depending on the chosen damping profiles $\sigma_x, \sigma_y, \sigma_z$ (see details e.g. in [23], [66]) acting in coordinate directions $x, y, z$ – see Figure 6.4, resp., and the vector $\mathbf{u}$ and the scalar $v$ are new auxiliary variables (needed for 3D PML formulation[9]). A more elegant formulation of PML given by the modified wave equation can be obtained in the frequency domain, see [90]. The time domain formulation[10] of PML given by (6.30), which requires in general four auxiliary scalar variables inside PML and no high order derivatives, is easy and efficient to implement in comparison with other possible formulations, see [66]. The proper choice of the damping profiles $\sigma_x, \sigma_y, \sigma_z$ is of great importance, especially in order to obtain a stable and efficient PML method, see analysis in paper [87]. In this thesis the inverse damping profile was chosen, see [90]. The PML implementation is a part of the CFS++ solver.

**Remark.** The direct derivation of PML formulation in the time domain, i.e. without transformation from the frequency domain, can be found e.g. in [32] or [94].

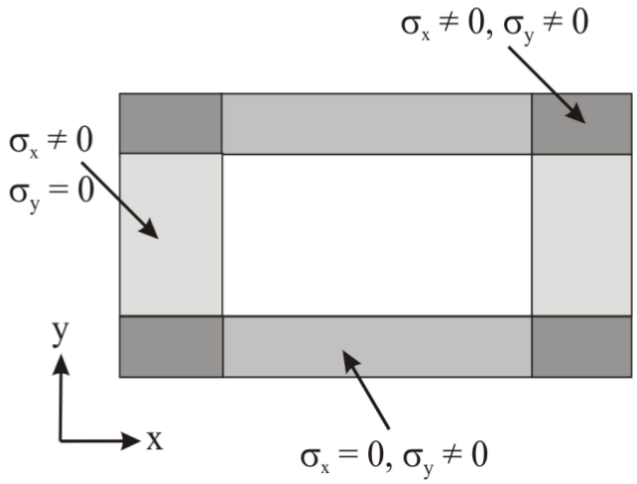


Figure 6.4: Sketch showing choice of 2D damping profiles, overtaken from [90]. The acoustic propagation domain is denoted by white and the PML layers representing enviroment behind open boundaries are depicted in gray. The setting e.g. $\sigma_x = 0$ means that the $x$-component of acoustic wave is not damped at given box. The damping profiles are not typically constants but coordinates dependent functions, see [90].

## 6.2 Coupled FSAI problems

In the FSAI problem the acoustic field is coupled with the FSI problem by the structure-acoustic and by the flow-acoustic couplings. For the sake of clarity these two subproblems are further considered as two different acoustic problems.

[9] In the 2D case of PML only the additional vector variable $\mathbf{u}$ with two components is needed.

[10] The transformation from the frequency domain to the time domain is performed by inverse Fourier transform. This is the reason why is the time domain PML formulation so demanding, [66].

### 6.2.1 Structure-acoustic coupling

The problem of the coupled elastic deformation and the sound propagation subproblems is also called vibroacoustics, see e.g. [68]. The vibroacoustic quantities are denoted by the upper index $^{\mathrm{va}}$. In the considered settings the vibroacoustic problem is given by elasticity equations (3.10) and by homogenous wave equation (2.13). The coupling has the form of boundary conditions on the common interface $\Gamma_{\mathrm{W_{ref}}}$, where from a nature of the problem the continuity of velocities and stresses in the normal direction is preserved.

From condition

$$(\frac{\partial \mathbf{u}}{\partial t} - \mathbf{v}^{\mathrm{va}}) \cdot \mathbf{n}^a = 0 \tag{6.31}$$

together with linearized momentum conservation of acoustics in the form $\frac{\partial \mathbf{v}^{\mathrm{va}}}{\partial t} = -\frac{1}{\rho^f}\nabla p^{\mathrm{va}}$ (see [90]) follows the boundary condition prescribed to the acoustic subproblem, see e.g. [90],

$$\frac{\partial p^{\mathrm{va}}}{\partial \mathbf{n}^a}(x,t) = -\rho^f \frac{\partial^2 \mathbf{u}}{\partial t^2} \cdot \mathbf{n}^a, \qquad x \in \Gamma_{\mathrm{W_{ref}}},\ t \in (0, \mathrm{T}). \tag{6.32}$$

This boundary condition expresses the acoustic emission from a vibrating surface represented by interface $\Gamma_{\mathrm{W_{ref}}}$ in the form of normal wall acceleration, see e.g. [90].

For the elastic problem the coupling is given by

$$\tau^s_{ij}\, n^s_j = p^{\mathrm{va}} n^s_i =: q^{\mathrm{va}}_i(X,t), \tag{6.33}$$

because there are no shear forces in the acoustic medium. Since the acoustic pressure is usually of a very tiny magnitude (high sound intensity of 100 dB corresponds to value of $p^a = 2\,\mathrm{Pa}$), the acting acoustic forces on the body surface are very small. Under additional assumption of different eigenfrequencies of the acoustic resonator (vocal tract) and the structure (VFs) this coupling can be omitted, see [90].

**Remark.** The time evolution of the VF interface represents another, geometric coupling which is usually disregarded due to negligible impact on the acoustic results, see e.g. [23]. An open and still unanswered questions remain how to approximate the dynamic process of glottis complete closure, how much does this process change resonant acoustic frequencies of vocal tract and how much it can potentially influence resulting acoustic spectra.

### 6.2.2 Flow-acoustic coupling

The acoustic waves are a part of the solution of the compressible NSE. However if the aeroacoustic problem is modelled by hybrid methods, acoustics and the fluid flow problem are solved separately, the sound sources from the fluid flow are used in the acoustics whereas the influence of acoustics onto the fluid flow is usually omitted.

**Remark.** There are special cases, when the hybrid approach is not suitable. This is for instance the case of the acoustically induced instability of the boundary layer known as Rossita modes, see e.g. [120]. Another example is the rare and atypical case

of self-sustained VF vibrations with the dominant frequency of VF oscillation close to the acoustic resonant frequency of the vocal tract, see [157]. Then the phenomena like various chaotic VF vibrations or abrupt frequency jumps of VF vibration were observed, see [157], [154], [167]. Further especially in the case of phonation into tubes the phonation onset threshold pressure can be significantly reduced due to complex flow-structure-acoustic coupling, see [74], [104].

### 6.2.3 FSAI formulations

Since for the aeroacoustic problem the hybrid approach is utilized here, the FSI problem can be solved first and the aeroacoustic simulation gets the form of post-processing of the FSI results. The sound sources are computed either according to the chosen acoustic analogy or based on the interface acceleration in the case of vibroacoustic problem. Further we assume uniform acoustic medium, i.e. $c_0, \rho_0$ are constants. The PML layer is applied in all considered cases inside the domain $\Omega^a_{\text{pml}}$.

As solution of **Lighthill analogy** it is considered a such function $p' \in C^2(\Omega^a_{\text{prop}} \times [0, \text{T}])$, that satisfies equation (6.13), i.e.

$$\left(\frac{1}{c_0^2}\frac{\partial^2}{\partial t^2} - \Delta\right) p' = \rho_0 \frac{\partial^2 v_i v_j}{\partial x_i \partial x_j}, \qquad \text{in } \Omega^a_{\text{prop}} \times (0, \text{T}),$$

together with zero initial conditions and boundary condition (6.28).

The formulation of *simplified* **PCWE approach** is very similar: Find a such function $\psi^a \in C^2(\Omega^a_{\text{prop}} \times [0, \text{T}])$ satisfying zero initial conditions and boundary condition (6.28) together with equation (6.26)

$$\frac{1}{c_0^2}\frac{\partial^2 \psi^a}{\partial t^2} - \Delta \psi^a = -\frac{1}{\rho_0 c_0^2}\frac{Dp^{ic}}{Dt}, \qquad \text{in } \Omega^a_{\text{prop}} \times (0, \text{T}), \tag{6.34}$$

where the substantial derivative is $\frac{D}{Dt} = \frac{\partial}{\partial t} + \overline{\mathbf{v}} \cdot \nabla$ and $\overline{\mathbf{v}}(x)$ means time averaged velocity.

Further, the formulation of **AWE approach** is following: Find such a function $p^a \in C^2(\Omega^a_{\text{prop}} \times [0, \text{T}])$ satisfying zero initial conditions and boundary condition (6.28) together with equation (6.27)

$$\frac{1}{c_0^2}\frac{\partial^2 p^a}{\partial t^2} - \Delta p^a = -\frac{1}{c_0^2}\frac{\partial^2 p^{ic}}{\partial t^2} \qquad \text{in } \Omega^a_{\text{prop}} \times (0, \text{T}).$$

In the case of purely **vibroacoustic problem** we seek such a function $p^{\text{va}} \in C^2(\Omega^a_{\text{prop}} \times [0, \text{T}])$, that equation (2.13)

$$\left(\frac{1}{c_0^2}\frac{\partial^2}{\partial t^2} - \Delta\right) p^{\text{va}} = 0, \qquad \text{in } \Omega^a_{\text{prop}} \times (0, \text{T}),$$

is fulfilled together with zero initial conditions and boundary condition (6.28) on $\partial\Omega^a$ with exception of boundary $\Gamma_{\text{W}_{\text{ref}}}$, where condition (6.32) is prescribed, i.e.

$$\frac{\partial p^{\text{va}}}{\partial \mathbf{n}^a}(x, t) = -\rho^f \frac{\partial^2 \mathbf{u}}{\partial t^2} \cdot \mathbf{n}^a, \qquad x \in \Gamma_{\text{W}_{\text{ref}}},\ t \in (0, \text{T}).$$

# Chapter 7

# Numerical approximations of acoustic problems

•This chapter describes the numerical realization of aeroacoustic and vibroacoustic problems introduced in the previous chapter. Further, the individual steps of the FSAI approximation algorithm are presented.
As already mentioned the full larynx configuration is used for the aeroacoustic as well as for the vibroacoustic simulation.

## 7.1 Aeroacoustic problems

The aeroacoustic problem is given either by Lighthill analogy (6.10) or by (simplified) PCWE equation (6.34) or by AWE equation (6.27). In all cases the problem is described by the wave equation with the same boundary conditions, where only the sound source terms on the right hand side differ according to the chosen formulation. Therefore the numerical scheme is in detail derived only for the case of the Lighthill analogy whereas for the other approaches only the differences are accentuated.

Sound hard boundary condition (6.28) is prescribed at the whole boundary $\partial\Omega^a$ and the PML technique is used at the boundary with outer space (see Figure 6.1). The finite element method is utilized for numerical solution of the presented aeroacoustic problems. For the sake of clarity the FE discretization is described only in the domain $\Omega^a_{\text{prop}}$ and the discretization of the governing equations for the PML layer is omitted, see [82], [87].

### Lighthill analogy

In order to approximate the solution of problem (6.10) by the FEM, we start with its weak reformulation. Equation (6.10) is multiplied by a test function $\eta \in Y = H^1(\Omega^a_{\text{prop}})$ and integrated over the propagation part of the acoustic domain $\Omega^a_{\text{prop}}$,

which leads to

$$\left(\frac{1}{c_0^2}\frac{\partial^2 p'}{\partial t^2}, \eta\right)_{\Omega^a_{\text{prop}}} - (\Delta p', \eta)_{\Omega^a_{\text{prop}}} = (\nabla \cdot (\nabla \cdot \mathbf{T}), \eta)_{\Omega^a_{\text{prop}}}. \tag{7.1}$$

The application of the Green's theorem and sound hard BC (6.28) gives

$$\left(\frac{1}{c_0^2}\frac{\partial^2 p'}{\partial t^2}, \eta\right)_{\Omega^a_{\text{prop}}} + (\nabla p', \nabla \eta)_{\Omega^a_{\text{prop}}} = -\left((\nabla \cdot \mathbf{T}), \nabla \eta\right)_{\Omega^a_{\text{src}}} + \left((\nabla \cdot \mathbf{T}), \eta\, \mathbf{n}^a\right)_{\partial\Omega^a_{\text{prop}}}, \tag{7.2}$$

where for the first integral on the right hand side only the integration domain $\Omega^a_{\text{src}} = \Omega^f_{\text{ref}}$ is used as the Lighthill tensor $\mathbf{T}$ is calculated from the fluid flow quantities (and $\mathbf{T} := \mathbf{0}$ elsewhere). The boundary integral containing the Lighthill tensor $\mathbf{T}$ can be in general nonzero, see e.g. [98].

In what follows let us discuss only the case when the Lighthill tensor is approximated by $T_{ij} \approx \rho_0 v_i v_j$, see Eq. (6.12), i.e. only the less general formulation of the Lighthill analogy for low Mach number flow given by (6.13) is considered here. In that case the boundary integral in Eq. (7.2) is set equal to zero, i.e.

$$\left(\rho_0 \frac{\partial (v_i v_j)}{\partial x_j}, \eta\, n_j^a\right)_{\partial\Omega^a_{\text{prop}}} = 0, \tag{7.3}$$

because on the boundary $\partial\Omega^f_{\text{ref}} \cap \partial\Omega^a_{\text{prop}} = \Gamma^f_{\text{Dir}} \cup \Gamma^f_{\text{W}} \cup \Gamma^f_{\text{In}}$ (compare with Figure 6.1) it holds:

- on boundary $\Gamma^f_{\text{Dir}}$ is $\mathbf{v} = \mathbf{0}$ and then the term $\rho_0 \frac{\partial (v_i v_j)}{\partial x_j}$ equals zero,
- for the purpose of aeroacoustic simulation the motion of $\Gamma^f_{\text{W}}$ is neglected, $\Gamma^f_{\text{W}} := \Gamma^f_{\text{W}_{\text{ref}}}$, and it holds there $\mathbf{v} = \mathbf{0}$.

On the remaining part of the boundary $\Gamma^f_{\text{In}}$ the velocity $\mathbf{v}$ is nonzero $\mathbf{v} \neq \mathbf{0}$, regardless which boundary condition (3.29 a,b,c) is used and therefore term $\rho_0 \frac{\partial (v_i v_j)}{\partial x_j}$ could be nonzero. Nevertheless it is physically obvious that this artificial boundary $\Gamma^f_{\text{In}}$ does not emit any sound and therefore the contribution of term $\rho_0 \frac{\partial (v_i v_j)}{\partial x_j}$ at this boundary is neglected[1].

Additionally, in order to eliminate potential jumps of $\rho_0 v_i v_j$ between the domains $\Omega^a_{\text{src}}$ and $\Omega^a_{\text{air}}$ caused by the numerical approximation, the sound sources are smoothed near boundary $\Gamma^f_{\text{Out}} = \partial\Omega^a_{\text{src}} \cap \partial\Omega^a_{\text{air}}$.

[1]For the simulation settings considered in this thesis it is valid: $v_1 \neq 0, v_2 = 0$ and $\frac{\partial v_1}{\partial x_1} \approx 0$ (for steady fluid flow holds $\frac{\partial v_1}{\partial x_1} = 0$) at boundary $\Gamma^f_{\text{In}}$, which has unit outward normal equal $\mathbf{n}^a = \mathbf{n}^f = (-1, 0)$, i.e. the fluid flow is oriented there purely along axis $x_1$ and its variation along this axis is negligible, see e.g. Figure 8.10. Therefore also term $\rho_0 \frac{\partial (v_i v_j)}{\partial x_j} \approx 0$ at this boundary.

The weak formulation for fixed time instant $t \in (0, \mathrm{T})$ reads: Find a function $p' : (0, \mathrm{T}) \mapsto Y$ such, that

$$\left(\frac{1}{c_0^2}\frac{\partial^2 p'}{\partial t^2}, \eta\right)_{\Omega^a_{\mathrm{prop}}} + (\nabla p', \nabla\eta)_{\Omega^a_{\mathrm{prop}}} = -\left(\nabla\cdot(\rho_0 \mathbf{v}\otimes\mathbf{v}), \nabla\eta\right)_{\Omega^a_{\mathrm{src}}} \tag{7.4}$$

is satisfied for any test function $\eta \in Y$. It is moreover assumed that $\frac{\partial^2 p'}{\partial t^2} \in L^2(\Omega^a)$.

The solution $p' \in Y$ at time $t$ is then approximated by $p'_h$ using the finite element subspace $Y_h$ of $Y$ with the dimension $N_h^a$. The solution $p' \in Y$ is approximated by $p'_h \in Y_h$ written as a time dependent linear combination of coefficients $\gamma_j^a(t)$ and basis functions $\eta_j(x) \in Y_h$, i.e.

$$p'_h(t,x) = \sum_{j=1}^{N_h^a} \gamma_j^a(t)\eta_j(x). \tag{7.5}$$

Using (7.5) in (7.4) with $\eta = \eta_i$ for $i = 1, .., N_h^a$ leads to the second order system of ODEs for unknown vector $\boldsymbol{\gamma}^a(t) = (\gamma_j^a)$ in the form

$$\frac{1}{c_0^2}\mathbb{M}^a\ddot{\boldsymbol{\gamma}}^a + \mathbb{K}^a\boldsymbol{\gamma}^a = \mathbf{b}^a(t), \tag{7.6}$$

where the mass and the stiffness matrices $\mathbb{M}^a = (m_{ij}^a)$ and $\mathbb{K}^a = (k_{ij}^a)$ are given as

$$m_{ij}^a = (\eta_i, \eta_j)_{\Omega^a_{\mathrm{prop}}}, \quad k_{ij}^a = \left(\frac{\partial\eta_i}{\partial x_l}, \frac{\partial\eta_j}{\partial x_l}\right)_{\Omega^a_{\mathrm{prop}}}, \tag{7.7}$$

respectively. The vector $\mathbf{b}^a(t)$ is for the Lighthill analogy taken as $\mathbf{b}^a = \mathbf{b}^{LH} = (b_i^{LH})$, where

$$b_i^{LH}(t) = -\left(\rho_0\frac{\partial(v_j v_l)}{\partial x_l}, \frac{\partial\eta_i}{\partial x_j}\right)_{\Omega^a_{\mathrm{src}}} \tag{7.8}$$

and the Einstein summing convection is applied, here specially for indices $j$ and $l$.

For practical computation the quadratic Lagrange finite elements are chosen. It provides formally third order accuracy of spatial approximation in $L^2$ norm. The system of ODEs (7.6) is numerically discretized in time by the Hilber-Hughes-Taylor-$\alpha$ (HHT-$\alpha$) method, which is an interesting generalization of the classical Newmark method, see [31]. This method addresses the question of algorithmic damping of the (unresolved) high-frequency modes, [80]. The HHT-$\alpha$ scheme is controlled by the choice of three parameters – $\alpha, \beta, \gamma$. For the recommended choice $0 \leq \alpha \leq 1/3$, $\beta = 2(1+\alpha)/4$, $\gamma = 1/2 + \alpha$ the scheme is unconditionally stable and second-order accurate, see [80]. This method is implemented in the program CFS++ .

In order to compute sound sources in the Lighthill analogy given by (7.8) or (7.1) the spatial differentiation has to be performed numerically once or twice, respectively. The (spatial) numerical differentiation of flow results has a predisposition to large numerical error. This can be understood as a disadvantage of the Lighthill analogy. Nevertheless in Section 7.2 several methods are proposed to decrease this numerical error of the aeroacoustic source calculation.

### PCWE approach

Let us consider now numerical discretization of the PCWE approach. The discretization of the right hand side is only described since this is the sole difference against the previous approach. The simplified version of the PCWE approach given by (6.34) reads

$$\frac{1}{c_0^2}\frac{\partial^2 \psi^a}{\partial t^2} - \Delta \psi^a = -\frac{1}{\rho_0 c_0^2}\left(\frac{\partial p^{ic}}{\partial t} + \overline{\mathbf{v}} \cdot p^{ic}\right), \tag{7.9}$$

where $p^{\mathrm{ic}}$ means the pressure obtained by the solution of the incompressible fluid flow model.

Using the same FE discretization procedure as for (7.4) we arrive to the system of ODEs (7.6), where the right hand side vector $\mathbf{b}^a(t)$ is now equal to $\mathbf{b}^{PCWE}(t)$ with components $b_i^{PCWE}$ computed according to

$$b_i^{PCWE} = -\left(\frac{1}{\rho_0 c_0^2}\left(\frac{\partial p^{ic}}{\partial t} + \overline{\mathbf{v}} \cdot \nabla p^{ic}\right), \eta_i\right)_{\Omega^a_{\mathrm{src}}}. \tag{7.10}$$

In practical computation the time derivation in formula (7.10) is realized by the BDF2 approach, while the pressure gradient is computed with the aid of the local reconstruction technique as described in paragraph 4.3.2.

The numerical solution provides in this case the acoustic potential $\psi_h^a$. The approximate acoustic pressure $p_h^a$ can be obtained from equation

$$p_h^a = \rho_0 \left(\frac{\partial \psi_h^a}{\partial t} + \overline{\mathbf{v}} \cdot \nabla \psi_h^a\right) \tag{7.11}$$

using the numerical differentiation (e.g. BDF2 formula) and applying gradient operator on the FE approximation $\psi_h^a$.

### AWE approach

The numerical discretization of the AWE approach is now being discussed. The discretization is performed as described in the previous paragraph with the only exception of the right hand side vector, described here in detail. The AWE approach given by (6.27) reads

$$\frac{1}{c_0^2}\frac{\partial^2 p^a}{\partial t^2} - \Delta p^a = -\frac{1}{c_0^2}\frac{\partial^2 p^{ic}}{\partial t^2}. \tag{7.12}$$

Similarly as before, the FE discretization procedure for (7.4) results into system (7.6), where the right hand side vector $\mathbf{b}^a(t)$ is now replaced by $\mathbf{b}^{AWE}(t)$ with components $b_i^{AWE}$ given as

$$b_i^{AWE} = -\frac{1}{c_0^2}\left(\frac{\partial^2 p^{ic}}{\partial t^2}, \eta_i\right)_{\Omega^a_{\mathrm{src}}}. \tag{7.13}$$

The second order time derivative is approximated by the central difference formula.

## 7.2 Aeroacoustic source evaluation

In next paragraphs the realized procedures of the sound sources computation and the interpolation between the acoustic and the fluid flow mesh are described.

First we start with modification of the sound sources formulation in the case of the **Lighthill analogy**. With the assumption of the incompressible flow the Lighthill tensor approximation given by relation (6.12), i.e. $\operatorname{div}(\operatorname{div}\mathbf{T}) \approx \operatorname{div}(\operatorname{div}(\rho_0 \mathbf{v}\otimes\mathbf{v}))$ can be rewritten to

$$\frac{\partial^2(v_i^{ic}v_j^{ic})}{\partial x_i \partial x_j} = \frac{\partial}{\partial x_j}\left(v_j^{ic}\underbrace{\frac{\partial v_i^{ic}}{\partial x_i}}_{=0} + v_i^{ic}\frac{\partial v_j^{ic}}{\partial x_i}\right) = \left(v_i^{ic}\frac{\partial}{\partial x_i}\underbrace{\frac{\partial v_j^{ic}}{\partial x_j}}_{=0} + \frac{\partial v_i^{ic}}{\partial x_j}\frac{\partial v_j^{ic}}{\partial x_i}\right) = \frac{\partial v_i^{ic}}{\partial x_j}\frac{\partial v_j^{ic}}{\partial x_i}, \tag{7.14}$$

where continuity equation (3.23) was used twice, see also [151]. Using (7.14) in equation (7.1) or more precisely in (7.8) yields the following formula for the sound sources evaluation

$$b_i^{LH} = \left(\rho_0 \frac{\partial v_l^{ic}}{\partial x_j}\frac{\partial v_j^{ic}}{\partial x_l}, \eta_i\right)_{\Omega^a_{\mathrm{src}}}. \tag{7.15}$$

### Gradient reconstruction techniques

In equation (7.15) the local reconstruction of velocity gradients is used based on the ideas described in paragraph 4.3.2. This reconstructed gradient at (fluid) mesh vertices can be understand as piecewise linear function. The local patch for a chosen vertex $x_i$ is selected as described in paragraph 4.3.2, i.e. the local patch consists of all such triangles $K \in \mathcal{T}_h^f$ having the point $x_i$ as their vertex, see Figure 7.1. Formula (7.15) together with the local recontruction technique is the default option of the sound source calculation for the Lighthill analogy in the program FSIFEM .

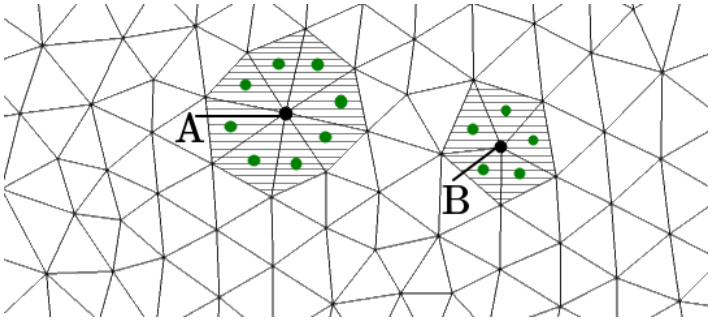


Figure 7.1: Example of two local patches. The patch of point $A$ consists of eight triangles, while the patch of point $B$ is constituted by five triangles.

### Weak formulation of acoustic forces

An alternative approach is based on the weak formulation of (6.13). Let us denote the sound sources given by the substitution of (6.12) into (7.1) as

$$S = \rho_0 \frac{\partial^2}{\partial x_i \partial x_j} \left( v_i v_j \right). \tag{7.16}$$

These sources can be approximated by a FE function $S_h \approx S$ as

$$S_h = \sum_{k=1}^{N_h^{src}} s_k \eta_k(x), \tag{7.17}$$

where $\eta_k$ are basis functions of FE space $Y_h^{src} = \{ f \in C(\overline{\Omega_{\text{src}}^a}) | f|_K \in \mathbb{P}_1(K) \; \forall K \in \mathcal{T}_h^{src} \}$ with triangulation of acoustic domain $\Omega_{\text{src}}^a$ denoted by $\mathcal{T}_h^{src}$, and $\mathbf{s} = (s_k)$ is the unknown vector of linear combination coefficients.

Using equation (7.17), multiplying (7.16) by a basis function $\eta_l$ and using the Green's theorem leads to

$$(S_h, \eta_l)_{\Omega_{\text{src}}^a} = \left( \rho_0 \frac{\partial \left( v_i v_j \right)}{\partial x_j}, \frac{\partial \eta_l}{\partial x_i} \right)_{\Omega_{\text{src}}^a}, \tag{7.18}$$

where the boundary term vanishes or is neglected on $\Gamma_{\text{In}}^f$ as discussed in previous Section 7.1. In the case of incompressible fluid flow the right hand side can be equivalently rewritten leading to

$$(S_h, \eta_l)_{\Omega_{\text{src}}^a} = \left( \rho_0 \frac{\partial v_i^{ic}}{\partial x_j} v_j^{ic}, \frac{\partial \eta_l}{\partial x_i} \right)_{\Omega_{\text{src}}^a}. \tag{7.19}$$

Equation (7.19) leads to the system of linear equations

$$\mathbb{M}^{src} \, \mathbf{s} = \mathbf{b}^{src}, \tag{7.20}$$

where $\mathbb{M}^{src}$ is the mass matrix and the $l$-th component of vector $\mathbf{b}^{src}$ is given by the right hand side of equation (7.19).

**Remark.** Another alternative of the Lighthill sound source computation would be to use formula (6.15), i.e. the sound sources given by the **Laplacian of pressure**. Both aforementioned techniques can be used also in this case, namely the removing one spatial derivative from the pressure field with the help of the Green's theorem or the local reconstruction of the pressure gradient.

### Interpolation of sound sources

In practical computations different computational meshes are used for the fluid flow approximation (CFD) and for the acoustic problem solution. This is due to the fact that the fluid mesh has to primarily resolve thin boundary layers around walls, while

the acoustic mesh from a nature of the problem is ideally approximately everywhere uniform. Therefore the interpolation of evaluated sound sources from the CFD to the acoustic mesh is performed in order to reduce computation cost. We use the interpolation procedure implemented in the program CFS++ and designed such, that it preserves the overall acoustic energy between meshes, see [88].

This interpolation is performed from elements $K^f$ of fluid mesh $\mathcal{T}_h^f$ onto elements $K^a$ of acoustic mesh $\mathcal{T}_h^a$ with $N^a$ vertices[2]. For simplicity let us suppose both meshes to be composed of triangles. We further assume that acoustic sources $S_h$ are known at any vertex of the triangulation $\mathcal{T}_h^f$ (as these sources are piecewise linear functions, they are uniquely determined by the values at vertices of $\mathcal{T}_h^f$).

In the begging we set vector of acoustic sources $\mathbf{F}^a \in \mathbb{R}^{N^a}$ to zero, i.e. $\mathbf{F}^a = \mathbf{0}$. Then for every triangle $K^f \in \mathcal{T}_h^f$ we perform the following steps, see [131]:

1. Find the intersection of triangle $K^f$ with triangles $K^a \in \mathcal{T}_h^a$ from the acoustic mesh. Denote these intersections by $P_{K_a} = K^f \cap K^a$, see Figure 7.2.

2. For each non-empty intersection $P_{K_a}$ compute the area $|P_{K_a}|$. Find the center of mass $X_{K_a}$ of the polygon $P_{K_a}$. Denote the vertices of the element $K^a$ by $j_1, j_2$ and $j_3$.

3. Compute contributions $f_l^{CFD}$ to the global vector $\mathbf{F}^a = (F^a)$ given by

$$f_l^{CFD} = |P_{K_a}|\ \eta_{j_l}(X_{K_a})\ S_h(X_{K_a}), \qquad l = 1, 2, 3, \tag{7.21}$$

   where $\eta_{j_l}$ is the linear FE basis function associated with the vertex $j_l$ of the acoustic mesh. By $S_h(X_{K_a})$ the aeroacoustic source computed on the CFD mesh and evaluated at point $X_{K_a}$ is denoted, see Figure 7.2 right.

4. Add these contributions to the global vector

$$F_{j_l}^a := F_{j_l}^a + f_l^{CFD}, \tag{7.22}$$

   where $j_l$ here denotes the index of the vertex $j_l$ in the acoustic mesh.

## 7.3 Vibroacoustics

Let us consider the vibroacoustic problem now. Since the influence of the acoustic field on the structure deformation is for simplicity disregarded, the coupled vibroacoustic problem simplifies to the acoustic problem with a given sound source at boundary. This problem is described by homogeneous wave equation (2.13) (the unknown denoted by $p^{\text{va}}$) with sound hard boundary condition (6.28) prescribed at boundary $\partial\Omega^a \setminus \Gamma_{\text{W}_{\text{ref}}}$ and with prescribed boundary condition (6.32) on boundary $\Gamma_{\text{W}_{\text{ref}}}$, representing the sound source.

[2]More precisely the interpolation procedure maps the sound sources from CFD mesh $\mathcal{T}_h^f$ onto a part of the whole acoustic domain – onto the sound source domain $\Omega^a_{\text{src}}$, since $\Omega^a_{\text{src}} = \Omega^f_{\text{ref}}$.

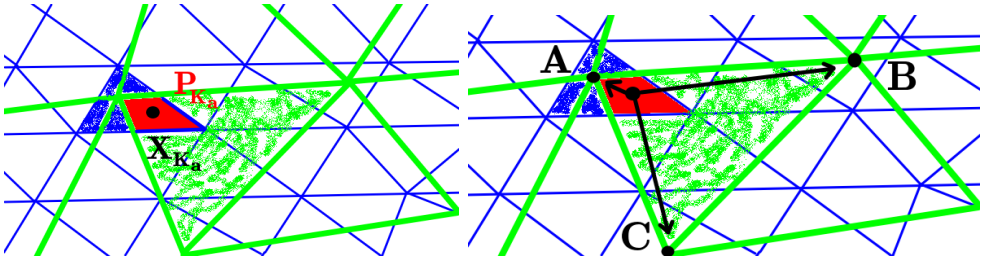


Figure 7.2: **Left:** Polygon $P_{K_a}$ (highlighted by red colour) denoting the intersection of an element $K^f$ of the CFD mesh (blue) with an element of the acoustic mesh (green). Point $X_{K_a}$ represents the center of mass of polygon $P_{K_a}$. **Right:** Illustration of the assembly of the interpolated vector $\mathbf{F}^a$. The value of sound sources at point $X_j$ is distributed to the positions of the vector $\mathbf{F}^a$ corresponding to the vertices $A, B, C$ of the acoustic mesh triangle (green) according to formula (7.22).

For the purpose of the FEM the problem is now weakly reformulated. Equation (2.13) is multiplied by test function $\eta \in Y^{\mathrm{va}} = Y$ and integrated over the whole domain $\Omega^a_{\mathrm{prop}}$. The application of the Green's theorem together with boundary conditions (6.32) and (6.28) yields the final weak formulation seeking a such function $p^{\mathrm{va}} \in Y^{\mathrm{va}}$, that

$$\left(\frac{1}{c_0^2}\frac{\partial^2 p^{\mathrm{va}}}{\partial t^2}, \eta\right)_{\Omega^a_{\mathrm{prop}}} + (\nabla p^{\mathrm{va}}, \nabla \eta)_{\Omega^a_{\mathrm{prop}}} = \left(\rho_0^f \frac{\partial^2 (\mathbf{u}\cdot\mathbf{n}^s)}{\partial t^2}, \eta\right)_{\Gamma_{\mathrm{W_{ref}}}}, \tag{7.23}$$

is satisfied for any $\eta \in Y^{\mathrm{va}}$.

Similarly as before, the space $Y = Y^{\mathrm{va}}$ is approximated by a finite element subspace $Y_h$ and the approximate solution $p_h^{\mathrm{va}}$ is sought in the form given by (7.5). This leads to the system of ODEs, see e.g. [90],

$$\mathbb{M}^a \ddot{\boldsymbol{\gamma}}^{\mathrm{va}} + \mathbb{K}^a \boldsymbol{\gamma}^{\mathrm{va}} = \mathbf{b}^{\mathrm{va}}(t), \tag{7.24}$$

where elements of matrices $\mathbb{M}^a = (m^a_{ij}), \mathbb{K}^a = (k^a_{ij})$ are given by formula (7.7) and the components of right hand side vector $\mathbf{b}^{\mathrm{va}}(t) = (b_i^{\mathrm{va}})$ are given by

$$b_i^{\mathrm{va}} = \left(\rho_0^f \frac{\partial^2 (\mathbf{u}\cdot\mathbf{n}^s)}{\partial t^2}, \eta_i\right)_{\Gamma_{\mathrm{W_{ref}}}}. \tag{7.25}$$

The second time derivative of structure displacement $\mathbf{u}$ is approximated as $\frac{\partial^2 \mathbf{u}}{\partial t^2}(t_n) \doteq \frac{\mathbf{u}^{n+1} - 2\mathbf{u}^n + \mathbf{u}^{n-1}}{\Delta t^2}$. For practical computation the quadratic Lagrange finite elements are used and system (7.24) is numerically discretized in time by the HHT-$\alpha$ method.

## 7.4 Solution of FSAI coupled problem

In order to couple FSI to acoustics one needs to carefully choose not only the spatial resolution but also the time resolution of both FSI and acoustic problems. The time resolution of the fluid flow results, i.e. $\mathbf{v}, p$ in $\Omega^f_t$, is recommended to be approximately $\Delta t = \frac{1}{20 f_{max}}$, where $f_{max}$ is the highest relevant frequency of simulated phenomena. In our case with considered $f_{max} \approx 3000$ Hz it means $\Delta t \approx 2 \cdot 10^{-5}$ s. The acoustic steps of the FSAI algorithm are following, see also Figure 7.3:

- Compute the sound sources based on the chosen aeroacoustic approach on the CFD mesh according to formula (7.15) for Lighthill analogy or according to formula (7.10) for PCWE approach or according to formula (7.13) for AWE approach.
- Interpolate the sound sources from the CFD mesh on the acoustic computational mesh as described in Section 7.2.
- Solve the sound propagation problem given by system (7.6) with the interpolated sound sources on the whole acoustic domain $\Omega^a$, i.e. including the vocal tract model, the free field region and the PML layer, whereas the sound sources are located purely in the sound source region $\Omega^a_{\text{src}}$.

In order to obtain the overall sound produced by the vocal folds vibration the sound sources of vibroacoustic origin has to be added to the aeroacoustic sound sources. Then the presented FSAI algorithm would differ only in the first step, where the additional vibroacoustic sound sources would be computed and would be added to the aeroacoustic sound sources.

Nevertheless the vibroacoustic problem is in the FSAI problem by default omitted due to assumed negligible contribution to the total sound pressure level of the sound with aeroacoustic origin. This assumption was verified by a separate analysis – see Section 8.3, which is composed of these steps:

- Calculate the vibroacoustic sound sources having the form of interface normal acceleration given by (7.25) according to the description in Section 7.3.
- No sound sources interpolation is needed due to the mesh conformity of the boundary $\Gamma_{\text{W}_{\text{ref}}}$ between the CFD and the (vibro-)acoustic mesh.
- Solve the sound propagation problem described by equation (7.24) on the whole acoustic domain $\Omega^a$, i.e. with the included vocal tract model, the free field region and the PML layer and the sound source region $\Omega^a_{\text{src}}$ , where the sound sources are located purely at boundary $\Gamma_{\text{W}_{\text{ref}}}$.

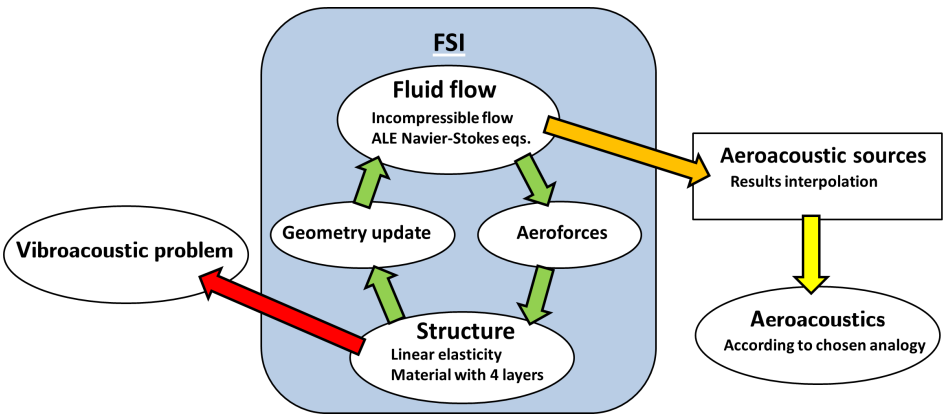


Figure 7.3: Scheme of FSAI workflow. Here the aeroacoustic and the vibroacoustic problem is considered as two separate independent problems.

# Chapter 8

# Numerical results of FSAI problem

This chapter presents the numerical results of acoustic problems. First the results of the FSI simulation are presented. Based on these results the acoustic sources are evaluated and used for acoustic computations. The acoustic computations start with the determination of the resonant frequencies of the vocal tract models (i.e. the acoustic domain). These resonancies, called formants, have a crucial influence on the produced sound. Further, the results of the vibroacoustic problem are shown. Finally the sources of aerodynamically produced sound are analyzed and the results of the sound propagation problem simulating human phonation are presented.

If not mentioned otherwise all acoustic simulations were performed with the solver CFS++ .

## 8.1 FSI numerical results

Here the geometry of the considered vocal fold model is described (including the structural parameters) and the results of modal analysis is presented. Further, the FSI simulations of VFs vibration in the pre-phonatory regime obtained by the FSIFEM solver are shown.

### Vocal fold model

The used vocal fold model is based on the VF shape published in article [174] , see also publication [2]. The VF model (denoted as ZORNER in what follows) is divided into four parts with different material parameters, see Figure 8.1 and corresponding Table 8.1. The geometric details of the model is given in Appendix B. The model with the initial (full) glottal gap equal to 2.0 mm is placed in the fluid flow domain $\Omega_0^f$, dimensions of which are displayed in Figure 8.1 right. Point A at the top of the bottom VF with coordinates $[11.57, -1.50]$ mm is used for analysis of numerically simulated VF vibrations. The first four eigenmodes of VF model ZORNER obtained by modal analysis (as explained in Appendix A) are shown in Figures 8.2 and 8.3.

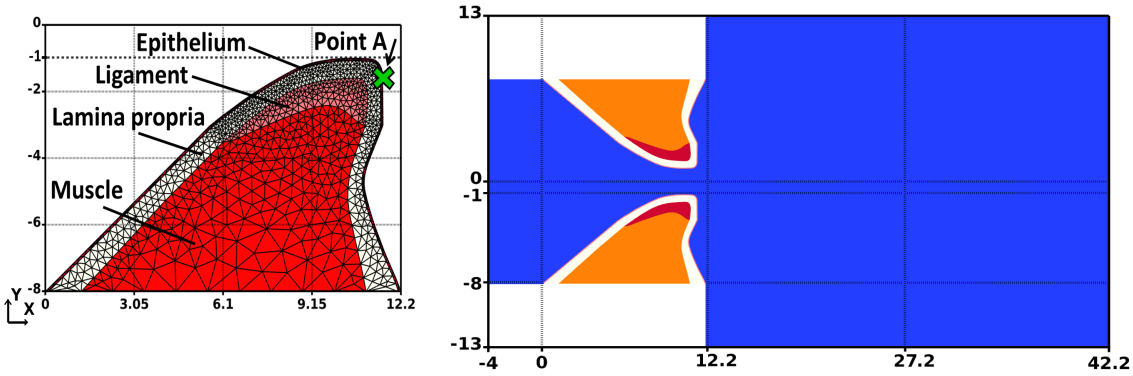


Figure 8.1: **Left:** Computational mesh for the (bottom half) structure domain with marked different layers of materials and with dimensions shown in mm. Point A used for analysis of VF vibration is located on the top of the (bottom) VF. **Right:** Computational fluid domain with dimensions in mm is marked by blue colour.

| Layer | Elastic modulus [kPa] | Poisson ratio |
|---|---|---|
| Epithelium | 50 | 0.45 |
| Lamina propria | 20 | 0.45 |
| Ligament | 25 | 0.45 |
| Muscle | 30 | 0.45 |

Table 8.1: The elastic modulus and the Poisson ratio of four layers of VF model ZORNER.

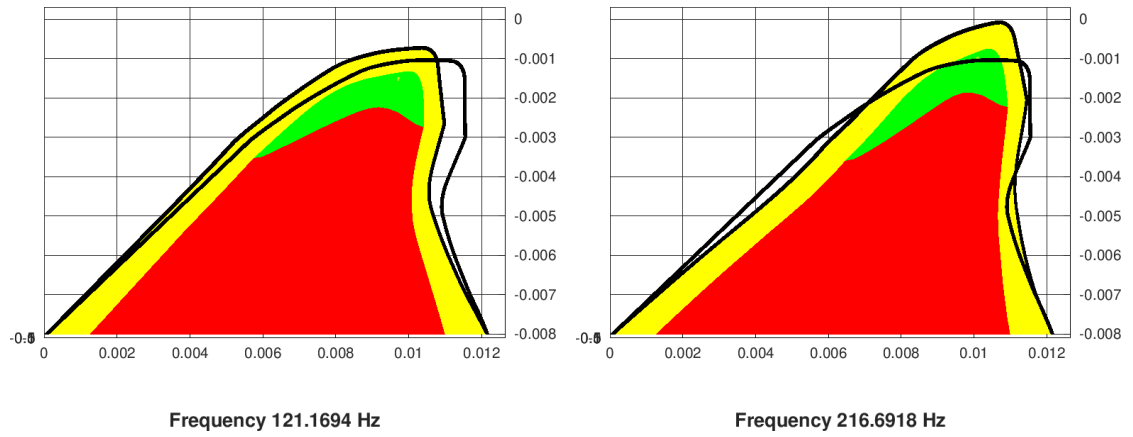


Figure 8.2: Modal analysis of VF model ZORNER. The first and the second eigenmode with the corresponding eigenfrequencies 121.2 Hz and 216.7 Hz are shown, respectively.

### 8.1.1 Analysis of FSI results with vocal fold model ZORNER

The numerical results of FSI achieved with VF model ZORNER are here presented with very similar numerical settings as described in Chapter 5. The constant time step $\Delta t$ is chosen as $2.5 \cdot 10^{-5}$ s. The structure density $\rho^s$ is set to $\rho^s = 1000\,\mathrm{kg/m^3}$, the fluid density $\rho_0^f = 1.185\,\mathrm{kg/m^3}$ and the kinematic fluid viscosity $\nu^f = 1.545 \cdot$

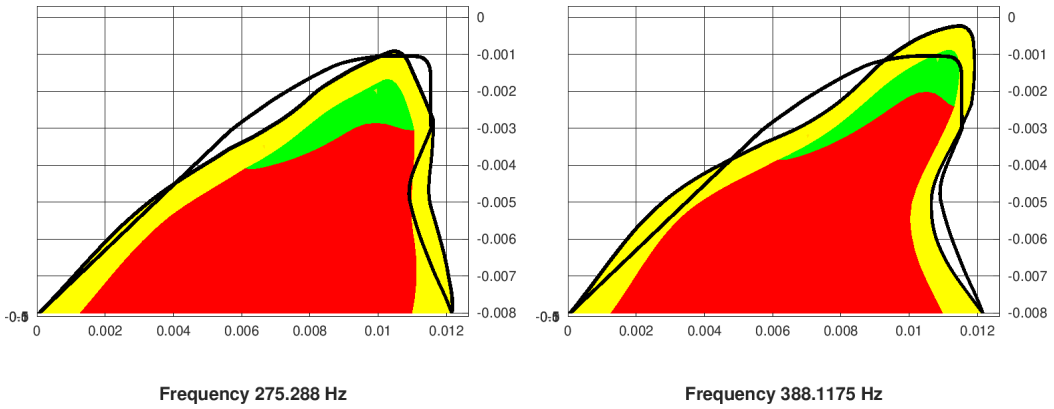


Figure 8.3: Modal analysis of VF model ZORNER. The third and the fourth eigenmode with the corresponding eigenfrequencies 275.3 Hz and 388.1 Hz are shown, respectively.

$10^{-5}\,\mathrm{m}^2/\mathrm{s}$. The damping parameters for vocal folds are given as $\epsilon_1^s = 5\,\mathrm{s}^{-1}, \epsilon_2^s = 2.0 \cdot 10^{-5}\,\mathrm{s}$. The static force described in paragraph 5.1.1 is omitted, i.e. $\mathbf{q}_{\mathrm{stat}}^s = \mathbf{0}$.

The FSI problem is solved with prescribed pressure drop $\Delta p$ between the inlet and the outlet $\Delta p = p_{\mathrm{in}} - 0 = 1500\,\mathrm{Pa}$. Vocal folds are released for the interaction after 0.01 s of the computation. Figure 8.4 illustrates a typical behaviour of flow-induced vibration at selected point $A$ (see its location in Figure 8.1). After a short time VF oscillations with bounded amplitude appear. The spectrum of VF displacement computed by the Fourier transform shows two dominant frequencies $f_1 = 121$ and $f_2 = 211\,\mathrm{Hz}$. The frequencies $f_1$ and $f_2$ agree relatively well with the first two VF eigenfrequencies what is in a good correspondence with the results of [174].

The trajectories of point A as well as of the VF center of mass in the X–Y plane are depicted in Figure 8.5, compare with previous results in Figure C.5. Further the pressure difference between the inlet and the outlet and the flow rate are presented in Figure 8.6. The oscillations of pressure difference can be explained by its weak prescription. The flow rate is quite high compared to results of previous Chapter 5 and literature, see [156], however the initial gap is substantially larger (2.0 vs. 0.8 mm) and therefore the critical flutter velocity and the phonation onset threshold pressure are higher. The pressure difference and the gap have similar oscillating character as the VF displacement, cf. Figure 8.4, and they do not rise (exponentially) as seen earlier in Chapter 5, where the simulations captured the phonation onset. The gap time variation is plotted in Figure 8.7 and the time averaged airflow velocity field is depicted in Figure 8.8. Figure 8.9 shows the typical distribution of the airflow vorticity.

Finally, Figure 8.10 shows the airflow velocity and the pressure field during one VF oscillation cycle. Large and intensive vortices created at the boundaries of the glottal jet are convected downstream, where they interacts with flow structures in the supraglottal region, cf. with previous results shown in Figure 5.23. Similar character of the complex flow field was reported in [89].

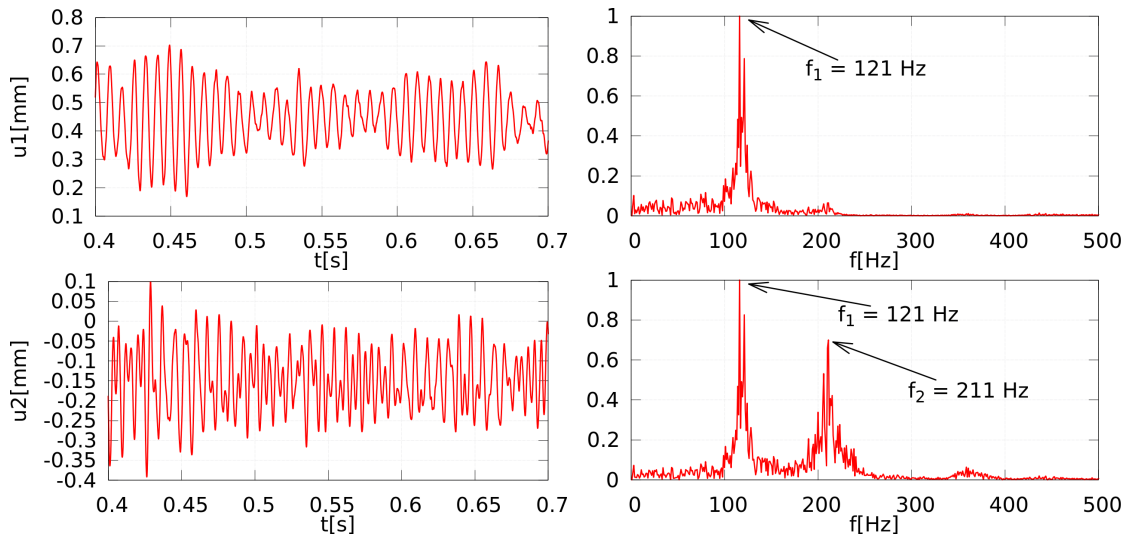


Figure 8.4: **Left:** Time evolution of the displacement of chosen point $A$ in $x$- and $y$-directions (top and bottom, respectively). **Right:** Normalized Fourier transform of the time signal of the displacements $u_1$ (top) and $u_2$ (bottom) at point A.

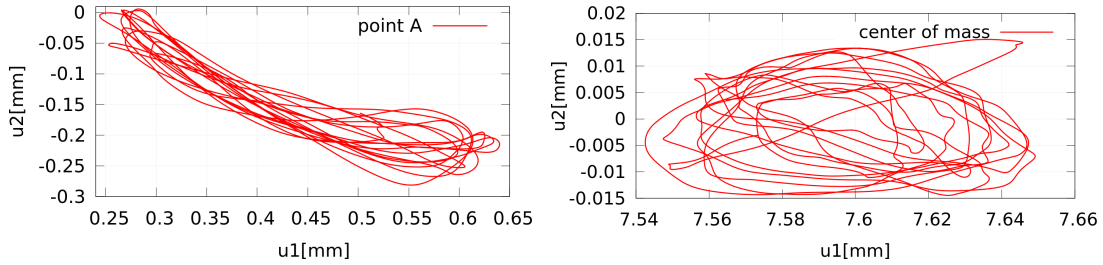


Figure 8.5: **Left:** Trajectory of point A in the X–Y plane. **Right:** Trajectory of the center of mass computed for the both parts of VFs as one elastic body in the X–Y plane. The center of mass in the reference configuration is located at $[7.35, 0.0]$ mm. Several last periods are displayed.

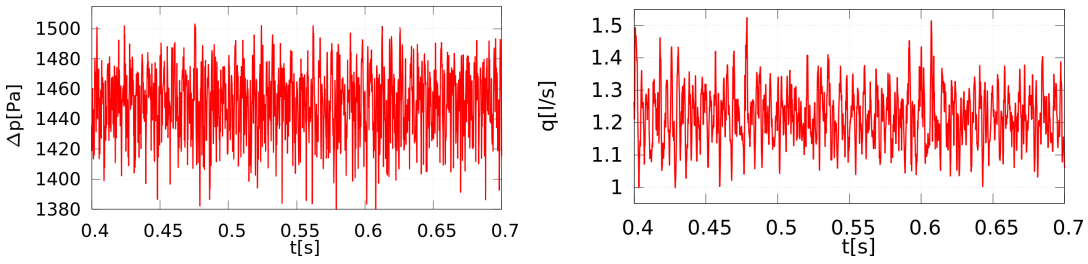


Figure 8.6: **Left:** The pressure difference between the inlet and the outlet. **Right:** The computed inlet flow rate using the channel depth of 1 cm (third dimension).

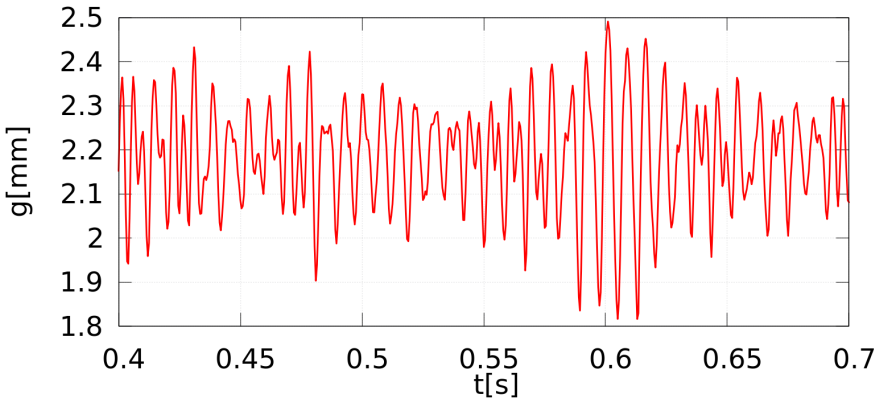


Figure 8.7: Time variation of the channel gap between VFs.

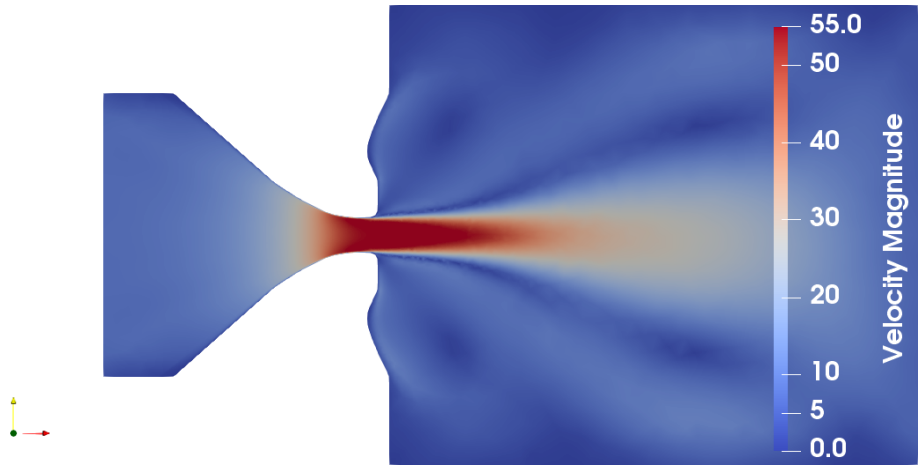


Figure 8.8: Time average of the computed airflow velocity field $\overline{\mathbf{v}}$ obtained by the FSI simulation.

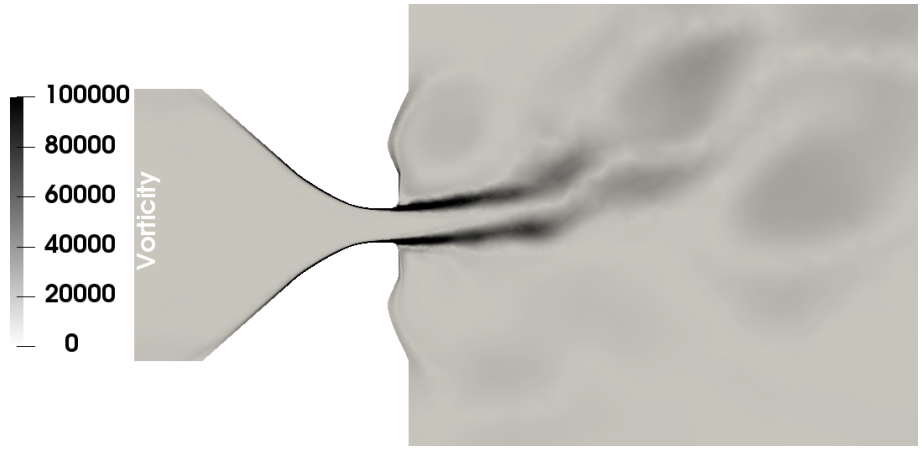


Figure 8.9: Snapshot of the flow field vorticity at time instant 0.6 s computed with the aid of the visualization program Paraview.

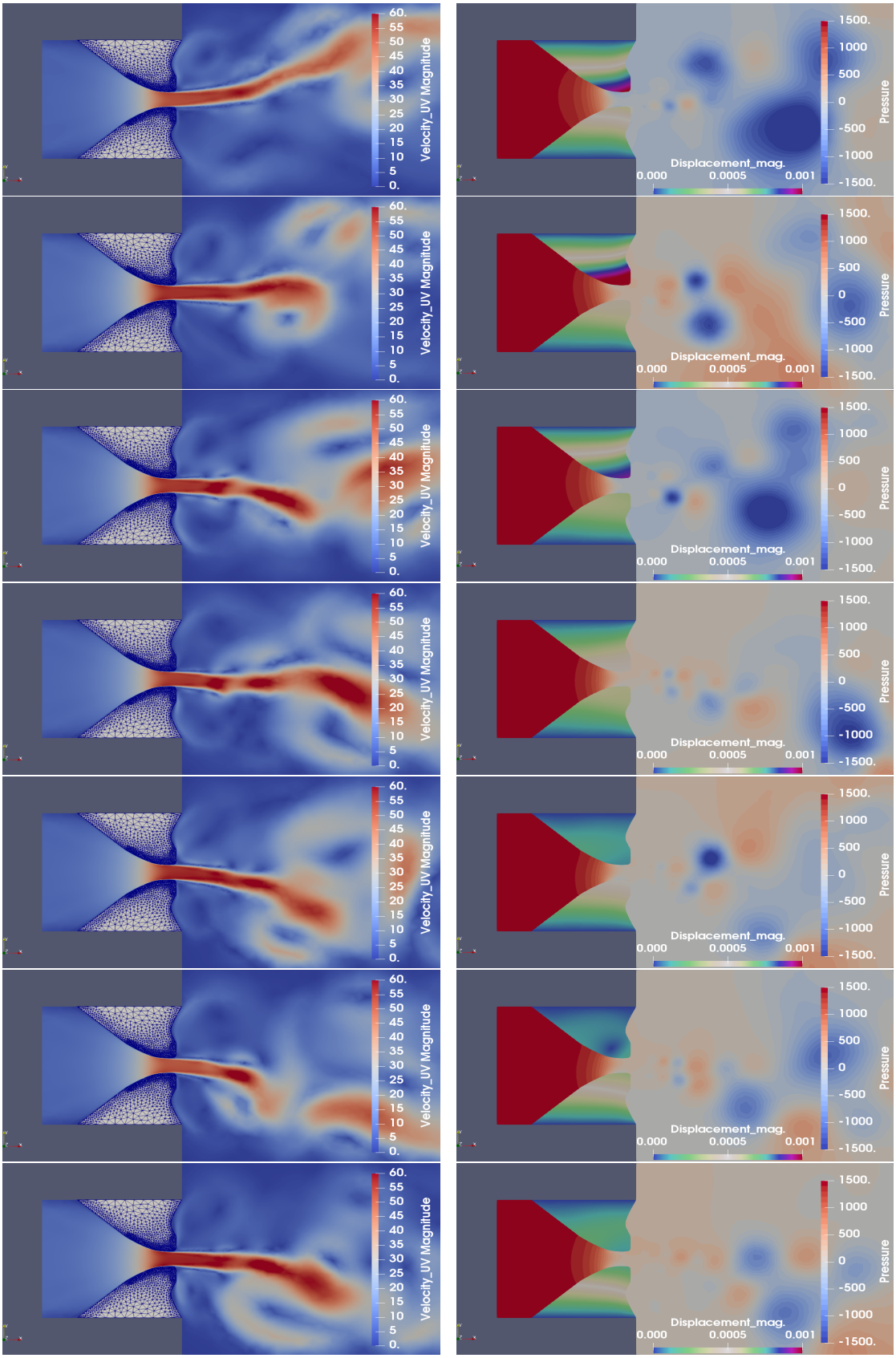


Figure 8.10: Magnitude of the airflow velocity (left) and the pressure and the vocal fold displacement in mm (right) shown for seven time instants during (almost) one vibration cycle of VFs with duration of approx. 6 ms.

## 8.2 Vocal tract resonances

The sound created by the flow-induced vibration of VFs at the larynx propagates by the vocal tract (VT) to the mouth and further exterior. The VT geometry co-determines the characteristics of propagated sound, where the VT resonances have one of the most important influences. That is why the several VT models are analyzed in order to find their acoustic resonant frequencies, in the human phonation context usually called formants[1]. According to the source-filter theory (see e.g. [156]) the function of the vocal tract (in a rough approximation) is to filter acoustic pressure waves generated in the larynx without considering their possible feedback onto the source mechanism (oscillating VFs modulating the airflow jet through glottis). The source-filter theory is valid for a wide range of physiological settings, except the cases when the VF vibration frequency is very close to the VT formant, for details see [157].

With this simplified approach each vowel corresponds to a characteristic shape of the vocal tract (and consequently to characteristic formants). The first two formants (denoted F1, F2, etc.) are usually decisive for a recognition of different vowels, see [156]. The averaged F1-F2 map of statistically representative samples for English and Czech vowels can be found e.g. in [142] and [161], respectively. Nevertheless, each speaker has the vowels formants located individually within the concrete F1-F2 map for a given language and the typical sound of his voice is formed also by a combination of higher frequencies above simulation limit of 3 kHz considered here.

The goal of this section is to determine the formants of the considered VT model variants with the numerical settings used further in Sections 8.3 and 8.4. The results are based on the publication [10].

### 8.2.1 Vocal tract models

The part of acoustic domain $\Omega^a_{\text{tract}}$ representing a VT model for the vowel [u:] is shown in Figure 8.11. It is based on the data of Story's study [143], where the vocal tract cross-section areas were carefully segmented and computed from MRI measurements. Here due to 2D computations the diameters $r_i$ of cross-sections perpendicular to $x$-axis of the domain $\Omega^a_{\text{tract}}$ (i.e. the cross-section $r_i$ represents the $y$-dimension) are determined from the cross-section area $A_i$ of [143] in chosen equidistant cut positions $x_i$ as

$$r_i = \sqrt{\frac{A_i}{\pi}}, \tag{8.1}$$

see Table D.1 in Appendix D. The distance between two cross-section measurements is equal to $d = 3.96825\,\text{mm}$. Thus the total length of the VT model of the vowel [u:], which is described by 46 cross-section areas, is $L = 45 \times d \doteq 17.86\,\text{cm}$.

Further, four variants of acoustic domain $\Omega^a$ are analyzed. In all cases the same shape of domains $\Omega^a_{\text{free}}$ and $\Omega^a_{\text{pml}}$ are considered and only the shapes of domains $\Omega^a_{\text{src}}$ and $\Omega^a_{\text{tract}}$ differ, see Figure 6.1. The first variant labeled as M1 (model 1) is

[1] Formants are usually characterized not only by the resonant frequency peak but also by the formants bandwidth, see [156], [23].

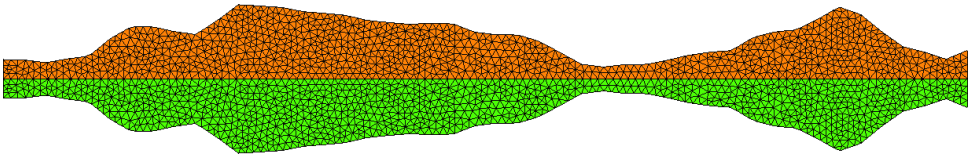

Figure 8.11: Geometry of the vocal tract model (for the vowel [u:]) used as the part $\Omega^a_{\text{tract}}$ (shown here) of the acoustic domain $\Omega^a$.

shown in Figure 8.12 together with its dimensions. It consists of the domains: sound source domain $\Omega^a_{\text{src}}$, vocal tract model $\Omega^a_{\text{tract}}$, the free field region $\Omega^a_{\text{free}}$ and PML domain $\Omega^a_{\text{pml}}$. Domain $\Omega^a_{\text{src}}$ (with $x$ coordinates in the range $x \in [-4.0, 42.2]$ mm) is the domain, where the fluid flow of FSI problem was solved, see Figure 8.1 (right). Domain $\Omega^a_{\text{tract}}$ ($x \in [42.2, 232.7]$ mm) is constituted by VT model ($x \in [54.2, 232.7]$ mm), which is preceded by (an artificial) prolongation region ($x \in [42.2, 54.2]$ mm) realizing a smooth connection of domains $\Omega^a_{\text{src}}$ and $\Omega^a_{\text{tract}}$.

The modifications of the VT model are performed with the goal to quantify an influence of additional acoustic volume represented by domain $\Omega^a_{\text{src}}$ and the prolongation region, which are (artificially) included for the reason of inclusion the CFD domain with the sound sources. The following four variants of acoustic domain geometry $\Omega^a$ are considered representing the subglottal and the supraglottal airways spaces together with the vocal tract model, see Figure 8.13:

M1: Model M1 consists of all parts ($\Omega^a_{\text{src}}, \Omega^a_{\text{tract}}, \Omega^a_{\text{free}}, \Omega^a_{\text{pml}}$) as described above, see Figure 8.12.

M2: Model M2 is equal to model M1 with the exception of the subglottal and the glottal regions, i.e. $x$-coordinates of model M2 are in the range $x \in [10.9, 277]$mm, see Figure 8.13 b).

M3: Model M3 is the same as model M1 with no artificial prolongation region and no subglottal region, i.e. parts of model M1 with $x \in [-4.0, 10.9]$ and $x \in [42.2, 54.2]$mm are omitted, and the narrower sound source domain $\Omega^a_{\text{src}}$ is used ($y \in [-8, 8]$mm instead of $y \in [-13, 13]$mm). The total $x$-dimension of model M3 is $x \in [10.9, 265]$mm, see Figure 8.13 c).

M4: Model M4 is based on model M3 with no sound source domain $\Omega^a_{\text{src}}$ (part of base model M1 with $x \in [-4.0, 42.2]$mm is omitted), see Figure 8.13 d). This 2D model resembles best the original shape of 3D propagation domain as it was measured by MRI in [143] for vowel [u:].

### 8.2.2 Analysis of vocal tract resonances

There are well-established methods of VT formant determination like e.g. the method of 1D transfer matrices, see e.g. [115], or the modal analysis, see e.g. [85] or Appendix A. The transfer matrices method (TMM) models the VT as a sequence of cylinders and calculates the propagation of planar waves through them. However this method is not suitable to be used together with PML approach and it prevents its application here. The modal analysis is a natural choice in the FEM framework. It is

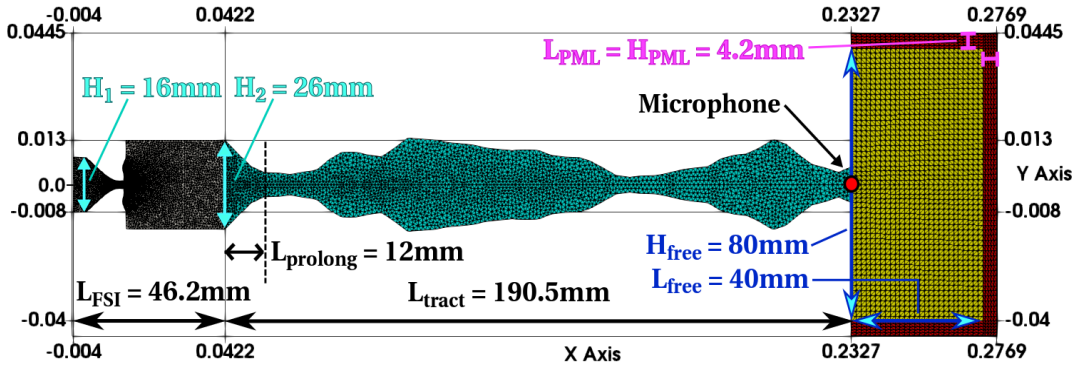


Figure 8.12: Computational acoustic domain $\Omega^a$ of model M1 with shown triangulation and described dimensions. Microphone is placed in the mouth opening.

based on the solution of a generalized eigenvalue problem and provides more details about VT eigenmodes and eigenfrequencies than TMM, see e.g. [162]. Nevertheless the linear original generalized eigenvalue problem would turn to a nonlinear problem with the employed PML approach, therefore a different method based on a transfer function approach is adopted here.

### Transfer function approach

The (inhomogeneous) wave equation (6.10) transformed into frequency domain is called the Helmholtz equation, see e.g. [78], and it reads

$$-\left(\frac{\omega^2}{c_0^2} + \Delta\right)\hat{p} = \hat{F}, \tag{8.2}$$

where $\omega$ denotes the angular frequency and the variables with caret denote the Fourier transforms of variables without caret, i.e. $\hat{p} = \hat{p}(x,\omega) : \Omega^a \to \mathbb{C}$ is the Fourier transform of $p = p(x,t) : \Omega^a \to \mathbb{R}$. Assuming a unit harmonic excitation given by right hand sources $\hat{F}(\omega)$ at a given frequency $\omega$ let us seek for the system answer at the same frequency.

Problem (8.2) is equipped with the boundary conditions used for the simulation of sound propagation in Sections 8.3 and 8.4, i.e. sound hard boundary condition (6.28) is considered on $\partial\Omega^a$ (especially the inlet boundary of the subglottal channel is treated as sound hard, which means it is acoustically closed) and the PML layer is applied on the boundary of the free field region in order to model the open boundary.

Transfer functions are usually functions providing the ratio of the output to the input signal, see e.g. [85]. Similarly to this approach here the transfer function $H(\omega)$ denotes the ratio of the amplitude of the (complex) acoustic pressure $\hat{p}$ monitored at a microphone position $x_M$ to the harmonic acoustic forcing $\hat{F}$ at a chosen excitation location (point or boundary) $\Gamma_{\text{exc}}$, i.e.

$$H(\omega) = \frac{|\hat{p}(x_M,\omega)|}{|\hat{F}(\Gamma_{\text{exc}},\omega)|}. \tag{8.3}$$

The evaluation of the transfer function $H(\omega)$ over a frequency interval can be used to detect the resonant frequencies as the absolute value of the transfer function at the corresponding value of $\omega$ should go to infinity if no damping of acoustic waves is included in the model.

### Transfer function results for different vocal tract models

Problem (8.2) is numerically solved in the frequency range $50 - 3000$ Hz. The logarithmic sampling $f_{i+1} = q \cdot f_i$ with $q$ equal 1.008 is applied in the academic solver CFS++ resulting in 460 separate solutions of system (8.2). Location $\Gamma_{\text{exc}}$ of the unit harmonic acoustic excitation $\hat{F}$ is chosen as a point on the symmetry axis in the narrowest part of the glottis and the microphone position $x_M$ is at the mouth opening, see Figure 8.12. The speed of sound is chosen as 343.2 m/s.

The transfer functions computed for vocal tract models M1-M4 are shown in Figure 8.13 (right column). The found formants, see Table 8.2, are compared with the first three formants of vowel [u:] from paper [143]. The behaviour of transfer functions for both models M1 and M2 is very similar, both show four formants in the range $50 - 2500$ Hz, M1 having an additional formant F5 at 2638 Hz (i.e. under 3 kHz). This resonance belongs to the subglottal part of the VT model, see Figure D.2 in Appendix D. The match of formants F1 and F2 is in the case M2 closer to the measured formants by Story than for the model M1. The third formant F3 has for both cases the same frequency 1432 Hz and the behaviour of transfer functions suggests that it is more damped than the others, for detailed discussion see Appendix D. The occurrence of F3 at this frequency contrary to results of [143] could be probably caused by the longer acoustic domain (the length of M1 and M2 domains are approximately 23 cm compared to Story's length of acoustic domain 18.25 cm). The M1 and M2 frequency of F4 lies in the vicinity of Story's reference F3.

All formants of model M3 are shifted up in the comparison with models M1 and M2, what can be explained by a shortening of the resonator length (i.e. $\Omega^a$). Further formant F2 of M3 is approximately 200 Hz higher than in cases M1 or M2 and it is rather close to the third resonant frequency. Finally model M4, the 2D version of published 3D vocal tract shape ([143]) without any inserted sound source domain (CFD domain) or prolongation region, has only three resonant frequencies in range $50 - 2500$ Hz as expected. The match of F1 is very good, F2 is significantly shifted up and formant F3 is underestimated by circa 150 Hz.

It should be mentioned that the comparison to the results of article [143] measured in humans during MRI examination is only inidicative due to multiple reasons. First, the scaling from 3D VT model to 2D can lead to a change of the formants location[2]. Second, the need to include the CFD domain significantly extends the VT model length and can also modify formants location. Finally paper [143] contains also numerical simulations of formants with completely different approach called the wave-reflection analog method, where multiple accoustic dissipation mechanisms and different boundary conditions were included, see [144]. Also his correspondence

[2] A different scaling from 3D model to 2D than used in the thesis was suggested e.g. by [23].

between the measured and the simulated formants was only up to 12% and even in a weaker agreement with the later reference[3].

Based on the previous results the VT models M1 and M2 are used for computations in Sections 8.3 and 8.4. For these models the match with Story's reference first three formants is acceptable and moreover both models M1 and M2 contrary to models M3 and M4 contain regions, where aeroacoustic or vibroacoustic sources were calculated. Model M1 includes the whole interface with the VFs and therefore it is used for the vibroacoustic calculations. Model M2, i.e. a wider version of the fluid flow domain with the prolongation part and without the subglottal area, is further used for the aeroacoustic computations.

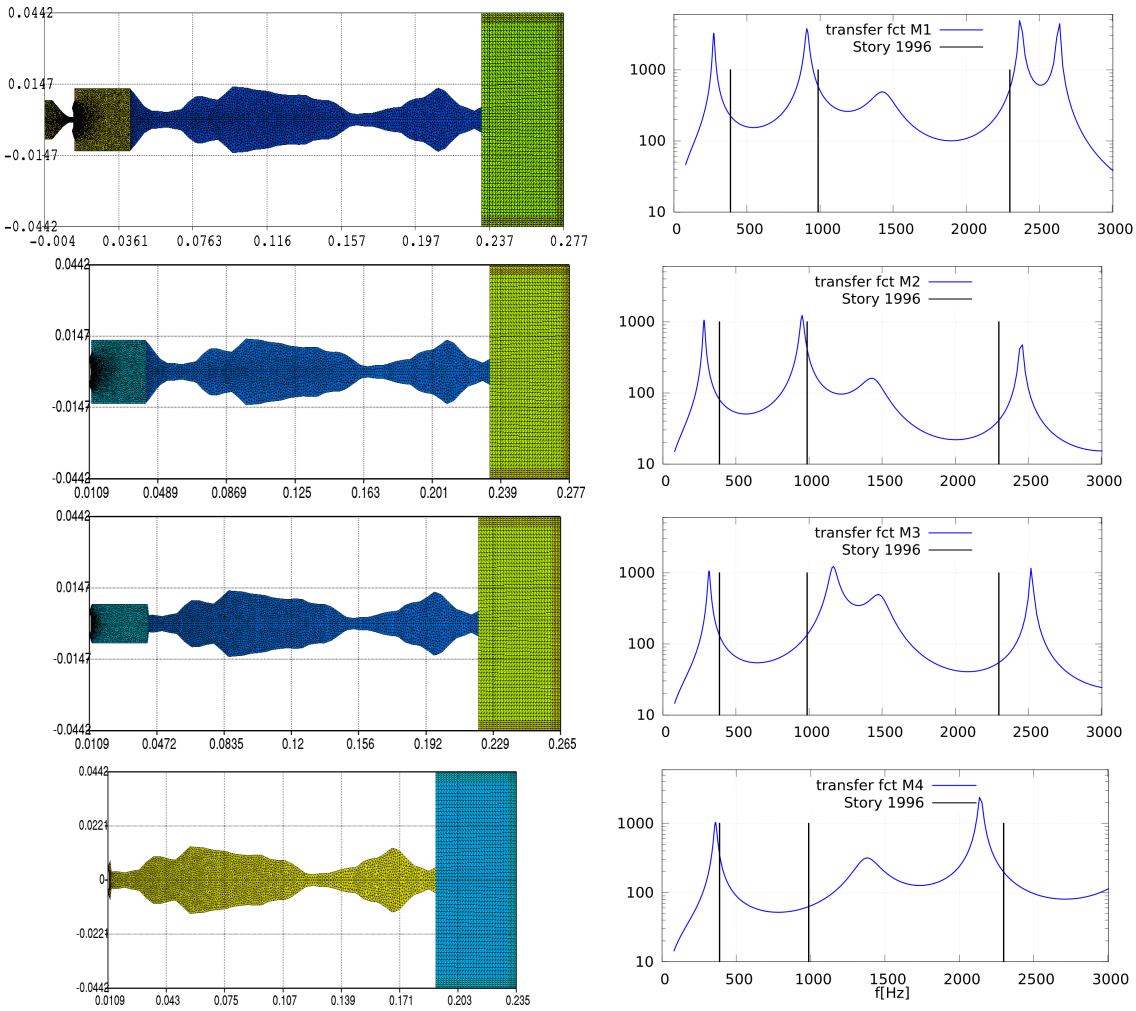


Figure 8.13: **Left:** Vocal tract acoustic models for cases M1-M4. **Right:** Graph of the computed transfer functions for given cases. The formants of the vowel [u:] are highlighted by black vertical lines located at $389, 987, 2299$ Hz (data from [143]).

[3]Story repeated his measurements and simulations with the same patients again in 2008. The VT shapes have changed and therefore also the formants, nevertheless his simulations showed much weaker agreement (27% error) than in 1996, see [141] and [23]

| | $F_1$ | $F_2$ | $F_3$ | $F_4$ |
|---|---|---|---|---|
| M1 | 271 | 909 | 1432 | 2365 |
| M2 | 280 | 952 | 1432 | 2440 |
| M3 | 313 | 1168 | 1478 | 2518 |
| M4 | 357 | 1388 | 2136 | 3313 |
| Story-meas | 389 | 987 | 2299 | – |
| Story-sim | 356 | 1108 | 2334 | – |

Table 8.2: Computed formant frequencies (in Hz) of the vocal tract models M1-M4. The measured (Story-meas) and the simulated (Story-sim) results for vowel [u:] from reference [143].

## 8.3 Vibroacoustic simulation

In this section the sound propagation is simulated, where the aeroacoustic sources are omitted and just the sound emitted by the vibrating vocal fold is taken into an account. Although the sound of vibroacoustic origin is usually considered to be small, see [171, 21], recent laboratory measurements of VF replica combined with numerical modelling [100] showed that the acoustic emission could be significant. It motivates this vibroacoustic study. The presented results are an extended version of results published in [15] and [5].

### 8.3.1 Acoustic domain

The acoustic problem as described in Chapter 6 is solved in acoustic domain $\Omega^a$, see Figure 8.14, i.e. the vocal tract model M1 from the previous section is considered. Two virtual microphones B and C are placed at positions $[x = 0.05, y = 0]$ m and $[x = 0.25, y = 0]$ m, respectively. Microphone B is located inside the CFD domain and microphone C is placed in the sound free field region, approximately 2 cm in front of the (virtual) mouth.

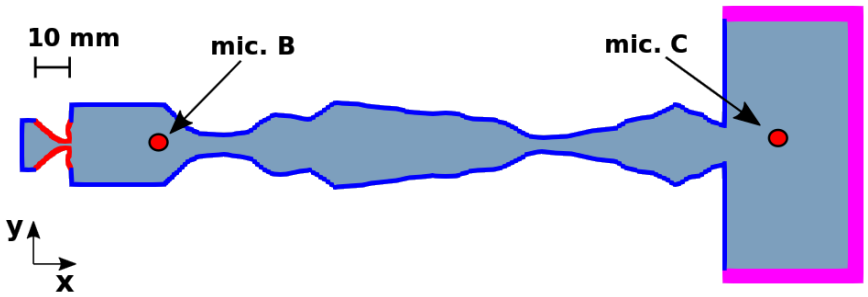


Figure 8.14: Scheme of acoustic domain $\Omega^a$ with boundaries. The blue boundary $\partial\Omega^a \setminus \Gamma_{W_0}$ is (sound) hard wall, the red boundary represents the interface of the vibrating vocal folds $\Gamma_{W_0}$ and the pink part marks five layers of PML elements. The positions of two virtual microphones B and C are shown.

### 8.3.2 Vibroacoustic results

The vibroacoustic model is given by equation (2.13) for unknown acoustic pressure $p^{\mathrm{va}}$ with the sound sources given by boundary condition (6.32), which reads

$$\frac{\partial p^{\mathrm{va}}}{\partial \mathbf{n}^a}(x,t) = -\rho^f \frac{\partial^2 \mathbf{u}}{\partial t^2} \cdot \mathbf{n}^a, \qquad x \in \Gamma_{\mathrm{W}_0},\ t \in (0,\mathrm{T}).$$

The right hand side represents the normal acceleration of the interface boundary, and it is determined by the FSI simulations, see Section 8.1. The solution of wave equation (2.13) by FEM follows as described in Section 7.3 with time step chosen as $\Delta t = 0.05\,\mathrm{ms}$ and with the speed of sound $c_0 = 343\,\mathrm{m/s}$. The propagation of acoustic pressure is monitored at two virtual microphones, Figure 8.15 shows time variations of the pressure at microphone C.

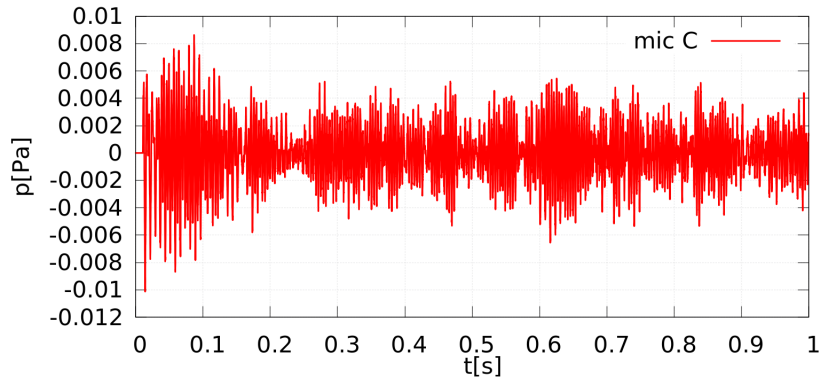


Figure 8.15: Acoustic pressure monitored at point C located in the free field region.

The Fourier transform of signals from both virtual microphones B and C are shown in Figure 8.16. The frequency spectrum of acoustic pressure at point B shows that the most dominant frequencies correspond approximately to the first two fundamental frequencies of VF vibration $(f_1, f_2)$ followed by the first two formants $(F_1, F_2)$ of VT model M1. The Fourier transform of the signal captured at point C exhibits the relative weakening of the first frequency peak 131 Hz and the relative strengthening of frequency 908 Hz perfectly matching the formant $F_2$. Also frequencies 2265 and 2495 Hz are more prominent in the signal at point C than at point B nevertheless these frequencies are shifted by approximately 100 Hz against the positions of M1 formants $F_4$ and $F_5$[4], see Table 8.2.

The sound induced by VF vibration is quite silent, the sound pressure level (SPL) at point C reaches circa 30 dB, see Figure 8.17. It is significantly less than the value obtained by the aeroacoustic simulation presented in the next section. The first two VF eigenfrequencies are again the very dominant frequencies, similarly as in [100] (pg. 161). Further the first two formants are also strongly represented in Figure 8.17, while the frequency peaks 2265 and 2495 Hz are less significant but clearly visible. The frequency of third formant $F_3$ is present but it has smaller intensity compared to the previously described ones.

[4]The formants are given by the location of the frequency peak plus not negligible bandwidth. Therefore the match of $F_4$ and $F_5$ with frequency peaks 2265 and 2495 Hz is still acceptable.

The presented vibroacoustic results show that the vibration-borne sound in the considered case without the VFs contact does not significantly contribute to the overall radiated SPL. These results of substantially lower SPL of the vibroacoustic origin than the aeroacoustically produced one (shown later) agree well with the simulations performed in [173]. On the other hand the combination of experimental and numerical results in [100] shows that the vibroacoustics is important in the case when a periodical contact of VFs occurs.

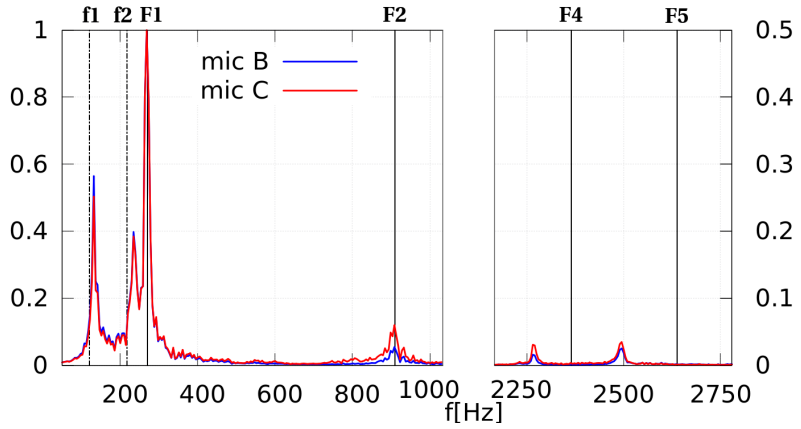


Figure 8.16: Normalised Fourier transform of pressure $p^{\mathrm{va}}$ from microphones B and C. Frequencies $f_1 = 121\,\mathrm{Hz}$ and $f_2 = 217\,\mathrm{Hz}$ highlighted by dot lines correspond to the first two eigenfrequencies of VFs, the other frequencies marked by $F_n, n \in \{1, 2, 4, 5\}$ are of acoustic origin and correspond to the formants of vocal tract model M1 (top axis notation). The missed frequency range $1050 - 2150\,\mathrm{Hz}$ does not contain any clearly visible resonant frequency. The right part of the figure has different scaling.

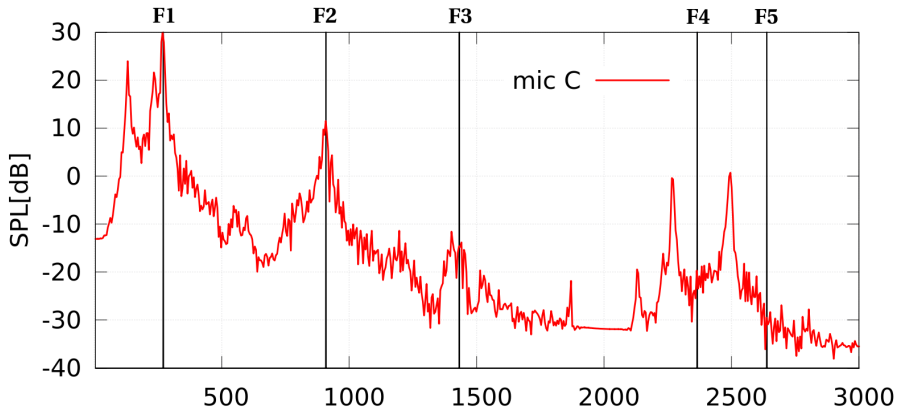


Figure 8.17: Sound pressure level in frequency domain computed from the pressure signal at point C. The black vertical lines demonstrate first five formants of vocal tract model M1.

## 8.4 Aeroacoustic simulation

This section presents the results of aeroacoustic simulations performed using the numerical results of FSI problem from Section 8.1. The sound sources are calculated as described in Section 7.2 and analyzed for all considered aeroacoustic approaches, namely the Lighthill analogy (further abbreviated as LH), the (simplified) PCWE as well as the AWE approach. This analysis is followed by the transient simulation of the produced sound propagation through vocal tract model M2. The resulting acoustic pressure measured in position C in front of the mouth is analyzed. The presented (and extended) results are primarily based on author's paper [2] and other published results [12, 8, 13].

### 8.4.1 Sound sources

First, the computed sound sources from the FSI results are analyzed in order to reveal the frequency content and its spatial distribution. Further, the computed acoustic sources are compared to their interpolations on the acoustic mesh.

#### Comparison of sound sources calculation

First, three different numerical methods for the LH sound source computation implemented in the program FSIFEM are confronted with the default LH sound source calculation in the program CSF++. Second, the sound sources of three different modelling approaches - LH, PCWE and AWE, are compared and discussed.

**LH sources.** The LH sound sources obtained by four different techniques are displayed in Figure 8.18 (more precisely the sound source densities, i.e. the sound sources scaled by the local triangle area). The first two pictures of Figure 8.18 capture the sound sources given by (7.15) and obtained with the gradient reconstruction technique described in Section 7.2 and without the reconstruction, here referred as pointwise evaluation (i.e. obtained by the numerical evaluation of derivatives at each triangle and the resulting vertex value averaged by the number of adjacent triangles), respectively. The fourth picture shows the sound sources based on pressure Laplacian (6.15), computed with the proposed gradient reconstruction technique but not weakly reformulated. These three methods are implemented in the program FSIFEM .

The third picture presents the LH sound sources based on formula (7.15) and obtained by the program CFSDat specialized on the numerical postprocessing of CFD data, a separate part of program CFS++ . The program CFSDat uses the framework of radial basis functions (RBF), i.e. a function $f$ is locally approximated by function with Gaussian kernel $f(x) \approx C \exp^{-\frac{x^2}{\alpha}}$ with shape parameter $\alpha$. This approach has the advantage of high accuracy, efficiency, robustness and optional inclusion of the interpolation procedure into one process, see [127]. Although a very higher order

of accuracy with increasing value of $\alpha$ (flattening of RBF shape) could be theoretically achieved, the increasing of the shape parameter above some optimal value significantly worsens the condition number of the interpolation matrix. The need of the shape parameter specification for optimal performance and accuracy could be regarded as the disadvantage of this method. For details see recent publication [130].

The LH sound sources obtained by the gradient reconstruction technique and by the pointwise evaluation are very similar, they differ only very slightly. The different local extreme values in the glottis region can be observed only in a zoomed detail[5] (not shown). The RBF approach provides the LH source evaluation with much more numerical noise, although the global sound source structure is captured well. In the end the pressure Laplacian represents an alternative formulation of the LH sound sources with the similar global structure of sources, nevertheless the local structure differs and a higher variability can be observed. A higher sensitivity of the pressure Laplacian to numerical noise was also reported by paper [151], where additional LH source formulations and comparisons can be found. By reason of minimizing numerical errors the LH sound sources obtained by the gradient reconstruction technique, which have the smallest local extremes, are used in further computations.

**Sound sources of different governing aeroacoustic approaches.** The sound sources computed on the CFD mesh for three different approaches – the LH analogy, the PCWE and the AWE approaches given by formulas (7.15), (7.10) and (7.13), respectively, are displayed in Figure 8.19. In the LH case the sound sources are primarily associated with the velocity gradients and in the current simulation they are greatly distributed downstream of the glottis, where the glottal jet creates strong shear layers as it enters the supraglottal spaces. There are also very significant sources in the vinicity of the VF boundary, where the glottal jet separates from the VF surface.

The dominant sound sources in the cases of the PCWE and the AWE approach are connected with pressure time changes, which local extremes are located primarily in the vortex centers. The vortices are formed by a complex decay of the glottal jet downstream the glottis. The difference of the PCWE against the AWE approach is that the sound sources are located more significantly inside the glottis due to included term with convected pressure gradient $\frac{1}{\rho_0 c_0^2}\overline{\mathbf{v}} \cdot \nabla p^{ic}$ – compare formulas (7.10) and (7.13). Particularly the large pressure gradient and the significant mean airflow velocity is present inside the glottis, see Figures E.2 and 8.8. The details of contributions from the time derivative and the convected pressure gradient term are plotted in Figure E.1 of Appendix E. The PCWE and the AWE sound sources are not so locally distributed around the supraglottal jet borders as the LH sources with an exception of the PCWE sound sources near the VF boundary, where the glottal jet separates from the VF surface. The outcomes obtained by the numerical postprocessing of the phase-locked PIV measurements, see pg. 136 of [100], or obtained by the numerical simulation, see pg. 121 of [82], resemble our findings.

[5]The LH sources obtained by the gradient reconstruction technique are in general the smallest compared to the other here presented evaluation approaches.

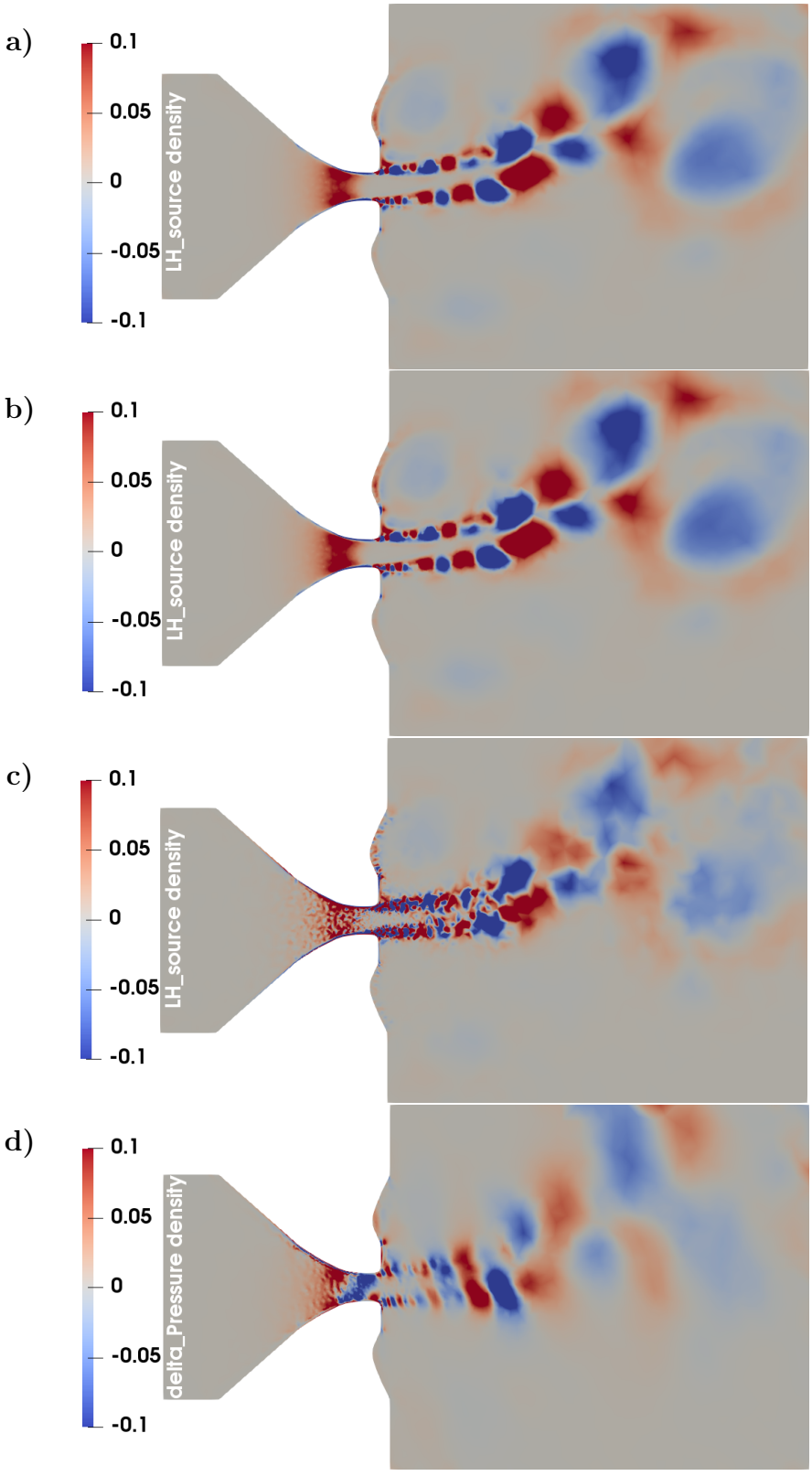


Figure 8.18: Comparison of (normalized) instant LH sound densities at time instant 0.6 s computed by: **a)** the gradient reconstruction technique, **b)** the pointwise evaluation, **c)** the RBF approach of program CFSDat (parameter $\alpha$ was chosen as $\alpha = 5 \cdot 10^{-7}$) and **d)** the pressure Laplacian.

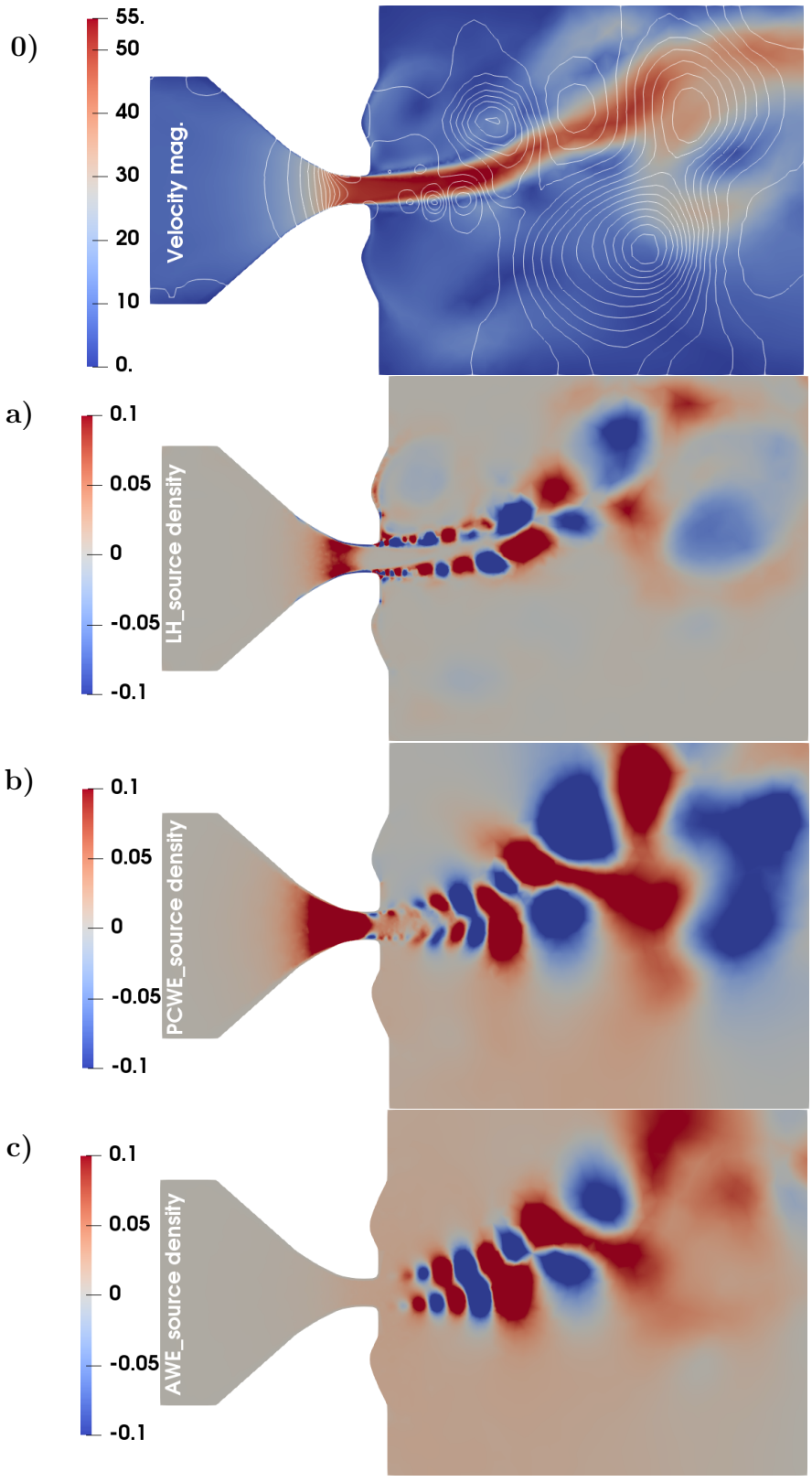


Figure 8.19: Comparison of (normalized) instant sound densities for different aeroacoustic approaches at time instant 0.6 s. **0)** The magnitude of airflow velocity together with 25 pressure contours in range $-2.5\,\mathrm{kPa}$ to $1.5\,\mathrm{kPa}$ is shown. Below instant sound densities are shown for: **a)** the LH analogy, **b)** the PCWE and **c)** the AWE approach.

### Frequency content

The frequency content of the sound sources can be investigated with the aid of the Fourier transform applied on the time signal at each point of the sound sources[6]. The power spectral densities (PSD) of the sound sources at two representative frequencies for all three aeroacoustic approaches are shown in Figure 8.20. The frequencies 232 Hz and 2486 Hz are the local spectral maxima representing one of the dominant VF vibration frequencies and an (higher) non-harmonic frequency, respectively. The quantitative comparison of sound sources PSD values is here irrelevant as in all cases a different acoustic quantity is depicted.

The location of main sound sources for frequency 232 Hz for all considered cases is inside the glottis. The frequency 232 Hz roughly corresponds to the second fundamental frequency of VF vibration, see Figure 8.4. The local structure of sound sources at 232 Hz matches the dipole source character (see Figure E.3 in Appendix E). In the LH case the dipole is located before the tip of VFs and it is less prominent than the quadrupole formed downstream from the narrowest part of the channel. In the PCWE and the AWE case the dipole clearly dominates. These findings coincide very well with the results of [139].

The higher frequency sources like e.g. at 2486 Hz (i.e. the frequency close to SPL maximum at $F_4$, see Figure 8.24) are mainly located in the supraglottal channel, see Figure 8.20 right. These sound sources can be associated with the free jet pouring out of an opening (glottis). They have quadrupole structure (see Figure E.3 in Appendix E) what is typical for sound aeroacoustically produced by free turbulence, see [96]. The AWE sound sources at 2486 Hz are situated in supraglottal area forming periodic series of vortices centers, while in the PCWE case such distinct points of PSD maximum are not observable. The PCWE sound sources at 2486 Hz are rather given by an union of two or three most dominants vortices centers. This can be caused by additional influence of the mean airflow velocity – cf. sound source formula 7.10, or possibly by the PSD calculation[7]. In the LH case the sound sources at 2486 Hz are located along boundaries of the glottal jet.

Globally, the LH sound sources are located predominantly in the vicinity of VF interface corresponding to high velocity gradients here, whereas the PCWE sources connected with time and spatial pressure derivative are slightly less compact. The AWE sound sources have a similar dipole character in the glottis and a larger spatial distribution of higher frequency content than the PCWE case. The similar sound sources frequency distributions were also reported by [139], [82] or by [100] on pg. 142.

### Interpolation to the acoustic mesh

Since the acoustic problem does not need so fine mesh as in the case of the fluid flow problem, the sound sources are projected onto a coarser acoustic mesh after their evaluation on the original CFD mesh resulting in the reduction of total computational time of the aeroacoustic simulation. The detail of the CFD and the acoustic

[6]The Fourier transform is evaluated on the CFD mesh.

[7]During PSD calculation the relevant acoustic quantities are raised to the second power.

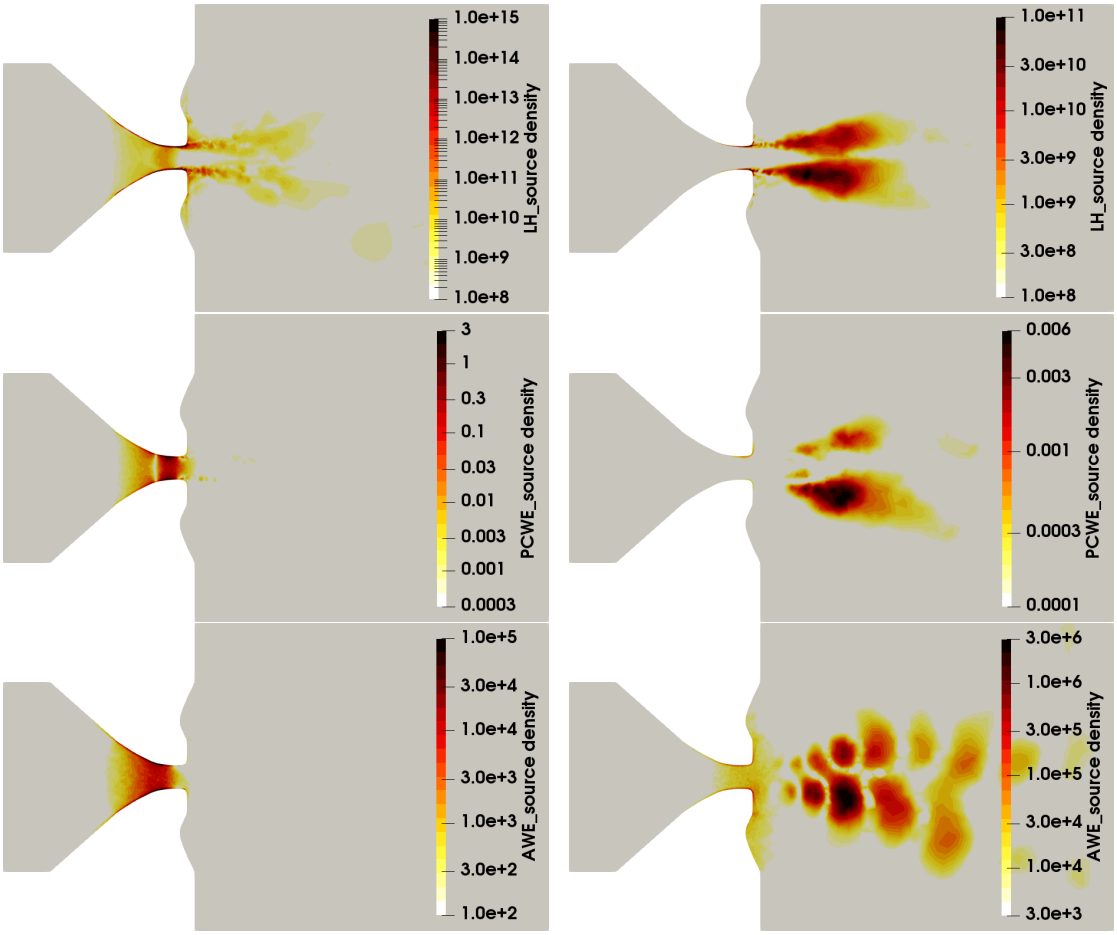


Figure 8.20: Computed power spectral densities of sound source densities at **232** Hz (left) and **2486** Hz (right). The LH results are shown in the top panel, the PCWE results in the middle, and the AWE results bottom. Color scale (and also acoustic quantities) is for each figure different and it has logarithmic scaling.

meshes in the narrowest part of the channel is depicted in Figure 8.21. The projection procedure, implemented in the program CFSDat and described in Section 7.2, conserves the overall acoustic energy, see [88], [127].

Figure 8.22 compares structure of the sound sources for three considered approaches before and after the interpolation. The sound sources structures are in all cases conserved, only the sound sources in the glottis area lose its relative significance (due to source weighting by elements area during the interpolation procedure, see Eq. (7.21)). The CFD and acoustic mesh consists of 12320 and 5078 elements, resp.

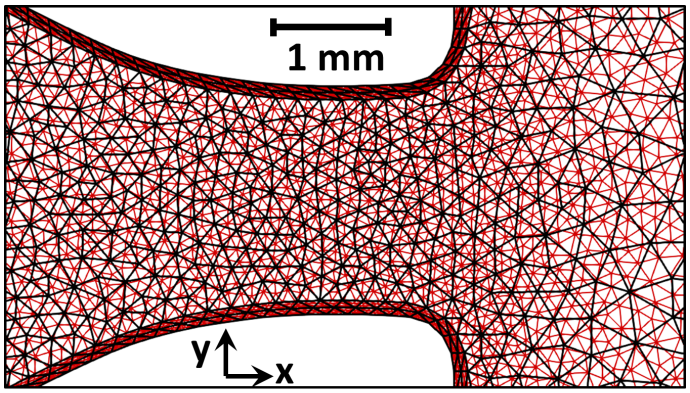


Figure 8.21: Detail of the CFD and the acoustic meshes inside the glottis region. The dense CFD mesh is shown in red colour and the acoustic mesh is plotted with black colour.

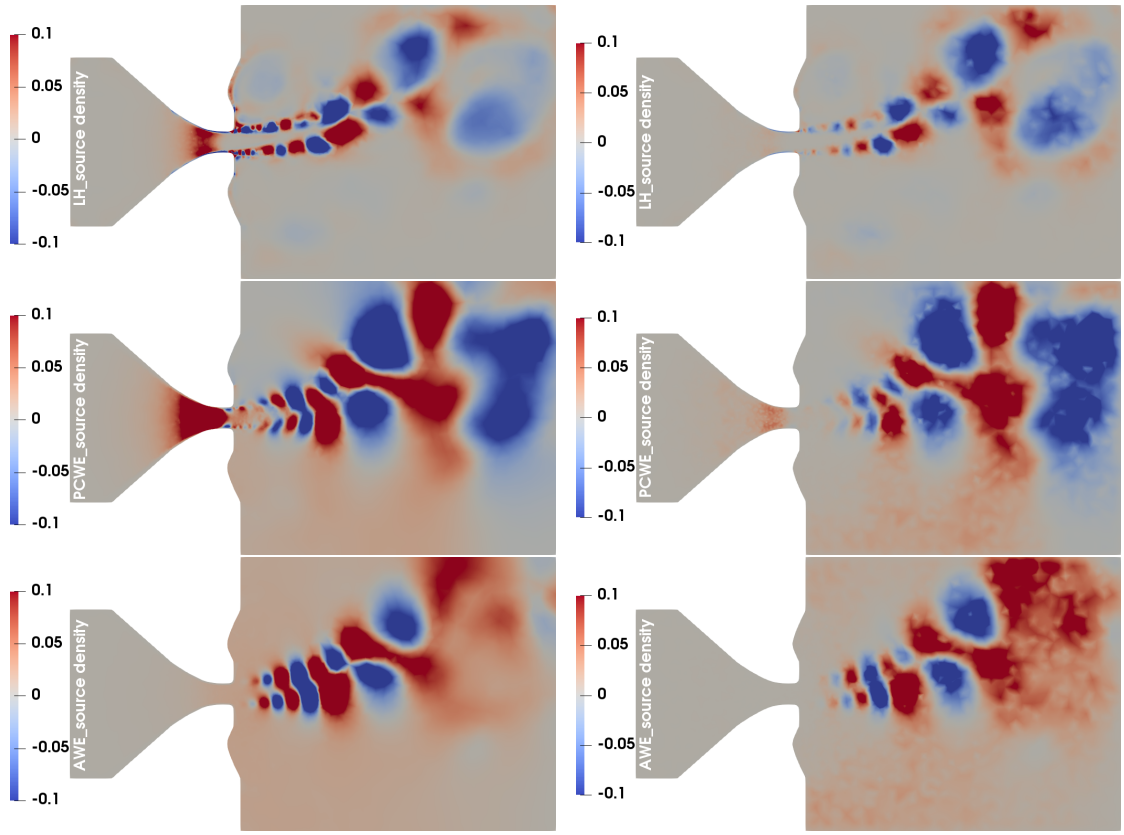


Figure 8.22: Sound source densities **before** (left) and **after** (right) interpolation on the (coarser) acoustic domain of vocal tract model M1. The LH sound sources are shown on the top, the PCWE sources in the middle panel and the AWE sources at the bottom.

### 8.4.2 Sound propagation in the vocal tract model

The interpolated sound sources are further employed for the LH, the simplified PCWE (sPCWE) and the AWE aeroacoustic simulations as formulated in paragraph 6.2.3 and numerically discretized by the FEM as described in Chapter 7. The vocal tract model M2 is chosen as acoustic domain $\Omega^a$. Consequently the subglottal sound sources are omitted as the VT model M2 does not contain glottis, see Figure 8.13. Further, the speed of sound is considered as $c_0 = 343\,\mathrm{m/s}$ and time step $\Delta t = 0.025\,\mathrm{ms}$ is kept constant. The acoustic pressure is monitored at the same microphone positions as before, i.e. at point B $= [0.05\,\mathrm{m}, 0\,\mathrm{m}]$ inside CFD domain and at point C $= [0.25\,\mathrm{m}, 0\,\mathrm{m}]$ in front of virtual mouth, see Figure 8.14.

The acoustic pressure (computed by all approaches) monitored at point B is shown in terms of the Fourier transform in Figure 8.23. The most significant frequencies are determined as 278 Hz and 942 Hz corresponding quite accurately to the first two formants $(F_1, F_2)$ of model M2, see Section 8.2. The results of the Lighthill analogy have rather a single dominant frequency 278 Hz and the significance of the second frequency 942 Hz is rather fractional. The frequency spectra of the sPCWE and the AWE approaches are almost equal. They are dominated equally by both formant frequencies $F_1$ and $F_2$ in contrast to the LH case. The frequency spectra over 1100 Hz are practically negligible with a very little locally increased value around 2400 Hz in the sPCWE and the AWE cases (not shown). Short series of snapshots illustrating the aeroacoustic simulation is shown in Figure E.5 of Appendix E.

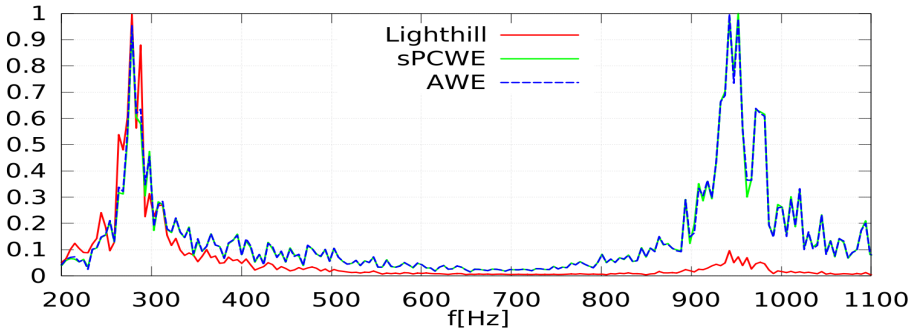


Figure 8.23: Normalized Fourier transform of acoustic pressure at point B obtained by the LH analogy, the sPCWE and the AWE approaches. The results were averaged by Welch method, see [165].

The sound pressure levels computed at point C using all three aeroacoustic approaches are shown in Figure 8.24. In the frequency range up to 3 kHz all three approaches detect four frequency peaks matching very well the first four formants of the vocal tract model M2, but there are substantial differences in the SPL maxima. For the LH case the first frequency of 278 Hz reaches the highest SPL of circa 135 dB followed by frequency peaks 942 Hz and 2421 Hz, each gradually lowered by approximately 20 dB. The sPCWE and the AWE approaches provides almost mutually indistinguishable results which differ only by an increase of incomplete 2 dB in the AWE case. Both of these approaches are able to predict all four formants with more equal distribution of SPL, where the most significant peak with circa 110 dB

is located at the frequency of $F_2$ contrary to the LH case. This is in agreement with [100] (see pg. 133), where the SPL of the LH simulation was also found to be clearly dominated by the first frequency peak and for the PCWE and the AWE results a very tiny SPL difference ($< 1$ dB) was observed. As there are only very little differences in the resulting spectra one can benefit from use of the AWE approach which is computationally less expensive than the (s)PCWE, see also [100]. The same character of acoustic results for all three considered approaches were also achieved with the VT model M1 (replacing the VT model M2), i.e. with the VT model with the included sub- as well as supraglottal spaces, see Figure E.4 in Appendix E.
A similar SPL difference of approximately by 20 dB higher SPL of LH approach (total SPL circa 90 dB) than in the PCWE case reaching approx. 70 dB was reached by the 3D numerical simulation, see [139]. Further, we regard in agreement with authors of [139] the SPL results of LH analogy as overestimated due to not performed the acoustic/hydrodynamic splitting resulting in the superimposition of hydrodynamic quantities in the sound sources represented by Lighthill tensor.

On the other hand the presented SPL results show rather high pressure levels exceeding 130 dB and 110 dB for the LH and the sPCWE/AWE cases, respectively. It is comparable to a loud singing/crying very close to listener's ear. The high values of SPL are probably caused first by a generally different 2D fluid flow dynamics contrary to more complex 3D fluid flow dynamics (having impact on the aerodynamical sound sources). Second there are fundamental differences in wave propagation for 2D formulation compared to 3D setup[8]. Similar aeroacoustic studies of the 2D flow-induced VF vibrations reached comparable high levels of SPL albeit the microphone position was in the CFD domain, see [173], [89].
In the end comparing the presented vibroacoustic and aeroacoustic simulations, where the aerodynamically generated sound is about 100 dB higher in SPL than the sound of the vibroacoustic origin (see Fig. 8.17), it can be concluded that the aerodynamically produced sound is a major sound source of human phonation mechanism in the case without contact of VFs.

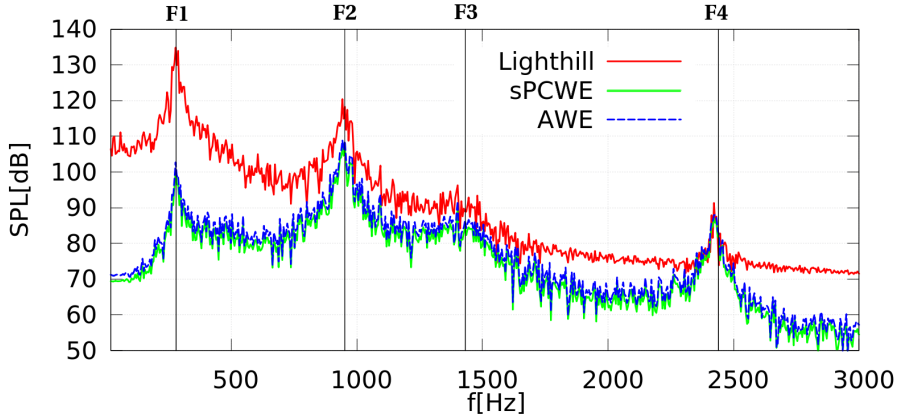


Figure 8.24: Sound pressure levels of acoustic pressure in frequency domain obtained by the LH analogy, the sPCWE and the AWE approaches at point C. The black vertical lines mark the formants of vocal tract model M2, see Table 8.2.

[8]Hence, some studies introduce SPL results correction from 2D to 3D sound radiation, see [100].

# Chapter 9

# Conclusion

**The first part** of the thesis presents the FSI problem in a channel with deformable walls conveying fluid. The mathematical formulation of FSI problem is based on the linear elasticity model and the viscous incompressible Navier-Stokes equations written in the ALE formulation in order to take into account the time-dependence of the flow domain. The numerical approximation of the FSI problem is performed with the finite element method in space and the finite difference method in time. Particularly, the fluid flow stabilization, the computation of aerodynamic forces and the construction of ALE mapping is described in detail. The strongly coupled partitioned algorithm is implemented for the solution of the FSI problem.

Further, a special attention is paid to the penalization inlet boundary condition which allows to relax an exact value of the inlet velocity at the inlet boundary during channel closing phase. The presented results contain the sensitivity test of flow characteristics in dependence on the change of the penalization parameter. A such suitable value of parameter $\epsilon$ can be found that the maximal pressure matches the desired benchmark value. In the considered simulation of flow-induced VFs vibration the recommended value lies in range $2 \cdot 10^{-4} < \epsilon < 1 \cdot 10^{-3}$. Next, the influence of the penalization parameter on the critical flutter velocity, i.e. the highest inflow velocity before loss of FSI system stability, is also studied. It is demonstrated in the presented FSI simulations that the flutter value changes very slowly up to value $\epsilon < 10^{-4}$ and then the flutter velocity starts to grow significantly for bigger values of $\epsilon$. The applicability of penalization BC is documented on FSI problems with and without the considered symmetry arrangement of the channel. The penalization BC together with the described FSI numerical model based on the FEM is implemented in the in-house program FSIFEM .

The FSI results modelling the human phonation are presented, which were achieved with a 2D geometry model of vocal fold composed of isotropic elastic material without consideration of detailed geometry of supraglottal spaces, e.g. without model of ventricular folds. This setting of the FSI problem allow to determine the flutter velocity, to compute flow rate through the glottis, to evaluate pressure distribution along the whole channel, to investigate the VF vibration shapes, to analyze the energy transfer between vibrating vocal fold and flow as one of the important predictor of stability of the aeroelastic system, etc.

**The second part** of the thesis is devoted to the mathematical modelling of acoustic problems connected with the human phonation. Two models of sound production are described, namely the vibroacoustic problem studies sound produced solely by vibrating boundary of an elastic body (e.g. vocal folds) and the aeroacoustic problem deals with generation and propagation of the sound with aerodynamic origin. The aeroacoustic part is addressed using the hybrid approach. It allows to predict sound based on the incompressible flow simulation, i.e. to use more appropriate and computationally less demanding acoustic solver than the solver of compressible flow and to simulate acoustic problem in larger domains, etc. On the other hand the hybrid methodology omits the influence of acoustics on the flow field. This is usually acceptable for low acoustic intensities.

The main novelty of the presented aeroacoustic approach is given by the connection between the FSI simulation with apriori unknown structure motion excited by the airflow and the acoustics solved in the acoustic propagation domain with included vocal tract model. This setting enables to obtain relevant aeroacoustic results. Nevertheless, the inclusion of the vocal tract model into the acoustic domain implicitly assumes the validity of source-filter theory, i.e. that the vocal tract model does not influence the acoustic sources at the glottis region. This assumption is often satisfied unless the formant frequencies of the vocal tract are very close to the fundamental frequency of VF oscillations. The hybrid methodologies supposing low acoustic intensities and validity of the source-filter theory can be applied in the simulations of falsetto, whispering, breathy voice or a silent singing.

The FSI results, used in the vibroacoustic and the aeroacoustic models as input for the sound source computation, were obtained with a four-layer VF model using the reference pre-phonation glottal gap 2.0 mm and a prescribed value of the pressure drop lying in the stable region.

The frequency characteristics of several vocal tract models were investigated in order to identify first formants. The resonant frequencies of vocal tracts are highly dependent on chosen boundary conditions (similarly as e.g. different frequencies of open and closed organ tube). The lowest four formants were obtained by the numerical solution of the Helmholtz equation in a 2D vocal tract with the considered PML technique modelling the radiation outside mouth and with the sound hard BC applied at boundaries of given vocal tract model. The determined formants match the laboratory measured formants in an acceptable way. The locations of resonant frequencies of the vocal tract models obtained by the presented approach agree very well with the later results of the vibroacoustic and the aeroacoustic simulations.

The vibroacoustic simulation presents the results of the sound propagation excited by the VF walls vibration. In the acoustic spectra monitored inside CFD domain it is clearly visible the first two eigenfrequencies of VF model together with formants of chosen vocal tract model. The higher harmonics of VF vibration are not present (naturally, as the VF contact did not occur). The resulting SPL composed of relevant acoustic frequency spectrum is considerably low in comparison with the SPL of aerodynamically produced sound.

Finally, the aeroacoustic simulations comprise the sound sources evaluation, the

sound sources interpolation on the acoustic mesh and the sound sources propagation through the vocal tract model. As the sound sources computation is of key importance a special care is paid to the sound source numerical computation including a few alternative sound source formulations. The computed sound sources are qualitatively compared indicating that the LH sound sources calculated with the local reconstruction technique are less noisy compared to the default sound source computation used in the program CFS++ . The frequency content of sound sources are also investigated showing the location of major sound sources at the VF harmonic frequencies is directly at the glottis or nearby. The sound sources of higher frequencies are rather located in the supraglottal areas.

The designed interpolation reduces the computational time while keeping the original sound source structure unchanged. The advantage of interpolation is growing mainly for 3D setup as the number of unknowns scales more unfavourably. The sound propagation results compare three different approaches, namely the LH analogy, the simplified PCWE and the AWE approach. The sound signals outside the mouth have frequency spectra consisting of all four formants of the used vocal tract model. The resulting SPL of LH analogy obviously overestimates the lower frequencies, especially the formants F1 and F2. The sPCWE and the AWE approaches provide almost the same acoustic results having more uniform spectral distribution compared to the LH results. Therefore the AWE approach is in considered human phonation simulation the best choice in the perspective of ratio of the result relevance to the computational cost.

## 9.1 Achieved results

The objectives of the dissertation as they were formulated in Introduction are achieved, namely:

- The behaviour of new penalization inlet boundary condition was studied for the internal aerodynamics configurations when the channel is closing. The comparison of the penalization inlet BC with the Dirichlet BC and the prescribed pressure drop was extensively described. The closing channel up to the half-gap value of 10 $\mu$m with reasonable pressure values was demonstrated for the VF prescribed motion in Chapter 5 indicating a promising way towards the modelling of the complete channel closure.

- The methodology how to find the stability boundary of the modelled aeroelastic system was developed for the classical Dirichlet BC and also for a wide range of penalization parameters in the case of the penalization BC at the inlet, see Section 5.3.

- The connection between the in-house solver FSIFEM and the academic solver CFS++ of TU Vienna was established. The program FSIFEM now supports an output in the file format HDF5, see [1].

- A special attention was paid to the sound sources computation. For the LH analogy the numerical procedure based on the local reconstruction technique was proposed and further its applicability was shown, see Chapters 7 and 8. This procedure provides better results during numerical postprocessing of the 2D flow results obtained by the solver FSIFEM than the default procedure of the subprogram CFSDat, based on the radial basis functions approach.

- The aeroacoustic simulations were performed by using the three different aeroacoustic approaches. Their description and numerical realization as the final step of the FSAI algorithm is given in Chapters 6 and 7. Further, the computed sound sources are analyzed and finally the spectra of produced sound in the point in front of the mouth are compared using the three approaches. The capability of chosen hybrid approach for the aeroacoustic simulation of human phonation was proven by several numerically solved examples, see Chapter 8.

- The simulated sound of the vibroacoustic origin, see Section 8.3, was found quite low suggesting to be relatively insignificant sound source in human phonation (at least for the presented FSI simulation without complete closure of the glottis and without VFs collision).

## 9.2 Research outlook

The developed computational model of the FSAI problem has demonstrated the capability to simulate the complex flow-induced VF vibrations and the produced vibroacoustic and aeroacoustic sound. In the near future, I would like to extended the work in several directions:

- Aeroacoustics based on the FSI simulation with penalization BC at the inlet. In the first step the aeroacoustic simulation can be based on the simplified FSI problem with given VF vibration. Nevertheless at least ten VF vibration cycles are needed for basic resolution of simulated acoustic phenomena, see e.g. [131]. Some very preliminary results were already presented at *Workshop: Strömungsschall in Luftfahrt, Fahrzeug- und Anlagentechnik, 2019*.
- Implementation of glottal channel closure based on the presented FSI model together with the penalty inlet boundary condition. Further model modification probably including remeshing and/or changing governing equations to incorporate some velocity attenuation in the glottis region will be necessary.
- Modelling of contact during vocal folds collisions. For a general VF shape it can be quite difficult task due to need of finding contact points on the interface represented by a general curve and further to calculate the contact force at each relevant point of the VF tissue.
- Further, I would like to incorporate the following problems in the FSAI model:
  - Consider the nonlinear elasticity in order to more precisely model the large deformations of the VF tissue.
  - Improve the larynx geometry to be more realistic, e.g. to include the ventricular vocal folds.

Another, for human phonation highly important modelling challenges can be found in the conclusion of papers [105] and [57].

# References

## Author's publications


[1] *FSIFEM*, https://github.com/jvalasek/FSIfem/, 1.6.2019 [software].

[2] J. Valášek, M. Kaltenbacher, and P. Sváček, *On the application of acoustic analogies in the numerical simulation of human phonation process*, Flow, Turbulence and Combustion **102**:1 (2019), 129–143.

[3] J. Valášek, P. Sváček, and J. Horáček, *Numerical solution of fluid-structure interaction represented by human vocal folds in airflow*, EFM15 – Experimental Fluid Mechanics 2015 (V. M. and D. P., eds.), vol. 114, EPJ Web of Conferences, mar 2016.

[4] J. Valášek, P. Sváček, and J. Horáček, *On suitable inlet boundary conditions for fluid-structure interaction problems in a channel*, Applications of Mathematics **64**:2 (2019), 225–251.

[5] J. Valášek, P. Sváček, and J. Horáček, *Fluid-structure-acoustic interaction problem in modelling of human vocal folds vibration*, Proceedings of the Conference Algoritmy 2020 (P. Frolkovič, K. Mikula, and D. Ševčovič., eds.), Publishing House of Slovak University of Technology in Bratislava, 2020, pp. 81–90.

[6] J. Valášek, P. Sváček, and J. Horáček, *The flow-induced vibrations of vocal folds approximated by the finite element method*, , Lecture Notes in Mechanical Engineering, Springer, 2021, pp. 377–388.

[7] J. Valášek, P. Sváček, and J. Horáček, *Numerical approximation of fluid-structure interaction problem in a closing channel near the stability boundary*, Numerical Mathematics and Advanced Applications ENUMATH 2019 (F. Vermolen and C. Vuik, eds.), Lecture Notes in Computational Science and Engineering, vol. 139, Springer International Publishing, 2021.

[8] J. Valášek, M. Kaltenbacher, and P. Sváček, *The comparison of different acoustic approaches in the simulation of human phonation*, Coupled Problems in Science and Engineering VII (E. O. Manolis Papadrakakis and B. Schrefler, eds.), International Center for Numerical Methods in Engineering (CIMNE), 2017, pp. 661–672.

[9] J. Valášek, and P. Sváček, *Finite element approximations of fluid-structure interaction problems: numerical analysis of three approaches of aerodynamic forces evaluation*, Topical problems of fluid mechanics 2021 (D. Šimurda and T. Bodnár, eds.), Institute of Thermomechanics, AS CR, 2021, pp. 140–148.

[10] J. Valášek, P. Sváček, and J. Horáček, *The influence of different geometries of human vocal tract model on resonant frequencies*, Topical problems of fluid mechanics 2018 (D. Šimurda and T. Bodnár, eds.), Institute of Thermomechanics, AS CR, 2018, pp. 307–314.

[11] J. Valášek, P. Sváček, and J. Horáček, *Aerodynamic transfer of energy to vibrating vocal folds for different driving mechanisms*, Topical problems of fluid mechanics 2019 (D. Šimurda and T. Bodnár, eds.), Institute of Thermomechanics, AS CR, 2019, pp. 197–204.

[12] J. Valášek, M. Kaltenbacher, and P. Sváček, *The application of Lighthill analogy on the numerical simulation of human phonation*, Topical problems of fluid mechanics 2017 (D. Šimurda and T. Bodnár, eds.), Institute of Thermomechanics, AS CR, 2017, pp. 303–312.

[13] J. Valášek, P. Sváček, and J. Horáček, *The numerical simulation of human phonation*, Computational Mechanics 2018 – Book of Extended Abstracts, University of West Bohemia, 2018, pp. 127–128.

[14] J. Valášek, P. Sváček, and J. Horáček, *The influence of penalization inlet boundary condition on the stability boundary*, Proceedings of Computational Mechanics 2019, University of West Bohemia, 2019, pp. 212–215.

[15] J. Valášek, P. Sváček, and J. Horáček, *The investigation of acoustical signal induced by vibrations of human vocal folds*, Studentská tvůrčí činnost 2018 - sborník konference (J. Moravec, ed.), České vysoké učení technické v Praze, Fakulta strojní, apr 2018.

## Bibliography

[16] *Intel math kernel library*, https://software.intel.com/en-us/mkl, 1.6.2019 [software].

[17] *Hierarchical data format of version 5*, https://www.hdfgroup.org/solutions/hdf5/, 1.6.2020 [software].

[18] *Website about vocal technique*, http://www.vocaltechniquetips.com/how-the-voice-works/the-vocal-cords, December 2018.

[19] R. Abgrall, H. Beaugendre, and C. Dobrzynski, *An immersed boundary method using unstructured anisotropic mesh adaptation combined with level-sets and penalization techniques*, Journal of Computational Physics **257** (2014), 83–101.

[20] R. A. Adams, *Sobolev spaces*, Academic Press, 1975.

[21] F. Alipour, C. Brucker, D. D Cook, A. Gommel, M. Kaltenbacher, W. Mattheus, L. Mongeau, E. Nauman, R. Schwarze, I. Tokuda, et al., *Mathematical models and numerical schemes for the simulation of human phonation*, Current Bioinformatics **6**:3 (2011), 323–343.

[22] J. D. J. Anderson, *Fundamentals of aerodynamics*, 6th edition ed., McGraw-Hill Education, 2017.

[23] M. Arnela, *Numerical production of vowels and diphthongs using finite element methods*, Ph.D. thesis, La Salle, Universitat Ramon Llull, Barcelona, 2014.

[24] I. Babuška, T. Strouboulis, S. Gangaraj, and C. Upadhyay, *Validation of recipes for the recovery of stresses and derivatives by a computer-based approach*, Mathematical and computer modelling **20**:6 (1994), 45–89.

[25] I. Babuška, *The finite element method with penalty*, Mathematics of Computation **27**:122 (1973), 221–228.

[26] S. Badia, F. Nobile, and C. Vergara, *Fluid–structure partitioned procedures based on Robin transmission conditions*, Journal of Computational Physics **227**:14 (2008), 7027–7051.

[27] Y. Bae and Y. J. Moon, *Computation of phonation aeroacoustics by an ins/pce splitting method*, Computers & Fluids **37** (2007), 1332 – 1343.

[28] C. Bailly and D. Juve, *Numerical solution of acoustic propagation problems using linearized euler equations*, AIAA journal **38**:1 (2000), 22–29.

[29] M. Balázsová, J. Česenek, M. Feistauer, P. Sváček, and J. Horáček, *Comparison of numerical methods for the solution of viscous incompressible and low Mach number compressible flow*, Computers & Fluids **174** (2018), 167–178.

[30] G. Batchelor, *An introduction to fluid dynamics*, Cambridge university press, 2000.

[31] K.-J. Bathe, *Finite element procedures*, Prentice Hall, 1996.

[32] J.-P. Berenger, *A perfectly matched layer for the absorption of electromagnetic waves*, Journal of computational physics **114**:2 (1994), 185–200.

[33] D. T. Blackstock, *Fundamentals of physical acoustics*, Wiley, 2000.

[34] T. Bodnár, G. P. Galdi, and v. Nečasová, *Fluid-structure interaction and biomedical applications*, Springer, 2014.

[35] M. Braack and P. B. Mucha, *Directional do-nothing condition for the Navier-Stokes equations*, Journal of Computational Mathematics **32** (2014), 507–521.

[36] M. Brdička, L. Samek, and B. Sopko, *Continuum mechanics*, Academia, 2000.

[37] R. W. Chan and I. R. Titze, *Viscoelastic shear properties of human vocal fold mucosa: measurement methodology and empirical results*, The Journal of the Acoustical Society of America **106**:4 (1999), 2008–2021.

[38] B.-T. Chu and L. S. G. Kovásznay, *Non-linear interactions in a viscous heat-conducting compressible gas*, Journal of Fluid Mechanics **3**:5 (1958), 494–514.

[39] P. G. Ciarlet, *The finite element methods for elliptic problems*, North-Holland Publishing, 1979.

[40] R. Clark and E. H. Dowell, *A modern course in aeroelasticity*, Springer, 2004.

[41] D. Crighton, *Computational aeroacoustics for low Mach number flows*, Computational aeroacoustics (J. C. Hardin and M. Y. Hussaini, eds.), Springer, 1993, pp. 50–68.

[42] A. Curnier, *Computational methods in solid mechanics*, Springer, 1994.

[43] D. J. Daily and S. L. Thomson, *Acoustically-coupled flow-induced vibration of a computational vocal fold model*, Computers & Structures **116** (2013), 50–58.

[44] T. A. Davis, *Direct methods for sparse linear systems*, SIAM, 2006.

[45] M. De Vries, H. Schutte, A. Veldman, and G. Verkerke, *Glottal flow through a two-mass model: comparison of navier–stokes solutions with simplified models*, The Journal of the Acoustical Society of America **111**:4 (2002), 1847–1853.

[46] J. Delfs, *Basics of aeroacoustics*, Technische Universitaet Braunschweig, 2016.

[47] N. G. Diez, S. Belfroid, and J. Golliard (eds.), *Flow-induced vibration & noise, proceedings of 11th international conference on flow induced vibration & noise*, TNO, Delft, The Hague, the Netherlands, 2016.

[48] J. S. Drechsel and S. L. Thomson, *Influence of supraglottal structures on the glottal jet exiting a two-layer synthetic, self-oscillating vocal fold model*, The Journal of the Acoustical Society of America **123**:6 (2008), 4434–4445.

[49] R. P. Dwight, *Robust mesh deformation using the linear elasticity equations*, Computational Fluid Dynamics 2006 (H. Deconinck and E. Dick, eds.), Springer Berlin Heidelberg, Berlin, Heidelberg, 2009, pp. 401–406.

[50] N. Edgar and M. Visbal, *A general buffer zone-type non-reflecting boundary condition for computational aeroacoustics*, 9th AIAA/CEAS Aeroacoustics Conference and Exhibit, 2003, p. 3300.

[51] H. C. Elman, D. J. Silvester, and A. J. Wathen, *Finite elements and fast iterative solvers: with applications in incompressible fluid dynamics*, Oxford University Press, USA, 2014.

[52] A. Ern and J. Guermond, *Theory and practice of finite elements*, Springer, New-York, 2004.

[53] R. Ewert and W. Schröder, *Acoustic perturbation equations based on flow decomposition via source filtering*, Journal of Computational Physics **188**:2 (2003), 365–398.

[54] G. Fant, *Acoustic theory of speech production*, Hague, 1960.

[55] M. Feistauer, *Mathematical methods in fluid dynamics*, Taylor & Francis, 1993.

[56] M. Feistauer, J. Felcman, and I. Straškraba, , Numerical mathematics and scientific computation, Oxford University Press, 2003.

[57] M. Feistauer, P. Sváček, and J. Horáček, *Numerical simulation of fluid-structure interaction problems with applications to flow in vocal folds*, Fluid-structure Interaction and Biomedical Applications (T. Bodnár, G. P. Galdi, and S. Nečasová, eds.), Birkhauser, 2014, pp. 312–393.

[58] J. Ffowcs Williams and D. L. Hawkings, *Sound generation by turbulence and surfaces in arbitrary motion*, Philosophical Transactions of the Royal Society of London A: Mathematical, Physical and Engineering Sciences **264**:1151 (1969), 321–342.

[59] J. Flanagan and L. Landgraf, *Self-oscillating source for vocal-tract synthesizers*, IEEE Transactions on Audio and Electroacoustics **16**:1 (1968), 57–64.

[60] L. Formaggia, N. Parolini, M. Pischedda, and C. Riccobene, *Geometrical multi-scale modeling of liquid packaging system: an example of scientific cross-fertilization*, 19th European Conference on Mathematics for Industry, 2016, p. 6.

[61] C. Förster, W. Wall, and E. Ramm, *On the geometric conservation law in transient flow calculations on deforming domains*, International Journal for Numerical Methods in Fluids **50**:12 (2006), 1369–1379.

[62] C. Föster, *Robust methods for fluid-structure interaction with stabilised finite elements*, Ph.D. thesis, Institut fuer Baustatik und Baudynamik der Universitaet Stuttgart, 2007.

[63] T. Gelhard, G. Lube, M. Olshanskii, and J.-H. Starcke, *Stabilized finite element schemes with LBB-stable elements for incompressible flows*, Journal of Computational and Applied Mathematics **177**:2 (2005), 243–267.

[64] V. Girault and P. A. Raviart, *Finite element methods for Navier-Stokes equations*, Springer-Verlag, 1986.

[65] X. Gloerfelt and P. Lafon, *Direct computation of the noise induced by a turbulent flow through a diaphragm in a duct at low mach number*, Computers & Fluids **37**:4 (2008), 388–401.

[66] M. J. Grote and I. Sim, *Efficient pml for the wave equation*, arXiv preprint arXiv:1001.0319 (2010).

[67] P. Hájek, P. Švancara, J. Horáček, and J. G. Švec, *Numerical simulation of the self-oscillating vocal folds in interaction with vocal tract shaped for particular czech vowels*, Recent Global Research and Education: Technological Challenges, Springer, 2017, pp. 317–323.

[68] C. Hansen, *Foundations of Vibroacoustics*, CRC Press, 2018.

[69] J. Hardin, *Regarding numerical considerations for computational aeroacoustics*, Computational aeroacoustics (J. C. Hardin and M. Y. Hussaini, eds.), Springer, 1993, pp. 216–228.

[70] J. Hardin and D. Pope, *An acoustic/viscous splitting technique for computational aeroacoustics*, Theoretical and Computational Fluid Dynamics **6**:5 (1994), 323–340.

[71] A. Hirschberg, *Some fluid dynamic aspects of speech*, Bulletin de la Communication Parlee **2** (1992), 7–30.

[72] J. Horáček, A.-M. Laukkanen, P. Šidlof, P. Murphy, and J. Švec, *Comparison of acceleration and impact stress as possible loading factors in phonation: A computer modeling study*, Folia Phoniatrica et Logopaedica **61** (2009), 137–145.

[73] J. Horáček, V. V. Radolf, V. Bula, and J. Košina, *Experimental modelling of phonation using artificial models of human vocal folds and vocal tracts*, Engineering Mechanics 2017 (V. Fuis, ed.), Brno University of Technology, FME, 2017, pp. 382–385.

[74] J. Horáček, V. V. Radolf, and A.-M. Laukkanen, *Experimental and computational modeling of the effects of voice therapy using tubes*, Journal of Speech, Language, and Hearing Research, American Speech-Language-Hearing Association, 2019, pp. 1–18.

[75] J. Horáček, P. Šidlof, and J. Švec, *Numerical simulation of self-oscillations of human vocal folds with Hertz model of impact forces*, Journal of Fluids and Structures **20**:6 (2005), 853 – 869.

[76] J. Horáček and J. Švec, *Aeroelastic model of vocal-fold-shaped vibrating element for studying the phonation threshold*, Journal of Fluids and Structures **16**:7 (2002), 931 – 955.

[77] ———, *Instability boundaries of a vocal fold modelled as a flexibly supported rigid body vibrating in a channel conveying fluid*, ASME 2002 International Me-

chanical Engineering Congress and Exposition, American Society of Mechanical Engineers, 2002, pp. 1043–1054.

[78] M. S. Howe, *Acoustics of fluid-structure interactions*, Cambridge University Press, 1998.

[79] M. S. Howe, *Theory of vortex sound*, Cambridge University Press, 2002.

[80] T. J. Hughes, *The finite element method: linear static and dynamic finite element analysis*, Dover Publications, 2000.

[81] T. J. Hughes, W. K. Liu, and T. K. Zimmermann, *Lagrangian-eulerian finite element formulation for incompressible viscous flows*, Computer methods in applied mechanics and engineering **29**:3 (1981), 329–349.

[82] A. Hüppe, *Spectral finite elements for acoustic field computation*, Ph.D. thesis, Alpen-Adria-Universität Klagenfurt, 2012.

[83] K. Ishizaka and J. L. Flanagan, *Synthesis of voiced sounds from a two-mass model of the vocal cords*, Bell System Technical Journal **51**:6 (1972), 1233–1268.

[84] W. Jiang, X. Zheng, and Q. Xue, *Computational modeling of fluid–structure–acoustics interaction during voice production*, Frontiers in Bioengineering and Biotechnology **5** (2017), 7.

[85] H. Jimin and F. Zhi-Fang, *Modal analysis*, Linacre House, Oxford OX2 8DP, 2001.

[86] C. Johnson, *Numerical solution of partial differential equations by the finite element method*, Cambridge University Press, 1992.

[87] B. Kaltenbacher, M. Kaltenbacher, and I. Sim, *A modified and stable version of a perfectly matched layer technique for the 3-D second order wave equation in time domain with an application to aeroacoustics*, Journal of Computational Physics **235** (2013), 407–422.

[88] M. Kaltenbacher, M. Escobar, S. Becker, and I. Ali, *Numerical simulation of flow-induced noise using LES/SAS and Lighthill's acoustic analogy*, International Journal for Numerical Methods in Fluids **63**:9 (2010), 1103–1122.

[89] M. Kaltenbacher, S. Zörner, and A. Hüppe, *On the importance of strong fluid-solid coupling with application to human phonation*, Progress in Computational Fluid Dynamics **14**:1 (2014), 2–13.

[90] M. Kaltenbacher, *Numerical simulation of mechatronic sensors and actuators: finite elements for computational multiphysics*, Springer, 2015.

[91] M. Kaltenbacher, S. Marburg, A. Beck, C.-D. Munz, U. Langer, and M. Neumüller, *Computational acoustics*, Springer, 2018.

[92] M. Kaltenbacher and S. Schoder, *Aeroacoustic formulation for flow-acoustic feedback*, 25th AIAA/CEAS Aeroacoustics Conference, 2019, p. 2672.

[93] A. Kosík, *Fluid-structure interaction*, Ph.D. thesis, Department of Numerical Mathematics, Faculty of Mathematics and Physics, Charles University in Prague, 2016.

[94] M. Kramář, *Metoda konečných prvků pro Helmholtzovu rovnici (czech)*, Master's thesis, 2009.

[95] M. Lasota, P. Šidlof, M. Kaltenbacher, and S. Schoder, *Impact of the sub-grid scale model in aeroacoustic simulation of human voice*, Applied Sciences, vol. 11, 2021.

[96] M. J. Lighthill, *On sound generated aerodynamically. I. General theory*, Proceedings of the Royal Society of London, vol. 211, The Royal Society, 1952, pp. 564–587.

[97] J. Liljencrants, *A translating and rotating mass model of the vocal folds*, Tech. Report 32-1, Dept. for Speech, Music and Hearing, KTH Computer Science and Communication, 1991.

[98] G. Link, M. Kaltenbacher, M. Breuer, and M. Döllinger, *A 2D finite-element scheme for fluid-solid-acoustic interactions and its application to human phonation*, Computer Methods in Applied Mechanics and Engineering **198** (2009), 3321 – 3334.

[99] H. Lippert, *Anatomie*, Urban & Fischer, 1983.

[100] M. A. Lodermeyer, *A laser-based technique to evaluate sound generation during phonation*, Ph.D. thesis, Friedrich-Alexander-Universität Erlangen-Nürnberg, 2019.

[101] J. Lukeš and J. Malý, *Measure and integral*, Matfyzpress, 1995.

[102] H. Luo, R. Mittal, and S. A. Bielamowicz, *Analysis of flow-structure interaction in the larynx during phonation using an immersed-boundary method*, The Journal of the Acoustical Society of America **126**:2 (2009), 816–824.

[103] S. Marburg and B. Nolte, *Computational acoustics of noise propagation in fluids: finite and boundary element methods*, vol. 578, Springer, 2008.

[104] L. Maxfield, A. Palaparthi, and I. Titze, *New evidence that nonlinear source-filter coupling affects harmonic intensity and fo stability during instances of harmonics crossing formants*, Journal of Voice **31**:2 (2017), 149 – 156.

[105] R. Mittal, B. D. Erath, and M. W. Plesniak, *Fluid dynamics of human phonation and speech*, Annual Review of Fluid Mechanics **45** (2013), 437–467.

[106] P. M. Morse and H. Feshbach, *Methods of theoretical physics*, McGraw-Hill, 1953.

[107] C.-D. Munz, M. Dumbser, and S. Roller, *Linearized acoustic perturbation equations for low mach number flow with variable density and temperature*, Journal of Computational Physics **224**:1 (2007), 352–364.

[108] J. Nečas, *Direct methods in the theory of elliptic equations*, Springer Science & Business Media, 2011.

[109] J. Nečas and I. Hlaváček, *Mathematical theory of elastic and elasto-plastic bodies: An introduction*, vol. 3, Elsevier, 1981.

[110] J. Niu, J. Lei, and J. He, *Radial basis function mesh deformation based on dynamic control points*, Aerospace Science and Technology **64** (2017), 122 – 132.

[111] R. W. Ogden, *Non-linear elastic deformations*, Courier Corporation, 1997.

[112] M. de Oliveira Rosa, J. C. Pereira, M. Grellet, and A. Alwan, *A contribution to simulating a three-dimensional larynx model using the finite element method*, The Journal of the Acoustical Society of America **114**:5 (2003), 2893–2905.

[113] P. Poříkzková, K. Kozel, and J. Horáček, *Simulation of unsteady compressible flow in a channel with vibrating walls-influence of the frequency*, Computers & Fluids **46**:1 (2011), 404–410.

[114] A. Quarteroni and A. Valli, *Numerical approximation of partial differential equations*, Springer-Verlag, Berlin, New York, 1999.

[115] V. Radolf, *Přímá a inverzní úloha v akustice vokálního traktu člověka (czech)*, Ph.D. thesis, ČVUT v Praze, Fakulta strojní, 2010.

[116] K. Rektorys, *Variační metody (czech)*, Academia Praha, 1999.

[117] H. S. Ribner, *Aerodynamic sound from fluid dilitations; a theory of the sound from jets and other flows*, Tech. report, University of Toronto, 1962.

[118] V. Řidký and P. Šidlof, *Numerical simulation of deformation of dynamic mesh in the human vocal tract model*, European Physical Journal Web of Conferences, European Physical Journal Web of Conferences, vol. 92, 2015, p. 02076.

[119] S. W. Rienstra and A. Hirschberg, *An introduction to acoustics*, Eindhoven University of Technology, 2015.

[120] J. Rossiter, *Wind tunnel experiments on the flow over rectangular cavities at subsonic and transonic speeds*, Tech. report, Ministry of Aviation; Royal Aircraft Establishment; RAE Farnborough, 1964.

[121] R. J. Ruben, *Redefining the survival of the fittest: communication disorders in the 21st century*, The Laryngoscope **110**:2 (2000), 241–241.

[122] H. S., Regenerative Medicine in Otolaryngology, ch. Regeneration of the Vocal Fold, pp. 171–195, Springer, Tokyo, 2015, pp. 171–195.

[123] H. Sadeghi, S. Kniesburges, M. Kaltenbacher, A. Schützenberger, and M. Döllinger, *Computational models of laryngeal aerodynamics: Potentials and numerical costs*, Journal of Voice (2018), Available online 7 February 2018.

[124] H. Sadeghi, M. Döllinger, M. Kaltenbacher, and S. Kniesburges, *Aerodynamic impact of the ventricular folds in computational larynx models*, The Journal of the Acoustical Society of America **145**:4 (2019), 2376–2387.

[125] R. C. Scherer, D. Shinwari, K. J. De Witt, C. Zhang, B. R. Kucinschi, and A. A. Afjeh, *Intraglottal pressure profiles for a symmetric and oblique glottis with a divergence angle of 10 degrees*, Journal of the Acoustical Society of America **109** (2001), 1616–1630.

[126] L. Schickhofer, J. Malinen, and M. Mihaescu, *Compressible flow simulations of voiced speech using rigid vocal tract geometries acquired by mri*, The Journal of the Acoustical Society of America **145**:4 (2019), 2049–2061.

[127] S. Schoder, *Aeroacoustic analogies based on compressible flow data*, Ph.D. thesis, TU Wien, 2019.

[128] S. Schoder and M. Kaltenbacher, *Hybrid aeroacoustic computations: State of art and new achievements*, Journal of Theoretical and Computational Acoustics (2020).

[129] S. Schoder, M. Kaltenbacher, and K. Roppert, *Helmholtz's decomposition applied to aeroacoustics*, 25th AIAA/CEAS Aeroacoustics Conference, 2019, p. 2561.

[130] S. Schoder, K. Roppert, M. Weitz, C. Junger, and M. Kaltenbacher, *Aeroacoustic source term computation based on radial basis functions*, International Journal for Numerical Methods in Engineering (2019).

[131] S. Schoder, M. Weitz, P. Maurerlehner, A. Hauser, S. Falk, S. Kniesburges, M. Döllinger, and M. Kaltenbacher, *Hybrid aeroacoustic approach for the efficient numerical simulation of human phonation*, Journal of the Acoustical Society of America **147** (2020), 1179–1194.

[132] B. Schott, C. Ager, and W. A. Wall, *A monolithic approach to fluid-structure interaction based on a hybrid Eulerian-ALE fluid domain decomposition involving cut elements*, International Journal for Numerical Methods in Engineering **119**:3 (2019), 208–237.

[133] R. Schwarze, W. Mattheus, J. Klostermann, and C. Brücker, *Starting jet flows in a three-dimensional channel with larynx-shaped constriction*, Computers & Fluids **48**:1 (2011), 68–83.

[134] J. H. Seo and R. Mittal, *A high-order immersed boundary method for acoustic wave scattering and low-Mach number flow-induced sound in complex geometries*, Journal of Computational Physics **230**:4 (2011), 1000–1019.

[135] J. H. Seo and Y. J. Moon, *Linearized perturbed compressible equations for low mach number aeroacoustics*, Journal of Computational Physics **218**:2 (2006), 702–719.

[136] P. Šidlof, *Fluid-structure interaction in human vocal folds*, Ph.D. thesis, ENSTA ParisTech, 2007.

[137] ———, *Large eddy simulation of airflow in human vocal folds*, In Proceedings Topical Problems of Fluid Mechanics 2015 (D. Šimurda and T. Bodnár, eds.), 2015, pp. 183–192.

[138] P. Šidlof, J. Kolář, and P. Peukert, *Flow-induced vibration of a long flexible sheet in tangential flow*, Topical problems of fluid mechanics 2018 (D. Šimurda and T. Bodnár, eds.), Institute of Thermomechanics, AS CR, 2018, pp. 251–256.

[139] P. Šidlof, S. Zörner, and A. Hüppe, *A hybrid approach to the computational aeroacoustics of human voice production*, Biomechanics and Modeling in Mechanobiology **14**:3 (2014), 473–488.

[140] W. S. Slaughter, *Linearized elasticity problems*, Springer, 2002.

[141] B. H. Story, *Comparison of magnetic resonance imaging-based vocal tract area functions obtained from the same speaker in 1994 and 2002*, The Journal of the Acoustical Society of America **123**:1 (2008), 327–335.

[142] B. H. Story and I. R. Titze, *Parameterization of vocal tract area functions by empirical orthogonal modes*, Journal of Phonetics **26**:3 (1998), 223 – 260.

[143] B. H. Story, I. R. Titze, and E. A. Hoffman, *Vocal tract area functions from magnetic resonance imaging*, The Journal of the Acoustical Society of America **100**:1 (1996), 537–554.

[144] B. H. Story, *Physiologically-based speech simulation using an enhanced wave-reflection model of the vocal tract.*, Ph.D. thesis, 1995.

[145] J. Suh and S. H. Frankel, *Numerical simulation of turbulence transition and sound radiation for flow through a rigid glottal model*, The Journal of the Acoustical Society of America **121**:6 (2007), 3728–3739.

[146] P. Sváček and M. Feistauer, *Finite element method (czech)*, Vydavatelství ČVUT, 2006.

[147] P. Sváček and J. Horáček, *Numerical simulation of glottal flow in interaction with self oscillating vocal folds: comparison of finite element approximation with a simplified model*, Communications in Computational Physics **12** (2012), 789–806.

[148] ———, *Finite element approximation of flow induced vibrations of human vocal folds model: Effects of inflow boundary conditions and the length of subglottal and supraglottal channel on phonation onset*, Applied Mathematics and Computation **319** (2018), 178–194.

[149] N. Takashi and T. J. R. Hughes, *An arbitrary Lagrangian-Eulerian finite element method for interaction of fluid and a rigid body*, Computer Methods in Applied Mechanics and Engineering **95** (1992), 115–138.

[150] C. Tao, Y. Zhang, D. G. Hottinger, and J. J. Jiang, *Asymmetric airflow and vibration induced by the Coanda effect in a symmetric model of the vocal folds*, The Journal of the Acoustical Society of America **122**:4 (2007), 2270–2278.

[151] M. Tautz, K. Besserer, S. Becker, and M. Kaltenbacher, *Source formulations and boundary treatments for lighthill's analogy applied to incompressible flows*, AIAA Journal **56**:7 (2018), 2769–2781.

[152] R. Temam, *Navier-Stokes equations: Theory and numerical analysis*, vol. 343, North-Holland Publishing Comp., 1977.

[153] S. L. Thomson, L. Mongeau, and S. H. Frankel, *Aerodynamic transfer of energy to the vocal folds*, The Journal of the Acoustical Society of America **118**:3 (2005), 1689–1700.

[154] I. Titze, T. Riede, and P. Popolo, *Nonlinear source–filter coupling in phonation: Vocal exercises*, The Journal of the Acoustical Society of America **123**:4 (2008), 1902–1915.

[155] I. R. Titze, *The physics of small-amplitude oscillation of the vocal folds*, The Journal of the Acoustical Society of America **83**:4 (1988), 1536–1552.

[156] I. R. Titze, *Principles of voice production*, Prentice Hall, 1994.

[157] I. R. Titze, *Nonlinear source–filter coupling in phonation: Theory*, The Journal of the Acoustical Society of America **123**:4 (2008), 1902–1915.

[158] I. R. Titze and W. J. Strong, *Normal modes in vocal cord tissues*, The Journal of the Acoustical Society of America **57**:3 (1975), 736–744.

[159] S. Turek, *Efficient solvers for incompressible flow problems: An algorithmic and computational approache*, vol. 6, Springer Science & Business Media, 1999.

[160] T. Vampola, J. Horáček, and I. Klepáček, *Computer simulation of mucosal waves on vibrating human vocal folds*, Biocybernetics and Biomedical Engineering **36**:3 (2016), 451–465.

[161] T. Vampola, J. Horáček, and J. G. Švec, *FE modeling of human vocal tract acoustics. Part I: Production of Czech vowels*, Acta acustica united with Acustica **94**:3 (2008), 433–447.

[162] T. Vampola, J. Horáček, J. Vokářál, and L. Černỳ, *FE modeling of human vocal tract acoustics. Part II: Influence of velopharyngeal insufficiency on phonation of vowels*, Acta Acustica United with Acustica **94**:3 (2008).

[163] G. Verkerke and S. Thomson, *Sound-producing voice prostheses: 150 years of research*, Annual Review of Biomedical Engineering **16**:1 (2014).

[164] V. S. Vladimirov, *Equations of mathematical physics*, Marcel Dekker, Inc., New York, 1971.

[165] P. Welch, *The use of fast fourier transform for the estimation of power spectra: a method based on time averaging over short, modified periodograms*, IEEE Transactions on audio and electroacoustics **15**:2 (1967), 70–73.

[166] Q. Xue, X. Zheng, R. Mittal, and S. Bielamowicz, *Subject-specific computational modeling of human phonation*, The Journal of the Acoustical Society of America **135**:3 (2014), 1445–1456.

[167] M. Zanartu, D. D. Mehta, J. C. Ho, G. R. Wodicka, and R. E. Hillman, *Observation and analysis of in vivo vocal fold tissue instabilities produced by nonlinear source-filter coupling: a case study*, The Journal of the Acoustical Society of America **129**:1 (2011), 326–339.

[168] C. Zhang, W. Zhao, S. H. Frankel, and L. Mongeau, *Computational aeroacoustics of phonation, part II: Effects of flow parameters and ventricular folds*, The Journal of the Acoustical Society of America **112**:5 (2002), 2147–2154.

[169] Z. Zhang, J. Neubauer, and D. A. Berry, *Aerodynamically and acoustically driven modes of vibration in a physical model of the vocal folds*, The Journal of the Acoustical Society of America **120**:5 (2006), 2841–2849.

[170] ———, *Physical mechanisms of phonation onset: A linear stability analysis of an aeroelastic continuum model of phonation*, The Journal of the Acoustical Society of America **122**:4 (2007), 2279–2295.

[171] W. Zhao, C. Zhang, S. H. Frankel, and L. Mongeau, *Computational aeroacoustics of phonation, part I: Computational methods and sound generation mechanisms*, The Journal of the Acoustical Society of America **112**:5 (2002), 2134–2146.

[172] S. Zörner, *Numerical simulation method for a precise calculation of the human phonation under realistic conditions*, Ph.D. thesis, TU Wien, 2013.

[173] S. Zörner and M. Kaltenbacher, *Fluid-structure-acoustic interaction algorithms and implementations using the finite element method*, Eccomas, vol. 2010, 2010, p. 28.

[174] S. Zörner, M. Kaltenbacher, and M. Döllinger, *Investigation of prescribed movement in fluid-structure interaction simulation for the human phonation process*, Computers & Fluids **86** (2013), 133–140.

[175] S. Zörner, P. Šidlof, A. Hüppe, and M. Kaltenbacher, *Flow and acoustic effects in the larynx for varying geometries*, Acta Acustica united with Acustica **102**:2 (2016), 257–267.

# Appendix A

# Modal analysis

Modal analysis is a method of determining the inherent characteristics of dynamic system in the form of decomposition into (natural) modes of vibration (also called eigenmodes) with associated (natural) frequencies also called eigenfrequencies and the corresponding damping factors, see [85]. This decomposition is based on a separation of the frequency and the position dependence in the underlying governing equations.

Here, for simplicity we consider a linear time-invariant dynamic system which dynamic behaviour can be expressed as a linear combination of simple harmonic motions called the natural modes of vibration. The natural modes of vibration are inherent to the dynamic system and they are determined completely by its physical properties, i.e. by mass, stiffness, damping, and their spatial distributions, [85], [31].

The starting point for modal analysis is the equation describing vibrating system, i.e. equation (3.10) or its discretized version (4.6), here considered without damping terms and without right hand side force

$$\mathbb{M}\ddot{\boldsymbol{\alpha}} + \mathbb{K}\boldsymbol{\alpha} = \mathbf{0}, \tag{A.1}$$

where $\mathbb{M}$ and $\mathbb{K}$ is mass and stiffness matrix given by formulas (4.8), respectively, and vector $\boldsymbol{\alpha}$ describes the time-dependent displacement at the points of computational structure mesh, see paragraph 4.1.1. A general solution of this system is represented by the superposition of vibration modes $\mathbf{u}_j$ with individual (angular) frequencies $\omega_j$

$$\boldsymbol{\alpha}(t) = \sum_{j=1}^{N} e^{i\,\omega_j t}\mathbf{u}_j, \tag{A.2}$$

where $i^2 = -1$, see e.g. [40].

Let us suppose for now the solution of (A.2) in the form $\boldsymbol{\alpha} = e^{i\,\omega_j t}\mathbf{u}_j$, i.e. the system would oscillate with only single frequency $\omega_j$. The substitution of this solution into (A.1) yields

$$e^{i\,\omega_j t}(-\omega_j^2\,\mathbb{M}\mathbf{u}_j + \mathbb{K}\mathbf{u}_j) = \mathbf{0}, \tag{A.3}$$

from which follows

$$(\mathbb{K} - \omega_j^2\,\mathbb{M})\mathbf{u}_j = \mathbf{0}. \tag{A.4}$$

Equation (A.4) is a homogeneous system of linear algebraic equations for unknown vector $\mathbf{u}_j$ and it is the called generalized eigenvalue problem, see e.g. [31].

The values of $\omega_j^2 =: \lambda_j \in \mathbb{C}$, for which equation (A.4) has nontrivial solutions $\mathbf{u}_j$, are called generalized eigenvalues. The nontrivial vector $\mathbf{u}_j$ solving (A.4) for certain $\lambda_j(\omega_j)$ are called eigenvector corresponding to the eigenvalue $\lambda_j$. In the case of positive and symmetric matrices $\mathbb{K}, \mathbb{M}$, the eigenvalues $\lambda_j$ are real and non-negative, allowing to write $\omega_j = \sqrt{\lambda_j}$, see e.g. [31]. In this context the eigenvectors represent eigenmodes of structure vibration, i.e. the spatial pattern of vibration, and numbers $f_j := \frac{\omega_j}{2\pi}$ are called eigenfrequencies. For practical computation of the generalized eigenvalue problem the export of sparse matrices $\mathbb{K}, \mathbb{M}$ into program *Octave* and its function `eigs()` is used.

**Modal analysis of VF model MALE-SYM.** The results of modal analysis can be visualized as a plot of (discrete) vector fields represented by individual eiqenmodes, see Figure A.1 motivated by paper [160]. This approach helps to better imagine the VF motion represented by individual eiqenmodes at each point of VF, compare Figure A.1 with (standard) visualization in Figures 5.2 and 5.3.

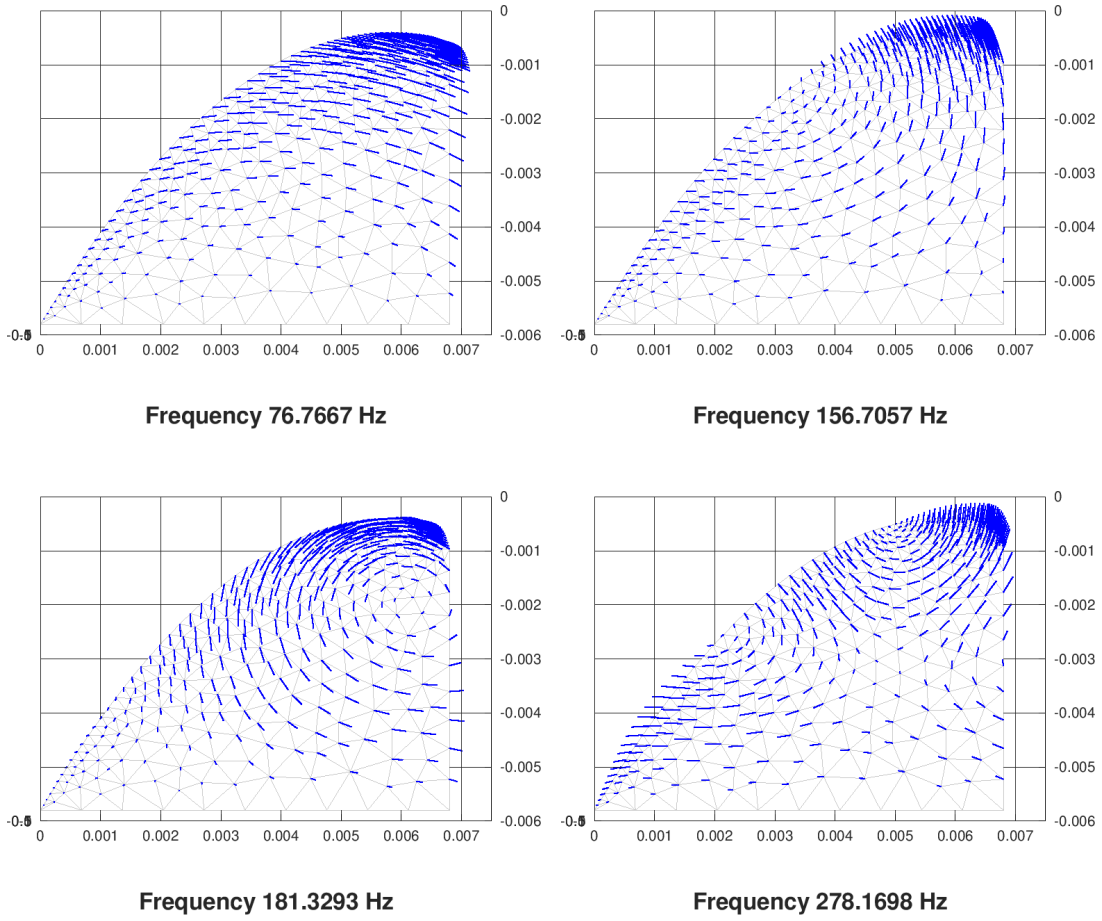


Figure A.1: First four eigenmodes of vocal fold model MALE-SYM with related eigenfrequencies 76.8 Hz, 156.7 Hz, 181.1 Hz and 278.2 Hz.

# Appendix B

# Geometry of vocal fold model ZORNER

The geometry and the mesh of VF model ZORNER, see detail in Figure B.1, is prepared in program GMSH, see `https://gmsh.info/`. This is a freeware FE mesh generator with its own syntax very similar to C language. The list of points defining VF model ZORNER is shown below. Figure B.2 facilitates the orientation in points labels.

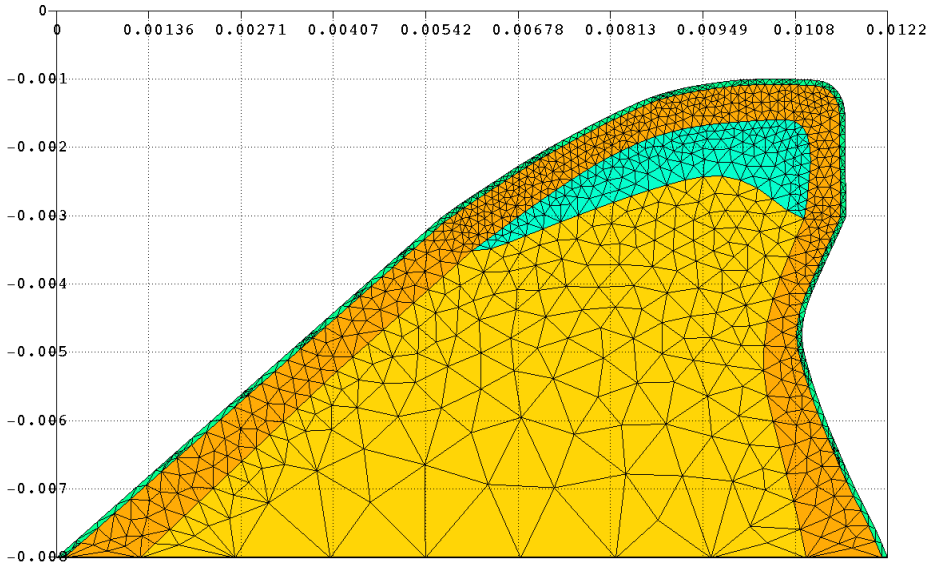


Figure B.1: Mesh of VF model ZORNER composed of four different layers distinguished by different colours, see also Figure 8.1.

```
// ZORNER VF model
mm = 1e-3; cl = 0.85*mm;

oA = newp; Point(oA)       = { 0, -7.01186*mm, 0,cl};
oB = newp; Point(oB)       = { 5.628350515*mm, -2.04381*mm, 0,cl};
L2[0] = newp; Point(L2[0]) = { 6.005670103*mm, -1.77655*mm, 0,cl};
L2[1] = newp; Point(L2[1]) = { 6.351546392*mm, -1.55267*mm, 0,cl};
L2[2] = newp; Point(L2[2]) = { 6.823195876*mm, -1.24673*mm, 0,cl};
```

```
L2[3] = newp; Point(L2[3]) = { 7.263402062*mm, -0.99046*mm, 0,cl};
L2[4] = newp; Point(L2[4]) = { 7.860824742*mm, -0.66974*mm, 0,cl};
L2[5] = newp; Point(L2[5]) = { 8.363917526*mm, -0.42448*mm, 0,cl};
L2[6] = newp; Point(L2[6]) = { 8.772680412*mm, -0.25300*mm, 0,cl};
L2[7] = newp; Point(L2[7]) = { 9.244329897*mm, -0.12577*mm, 0,cl};
L2[8] = newp; Point(L2[8]) = { 9.731701031*mm, -0.04716*mm, 0,cl};
L2[9] = newp; Point(L2[9]) = { 10.03041237*mm, -0.01572*mm, 0,cl};
L2[10] = newp; Point(L2[10]) = { 10.47061856*mm, 0.00000*mm, 0,cl};
L2[11] = newp; Point(L2[11]) = { 10.97371134*mm, -0.00943*mm, 0,cl};
L2[12] = newp; Point(L2[12]) = { 11.25670103*mm, -0.03773*mm, 0,cl};
L2[13] = newp; Point(L2[13]) = { 11.41391753*mm, -0.12577*mm, 0,cl};
L2[14] = newp; Point(L2[14]) = { 11.50824742*mm, -0.25155*mm, 0,cl};
L2[15] = newp; Point(L2[15]) = { 11.55541237*mm, -0.37732*mm, 0,cl};
L2[16] = newp; Point(L2[16]) = { 11.57113402*mm, -0.50309*mm, 0,cl};
oD     = newp; Point(oD)     = { 11.58685567*mm, -2.01237*mm, 0,cl};

L4[0] = newp; Point(L4[0]) = { 11.47680412*mm, -2.26392*mm, 0,cl};
L4[1] = newp; Point(L4[1]) = { 11.28814433*mm, -2.67268*mm, 0,cl};
L4[2] = newp; Point(L4[2]) = { 11.02087629*mm, -3.30155*mm, 0,cl};
L4[3] = newp; Point(L4[3]) = { 10.94226804*mm, -3.77320*mm, 0,cl};
L4[4] = newp; Point(L4[4]) = { 11.03659794*mm, -4.24485*mm, 0,cl};
L4[5] = newp; Point(L4[5]) = { 11.25670103*mm, -4.90515*mm, 0,cl};
L4[6] = newp; Point(L4[6]) = { 11.47680412*mm, -5.43969*mm, 0,cl};
L4[7] = newp; Point(L4[7]) = { 11.69690722*mm, -5.94278*mm, 0,cl};
L4[8] = newp; Point(L4[8]) = { 12.01134021*mm, -6.57165*mm, 0,cl};
L4[9] = newp; Point(L4[9]) = { 12.20000000*mm, -7.01186*mm, 0,cl};
oF = newp; Point(oF) = { 11.00515464*mm, -7.01186*mm, 0,cl};
oG = newp; Point(oG) = { 1.22628866*mm, -7.01186*mm, 0,cl};
oH = newp; Point(oH) = { 4.119072165*mm, -4.27629*mm, 0,cl};
oI = newp; Point(oI) = { 6.1*mm, -2.51546*mm, 0,cl};

M2[0] = newp; Point(M2[0]) = { 6.886082474*mm, -1.93691*mm, 0,cl};
M2[1] = newp; Point(M2[1]) = { 7.483505155*mm, -1.52500*mm, 0,cl};
M2[2] = newp; Point(M2[2]) = { 7.986597938*mm, -1.21057*mm, 0,cl};
M2[3] = newp; Point(M2[3]) = { 8.458247423*mm, -0.97474*mm, 0,cl};
M2[4] = newp; Point(M2[4]) = { 8.867010309*mm, -0.81753*mm, 0,cl};
M2[5] = newp; Point(M2[5]) = { 9.401546392*mm, -0.69175*mm, 0,cl};
M2[6] = newp; Point(M2[6]) = { 9.998969072*mm, -0.62887*mm, 0,cl};
M2[7] = newp; Point(M2[7]) = { 10.50206186*mm, -0.59742*mm, 0,cl};
M2[8] = newp; Point(M2[8]) = { 10.75360825*mm, -0.59742*mm, 0,cl};
M2[9] = newp; Point(M2[9]) = { 10.91082474*mm, -0.66031*mm, 0,cl};
M2[10] = newp; Point(M2[10]) = { 11.00515464*mm, -0.78608*mm, 0,cl};
M2[11] = newp; Point(M2[11]) = { 11.05231959*mm, -0.97474*mm, 0,cl};
M2[12] = newp; Point(M2[12]) = { 11.06804124*mm, -1.19485*mm, 0,cl};
M2[13] = newp; Point(M2[13]) = { 11.04603093*mm, -1.47784*mm, 0,cl};
M2[14] = newp; Point(M2[14]) = { 11.01458763*mm, -1.79227*mm, 0,cl};
M2[15] = newp; Point(M2[15]) = { 10.97371134*mm, -2.04381*mm, 0,cl};

M3[0] = newp; Point(M3[0]) = { 10.87938144*mm, -2.26392*mm, 0,cl};
M3[1] = newp; Point(M3[1]) = { 10.75360825*mm, -2.57835*mm, 0,cl};
M3[2] = newp; Point(M3[2]) = { 10.62783505*mm, -2.89278*mm, 0,cl};
M3[3] = newp; Point(M3[3]) = { 10.50206186*mm, -3.27010*mm, 0,cl};
M3[4] = newp; Point(M3[4]) = { 10.40773196*mm, -3.71031*mm, 0,cl};
M3[5] = newp; Point(M3[5]) = { 10.37628866*mm, -4.21340*mm, 0,cl};
M3[6] = newp; Point(M3[6]) = { 10.43917526*mm, -4.68505*mm, 0,cl};
M3[7] = newp; Point(M3[7]) = { 10.56494845*mm, -5.18814*mm, 0,cl};
```

```
M3[8] = newp; Point(M3[8]) = { 10.72216495*mm, -5.81701*mm, 0,cl};
M3[9] = newp; Point(M3[9]) = { 10.86365979*mm, -6.35155*mm, 0,cl};

M4[0] = newp; Point(M4[0]) = { 6.382989691*mm, -2.48402*mm, 0,cl};
M4[1] = newp; Point(M4[1]) = { 6.886082474*mm, -2.29536*mm, 0,cl};
M4[2] = newp; Point(M4[2]) = { 7.420618557*mm, -2.08469*mm, 0,cl};
M4[3] = newp; Point(M4[3]) = { 7.860824742*mm, -1.91804*mm, 0,cl};
M4[4] = newp; Point(M4[4]) = { 8.301030928*mm, -1.76082*mm, 0,cl};
M4[5] = newp; Point(M4[5]) = { 8.678350515*mm, -1.63505*mm, 0,cl};
M4[6] = newp; Point(M4[6]) = { 8.992783505*mm, -1.54072*mm, 0,cl};
M4[7] = newp; Point(M4[7]) = { 9.370103093*mm, -1.44639*mm, 0,cl};
M4[8] = newp; Point(M4[8]) = { 9.715979381*mm, -1.41495*mm, 0,cl};
M4[9] = newp; Point(M4[9]) = { 10.03041237*mm, -1.47784*mm, 0,cl};
M4[10] = newp; Point(M4[10]) = { 10.25051546*mm, -1.57216*mm, 0,cl};
M4[11] = newp; Point(M4[11]) = { 10.47061856*mm, -1.72938*mm, 0,cl};
M4[12] = newp; Point(M4[12]) = { 10.62783505*mm, -1.85515*mm, 0,cl};
M4[13] = newp; Point(M4[13]) = { 10.81649485*mm, -1.98093*mm, 0,cl};

// setting GLOTTIS WIDTH == move all point by WIDTH down
WIDTH = 0.5*mm;
A     = Translate {0, -WIDTH, 0} { Point{oA}; };
B     = Translate {0, -WIDTH, 0} { Point{oB}; };
Lp2[] = Translate {0, -WIDTH, 0} { Point{L2[]}; };
D     = Translate {0, -WIDTH, 0} { Point{oD}; };
Lp4[] = Translate {0, -WIDTH, 0} { Point{L4[]}; };
F     = Translate {0, -WIDTH, 0} { Point{oF}; };
G     = Translate {0, -WIDTH, 0} { Point{oG}; };
H     = Translate {0, -WIDTH, 0} { Point{oH}; };
I     = Translate {0, -WIDTH, 0} { Point{oI}; };
Mp2[] = Translate {0, -WIDTH, 0} { Point{M2[]}; };
Mp3[] = Translate {0, -WIDTH, 0} { Point{M3[]}; };
Mp4[] = Translate {0, -WIDTH, 0} { Point{M4[]}; };
C = Lp2[16]; E = Lp4[9]; J = Mp2[15];
```

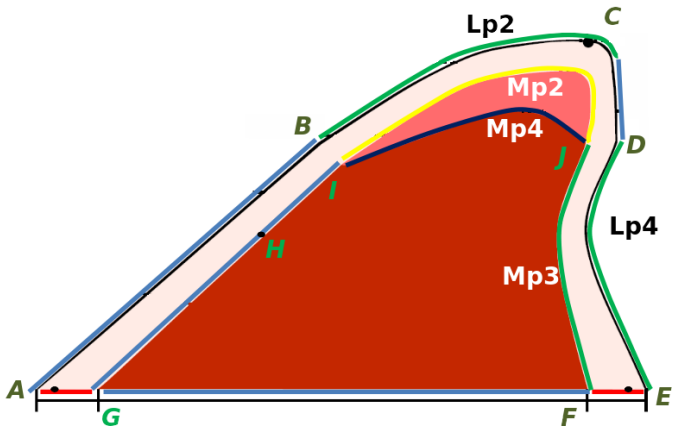


Figure B.2: Scheme of VF model ZORNER with denoted points. Lines *Lp2, Lp4, Mp2, Mp3* and *Mp4* denote set of points.

# Appendix C

# Additional results of FSI problem

In this appendix few additional figures extending results of Sections 5.3 and 5.4, where numerical solution of the (full) FSI problem is described, can be found.

First, illustrative snapshots of the simulation with prescribed airflow symmetry at the top boundary referred as "Pen-W" in paragraph 5.3.1 are shown in Figure C.1. The simulation was conducted with airflow inlet velocity $\mathbf{v}_{\mathrm{Dir}} = (1.9, 0.0)\,\mathrm{m/s}$ prescribed with the aid of penalization parameter $\epsilon = 5 \cdot 10^{-4}\,\mathrm{s/m}$. These snapshots are taken close before the end of the simulation caused by too distorted mesh. The VF displacement is already quite large, observable clearly by an eye. The typical convergent-divergent changing of VF position can be seen.

Figure C.2 supplements Figure 5.22 and paragraph 5.3.3 describing the energy transfer from airflow to VFs. Here, the acting aerodynamic forces during one oscillation period for case "Driven"(VF prescribed harmonic motion in $y$-direction) is shown, see paragraph 5.3.3. The aerodynamic forces are dominantly acting downwards, the highest values are reached at time instant 0.098 s (labeled d7), when the channel is maximally narrowed. Up to this moment the energy is transferred from VF to airflow due to the acting of the aerodynamic forces against the direction of VF motion, see Figure 5.21. Then the opening phase follows when the VF motion and the aerodynamic forces have the same direction (see Figure 5.21), however the cumulative sum of power during opening phase (i.e. energy, which is described e.g. by function $E_{cumul}$) has lower absolute value than during closing phase (which is negative) yielding negative total sum of the transferred energy from airflow to VF during each oscillation period, see Figure 5.21. In other words the energy is transferred in sum from the (prescribed) VF vibration to the airflow during each oscillation cycle. The energy exchange takes place dominantly at the VF subglottal boundary (leading edge) with relatively uniform participation.

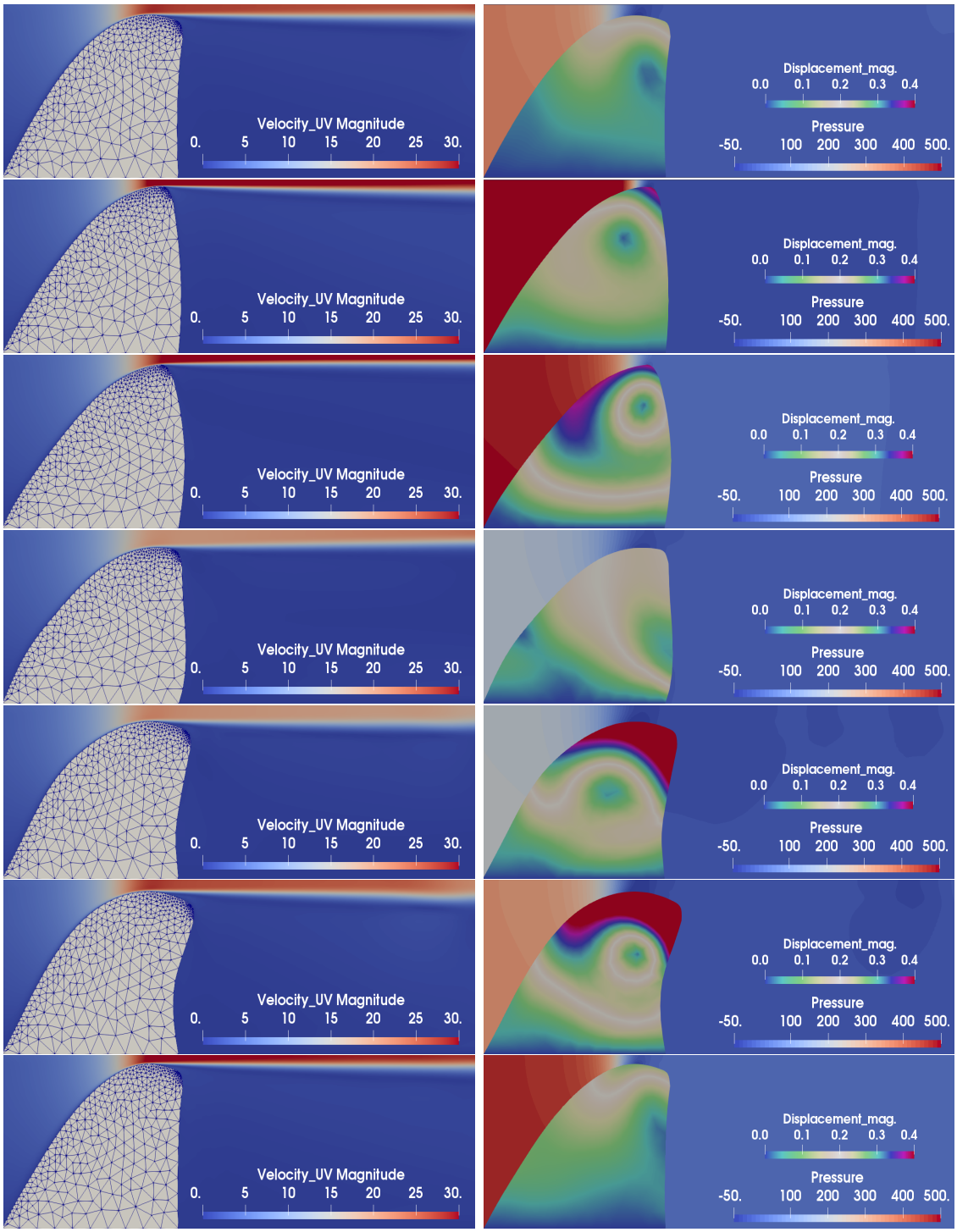


Figure C.1: Magnitude of the airflow velocity (left) and pressure together with the vocal fold displacement in mm (right) shown for seven time instants during one vibration cycle of VFs with duration of approx. 7 ms. Simulation of case "Pen-W".

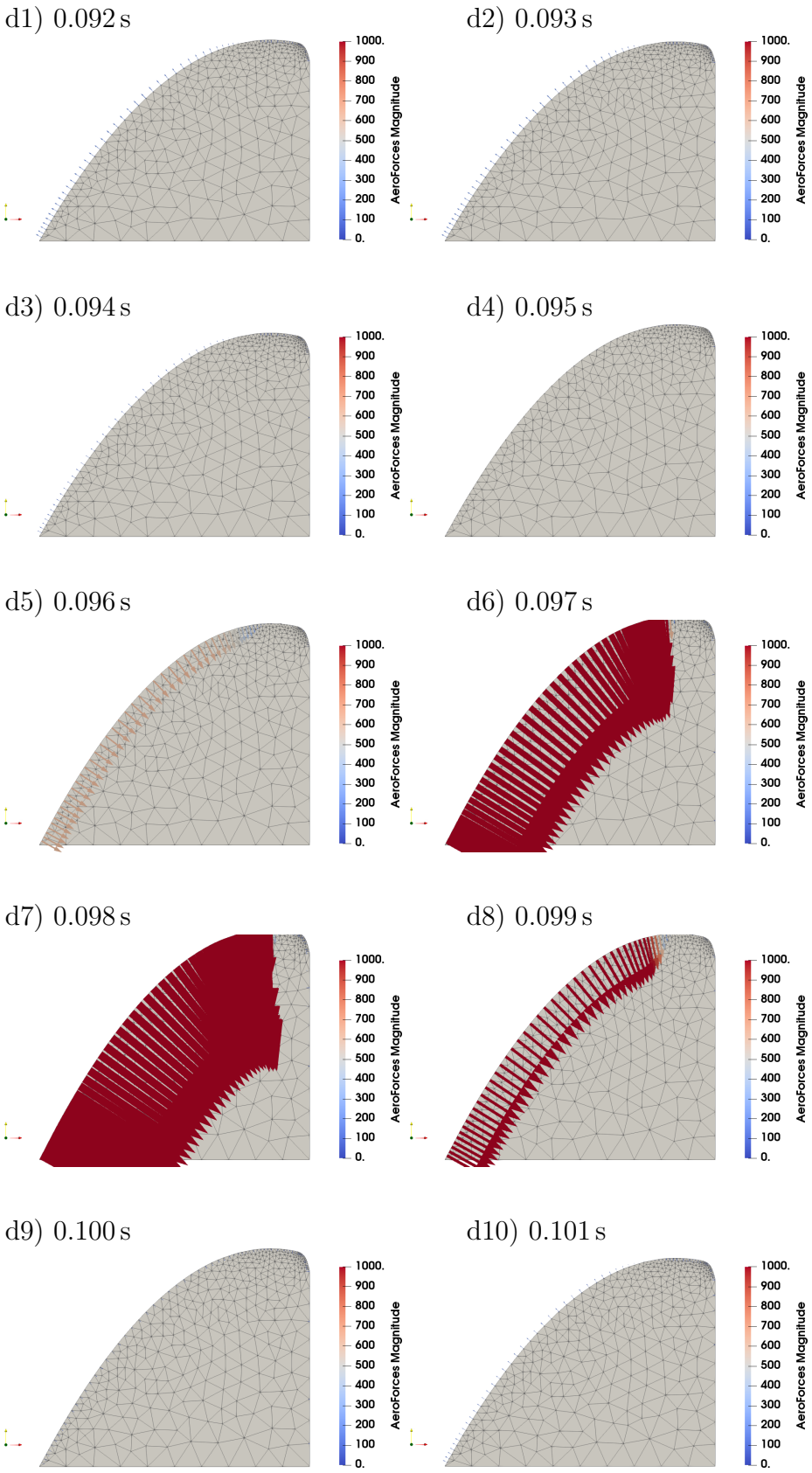


Figure C.2: Details of the VF deformation and the acting aerodynamic forces during one oscillation period for case "Driven" (VF prescribed motion), see paragraph 5.3.3. Between time instants d7) and d8) the VF reachs the maximal positive displacement $u_2$ and then it starts to open again the glottal channel.

Further, the dependence of the transglottal pressure on the gap is plotted for three reference solutions of the FSI problem similarly as in paragraph 5.2.3 (where the pressure-gap dependence was discussed for prescribed VF motion). Here, the cases "Vel" (inlet velocity $\mathbf{v}_{\mathrm{Dir}}$ prescribed by Dirichlet BC), "Pen-W" (see above) and "Pres" (pressure drop $\Delta p = p_{\mathrm{in}} - 0 = 450\,\mathrm{Pa}$) are compared, see paragraph 5.3.1. The graph captures (a part of) the flutter regime of the VF flow induced vibrations since prescribed inlet velocity $\mathbf{v}_{\mathrm{Dir}}$ as well as pressure drop $\Delta p$ exceeds the critical value. The simulations end in all cases by fluid flow solver failure due too distorted CFD mesh – at vinicity of the VF points near half-gap value $g_0 = 0.1\,\mathrm{mm}$. Therefore the curves are not closed since the regular periodic VF vibration cycle has not emerged as in the laboratory experiments with VF mutual contact, see [74]. Nevertheless it is obvious from Figure C.3 that the value of transglottal pressure connected with reaching of given minimal value of half-gap $g_0$ is much lower for case "Pen-W" than for case "Vel". In both cases "Vel" and "Pen-W" the working pressure range is very similar to the laboratory experiment, compare with Figure 5.9. The orientation of curves in all cases is clockwise proposing the (positive) energy transfer from airflow to VF what is in contradiction to results with prescribed motion of VF (compare with Figure 5.10).

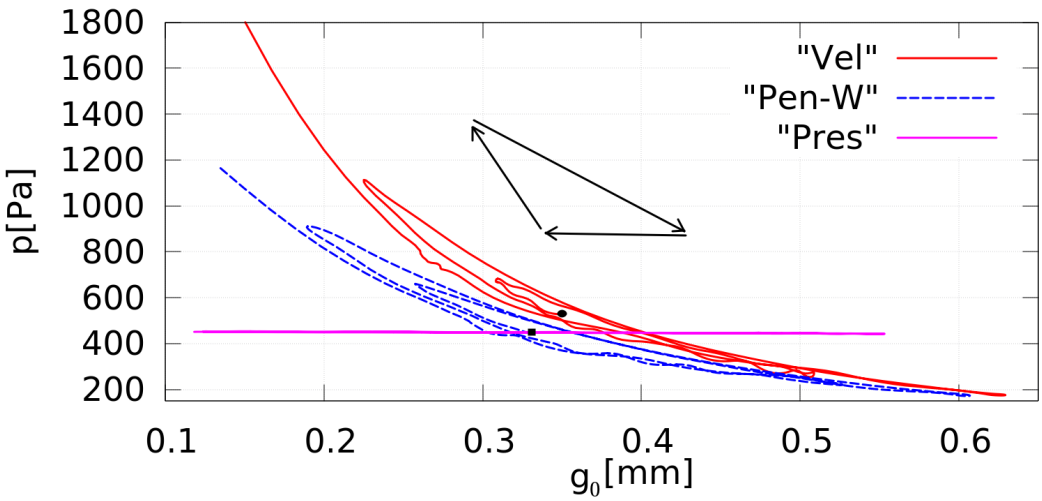


Figure C.3: Dependence of the transglottal pressure on the half-gap for three simulations of the FSI problem: "Vel", "Pen-W" and "Pres". The graph depicts only last three incomplete oscillation cycles. The symbols of dot (•) and square (■) denote the starting point of the curve for cases "Vel" and "Pen-W", resp. The arrows show the (time) direction of curve circulation.

Next, static aerodynamic force $\mathbf{q}^s_{\mathrm{stat}}$ for the full-larynx configuration, i.e. configuration without prescribed symmetry of the airflow in the channel, is depicted in Figure C.4 for case *PEN-W* as described in Section 5.4. The graph shows a slight asymmetry of the static forces especially at the supraglottal boundary of bottom VF. The asymmetry could be in future (if wanted) eliminated by averaging of the forces acting on the top and the bottom VF.

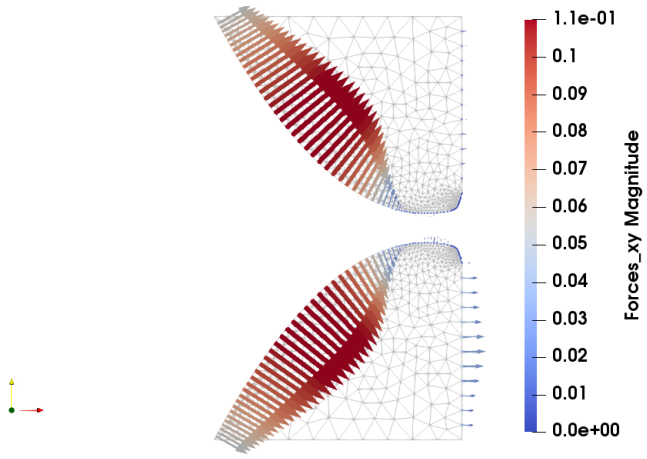


Figure C.4: Detail of static aerodynamic force $\mathbf{q}^s_{\text{stat}}$ determined at $t_{release} = 0.03\,\text{s}$ for the simulation referred in previous text as *PEN-W*.

Finally, the phase portraits of point S (the same position as for VF model MALE-SYM) for all four cases of paragraph 5.4 are shown in Figure C.5. The phase portraits of cases *VEL*, *PEN-S* and *PEN-W* indicate a much faster development of the flutter phenomenon than in case *PRES* as mentioned already in paragraph 5.4. The phase portrait of case *PRES* moreover differs in the motion of point S, the different motion pattern(s) is evidently excited, compare it with phase portraits in paper [160].

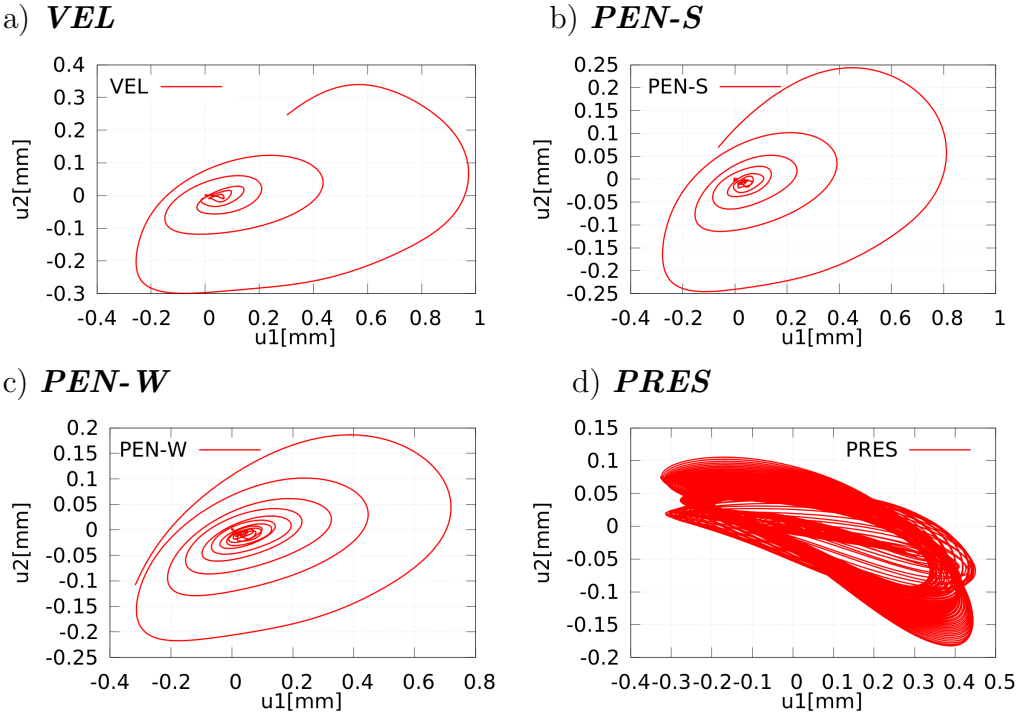


Figure C.5: Trajectory of point S in the X–Y plane for considered cases: a) *VEL*, b) *PEN-S*, c) *PEN-W* and d) *PRES*, see paragraph 5.4.

# Appendix D

# Analysis of vocal tract resonances

This appendix contains a detailed behaviour of the pressure distributions of the formants as are determined in Section 8.2.

### Vocal tract diameters

The diameters $r_i$, i.e. $y$-dimensions of domain $\Omega^a_{\text{tract}}$, are given by formula (8.1) and listed in Table D.1.

| Cut | $r_i$ |
|---|---|
| 1 | 3.568 |
| 2 | 3.478 |
| 3 | 2.985 |
| 4 | 3.700 |
| 5 | 4.184 |
| 6 | 7.399 |
| 7 | 9.624 |
| 8 | 9.575 |
| 9 | 8.686 |
| 10 | 8.176 |
| 11 | 10.749 |
| 12 | 13.658 |
| 13 | 13.387 |
| 14 | 13.147 |
| 15 | 12.361 |

| Cut | $r_i$ |
|---|---|
| 16 | 12.048 |
| 17 | 11.686 |
| 18 | 10.749 |
| 19 | 10.357 |
| 20 | 10.029 |
| 21 | 10.265 |
| 22 | 10.124 |
| 23 | 8.612 |
| 24 | 8.117 |
| 25 | 8.117 |
| 26 | 6.956 |
| 27 | 4.853 |
| 28 | 2.706 |
| 29 | 2.185 |
| 30 | 2.646 |

| Cut | $r_i$ |
|---|---|
| 31 | 2.646 |
| 32 | 3.432 |
| 33 | 4.370 |
| 34 | 4.918 |
| 35 | 5.232 |
| 36 | 7.611 |
| 37 | 8.649 |
| 38 | 9.009 |
| 39 | 10.896 |
| 40 | 13.195 |
| 41 | 11.915 |
| 42 | 8.722 |
| 43 | 5.917 |
| 44 | 4.951 |
| 45 | 3.613 |
| 46 | 5.232 |

Table D.1: Diameters $r_i$ in mm of cross-sections (Cuts) of the domain $\Omega^a_{\text{tract}}$ as calculated by formula (8.1) using data of [143] for vowel [u:]. The distance between two cross-sections is $d = 3.96825\,\text{mm}$. The first cut was performed in the glottis.

### Simplified 1D model of vocal tract

From the theoretical viewpoint many aspects of vocal tract functions can be explained by a simple closed-open tube of length $L$. This configuration represents a quartet-wave resonator, which resonances are located at frequencies

$$F_n = (2n-1)\frac{c}{4L}, \quad n \in \mathbb{N}, \tag{D.1}$$

with the speed of sound denoted by $c$, see e.g. [156], [33]. Subsequently the $n$-th resonance pressure distribution has $n-1$ cross-sections with zero (it changes $n-1$ times the sign). The difference of the 'tube model' against the 2D VT model (as presented in Section 8.2) is that the 1D model neglects the influence of $y$-dimension of 2D model resulting into equidistant distribution of resonances predicted by the quarter-wave formula D.1. On the other hand the 2D model can have location of resonant frequencies shifted contrary to 1D model due to a non-uniform $y$-shape of the domain and from certain frequency limit also non-planar waves occur[1].

Table D.2 shows the resonances calculated by formula (D.1) for models M1-M4 with consideration of the domains $\Omega^a_{\text{src}}$ and $\Omega^a_{\text{tract}}$ only, compare it with Table 8.2 in Section 8.2. It predicts the existence of four formants up to frequency 3 kHz for VT models M1-M3 similarly as the 2D model for VT models M2 and M3. Nevertheless the exact formant locations for cases M1-M3 substantially differ because of the probable aforementioned influence of the $y$ dimension of the 2D models. Further the quarter-wave formula as applied in Table D.2 relates increasing values of resonant frequencies with decreasing of tube length, what was also documented in (all) 2D results (Table 8.2). The best match with the 1D tube model evinces the model M4 concerning the location of all first four formants. Model M4 does not have abrupt change of domain shape with hard walls as e.g. models M1 (behind the glottis) and M3 (at the end of the sound source region).

| | $L$[mm] | $F_1$ | $F_2$ | $F_3$ | $F_4$ |
|---|---|---|---|---|---|
| M1 | 237 | 362.1 | 1086.4 | 1810.6 | 2534.8 |
| M2 | 222 | 386.6 | 1159.8 | 1933.0 | 2706.3 |
| M3 | 209 | 408.7 | 1226.2 | 2043.6 | 2861.1 |
| M4 | 179 | 476.9 | 1430.8 | 2384.6 | 3338.4 |

Table D.2: Formants of vocal tract models M1-M4 predicted with the help of quarter-wave formula (D.1). Results are in Hz and length $L$ is the length of VT model after an exclusion of the free field region and the PML layer.

### Detailed acoustic pressure distributions at formant frequencies

This paragraph presents a detailed version of results from paragraph 8.2.2, i.e. the solutions of Helmholtz equation (8.2) with different VT models with applied PML at the outer boundary of free field region. The upper restriction of investigated frequencies to 3 kHz allows to determine the formants of purely acoustic planar waves ([115] roughly estimates this limit to 5 kHz), i.e. the solutions change only

[1]Non-planar wave in the 2D model is a wave with significant variation along the $y$-direction.

along $x$-axis, not along $y$-axis. Therefore the pressure distributions along VT axis of symmetry ($y = 0$) fully characterize the solution (at a chosen frequency) in the whole domain, see Figure D.1.

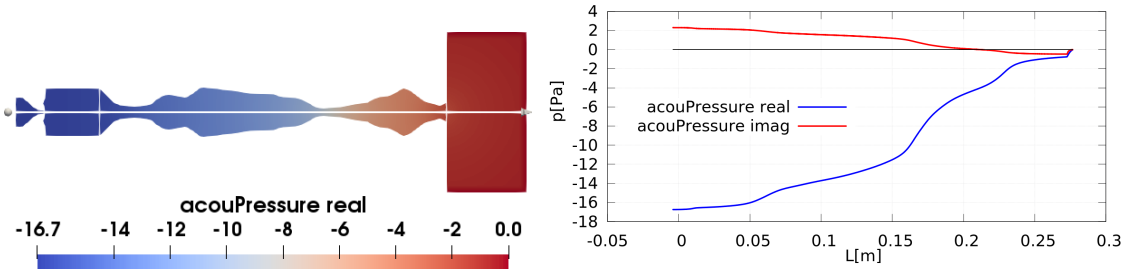


Figure D.1: **Left:** The (real part of) solution of Helmholtz equation at frequency 271 Hz, the line $y = 0$ is highlighted by white colour. **Right:** Both (complex) components of pressure distribution along line $y = 0$ of the solution from left.

The pressure distributions along $x$-axis for VT models M1-M4 are shown in Figures D.2, D.3 and D.4. First, all pressure distributions at formants frequencies $F_n$ have $n-1$ changes of solution sign along $x$-axis (the graph of each pressure distribution crosses $n-1$ zero value), fully in agreement with the quarter-wave formula. Particularly, it is valid also for the solutions in frequency range $1400-1500$ Hz for VT models M1-M3, hence these resonance frequencies really represent formant F3 (albeit damped – see Figure 8.13) and they are not numerical artifacts. The absence of formant at range $1400-1600$ Hz in the case of model M4 can be caused by a shorter VT length compared to other models. This is also a final justification of additional formant appearance of VT models M1-M3 in frequency range up to 3,kHz contrary to VT model M4 and mainly contrary to results of paper [143].

The pressure distribution of VT model M1 at frequency 2638 Hz shown in Figure D.2 has situated maximal amplitude at the subglottal part of the VT model and the pressure amplitude inside the vocal tract model (highlighted by bold in graph) reaches four times smaller values. It confirms that this fifth formant of VT model M1 can be associated with the subglottal cavity of the chosen VT model.

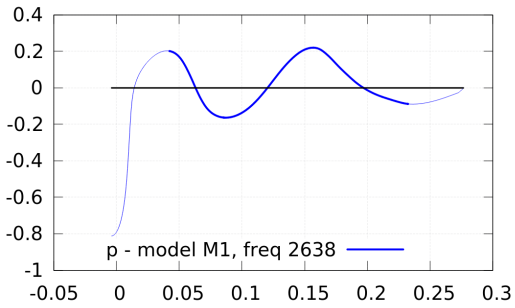


Figure D.2: Pressure distribution along $x$-axis at frequency 2638 Hz for VT model M1. The part of solution inside vocal tract region $\Omega^a_{\text{tract}}$ is accentuated by bold curve.

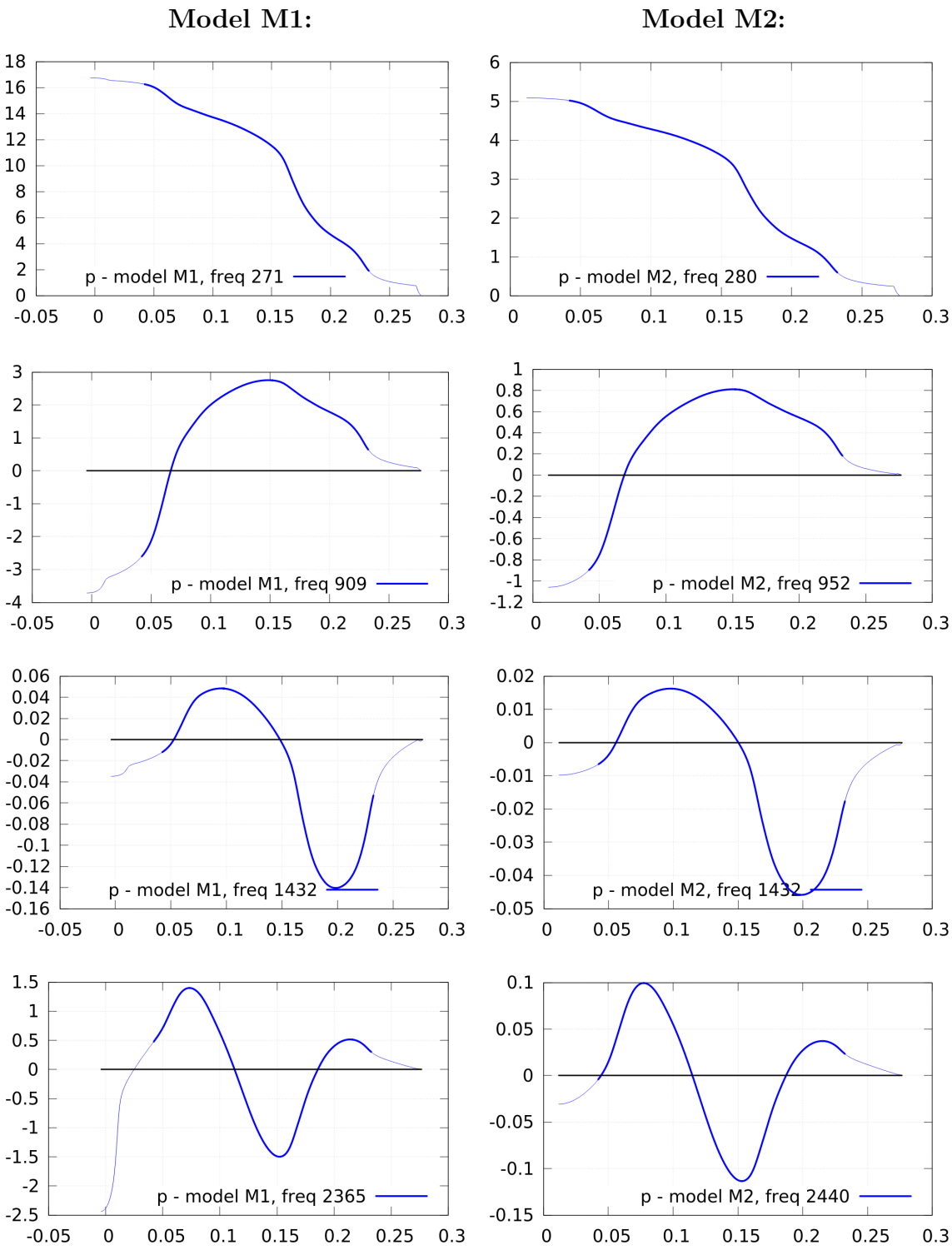


Figure D.3: Pressure distributions along $x$-axis at resonant frequencies for vocal tract models M1 and M2. The real component of generally complex solution of the Helmholtz equation is shown and the part of solution inside vocal tract region $\Omega^a_{\text{tract}}$ is accentuated by bold curve.

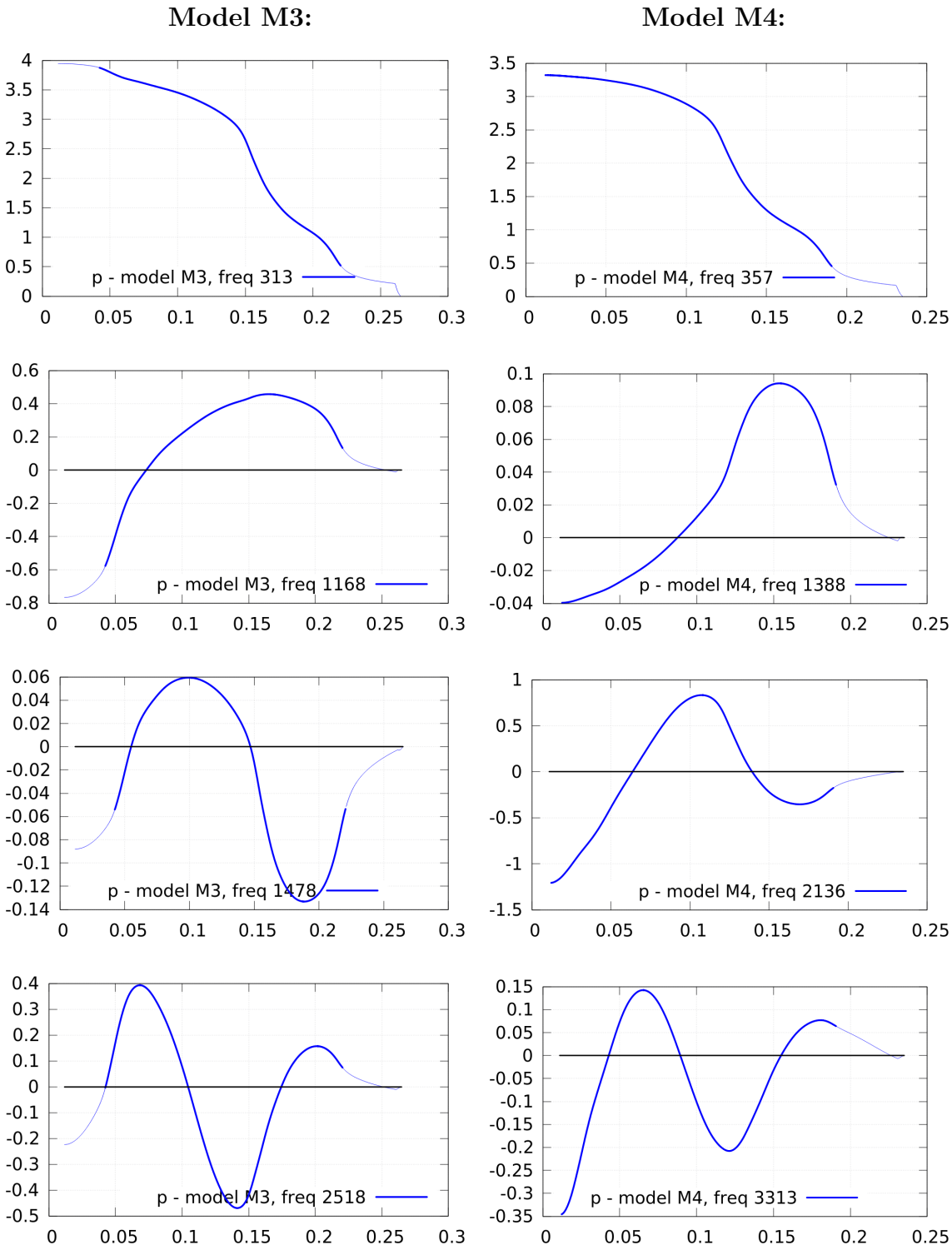


Figure D.4: Pressure distributions along $x$-axis at resonant frequencies for vocal tract models M3 and M4. The real component of generally complex solution of the Helmholtz equation is shown and the part of solution inside vocal tract region $\Omega^a_{\text{tract}}$ is accentuated by bold curve.

# Appendix E

# Additional aeroacoustic results

In this appendix few additional figures extending results of Sections 8.4, where the numerical solution of aeroacoustic problem is described, can be found.

First, the sound sources of the PCWE approach is computed based on the FSI simulation with the ZORNER VF model as described in Section 8.1. These sources are composed of two components, see the right side of equation (6.26), the both of them computed on the CFD mesh are displayed in Figure E.1. First one given by the time derivative of the pressure obtained from the incompressible flow simulation is connected with pressure time changes located primarily in the vortex centers and negligibly present in the glottis. The second component of the PCWE source is the product of the average velocity and the pressure gradient, see Figures 8.8 and E.2. Therefore the contribution of these sound sources is restricted to the glottis area and to the location of strong glottal jet[1]. The both PCWE source components are of similar absolute strength and their frequency content is interestingly also similar (not shown).

Next, an alternative visualization of the Fourier transform applied on the sound sources is shown in Figure E.3, where only the real part of a complex number (result of the Fourier transform) is shown, compare with the plotted complex number amplitude in Figure 8.20. The graph of the real part allows to depict and notice better the multipole structure of sound sources.

The dipole, prototypically two sound emitting (point) sources of the opposite phase separated by a small distance – see Section 2.4, is obviously present for the frequency of 232 Hz in all cases in the glottis, see the accentuation in Figure E.3 top. In the case of the LH analogy an additional location of not negligible sound sources is downstream from the tip of VFs, in the location of a probable boundary layer separation.

On the other hand the quadrupole, a configuration of four (point) sound sources of the opposite phase located very close to each other, can be observed to be dominant for frequency 2486 Hz in all cases with location in the supraglottal region – see Figure E.3, in the area of mixing glottal jet with a quiescent air behind the glottis – see Figure 8.10.

[1]The moving average of 200 time step is here used instead of the mean airflow velocity computed from the whole simulation time.

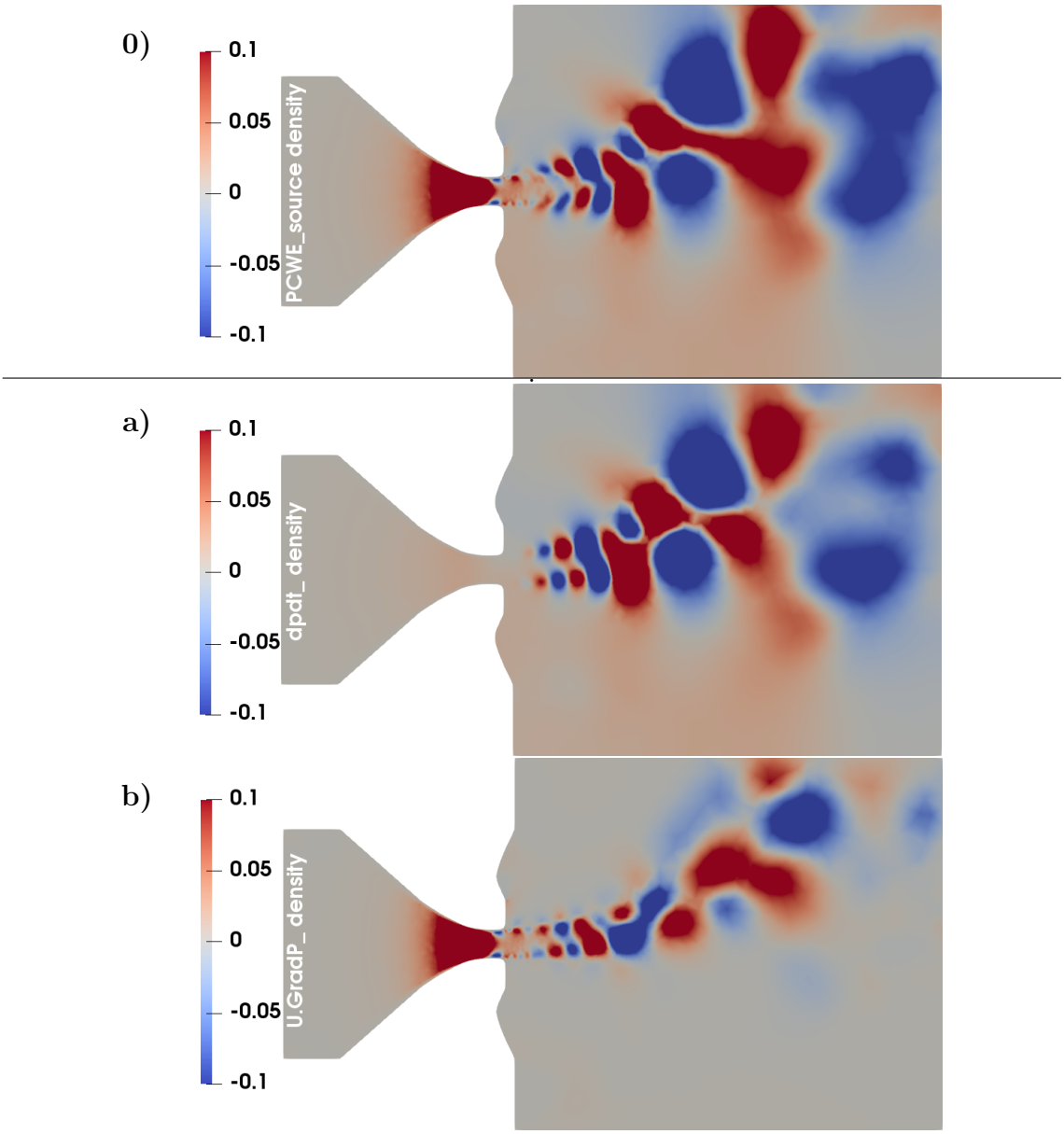


Figure E.1: Detail of sound sources structure of the PCWE approach. **0)** Detail of (normalized) instant sound density of the PCWE approach. It is given by the sum of components (see RHS of Eq. (6.26)): **a)** the time derivative of the pressure obtained from the incompressible flow simulation, **b)** the product of the average velocity and the pressure gradient. In all figures the normalized values are depicted at time instant 0.6 s.

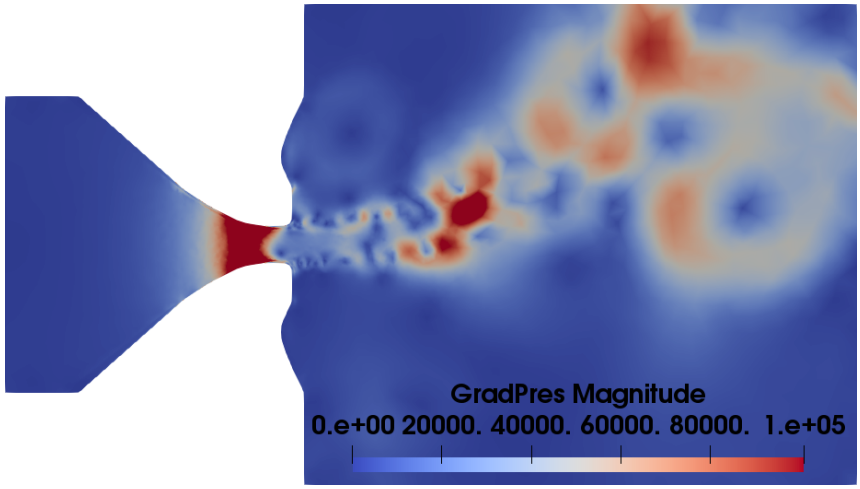


Figure E.2: Detail of airflow pressure gradient magnitude at time instant 0.6 s.

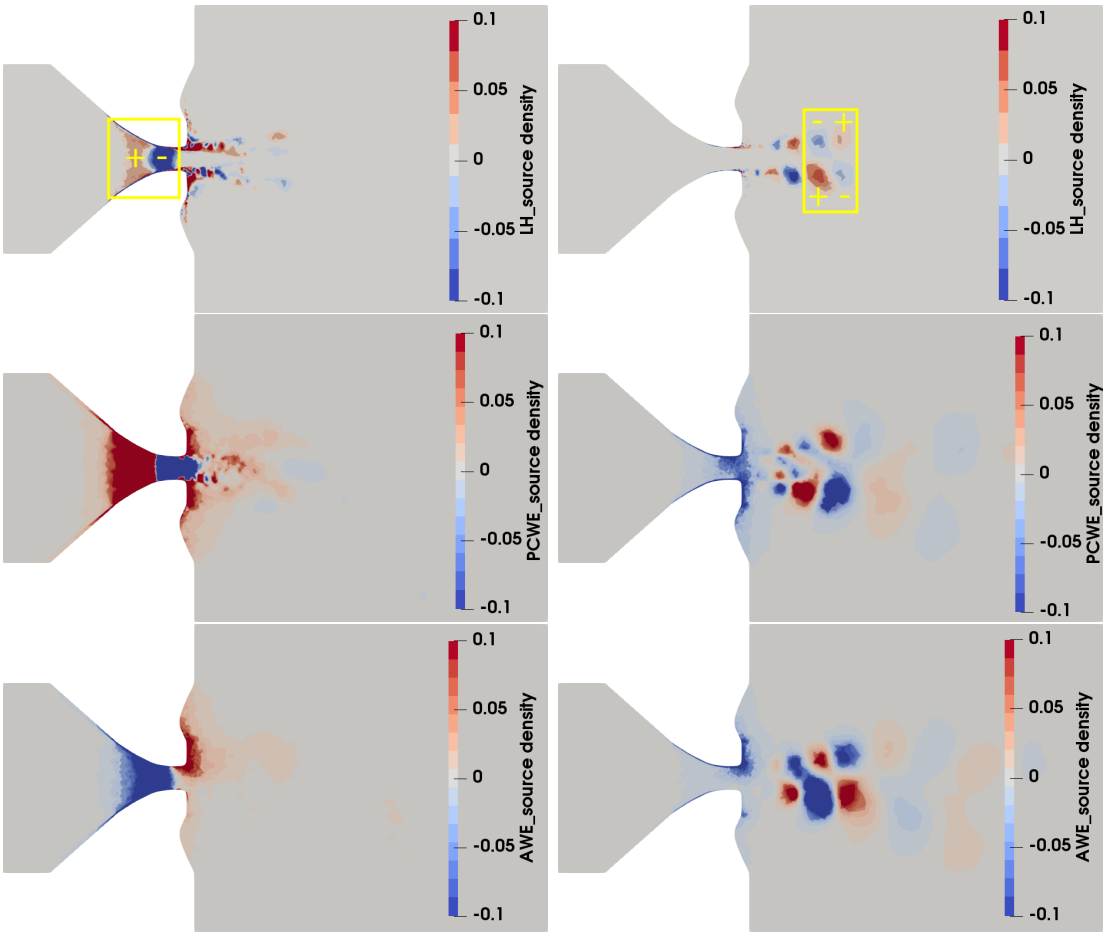


Figure E.3: Computed and normalized real part of (complex) sound source densities at **232** Hz (left) and **2486** Hz (right). The LH results are shown in the top panel, the PCWE results in the middle, and the AWE results bottom. The dipole and the quadrupole sound source structure is highlighted in the first line (LH results).

Further, the simulation of sound propagation in the vocal tract model M1 (particularly having the subglottal spaces – see Figure 8.13) with the same numerical settings as in Section 8.4 using the Lighthill analogy (LH), the simplified PCWE (sPCWE) and the AWE approaches is performed. The sound pressure levels computed at point C in front of mouth for all three aeroacoustic simulations are shown in Figure E.4. In the considered frequency range up to 3 kHz all three approaches have present five frequency peaks matching very well first five formants of vocal tract model M1, see Section 8.2. The conclusions of the aeroacoustic simulation of Section 8.4, i.e. with the VT model M2, remain valid also here. Particularly the sPCWE and the AWE approaches provides nearly identical SPL results, while the SPL in the LH case (dominated by the first frequency peak representing F1 reaching cca 140 dB) seem to be overestimated on the whole frequency range of the interest, see [139].

Since the sound sources located in the glottis and upstream in the case of VT model M1 are taken into account it is a little unexpected that the results of the sPCWE and the AWE approaches are practically the same. Also in the LH case the results do not evince any qualitative difference against the case with VT model M2. The slightly higher overall SPL of these aeroacoustic simulations compared to the performed ones with the VT model M2 can be caused by two reasons. One explanation can provide higher values of the transfer function of the VT model M1 than M2, see Figure 8.13. Another, more probable reason could be the inclusion of glottis region with significant sound sources, see Figure E.3, although during the interpolation the absolute sound sources strength in the glottis is decreased due to triangle weighting during the interpolation procedure, see Section 7.2.

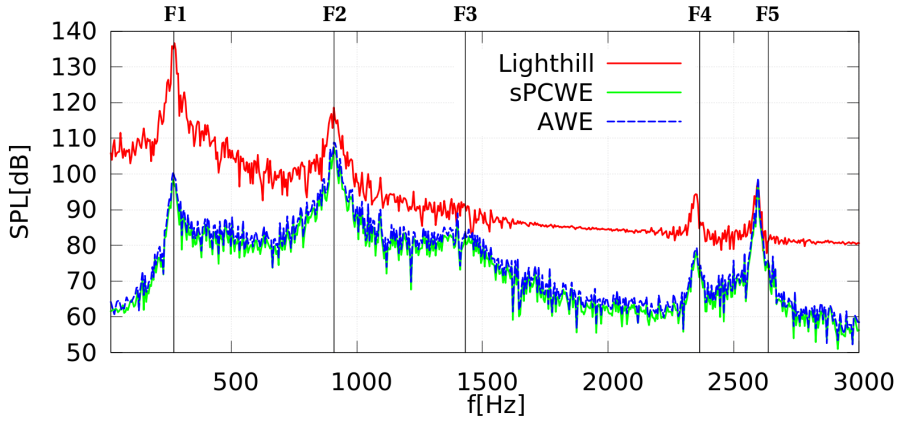


Figure E.4: Sound pressure levels of acoustic pressure in frequency domain obtained by the LH analogy, the sPCWE and the AWE approaches at point C. The black vertical lines mark the formants of vocal tract model M1, see Table 8.2.

Finally the time development of aeroacoustic numerical solution is illustrated in Figure E.5. A relatively short time interval of roughly one half of period of formant F5 = 2638 Hz of the solution sPCWE in VT model M1 is shown. A high intensity of the acoustic sources in the supraglottal cavity and a properly working damping of PML layer (obviously without reflections) can be observed.

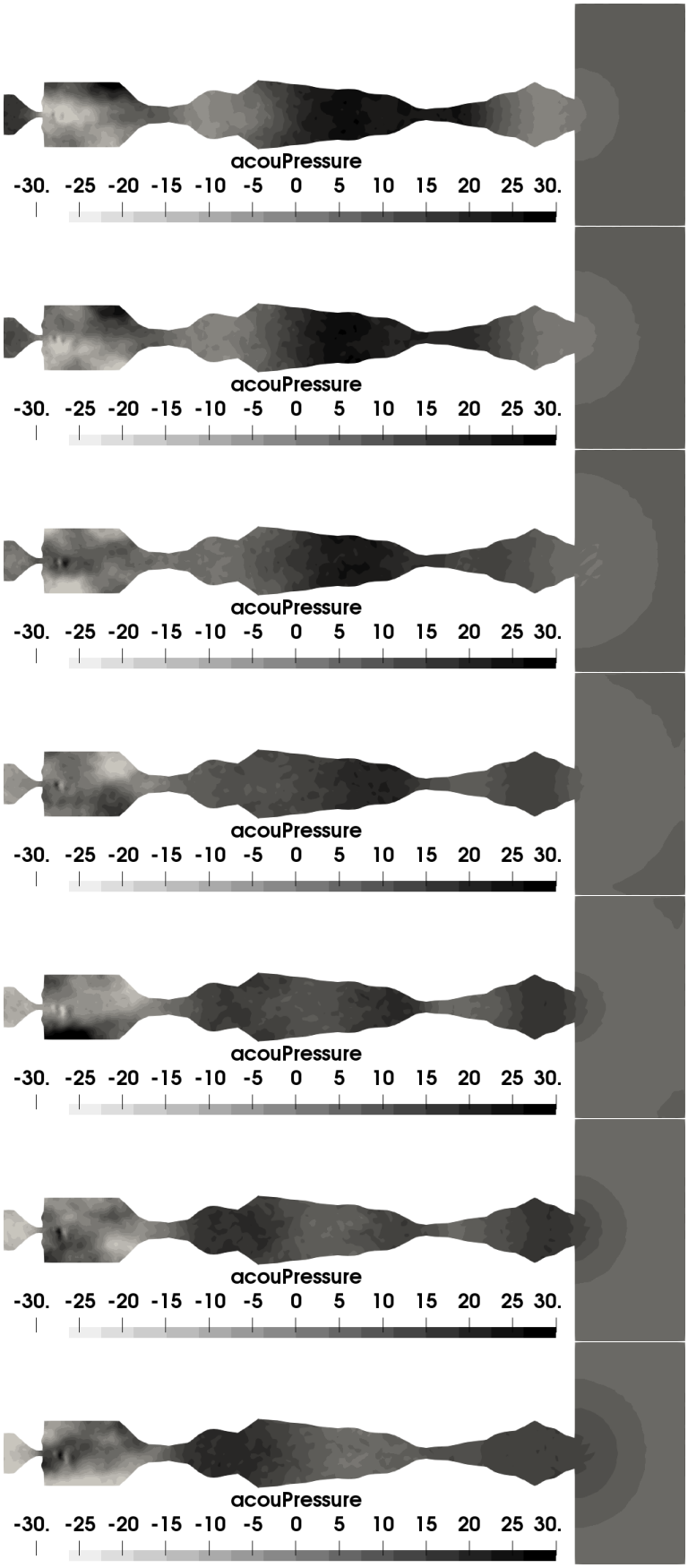


Figure E.5: Spatial distributions of acoustic pressure (scale in Pa) obtained by the sPCWE approach with the VT model M1 shown in time interval of 0.15 ms.